NASA Contractor Report 3079

(NASA-CR-3079) A GENERAL PANEL METHOD FOR THE ANALYSIS AND DESIGN OF ARBITRARY CONFIGURATIONS IN INCOMPRESSIBLE FLOWS Final Report (Boeing Commercial Airplane Co., Seattle) 200 p HC A09/MF A01 CSCL 01A H1/02
N80-24268
Unclas
22122

A General Panel Method for the Analysis and Design of Arbitrary Configurations in Incompressible Flows

Forrester T. Johnson
Boeing Commercial Airplane Company
Seattle, Washington

Prepared for
Ames Research Center
under Contract NAS2-7729

NASA
National Aeronautics
and Space Administration

Scientific and Technical
Information Office

1980

1 Report No NASA CR-3079	2 Government Accession No	3 Recipient's Catalog No
4 Title and Subtitle A General Panel Method for the Analysis and Design of Arbitrary Configurations in Incompressible Flows		5 Report Date May 1980
		6 Performing Organization Code
7 Author(s) Forrester T. Johnson		8 Performing Organization Report No D6-43808
9 Performing Organization Name and Address Boeing Commercial Airplane Company P.O. Box 3707 Seattle, Washington 98124		10 Work Unit No
		11 Contract or Grant No NAS2-7729
12 Sponsoring Agency Name and Address National Aeronautics and Space Administration Washington, DC 20546		13 Type of Report and Period Covered Contractor Report Task III, Cat. I
		14 Sponsoring Agency Code

15 Supplementary Notes

Ames Technical Monitor: Larry L. Erickson
Final Report

16 Abstract

An advanced method for solving the linear integral equations of incompressible potential flow in three dimensions is presented. Both analysis (Neumann) and design (Dirichlet) boundary conditions are treated in a unified approach to the general flow problem. The method is an influence coefficient scheme which employs source and doublet panels as boundary surfaces. Curved panels possessing singularity strengths, which vary as polynomials are used, and all influence coefficients are derived in closed form. These and other features combine to produce an efficient scheme which is not only versatile but eminently suited to the practical realities of a user-oriented environment. A wide variety of numerical results demonstrating the method are presented.

17 Key Words (Suggested by Author(s)) Analysis Design Higher order Influence coefficient Linear Panel method Potential flow Subsonic Three dimensional	18. Distribution Statement Unclassified–Unlimited Subject Category 02

19. Security Classif. (of this report) Unclassified	20. Security Classif. (of this page) Unclassified	21. No. of Pages 193	22. Price* $9.00

* For sale by the National Technical Information Service, Springfield, Virginia 22161

CONTENTS

Preceding page blank NOT FILMED

CONTENTS (Concluded)

FIGURES

FIGURES (Concluded)

1.0 SUMMARY

A general panel method for solving the boundary value problems of linear subsonic potential flow in three dimensions is presented. The method is characterized by a building block approach wherein an influence coefficient equation set is developed by assembling panel networks appropriate to the boundary value problem. Each network is composed of a paneled portion of the boundary surface on which a source or doublet singularity distribution is defined, accompanied by a properly posed set of boundary conditions. Curved panels possessing linearly varying source or quadratically varying doublet singularities are employed, and all influence coefficients are calculated in closed form. Both analysis (Neumann) and design (Dirichlet) boundary conditions are treated. In this treatment standard aerodynamic auxiliary conditions (e.g., Kutta, closure, and continuity conditions) arise as natural boundary conditions associated with various network types.

A pilot computer program was developed to assess the feasibility of the method and a wide variety of check cases were run. These included thin and thick wing analysis and design problems, wing-body analysis and design problems, convergence studies, trade studies, and timing checks. These check cases indicate that the method has the necessary flexibility, stability and accuracy, and efficiency.

1. Flexibility: The method offers the user a variety of modeling options including actual and mean surface paneling as well as velocity and potential boundary conditions.

2. Stability and Accuracy: The method displays a marked insensitivity to the size, shape and arrangement of panels and achieves accurate results with relatively sparse panel densities.

3. Efficiency: The method appears to be almost as efficient as existing first order techniques on a panel by panel basis. On a case-by-case basis the present method has significant advantages because it requires fewer panels than first order methods. These advantages become extremely important for complex configurations.

2.0 INTRODUCTION

Steady, inviscid, irrotational, and incompressible fluid flow in a domain D is characterized by a perturbation velocity potential $\phi(P)$ satisfying Laplace's equation

$$\phi_{xx} + \phi_{yy} + \phi_{zz} = 0 \qquad P \epsilon D \tag{1}$$

(compressibility effects over a wide range of subsonic Mach numbers can be approximated by the Gothert rule in which case a coordinate transformation again results in Laplace's equation).

Fluid flow boundary conditions associated with Laplace's equation are generally of analysis or design type. Analysis conditions are employed on portions of the boundary where geometry is considered fixed, and resultant pressure distributions are desired. The permeability of the fixed geometry is known; hence, analysis conditions are of the Neumann type (specification of normal velocity). Design boundary conditions are used wherever a geometry perturbation is allowed for the purpose of achieving a specific pressure distribution. Here a perturbation to an existing tangential velocity vector field is made; hence, design conditions are fundamentally of the Dirichlet type (specification of potential). The design problem in addition involves such aspects as stream surface lofting (i.e., integration of streamlines passing through a given curve), and the relationship between a velocity field and its potential.

Green's theorem (ref. 1) shows that any solution of Laplace's equation can be expressed as the potential induced by source and/or doublet singularities distributed on the boundary B of D with the singularity strengths being determined by the boundary conditions. This fact has been exploited for some time in the design of numerical solution techniques for use on large-scale digital computers.

The Douglas Neumann program (ref. 2) was spectacularly successful for its time in solving complex potential flow problems with Neumann boundary conditions. The numerical method represented the boundary by constant strength source panels with the strengths determined by an influence coefficient equation set relating the velocities induced by the source panels to the boundary conditions. The lack of provision for doublet panels limited the class of solutions to those without potential jumps and hence without lift.

On the otherhand, lifting solutions had long been generated by vortex lattice techniques using, in effect, constant strength doublet panels (ref. 3). These schemes were developed primarily for the analysis and design of thin wings. The lack of provision for source panels made the treatment of thick configurations difficult.

One of the first computer program systems for attacking arbitrary potential flow problems with Neumann boundary conditions (refs. 4, 5, and 6) combined the source panel scheme of the Douglas Neumann program with variations of the vortex lattice technique to form a general boundary value problem solver (known as the Boeing TEA 230 program). In addition to this method, many other general schemes have been developed, typical of which are the methods of references 7, 8, 9, 10, 11, and 12. These methods are all similar in technique, differing primarily in the specific integral equation used and/or the construction of the singularity distributions employed in its solution. Each scheme has achieved considerable success in a variety of applications.

A very useful feature of the TEA 230 program is the ability to handle, in a logical fashion, any well-posed Neumann boundary value problem. From its inception, the method has employed a building block approach wherein the influence coefficient equation set for a complex problem is constructed by simply assembling networks appropriate to the boundary value problem. A network is viewed as a paneled surface segment on which a source or doublet distribution is defined, accompanied by a properly posed set of Neumann boundary conditions. The surface segment can be oriented arbitrarily in space and the boundary conditions can be exact or linearized. Several doublet network types with differing singularity degrees of freedom are available to simulate a variety of physical phenomena producing discontinuities in potential. These features combine to allow the analysis of configurations having thin or thick wings, bodies, nacelles, empennage, flaps, wakes, efflux tubes, barriers, free surfaces, interior ducts, fans, etc.

While the extreme versatility of TEA 230 has been well appreciated over the past decade, the need for basic improvements has become clearly evident. Some of these stem from the fact that it sometimes takes weeks requiring the expertise of an engineer having years of experience with the method to set up and run a complex configuration. To some extent this is unavoidable; in order to correctly model a complex flow for which no prior user experience is available, the engineer must understand the properties and limitations of potential flow. However, once the boundary value problem has been formulated, the user must still contend with certain numerical idiosyncrasies and inefficiencies which require adherence to stringent paneling rules–rules which are frequently incompatible with the complex geometrical contours and rapidly changing aerodynamic length scales of the vehicle under analysis. These difficulties are directly related to the use of flat panels with constant source and doublet strengths. Methods employing these features seem to be quite sensitive to panel layout. Numerical problems arise when panel shapes and sizes vary, and fine paneling in regions of rapid flow variations often forces fine paneling elsewhere. In addition, large numbers of panels are required since numerical accuracy is often strongly affected by local curvature and singularity strength gradient. Such problems place severe limitations on the development of automatic panelers or other complementary aids aimed at relieving the user of the large amount of handwork and judgements associated with producing accurate numerical solutions involving complex geometrical shapes.

The versatility of the Boeing TEA 230 program in a user oriented environment has motivated the adoption of a similar, but less sensitive building block approach for the present method. In fact, the same network concept has been adopted and generalized to include Dirichlet boundary conditions. The treatment of Dirichlet boundary conditions not only provides the capability for designing surface segments to achieve desired pressure distributions, but also clarifies the nature of the boundary value problem associated with modeling viscous wakes and other effects through the introduction of discontinuities in the potential.

In addition, the present method has sought to enhance practical usability by improving upon the flat, constant singularity strength panels employed in the construction of the networks. The details of the present method arose from a prior analysis identifying the numerical features required to eliminate the practical difficulties encountered by the TEA 230 program. These features include the use of curved panels, linearly varying source strengths and quadratically varying doublet strengths. The present method implements these features in such a manner that all influence coefficients are evaluated in closed form thereby avoiding numerical integration—a weak link where singular integrals are involved. Other higher order panel methods have recently been studied and in some cases implemented (refs. 9, 13, and 14) with excellent results, but the present method is the first to cover in comprehensive fashion the complete spectrum of possible analysis and design boundary value problems.

The author wishes to acknowledge that section G.1 and portions of appendix D were prepared by Larry L. Erickson, NASA-Ames Research Center.

3.0 ABBREVIATIONS AND SYMBOLS

a	defined by equation (A.20)
$\bar{a}$	coordinate in direction of ν defined in figure D.3 (meters)
A_{ij}	elements of A defined by equation (D.149)
Æ	wing aspect ratio
$\bar{A}$	matrix of influence coefficients; also, orthogonal coordinate transformation defined by equation (A.5)
b	vector of specified boundary conditions; also, defined by equation (A.20); also, wing span (meters)
b_i	element of b
B	boundary of D
$\bar{B}$	matrix relating panel source or doublet distribution coefficients to singularity parameters in a neighborhood of the panel
B'	portion of B
$\bar{B}''$	portion of B
c	defined by equation (D.24); also, wing chord (meters)
c_A	defined by equation (C.7)
c_D	defined by equation (C.7)
c_L	defined by equation (C.3)
c_U	defined by equation (C.3)
$\bar{c}$	reference chord (meters); also, column matrix of source or doublet coefficients
$c(\eta)$	section chord (meters)
C_D	drag coefficient
C_F	force coefficient
C_{FY}	force coefficient in Y direction
C_{FZ}	force coefficient in Z direction
C_L	lift coefficient

℄	centerline
C(M, N)	panel far field moments defined by equation (D.83)
C_{M_X}	moment coefficient about X axis
C_{M_Y}	moment coefficient about Y axis
CP	central processor
C_p	pressure coefficient
C_{p_o}	existing or initial pressure coefficient
c_R	reference chord (meters)
c_1, c_2	defined by equation (G.18)
d	tail span (meters)
d_F	defined preceding equation (D.60)
d_H	defined preceding equation (D.41)
d_1, d_2	defined by equation (G.22)
D	fluid domain
D(M, N)	defined by equation (D.98)
D′	domain adjacent to D
E(M, N, K)	panel edge endpoint functions defined by equation (D.58)
$E1, \overrightarrow{E2}, E3, \overline{E4}$	recombinations of far field moments
F(M, N, K)	panel edge line integrals defined by equation (D.40)
g	$\sqrt{\bar{a}^2 + h^2}$
$\hat{g}$	see equation (D.141)
G(M, N)	defined by equation (D.95)
h	defined by equation (D.15)
H (M,N, K)	panel surface integrals defined by equation (D.25)

$H^*(M, N, K)$	complementary H integrals defined by equation (D.51)
$I(M, N)$	defined by equations (D.23), (D.32), (D.77) or (D.87)
$\vec{J}(M, N)$	defined by equation (D.29), (D.34), (D.85) or (D.92)
k_U	defined by equation (C.11)
k_L	defined by equation (C.11)
ℓ	panel edge coordinate defined in figure D.3 (meters)
$\hat{\ell}$	unit tangent vector along edge of Σ
ℓ_1, ℓ_2	values of ℓ at edge endpoints
L	typical side of Σ
M	number of corner point rows (appendix A)
MXK	defined by equation (D.36)
MXQ	defined by equation (D.36)
MXFK	defined by equation (D.54)
M_Y	moment coefficient about axis parallel to Y axis through reference point
M_∞	freestream Mach number
n	number of panels
$\hat{n}$	unit surface normal
N	number of corner point columns (appendix A)
NHK	defined by equation (D.49)
N_0	x coordinate of center of pressure (meters)
P	field point (meters); also, magnitude of $\vec{P}$ (meters)
$\vec{P}$	field point position vector
$\vec{P}_c$	centroid of Σ
$\vec{P}_0$	panel center defined by equation (A.2)
$\vec{P}_1, \vec{P}_2, \vec{P}_3, \vec{P}_4$	panel corner points

$\hat{P}$	$\vec{P}/P$
Q	point on boundary B (meters); also, magnitude of $\vec{Q}$; also, point on panel S
$\vec{Q}$	panel point position vector
r	distance from P to Q (meters)
R	weighted residual function; also, defined by equation (D.2)
$\vec{R}$	position vector (x, y, z) (meters)
$\vec{R}_O$	origin of local panel coordinate system
$\vec{R}_R$	origin of moment
S	simply connected portion of B; also panel surface
S_R	reference area (meters^2)
s_1, s_2	defined by equation (G.18)
$\vec{t}$	tangential vector field on S
$\vec{t}_A$	defined by equation (C.8)
$\vec{t}_D$	defined by equation (C.8)
$\vec{t}_L$	defined by equation (C.4)
$\vec{t}_U$	defined by equation (C.4)
$\hat{t}$	unit vector in direction $\vec{t}$
T	superscript denoting transpose
T_R	reference length for computing moments about axis $\hat{t}_R$ (meters)
$\vec{v}_A$	defined by equation (D.113) or (D.131)
$\vec{v}$	perturbation velocity (meters/sec.)
V	magnitude of $\vec{V}$ (meters/sec)
V_t	magnitude of $\vec{V}_t$ (meters/sec)

V_∞	magnitude of $\vec{V}_\infty$ (meters/sec)
$\vec{V}$	total fluid velocity vector (meters/sec)
$\vec{V}_A$	average of upper and lower surface velocities (meters/sec)
$\vec{v}_B$	defined by equation (D.114) or (D.132)
$\vec{v}_C$	defined by equation (D.115) or (D.133)
$\vec{v}_D$	defined by equation (D.134); also, difference at upper and lower surface velocities (meters/sec)
$\vec{V}_L$	lower surface velocity (meters/sec)
$\vec{V}_t$	tangential component of $\vec{V}$, i.e., $\vec{V} - (\hat{n} \cdot \vec{V})\hat{n}$ (meters/sec)
$\vec{V}_U$	upper surface velocity (meters/sec)
$\vec{V}_\infty$	freestream velocity vector (meters/sec)
x	chordwise coordinate (meters)
(x, y, z)	field point coordinates in local panel coordinate system
(x_0, y_0, z_0)	defined by equation (D.15)
y	spanwise coordinate (meters)
z	vertical coordinate (meters)
α	angle of attack (degrees or radians)
β	defined by equation (G.12)
β_n	defined by equation (C.3) or (C.7)
β_t	defined by equation (C.4) or (C.8)
β_1, β_2	defined by equation (G.17)
β_ϕ	defined by equation (C.11)
Γ	set of control points; also, circulation (meters^2/sec); also, gamma function

Δ	jump in value across surface
ΔC_p	jump in C_p across surface
δ	defined by equation (A.21)
δg	defined preceding equation (D.60)
δh	defined preceding equation (D.41)
ϵ	defined by equation (D.17); also, defined by equation (D.72); also, spanwise gap (meters)
$\notin$	does not belong to set
$\epsilon(M, N, K)$	defined by equation (D.52)
ζ	defined by equation (A.19)
η	defined by equation (A.19); also, tangential coordinate normal to panel edge (meters); also, fractional semispan
η_H	fractional semispan (horizontal)
η_V	fractional semispan (vertical)
θ	polar angle (degrees)
$\overline{\lambda}$	vector of unknown singularity parameters
λ_j	element of λ
λ_k	k^M singularity parameter
$\lambda(\xi, \eta, \zeta)$	singularity distribution on a panel
μ	doublet strength (meters^2/sec)
μ'	tangential derivation of doublet strength normal to a panel edge (meters/sec)
$(\mu_0, \mu_\xi, \mu_\eta, \mu_{\xi\xi}, \mu_{\xi\eta}, \mu_{\eta\eta})$	panel doublet distribution coefficients
$(\mu_0, \mu_x, \mu_y, \mu_{xx}, \mu_{xy}, \mu_{yy})$	panel doublet distribution coefficients expanded about the point (x, y, 0)
$\nu(M, N, K)$	defined by equation (D.52)
$\hat{\nu} = (\nu_\xi, \nu_\eta)$	unit edge normal defined in figure D.3
ξ	defined by equation (A.19)
(ξ, η, ζ)	panel point coordinates in local panel coordinate system

$(\hat{\xi}, \hat{\eta}, \hat{\zeta})$	orthogonal unit vector defining local panel coordinate system
ρ	defined by equation (D.19)
σ	source strength (meters/sec)
$\sigma_o, \sigma_x, \sigma_y$	panel source distribution coefficients expanded about the point (x, y, o)
$\sigma_o, \sigma_\xi, \sigma_\eta$	panel source distribution coefficients
Σ	plane quadrilateral formed by projecting panel corner points onto the local (ξ, η) plane, which for the flat approximation is the same as the near plane
$\sum_1^4$	summation over four panel edges
ϕ	polar coordinate defined by figure G.1; also, perturbation velocity potential (meters^2/sec)
ϕ_A	average perturbation potential (meters^2/sec)
ϕ_D	difference perturbation potential (meters^2/sec)
ϕ_U	upper surface perturbation potential (meters^2/sec)
ϕ_L	lower surface perturbation potential (meters^2/sec)
Φ	total velocity potential (meters^2/sec)
Φ_o	existing or initial velocity potential (meters^2/sec)
ψ	angle of yaw (radians)
Ω	set of singularity parameter locations
Λ	leading edge sweep angle (degrees); also, set of all singularity parameters
$\partial/\partial n$	$\hat{n} \cdot \vec{\nabla}$
$\partial/\partial n_P$	$\hat{n} \cdot \vec{\nabla}_P$
$\partial/\partial n_Q$	$\hat{n} \cdot \vec{\nabla}_Q$
∂C_p	desired change in C_p

$\vec{\nabla}$	gradient operator
$\vec{\nabla}_P$	gradient operator with respect to coordinates of P
$\vec{\nabla}_Q$	gradient operator with respect to coordinates of Q
$(\vec{\ })$	denotes a vector, e.g., the position vector $\vec{P}$
$(\bar{\ })$	generally denotes a matrix, e.g., $\bar{P} = \begin{pmatrix} x \\ y \\ z \end{pmatrix}$ is the column matrix whose elements are the coordinates of $\vec{P}$
$\otimes$	denotes vector cross product

4.0 THEORY

In this section we develop the integral equations which are the basis of the solution technique of the present method. In section 4.1 we consider the fluid flow boundary value problems associated with equation (1) and then in section 4.2 we use Green's theorem to derive equivalent integral equations.

4.1 FLUID FLOW BOUNDARY CONDITIONS

In this section we consider the specification of boundary values for the perturbation potential ϕ of equation (1). The boundary B of the fluid domain D contains of course the surface of the configuration being analyzed or designed. To account for viscous wakes, B is often augmented by artificial wake surfaces with boundary conditions which allow for potential jumps. In particular, a domain D which is originally multiply connected is usually made simply connected in this manner, thereby allowing the imposition of Kutta or other conditions (see fig. 1). The placement of these artificial surfaces and the selection of appropriate boundary conditions is a physical modeling problem of some complexity. We do not address such a problem specifically as it is beyond the scope of this report. However, we do consider boundary conditions which are sufficiently general to allow for the treatment of a wide variety of physical models.

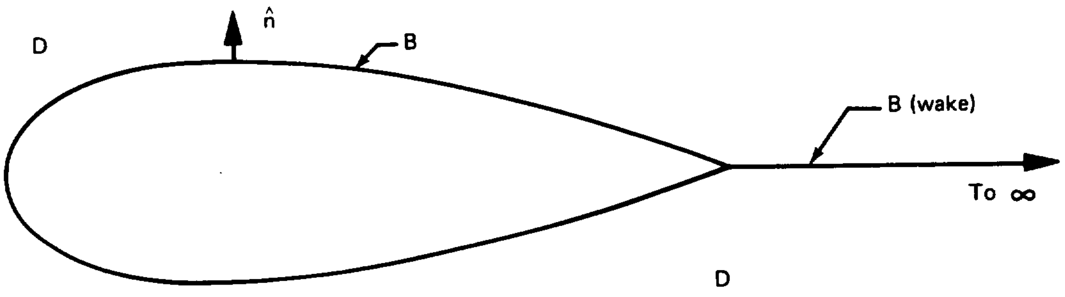

(Note: For simplicity, we display a two rather than three-dimensional domain)

Figure 1. – Fluid Domain and Boundary

As a general rule, a boundary value problem associated with equation (1) is well posed if either ϕ or its normal derivative $\frac{\partial \phi}{\partial n}$ is specified at every point of B (ref. 1, chapter 12). (For simplicity, we do not address the regularity assumptions required for a rigorous treatment of the subject.) One major exception is the interior Neumann problem where D is a finite domain and only $\frac{\partial \phi}{\partial n}$ is specified on B (fig. 2). Gauss' theorem shows that a solution can exist only if

$$\iint_B \frac{\partial \phi}{\partial n} \, ds = 0 \tag{2}$$

In case the specified values of $\frac{\partial \phi}{\partial n}$ satisfy equation (2), an infinite number of solutions for ϕ exist, although they differ by an additive constant only. If D is an infinite domain, (fig. 1) the behavior of ϕ near infinity must be restricted for a unique solution; however, sufficient restriction is an automatic consequence of the integral equation formulation of the next section, (see ref. 15, chapter 3).

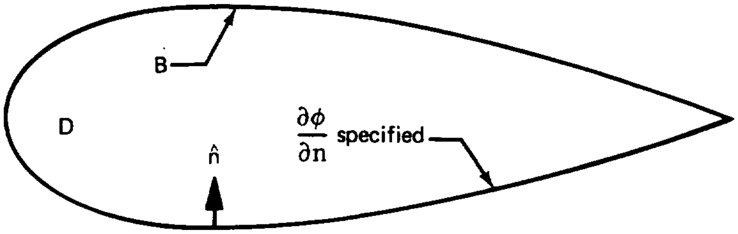

Figure 2. — Neumann Problem for Finite Domain

Neumann boundary conditions (specification of $\frac{\partial \phi}{\partial n}$) arise naturally in the analysis of fixed configurations bounded by surfaces of known permeability. For example, let S be a portion of B bounding D on the side with surface normal $\hat{n}$ (fig. 3). If S is impermeable, the normal component of the total velocity $\vec{V}$ must vanish on S. By definition, $\vec{V}$ is the gradient of the total potential Φ defined by

$$\Phi = \phi + \vec{R} \cdot \vec{V}_\infty \tag{3}$$

where $\vec{R}$ is the position vector (x,y,z) and $\vec{V}_\infty$ is the freestream velocity vector. Hence,

$$\vec{V} = \vec{V}_\infty + \vec{\nabla}\phi \tag{4}$$

and the Neumann boundary condition expressing impermeability is

$$\frac{\partial \phi}{\partial n} = - \vec{V}_\infty \cdot \hat{n} \tag{5}$$

where

$$\frac{\partial \phi}{\partial n} \equiv \vec{\nabla}\phi \cdot \hat{n} \tag{6}$$

Here, $\vec{\nabla}\phi$ is the perturbation velocity vector.

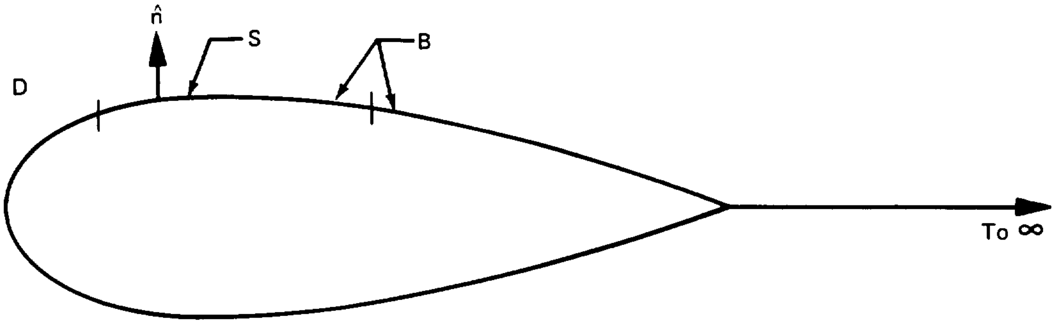

Figure 3. – Subset of Boundary and Normal

Once a solution ϕ to any boundary value problem has been found, a pressure coefficient C_p at each point on S may be computed by the formula

$$C_p = 1 - (V/V_\infty)^2 \tag{7}$$

where V_∞ is the magnitude of $\vec{V}_\infty$ and V is the magnitude of $\vec{V}$. For the particular case of an impermeable boundary, equation (7) becomes

$$C_p = 1 - (V_t/V_\infty)^2 \tag{8}$$

where V_t is the magnitude of the tangential projection of $\vec{V}$.

Dirichlet boundary conditions (specification of ϕ) arise in connection with the inverse problem, that of solving for a specified pressure distribution on S. However, the achievement of a desired pressure distribution on S is not physically significant without restrictions on the flux through S. To achieve both specified pressure and normal flow distributions on S, the position of S must in general be perturbed. To elaborate further, we must assume (for simplicity) that S is required to be a stream surface. The specification of ϕ guarantees a predetermined tangential velocity vector field, a-fortiori a predetermined pressure coefficient distribution on S via equation (8). However, the resultant normal velocity on S will not in general, satisfy equation (5) and for this, a modification of the normal vector distribution (hence position) of S is required. The total design problem is thus composed of two problems. The first is to find a perturbation potential on S yielding a specified distribution of pressure coefficient as defined by equation (8), and the second is to update S to be a stream surface in the resultant flow. The two problems are coupled and in general, an iterative procedure is required for solution. Sophisticated iteration techniques are available for this purpose (ref. 16). However, in most cases, the coupling is surprisingly weak and the two problems may be solved sequentially in such a manner that (5) and (8) hold simultaneously after relatively few iterations.

To solve the first problem, we assume that an approximation to the solution already exists. Such an approximation can be the result of a previous iteration or be defined initially by guessing a location of S and solving the pure analysis problem. The problem then, is to modify the existing potential so that its tangential velocity field yields a more desirable pressure coefficient distribution. For this purpose, we prefer to deal directly with the tangential velocity field itself. Our approach is to assume that ϕ is continuous on S and to specify a vector field $\vec{t}$ on and tangent to S such that

$$\vec{V} \cdot \hat{t} = |\vec{t}| \quad \text{where} \quad \hat{t} = \vec{t} / |\vec{t}| \tag{9}$$

For simplicity, we assume that S is simply connected and that the field $\vec{t}$ is continuous and $|\vec{t}| \neq 0$. ($\vec{t}$ is otherwise arbitrary). A good choice for $\vec{t}$ can be obtained by linearizing equation (8) about existing values, i.e.,

$$\vec{t} = \left[1 - \frac{1}{2}\,\frac{\partial C_p}{1 - C_{po}}\right]\vec{V}_{to} \tag{10}$$

where C_{po} and $\vec{V}_{to}$ are the existing values of pressure coefficient and tangential velocity respectively and ∂C_p is the desired change in pressure coefficient. (We assume $\partial C_p/2(1 - C_{po})$ is small compared to 1.)

Once a field $\vec{t}$ has been selected, certain constants of integration remain to be specified before equation (9) defines actual Dirichlet boundary conditions. One possible choice is the specification of Φ (and hence ϕ) at all points of inflow of the field $\vec{t}$ into S, i.e., points on the boundary of S where $\vec{t}$ is directed into S (see fig. 4). This choice allows the integration of Φ on S and is thus directly equivalent to Dirichlet boundary conditions. The specified values of Φ should be close to the existing values Φ_o, otherwise the resultant tangential velocity $\vec{V}_t$ will not be close to $\vec{t}$ and consequently C_p will not be close to $C_{po} + \partial C_p$. However, there is little else to guide one's choice of integration constraints without anticipating the subsequent problem of relofting S to be a stream surface.

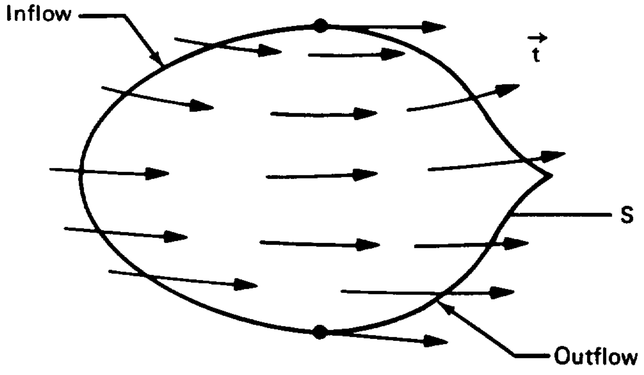

Three Dimensions

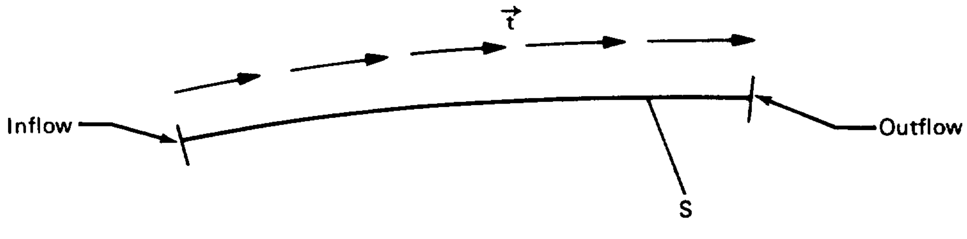

Two Dimensions

Figure 4. – Schematic of Tangential Vector Field on S

In this report we do not address the theory and mechanics of stream surface lofting although specific examples will be described in section 6. For present purposes, we assume that every point of inflow on the perimeter of S remains fixed and every other point is displaced in the direction of the local normal (or in some other nonsingular direction). In general, S will not close, i.e., the points of outflow will not remain fixed. In order to obtain such closure, we replace the specification of Φ at every point of inflow by the auxiliary condition

$$\int_L \frac{\partial \Phi}{\partial n} d\ell = 0 \qquad (11)$$

where L denotes a streamline of $\vec{t}$ on S. The condition (11) attempts to force streamlines of the resultant flow passing through points of inflow to also pass through points of outflow.

An alternative auxiliary condition can be employed when closure is unimportant, but it is desired that the resultant flow behave smoothly at each point of inflow to S (e.g. where S is a vortex sheet emanating from a wing leading or trailing edge). Here the available degrees of freedom can be used to annihilate the highest order singularity in the flow at such points. This can be achieved by specifying

$$\frac{\partial \Phi}{\partial n} = \text{finite} \qquad (12)$$

which in effect controls certain singularity strength continuity properties (see app. C).

The use of the auxiliary conditions (11) and (12) together with equation (9) results in boundary values on S which are no longer exactly equivalent to the specification of potential, but from experience appear to be generally well posed. The major exception here is the case where D is finite (fig. 2) and potential is nowhere specified on B.

We close this section by noting an important generalization of the boundary conditions of this section in the case where S bounds D on both sides (fig. 5). Then the specification of ϕ on one side may be replaced by the specification of $\Delta\phi$ (the jump in ϕ across S). Similarly, the specification of $\frac{\partial \phi}{\partial n}$ on one side may be replaced by the specification of $\Delta \frac{\partial \phi}{\partial n}$ (the jump in $\frac{\partial \phi}{\partial n}$ across S).

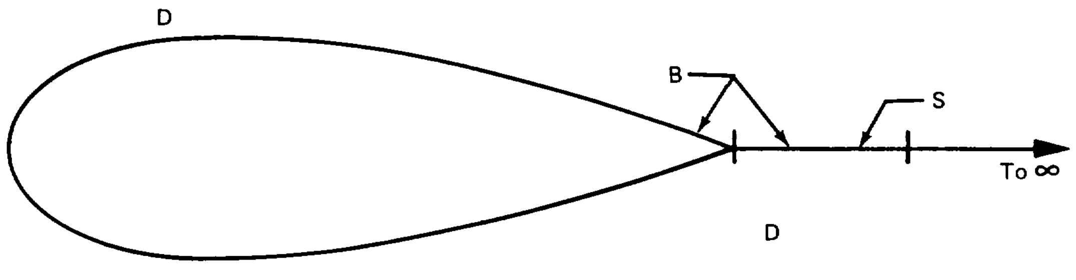

Figure 5. – Subset of Boundary Which Bounds Domain on Both Sides

4.2 DERIVATION OF INTEGRAL EQUATIONS

Under rather general assumptions (ref. 1, page 221), Green's third identity shows that any solution of (1) may be expressed as the perturbation potential induced by a combination of source singularities of strength σ and doublet singularities of strength μ distributed on the boundary B, i.e.,

$$\phi(P) = \iint_B \sigma(Q)\underline{\left(\frac{-1}{4\pi r}\right)} dS + \iint_B \mu(Q)\,\underline{\frac{\partial}{\partial n_Q}\left(\frac{1}{4\pi r}\right)} dS \qquad (13)$$

Here r is the distance from the field point P to the boundary point Q and $\frac{\partial}{\partial n_Q}$ is the derivative in the direction of the inner surface normal, i.e., directed into the domain D (see fig. 1). (On portions of B where both sides bound D the integration is performed over one side only.) If D is infinite, the representation (13) presupposes a certain behavior at infinity, namely that $\phi(P)$ is arbitrarily small when P is sufficiently distant from B.

Equation (13) represents an explicit solution to any boundary value problem of the previous section once densities σ and μ have been determined for which ϕ takes on the specified boundary values. For this purpose, equation (13) can be differentiated to yield

$$\vec{v}(P) = \vec{\nabla}_P \phi(P) = \iint_B \sigma(Q)\, \underline{\vec{\nabla}_P \left(\frac{-1}{4\pi r}\right)}\, dS + \iint_B \mu(Q)\, \underline{\vec{\nabla}_P \frac{\partial}{\partial n_Q} \left(\frac{1}{4\pi r}\right)}\, dS \tag{14}$$

(The underlined terms in equations (13) and (14) are generally referred to as kernel functions for the perturbation potential and velocity, respectively.)

Upon sending P to B in (13) and (14) and substituting the right sides of these equations into the boundary condition equations of the previous section, we obtain integral equations for σ and μ. If the boundary value problem in D is well posed, these equations are sufficient to determine unique solutions σ and μ on any portion B′ of B where both sides bound D (fig. 6). To see this, we note (ref. 1, page 221) that

$$\mu(Q) = \Delta \phi(Q) \qquad Q \epsilon B' \tag{15}$$

and

$$\sigma(Q) = \Delta \frac{\partial \phi(Q)}{\partial n} \qquad Q \epsilon B' \tag{16}$$

where the symbol Δ denotes the difference between the limiting value of the quantity on the side of B′ whose normal is $\hat{n}$ and the limiting value on the other side. However, on any portion B′ of B which bounds an adjacent domain D′ (fig. 7), an infinite number of different source and doublet distributions can produce the desired potential in D. To understand this phenomenon, we note that equation (13) defines a potential in D′ as well as D. Applying equations (15) and (16) in the present context, it follows that σ and μ are uniquely determined only when potentials in both D and D′ are specified. Thus, the determination of source and doublet distributions solving the boundary value problem in D requires the specification of potential in every domain D′ adjacent to D. This can be done explicitly, by specifying a known potential or implicitly by assigning boundary values determining a unique potential. For this purpose, the boundary B′ of D′ can be augmented by any number of additional surfaces in the interior of D′. The choice of a potential here is guided by considerations of efficiency and accuracy. For example, it is advantageous to minimize the number of integral equations required to solve for σ and μ by choosing the potential in D′ so that either σ or μ is specified on the boundary via equations (15) and (16). In this connection, the specification $\sigma = 0$ or $\mu = 0$ reduces the computation cost in solving the remaining integral equations. Finally, the potential in D′ should be chosen so as to reduce numerical errors associated with large singularity strength gradients.

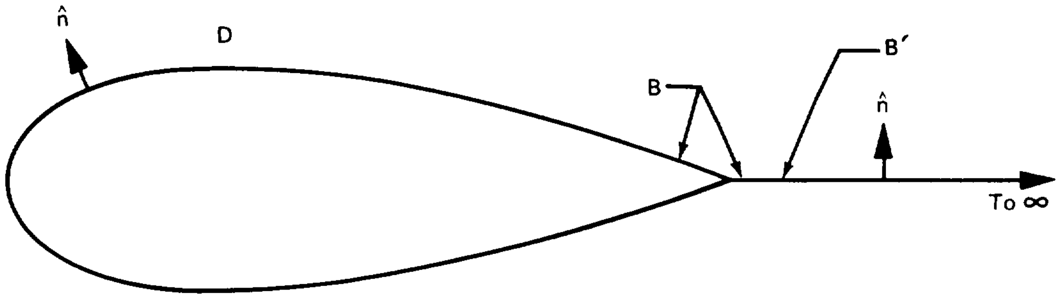

Figure 6. – Portion of Boundary Which Bounds Domain on Both Sides

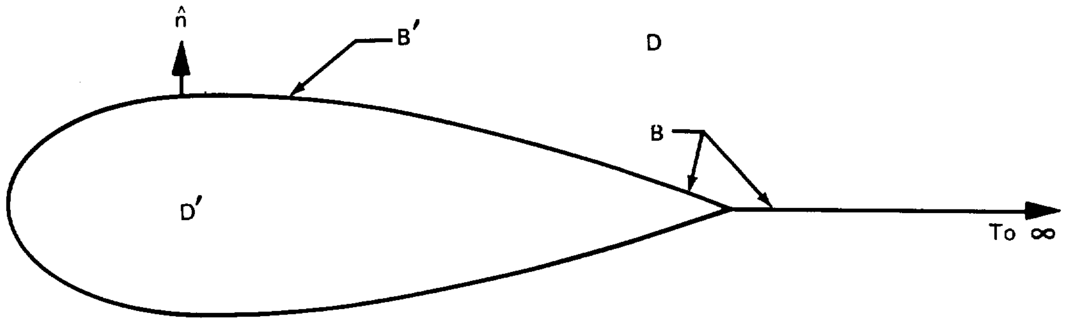

Figure 7. – Portion of Boundary Which Bounds Adjacent Domain

Several common choices illustrate these considerations. The first is the specification of zero perturbation potential in D′. From equations (15) and (16), we see that this choice implies that μ and σ are equal respectively, to the limiting values of ϕ and $\frac{\partial\phi}{\partial n}$ on the side of B′ bounding D. Specification of $\frac{\partial\phi}{\partial n}$ on this side is then equivalent to the direct specification of σ. This particular choice has the advantage that the potential in D′ does not by itself cause large gradients in σ and μ, although it does not specifically reduce the gradients caused by the potential in D. The method of reference 11 has implemented a similar choice with considerable success. A typical boundary value problem for this choice is shown in figure 8.

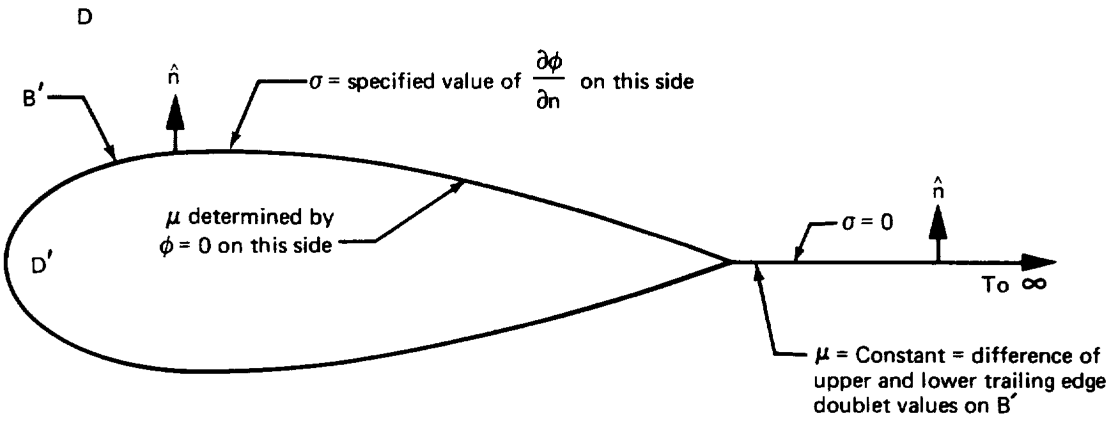

Figure 8. — Zero Perturbation Potential in Adjacent Domain

A second popular choice is the potential in D′ with the same value on B′ as the potential in D. This choice enjoys the advantage that μ is zero on B′, since ϕ is continuous across B′. The method of reference 2 pioneered this alternative. One problem with this choice in connection with lifting configurations is that the source strength becomes unbounded at any point of B′ common to a surface B″ bounding D across which potential is discontinuous, e.g., a wake. For this reason, the (doublet) surface B″ is usually continued into D′ and assigned boundary values designed specifically to reduce the source strength gradients everywhere on B′. (Depending on the specific technique, the solution of additional equations may be required.) The methods of reference 6 and 9 have used this device with excellent results. A typical boundary value problem for this choice is shown in figure 9.

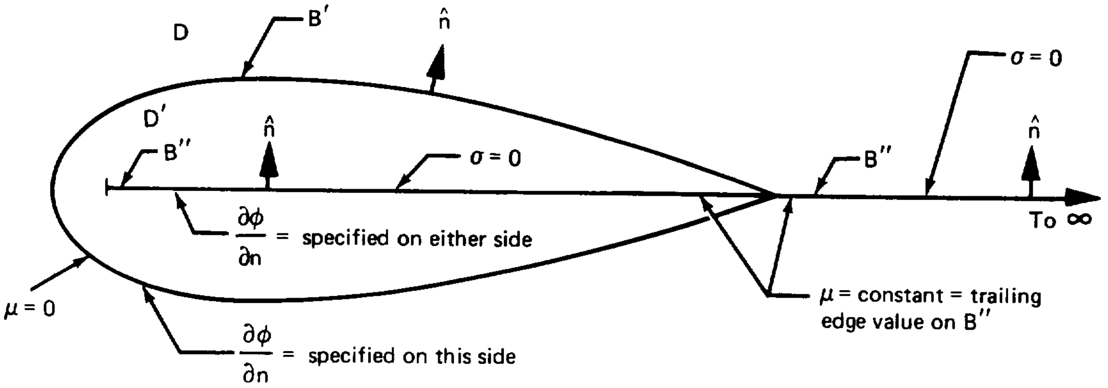

Figure 9. – Source Surface Modeling

A third successful alternative is the technique used in reference 8. Sources are again the primary singularity on B′, but the requirement of additional boundaries in D′ is avoided by allowing a limited (e.g., linear) variation of doublet strength on B′. A typical boundary value problem for this choice is shown in figure 10.

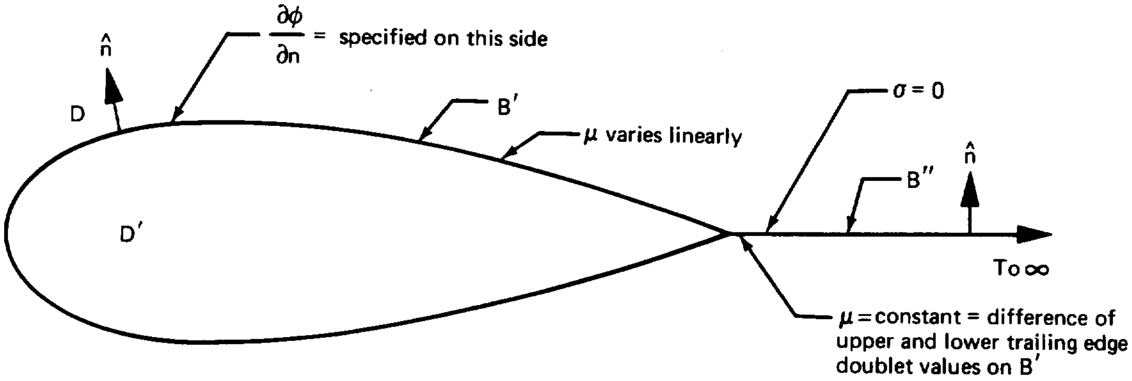

Figure 10. – Limited Variation of Doublet Strength on Boundary

A fourth alternative is the specification of a potential in D′ with the same normal derivative on B′ as that of the potential in D. This choice enjoys the advantage that σ is zero on B′ since $\frac{\partial\phi}{\partial n}$ is continuous across B′. Moreover, special treatment of intersecting doublet surfaces is not required. However, if D′ is finite, such a specification does not determine a unique potential in D′ in view of our earlier discussion of the interior Neumann problem. This indeterminancy is reflected by the fact that a constant doublet density on a closed surface induces no velocity in the interior; therefore, it would be impossible to solve for a unique doublet density on B′. Here again, the problem can be remedied by introducing an artificial boundary surface in D′ on which potential is specified, e.g., a source surface on which $\phi = 0$. If the specified values of $\frac{\partial\phi}{\partial n}$ on B′ satisfy equation (2), total source strength on such a surface will vanish. Otherwise, the source strength sum will be precisely that required to produce the net flow through B′ desired. A typical boundary value problem for this choice is shown in figure 11.

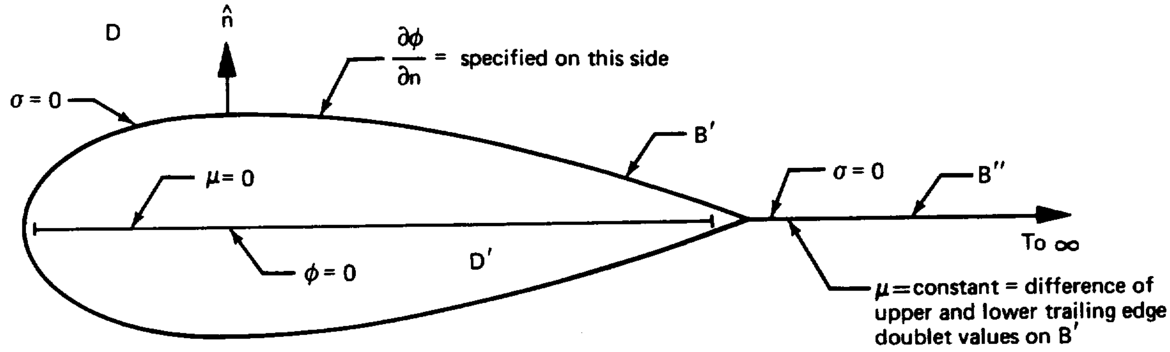

Figure 11. – Doublet Surface Modeling

5.0 METHOD

The present method uses a panel scheme to achieve a numerical solution to equations of section 4.2. Panel schemes proceed by first dividing the boundary surfaces into panels. In the present method, source (σ) and/or doublet (μ) distributions are assigned to each panel. These distributions are expressed in terms of unknown singularity parameters λ_j associated with the panel and neighboring panels. A finite set of control points (equal in number to the number of singularity parameters) is selected at which the boundary conditions are imposed. Evaluation of the boundary conditions results in a finite set of linear equations denoted symbolically by

$$\bar{A}\bar{\lambda} = \bar{b} \tag{17}$$

Here, $\bar{\lambda}$ is the vector of unknown singularity parameters, $\bar{b}$ the vector of specified boundary conditions, and $\bar{A}$ the matrix of "influence coefficients." (A_{ij} represents the influence of λ_j on the boundary condition b_i.) The solution of (17) for $\bar{\lambda}$ may be accomplished by any number of computer algorithms; whereupon substitution of the corresponding distributions of σ and μ into equations (13) and (14) yields the potential and velocity at any point in D or on B. Pressure coefficients may be computed from the velocities; following which force and moment coefficients may be obtained by integration.

The approach of the present method in performing these tasks is a building block approach in which the influence coefficient equation set (17) is defined by assembling independent networks of panels, each of which contributes as many equations as unknowns. A network is defined as a paneled portion of the boundary on which either a source or doublet distribution is defined accompanied by a properly posed set of analysis (Neumann) or design (Dirichlet) boundary conditions. All networks fall into four catagories: source/analysis, doublet/analysis, source/design, and doublet/design. The present method employs a variety of standard networks including one source/analysis, one doublet/analysis, two source/design, two doublet/design and two special wake/design networks. The construction of each network requires numerical development in three areas: A. Surface geometry definition; B. Singularity strength definition; and C. Control point selection and boundary condition specification. Essential features of the computational schemes in each of these areas are summarized below and discussed in detail in appendixes A, B, and C, respectively.

A. Geometry input for a network is assumed to be a grid of corner point coordinates partitioning the network surface into panels. Panel surface shape is obtained by fitting a paraboloid to corner points in an immediate neighborhood by the method of least squares. (See app. A.)

B. Discrete values of singularity strength at certain standard points on each network are assigned as singularity parameters (the λ_j of equation (17)). Singularity splines are constructed for each network type by fitting a linear (source) or quadratic (doublet) distribution on each panel of the network to a subset of these discrete singularity parameters by the method of least squares. (That is, the singularity distribution $\sigma(Q)$ or $\mu(Q)$ for each panel is expressed as a sum of products of singularity parameters in an immediate neighborhood times linear or quadratic distributions of Q.) The least square technique allows minor discontinuities in value and gradient of the singularity strength across panel edges, although virtual continuity is assured if paneling is sufficiently dense. An alternate spline enforcing strict continuity of value at panel corners is available for the doublet/analysis network. For coarse paneling, this spline yields local doublet gradients which better reflect the global variations of doublet strength. (See app. B.)

C. Certain standard points on each network are assigned as control points. These points include panel center points as well as network edge points. Boundary conditions involving the specification of potential or velocity are applied at panel center points for the purpose of controlling local properties of the flow, e.g., no flow through the surface. Auxiliary boundary conditions at edge control points serve to convey the proper continuity of singularity strength and gradient across network junctions, or else to control global properties of the flow such as closure. In the case of design networks, these boundary conditions remove the degrees of freedom produced by specifying only tangential derivatives of the potential at panel center control points (see the discussion for equations (9), (10), (11), and (12)). In the process, they enforce standard aerodynamic auxiliary conditions such as the Kutta condition, closure condition, and the Helmholtz law. (See app. C.)

Once each network has been constructed, the solution of the flow problem requires numerical development in three additional areas: D. Calculation of the influence coefficients comprising the matrix A of equation (17); E. Solution of the matrix equation (17) for the singularity parameters λ; and F. Computation of aerodynamic quantities of interest. Essential features of the schemes used in each of these areas are summarized below and discussed in detail in appendixes D, E and F respectively.

D. Two expansions of the induced potential and velocity kernels are employed. The near field expansion is based upon the assumption of a small panel curvature; the far field expansion requires a relatively large separation between the field point and panel. All resultant integrals are evaluated in closed form, using linear recursion relations that have as initial conditions the fundamental logarithm and arctangent transcendental terms appearing in flat panel, constant singularity strength techniques. (See app. D.)

E. The Crout decomposition technique is employed by the pilot code to solve equation (17). This technique decomposes the matrix A into the product of a lower triangular matrix and an upper triangular matrix from which point the solution λ is easily obtained by forward and backward substitution. Application of the technique is accomplished with the aid of mass storage devices. For this purpose, the matrices (initially generated row by row) are partitioned into randomly accessible blocks. In-block partial pivoting is used to control error growth. (See app. E).

F. Once the singularity parameters λ_j are found and the corresponding source and doublet distributions determined, the potential and velocity at each panel center control point are calculated from equations (13) and (14). A distribution of pressure coefficients on each network is then found using the least square fit techniques of appendix B. Finally, this distribution is integrated to yield force and moment coefficients. (See app. F.)

6.0 RESULTS

6.1 INTRODUCTION

In this section, we present computed results demonstrating the numerical characteristics of the present method. These results were generated by a pilot computer program written in FORTRAN IV and COMPASS 3 languages for the CDC 6600 digital computer. Because of the versatility of the method, a complete analysis and display of all its capabilities would require an enormous amount of effort. Each application of the method, especially when design networks are involved, could well be the subject of a separate study and report, involving modeling alternatives, timing and convergence checks, experimental comparisons, etc. One such study has already been performed in connection with the application of a doublet/design network to the solution of leading-edge vortex flow problems (ref. 17).

Hence, the results presented in this report are intended to give a broad view of the capabilities of the method. Because the method may be the basis of future production codes covering the subsonic, supersonic, steady and unsteady flow regimes, we have included cases which go somewhat beyond demonstrating mere feasibility. Such cases are the result of systematic efforts to test critical numerical features of the method, optimize modeling for accuracy and efficiency, and explore techniques for practical use.

Numerical results are presented in sections 6.2 through 6.7 and are classified according to the network types featured. In section 6.2, we demonstrate use of the source/analysis network with some rather simple test cases. In section 6.3, we present results for the doublet/analysis network. In contrast to source networks, the doublet networks have always required more careful treatment, because doublets create a discontinuity in potential itself, and also induce a higher order singularity in the flow [equations (D.121) and (D.141)]. Therefore, we present cases testing convergence and sensitivity, related to the use of this network. Section 6.4 contains results for general analysis problems involving both source/analysis and doublet/analysis networks. Cases are presented comparing alternate formulations. In section 6.5, we demonstrate the use of source/design networks with cases involving actual surface relofting. In section 6.6, we describe the application of a doublet/design network to the solution of leading-edge vortex flow problems (ref. 17). Finally, in section 6.7 we discuss the numerical efficiency of the present method and pilot code.

6.2 SOURCE/ANALYSIS NETWORKS

6.2.1 CIRCULAR CYLINDER

An impermeable circular cylinder in a uniform flow was simulated with a type 1 (source/analysis) network* containing 6, 12, and 18 equally spaced curved panels for the whole cylinder. The panels were elongated in the cross flow direction to approximate two dimensional flow.

---

* Schematics of singularity parameter locations and control point locations are given in figures B.1. and C.1, respectively, for various network types.

Boundary conditions of type equation (C.3) with $c_U = 0$, $c_L = 0$ and $\beta_n = 0$ were applied at each panel center control point. Resultant source strengths and tangential velocity magnitudes are plotted in figure 12, along with exact data and results generated by earlier flat-panel, constant-strength methods. The 18 panel case is virtually indistinguishable from the exact solution. (In contrast, 35 flat, constant strength panels still produce a noticeable error in source strength. Due to fortuitous error cancellation (ref. 13), flat, constant strength source panels produce exact tangential velocities for a cylinder.) The six panel case begins to deviate significantly from the exact solution. Analysis shows the errors are primarily due to the violation of restriction (A.21) of appendix A. The inadequate panel density results in an approximate surface which bulges to a radius of 1.15 at panel center points.

6.2.2 SPHERE WITH RANDOM PANELING

An impermeable sphere in a uniform flow was simulated with an 81 panel source/analysis network. For this purpose, advantage was taken of one plane of symmetry by paneling half the sphere only, and then calculating the perturbation potential as the sum of the potentials induced at a point and its image. A 10 x 10 corner point grid was generated, using a random number generator leading to a wide variation in panel size and shape as shown in figure 13a. The use of curved panels produced a geometry remarkably close to spherical. All 81 control points fell within a distance of 0.005 from the surface of the unit sphere, despite the fact that the maximum diameter of some panels spanned an arc of over 60°. As in the previous case, the use of such large panels violates restriction (A.21). (The consequences are not so serious in the present example because of the number and proximity of adjacent grid points used to obtain panel surface fits.)

Velocity magnitude at each control point is plotted in figure 13b as a function of polar angle relative to the freestream direction. Agreement with the exact solution is good. In contrast, an analysis with flat constant strength source panels (representative of earlier technology) using the same panel arrangement, resulted in velocity magnitudes (V/V_∞) that were scattered between 1.2 and 1.7 in the range $85° < \theta < 95°$. This example demonstrates the extreme forgiveness of the method to irregular paneling, a feature which greatly enhances its practical usability for applications involving complex configurations where regular, evenly spaced paneling cannot always be arranged.

6.3 DOUBLET/ANALYSIS NETWORKS

6.3.1 THIN CIRCULAR WING

In this example, a thin circular wing at an angle of attack was simulated with a mean surface doublet/analysis network (type 2 with the least square doublet spline of section B.2 of appendix B). A doublet/wake network (type 8 with the least square spline) was abutted to the trailing edge to yield a lifting solution. (See, for example, ref. 18, page 538 for the necessity of using a wake to generate a lifting solution.) Paneling for the right half of the wing and wake is displayed in figure 14a. On the wing, cosine spacing was employed along latitude and longitude lines with panels becoming triangular at the tip. The wake panels were attached to corresponding trailing edge panels and elongated in the stream direction. The entire wing and wake consisted of 108 effective panels (54 actual panels since symmetry was exploited). The freestream was directed in the plane of the wing and (linearized) boundary conditions of

(a) SOURCE STRENGTH

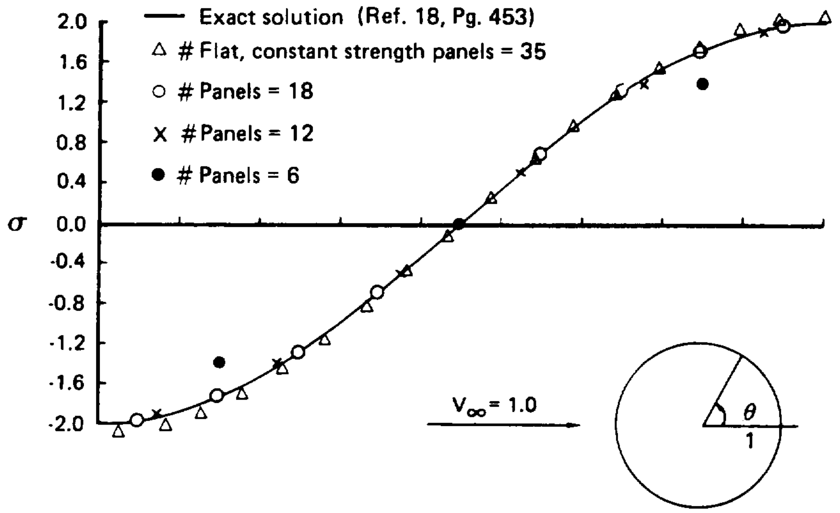

(b) TANGENTIAL VELOCITY

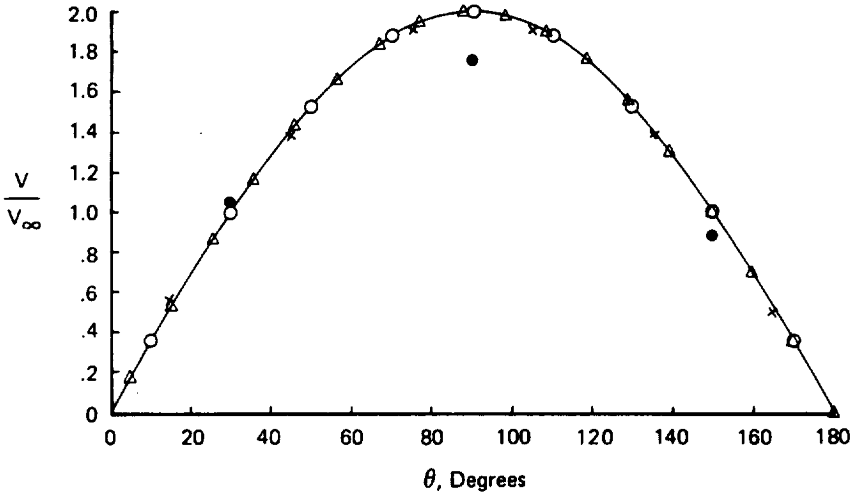

Figure 12. – Circular Cylinder

(a) RANDOM PANELING OF SPHERE, SIDE VIEW

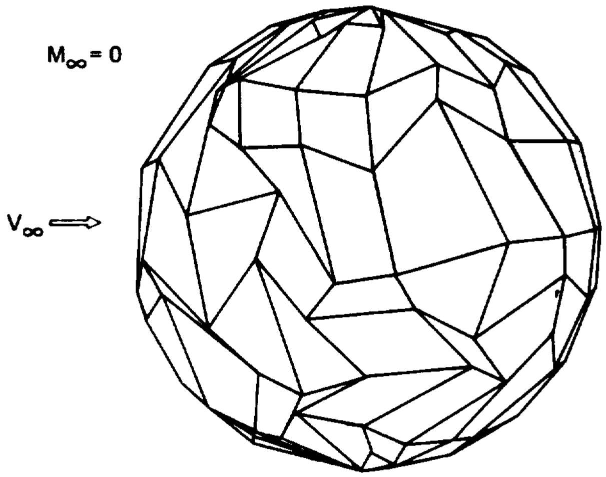

(b) VELOCITY MAGNITUDE AT CONTROL POINTS

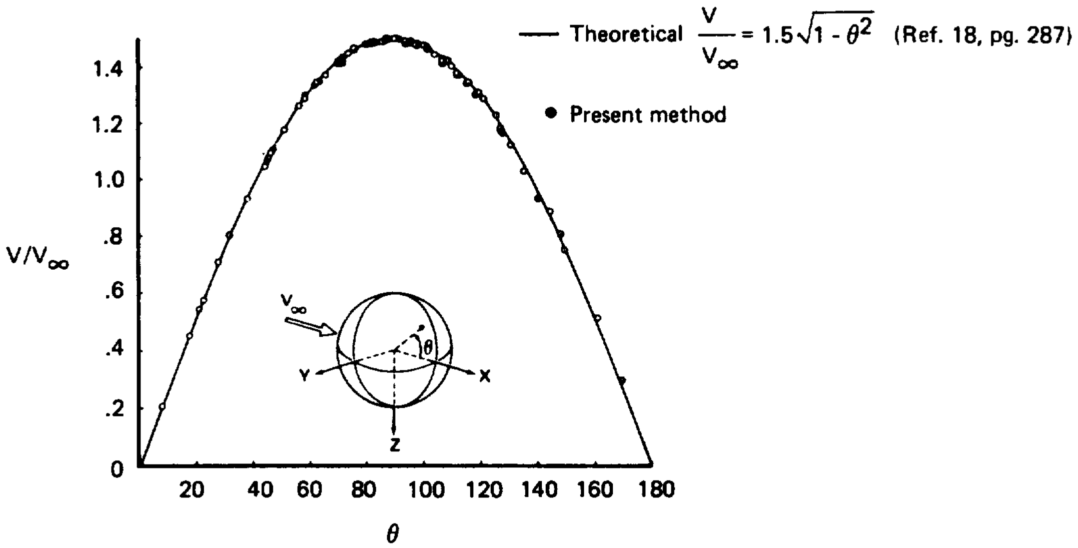

Figure 13. – Sphere

(a) CIRCULAR WING AND WAKE PANELING

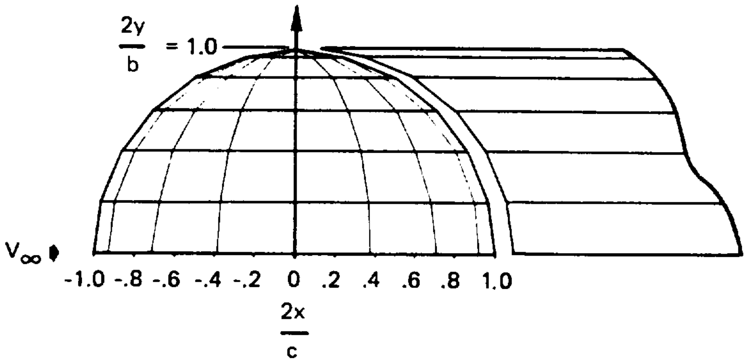

(b) SPANWISE LIFT DISTRIBUTION

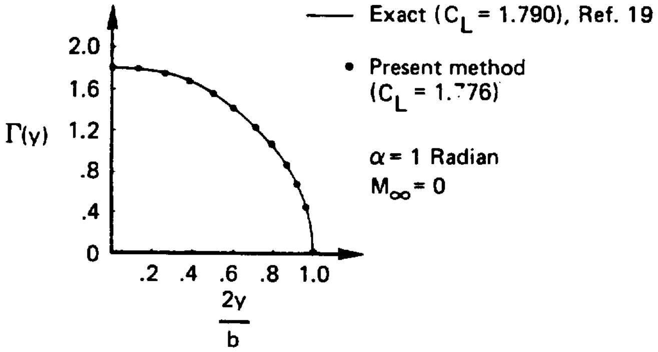

(c) CHORDWISE PRESSURE DISTRIBUTIONS

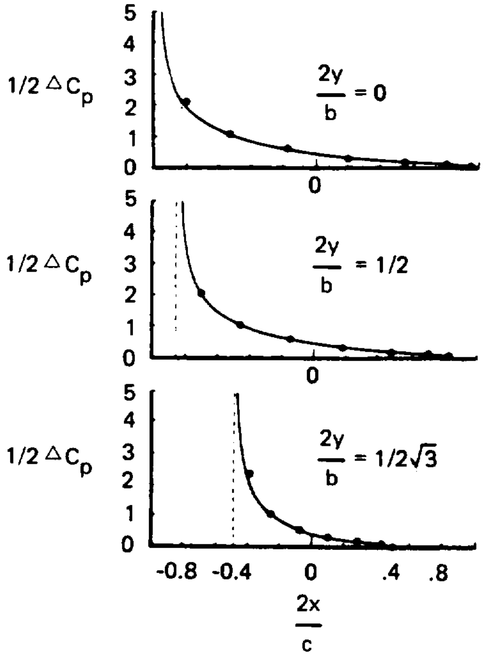

Figure 14. — Circular Wing

type equation (C.3) with $c_U = 1$, $c_L = 0$, $\beta_n = -1$ employed to simulate unit angle of attack for comparison with angle of attack slope data.

The resultant spanwise circulation distribution is plotted in figure 14b. The plotted points were obtained from doublet strength along the trailing edge and agree well with the exact solution. Integration of this distribution produced a lift coefficient of 1.776 versus the exact coefficient of 1.790. (In particular, we have $C_L = \frac{2}{V_\infty S_R} \int_{T.E.} \mu dy$. See page 546 of Ref. 18.) Pressures at three span stations are shown in figure 14c and also agree well with the exact solution.

It is instructive to consider the role of the network edge control points in this case (see fig. C.1 and section C.3 of app. C). The boundary conditions at leading edge control points automatically forced doublet strength to be zero on that edge since doublet strength was zero ahead of the leading edge. The boundary conditions at centerline control points forced the spanwise derivative of doublet strength to be zero on the centerline because of the implied presence of an image doublet surface. Finally, the boundary conditions at trailing edge control points in conjunction with those at opposing wake control points produced continuity of doublet strength and its transverse derivative onto the wake. Because of the particular construction of the doublet distribution on the wake network, this resulted in a vanishing chordwise derivative of doublet strength at the wing trailing edge. Recalling that doublet strength is identical to potential jump (equation 15), we see that all the usual planar wing edge conditions including the Kutta condition were automatically satisfied.

6.3.2 THIN SWEPT WING WITH RANDOM PANELING

Figure 15 shows the stability of the mean surface doublet/analysis network (type 2 with least square doublet spline) under extreme conditions of panel size, shape and control point location. Here, 48 panels were used to represent the right half of a thin swept wing at 5.7° angle of attack. (The wake network is not shown but is similar to that of the previous case). Boundary conditions were specified as in the previous example. The wing panel layout was defined by means of a random number generator, resulting in panels that varied considerably in shape and size, that were occasionaly nonconvex, overlapping, and even inverted. Nevertheless, the spanwise lift distribution as shown in figure 15b is highly accurate. Chordwise pressure distributions displayed in figure 15c are likewise stable and deviate appreciably from the reference solution only near the leading edge where pressure becomes singular. Mismatches in doublet strength and derivative across panel edges occurred in this region, indicating that finer leading edge paneling is required for accuracy. (For the two values of η shown, there are only two panels over approximately the first one-third of the wing chord at $\eta = 0$ and three panels at $\eta = 0.5$).

6.3.3 THIN RECTANGULAR WING WITH VARYING PANEL DENSITIES

For this case, a thin rectangular wing of aspect ratio 2 at 0.01 radians angle of attack was analyzed, using varying panel densities to check convergence of the solution. Symmetry was exploited and the right half of the wing was simulated with a mean surface doublet/analysis network (type 2 with the continuous doublet spline of section B.3 of appendix B). The right half of the wake was simulated with a doublet/wake network (type 8 with the continu-

(a) SWEPT WING RANDOM PANELING

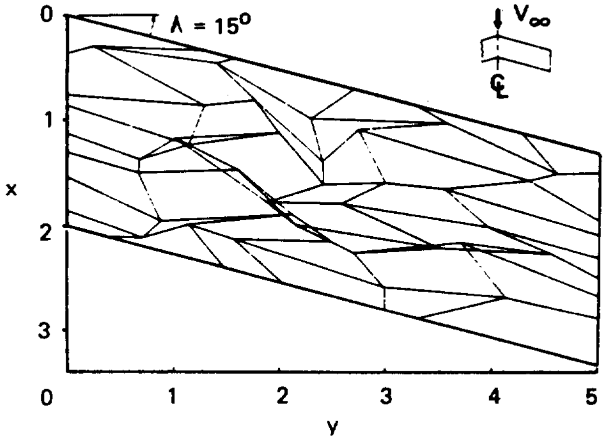

(b) SPANWISE LIFT DISTRIBUTION OF SWEPT WING

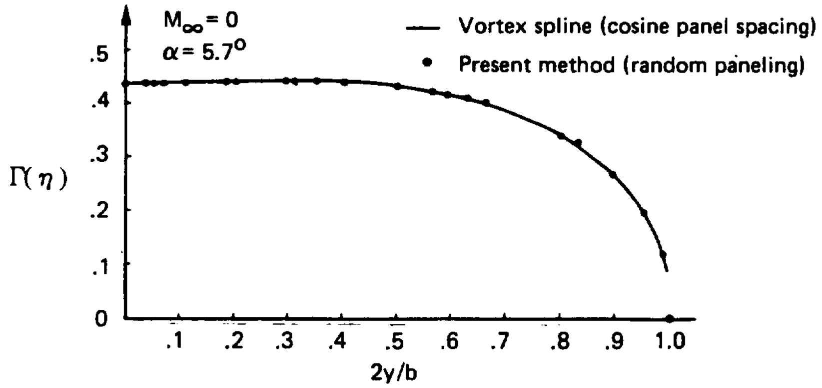

(c) CHORDWISE PRESSURE DISTRIBUTION FOR SWEPT WING

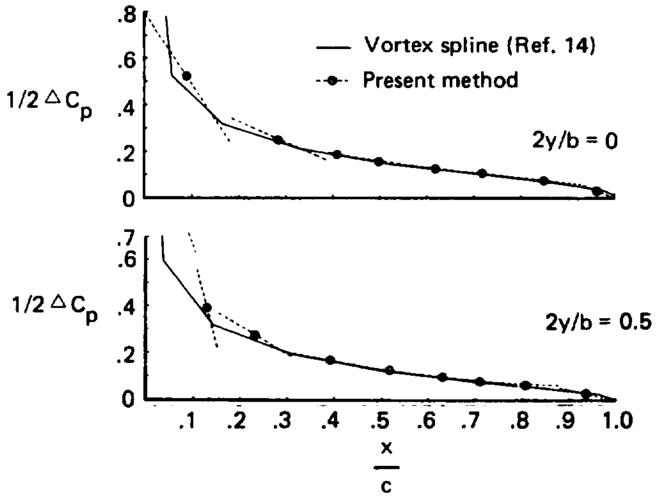

Figure 15. – Swept Wing

ous doublet spline). Both uniform and cosine spacing were employed with typical panel layouts shown in figure 16a. Cases were run with 4, 16, 49, 64, and 256 wing panels. Boundary conditions were imposed in the same manner as in the two previous examples.

Resultant lift coefficients are plotted in figure 16b. (All values have been scaled to one radian angle of attack.) Lift coefficients shown were obtained by integrating trailing edge doublet strength as before. Lift coefficients can also be calculated by integrating panel pressures as described in appendix F. For the continuous doublet/analysis spline, these values approach close agreement when paneling becomes sufficiently dense to produce negligible truncation errors. For example, the lift coefficients calculated by integrating panel pressures differed by 4.3%, 1.3%, 0.49%, 0.36%, -0.03% for the 4, 16, 49, 64 and 256 panel cases with cosine spacing, and 4.3%, 1.5%, 0.66%, 0.53%, -0.04%, for the same cases with uniform spacing. (Our observation has been that the deterioration of computed lift coefficients with decreasing panel density is less for values calculated by integrating trailing edge doublet strength, although in this case, the values calculated by integrating pressures happen to be better because of fortuitous truncation errors, due to rapid span variations near the tip.) The lift coefficients are apparently convergent with that of the 256 panel case using cosine spacing differing from that of the highly accurate and converged solution of reference 20 by less than 0.05%. The triangular symbols indicate the number of pressure modes rather than panels. The equal spacing cases converge somewhat slower than cosine spacing cases and this is probably a result of the relatively sparse paneling near the leading edge where pressure gradients are large.

The locations of the centers of pressure are plotted in figure 16c and demonstrate convergence as well. Spanwise lift distributions are plotted in figure 16d and 16e. Chordwise pressure distributions at several span stations are plotted in figures 16f and 16g. These plots confirm convergence. The 16 panel case with cosine spacing is already sufficiently accurate for most purposes. The 64 panel case with cosine spacing is highly accurate.

6.3.4 THIN RECTANGULAR WING WITH PANEL MISMATCHES

The ability to refine panel density in regions of interest without refining panel density elsewhere is essential for the practical usability of any panel method. The present example demonstrates the characteristics of the present method in this regard, using the wing and network types of the previous example. In figure 17a, we display panelings for the right half of the wing and associated lift and moment data. In each case, three networks were used to represent the wing and two were used to represent the wake as shown on the left of the figure. Networks I, II and III were assigned panelings corresponding to the representation of the wing by 144 uniformly spaced panels. Network IV was assigned N x N, uniformly spaced panels with N = 2, 3, 4, 6, 12 and network V was paneled accordingly.

It was anticipated that the only successful cases would be those with N = 2 and N = 6 where the edge control points of network IV were directly opposed by those of the adjacent networks (see fig. C.1. of app. C.) Surprisingly, all cases displayed basic stability. The matching of pressure (ΔC_p) and circulation (Γ) across the edges of network IV was virtually exact for the case N = 6. Matching for the case N = 2 is displayed in figures 17b and 17c, and matching for the case N = 4 is displayed in figures 17 d and 17e. The circulation is of prime

(a) TYPICAL PANEL LAYOUTS

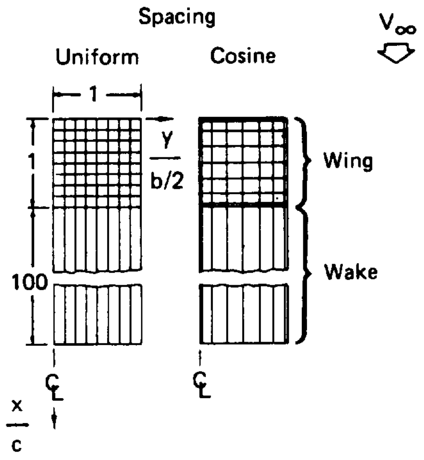

(b) LIFT COEFFICIENTS

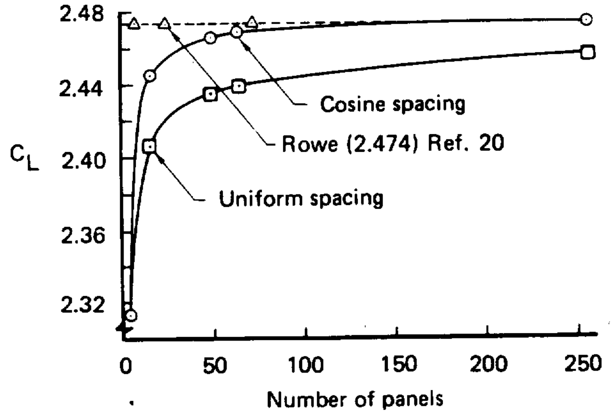

(c) CHORDWISE LOCATION OF CENTER OF PRESSURE

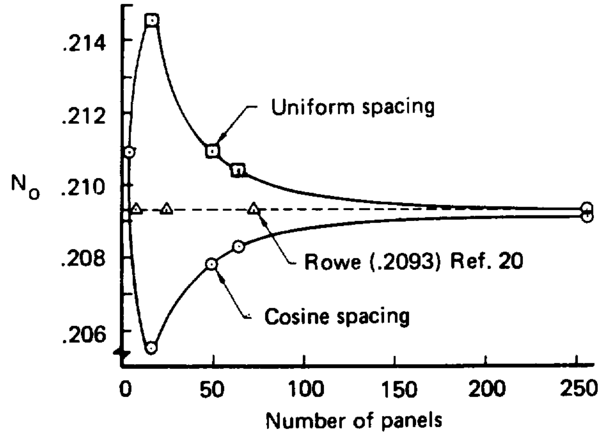

Figure 16. — Thin Rectangular Wing With Varying Panel Densities (α = 1 radian)

(d) SPANWISE LIFT DISTRIBUTIONS

(Cosine spacing)

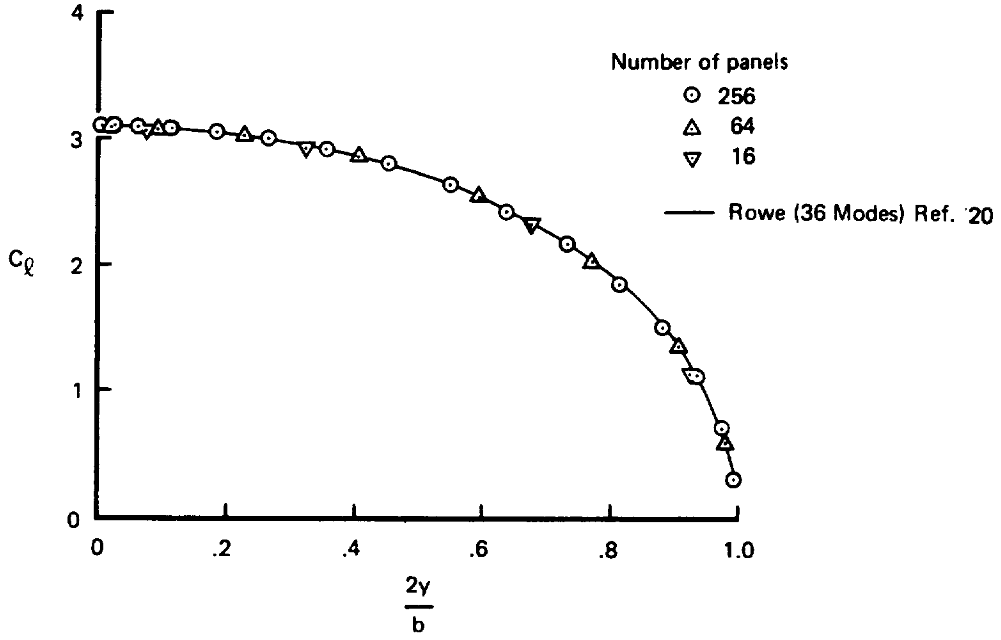

(e) SPANWISE LIFT DISTRIBUTIONS

(Uniform spacing)

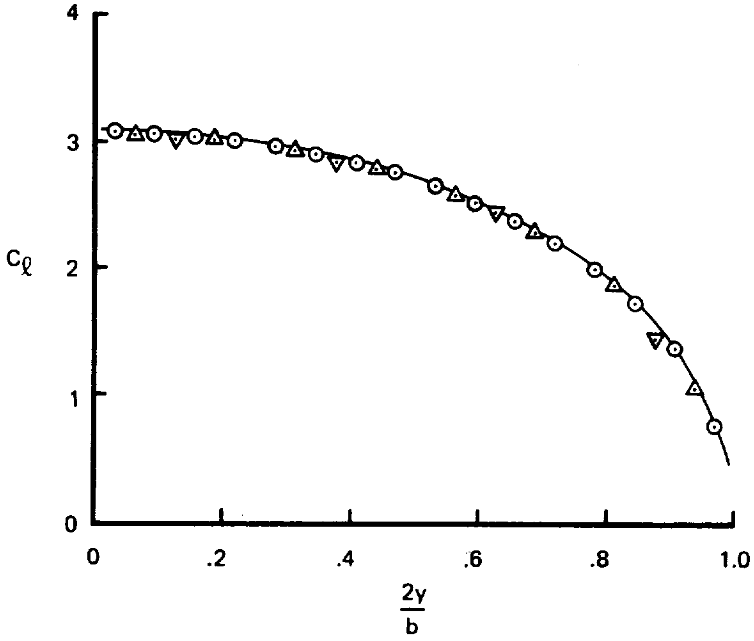

Figure 16. — (Continued)

(f) CHORDWISE PRESSURE DISTRIBUTIONS (COSINE SPACING)

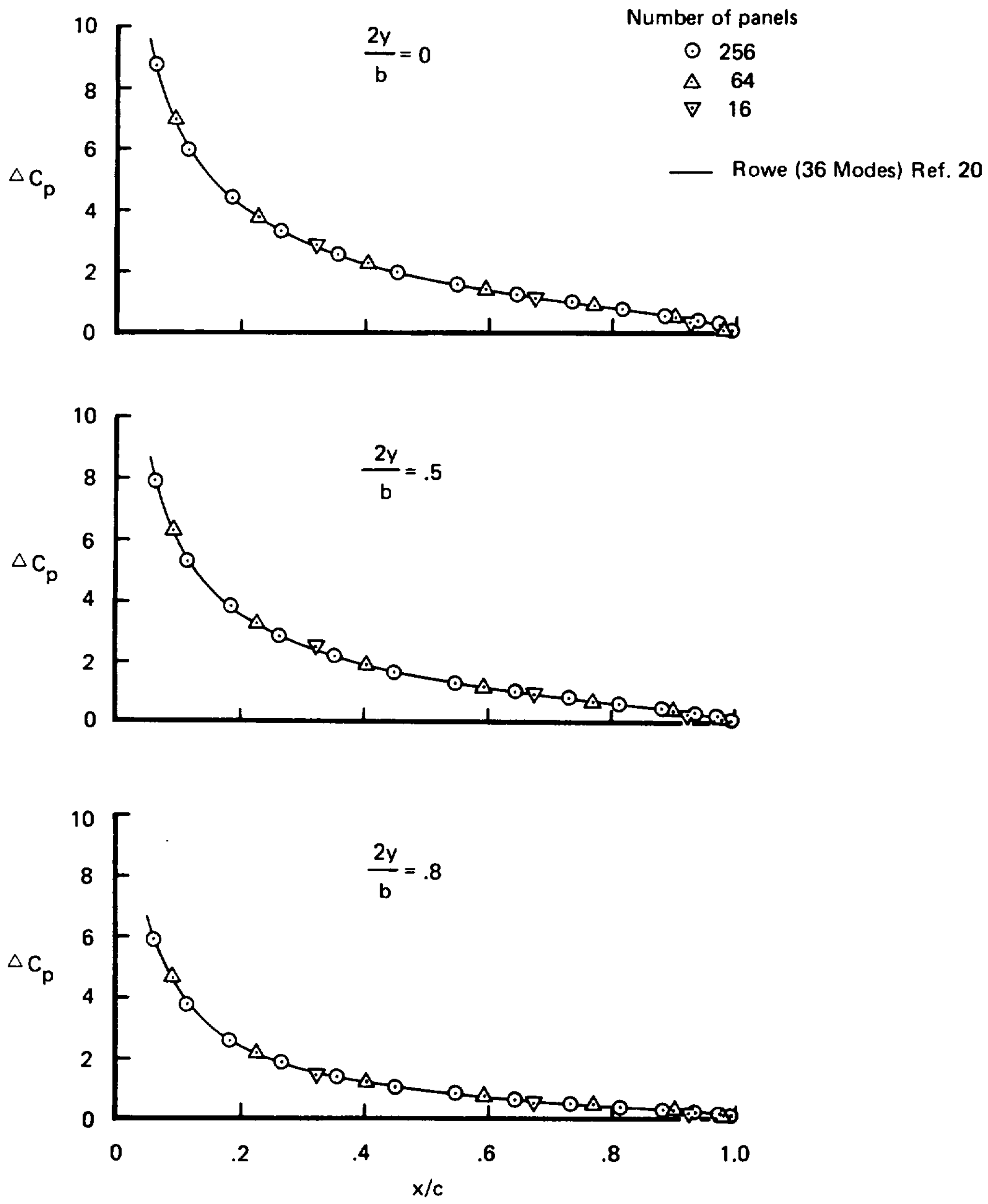

Figure 16. — (Continued)

(g) CHORDWISE PRESSURE DISTRIBUTIONS (UNIFORM SPACING)

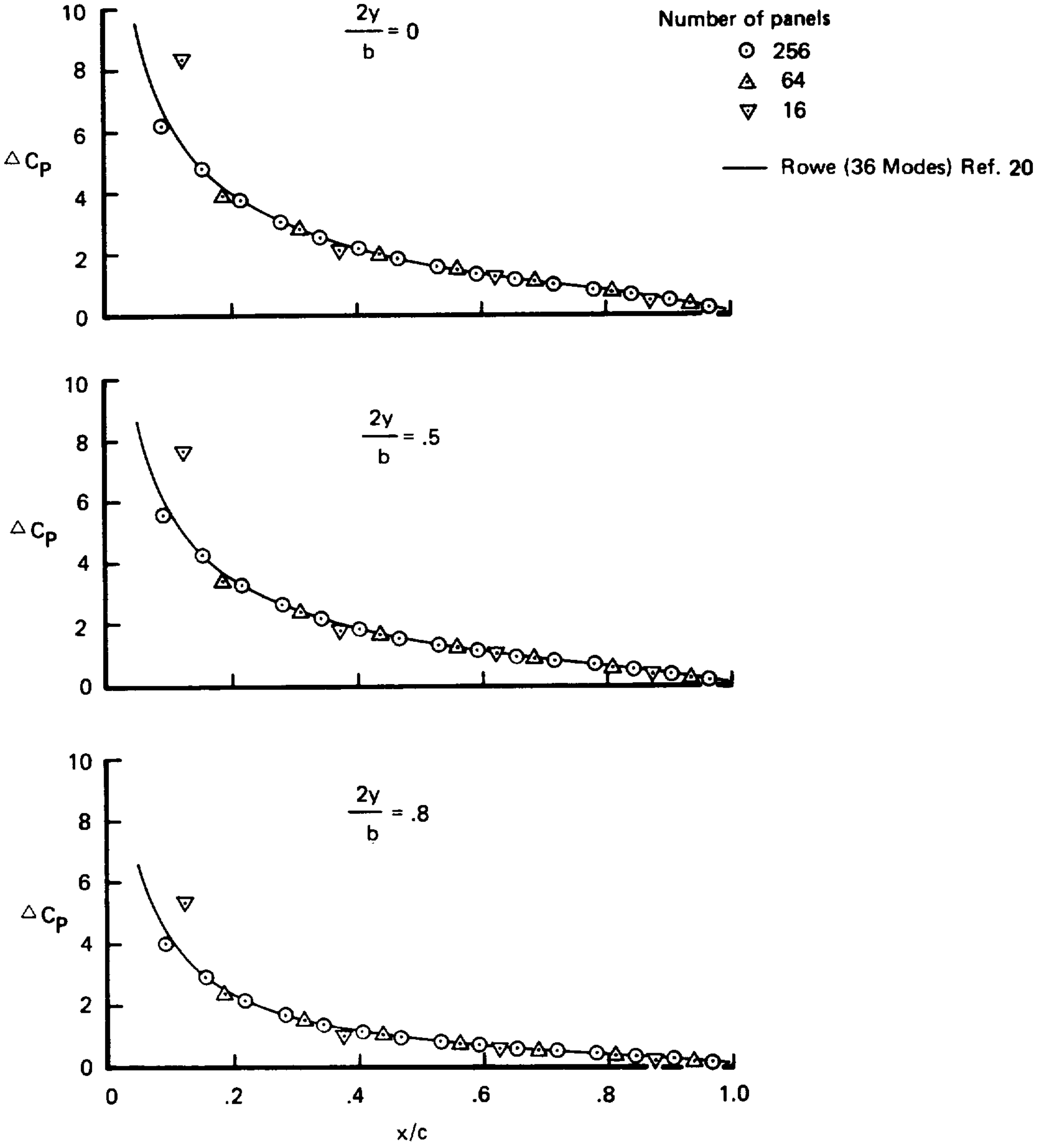

Figure 16. – (Concluded)

(a) PANEL LAYOUTS, LIFT COEFFICIENTS AND CHORDWISE COORDINATES OF CENTERS OF PRESSURE

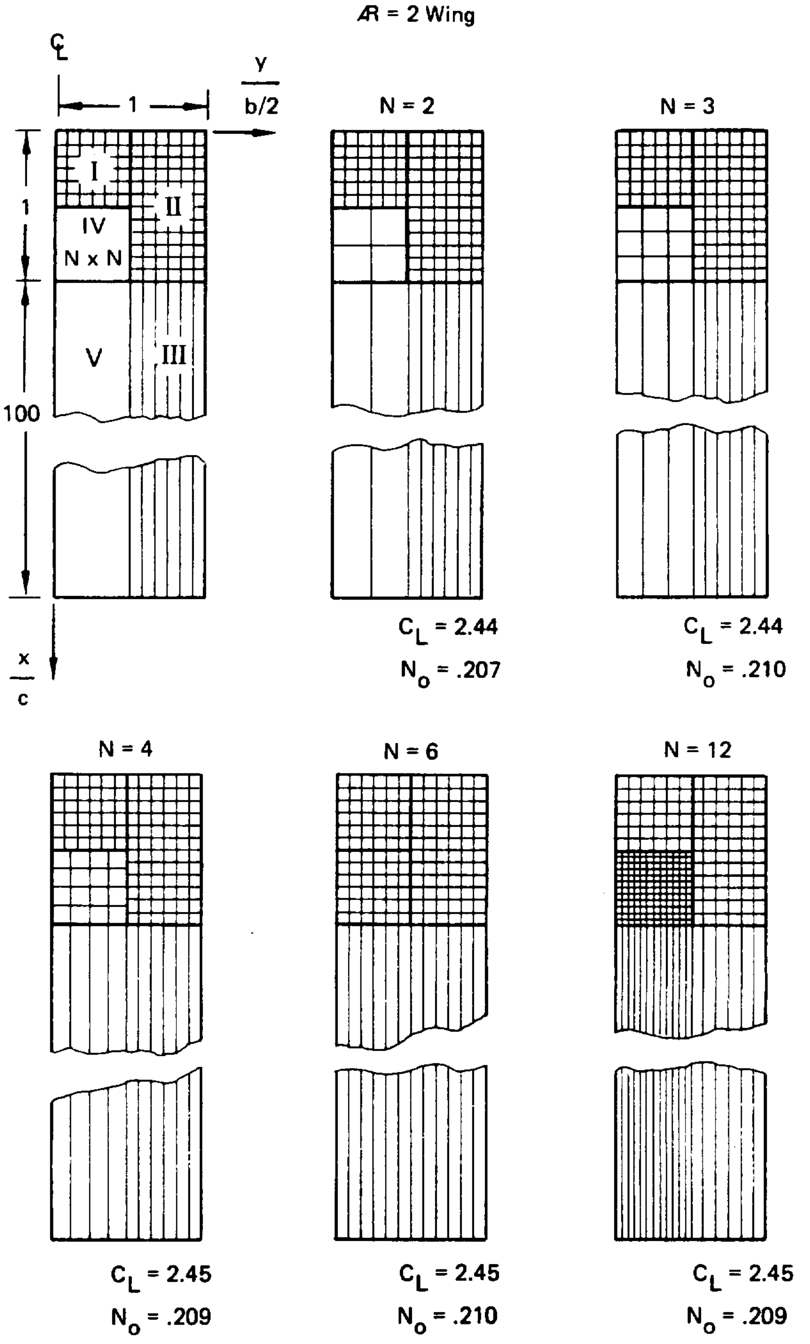

Figure 17. — Thin Rectangular Wing with Panel Mismatches at Network Boundaries; α = 1 radian

(b) MISMATCHES ACROSS NETWORK LEADING EDGE (N = 2)

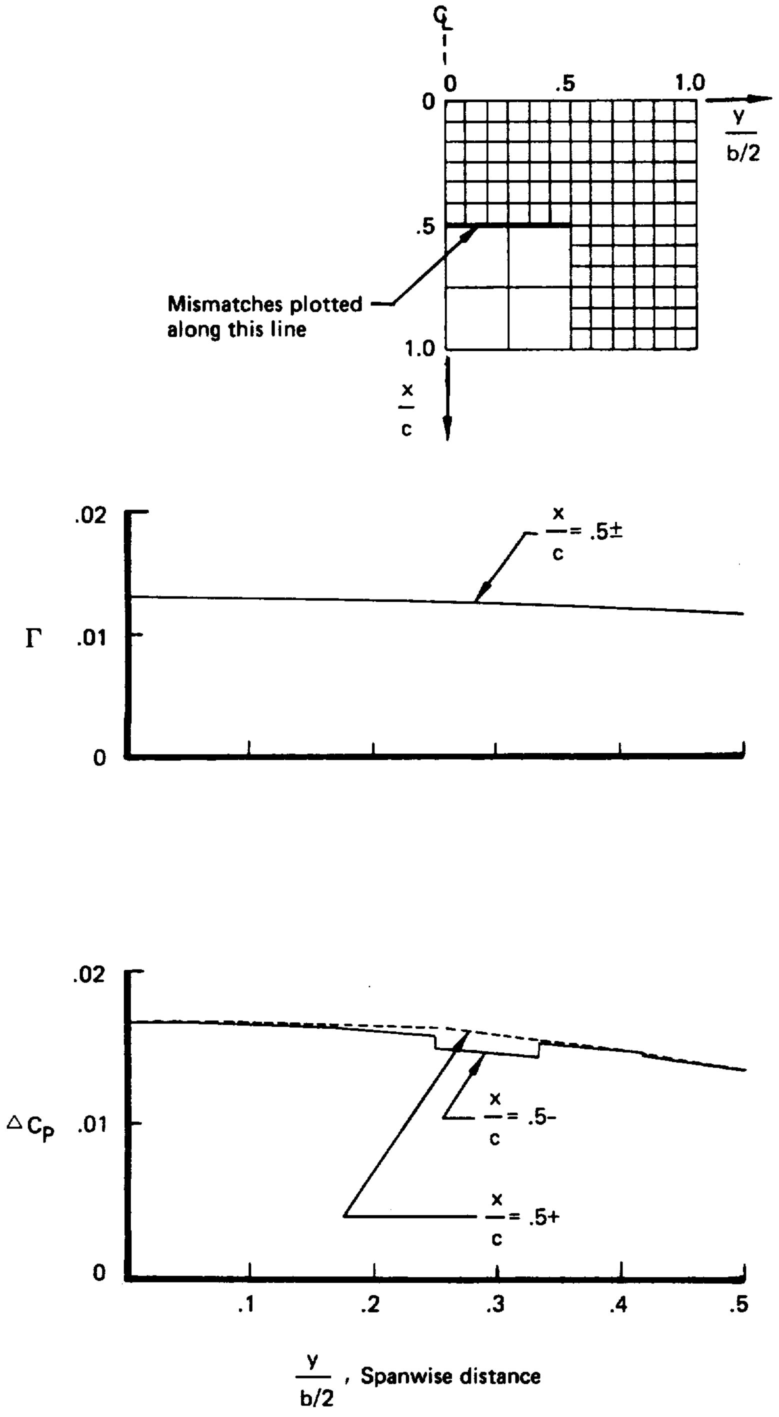

Figure 17. — (Continued)

(c) MISMATCHES ACROSS NETWORK SIDE EDGES (N = 2)

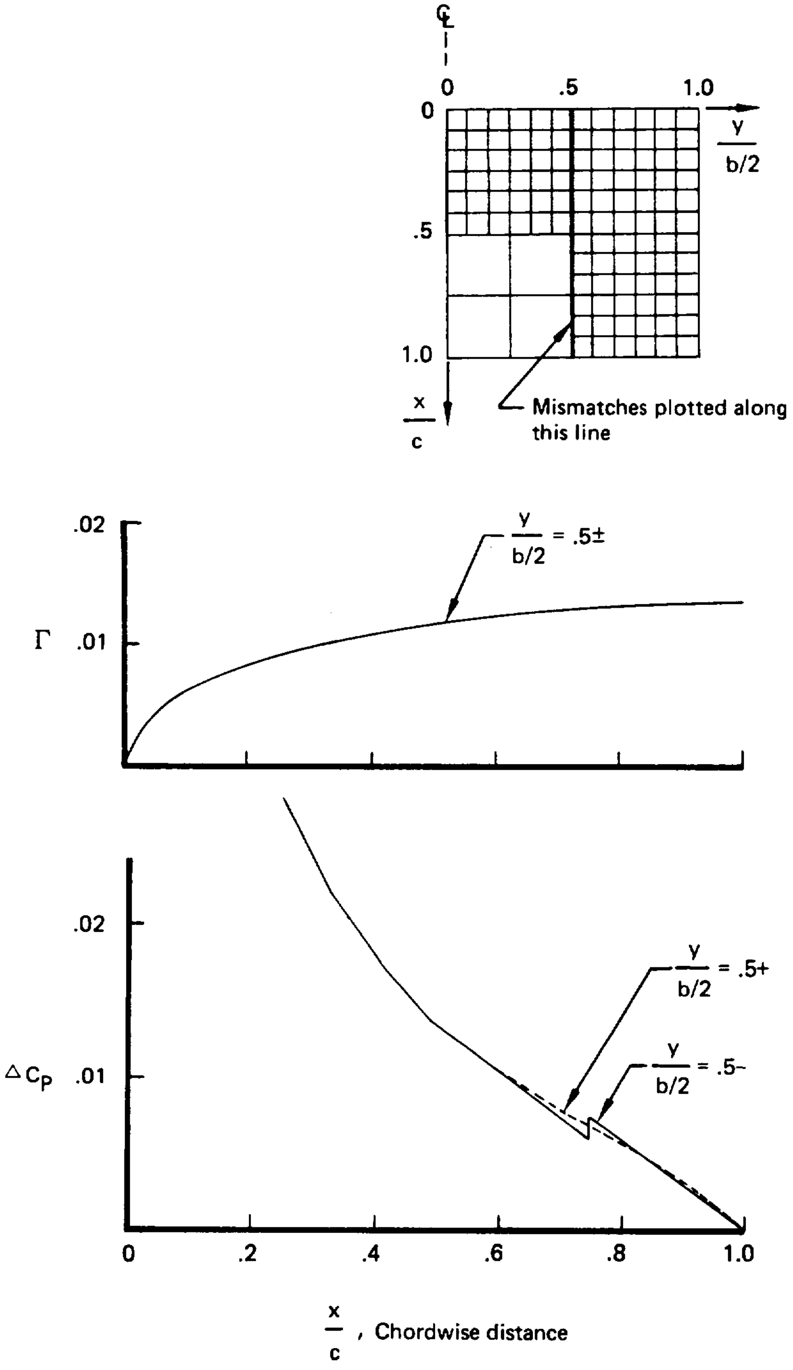

Figure 17. — (Continued)

(d) MISMATCHES ACROSS NETWORK LEADING EDGE (N = 4)

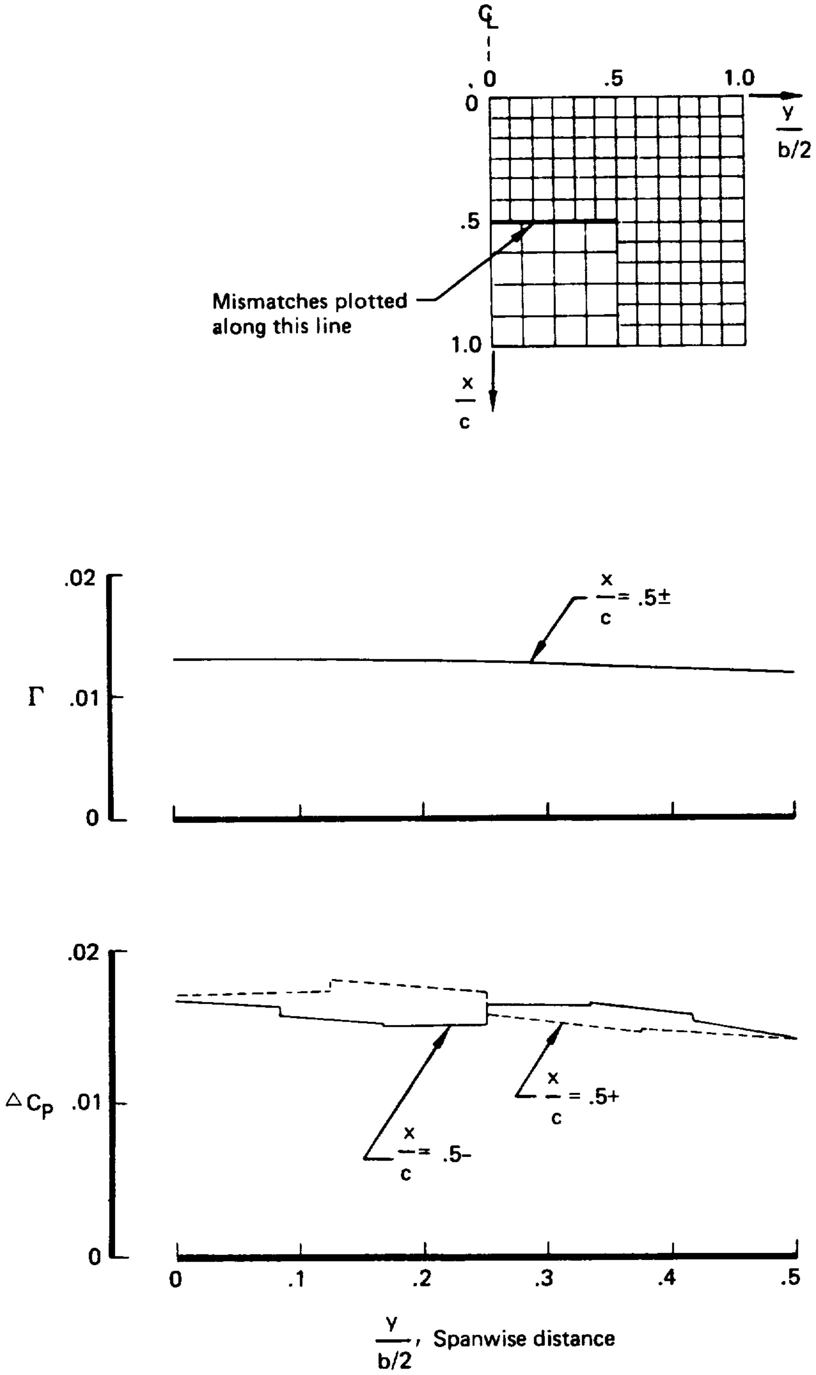

Figure 17. — (Continued)

(e) MISMATCHES ACROSS NETWORK SIDE EDGES (N = 4)

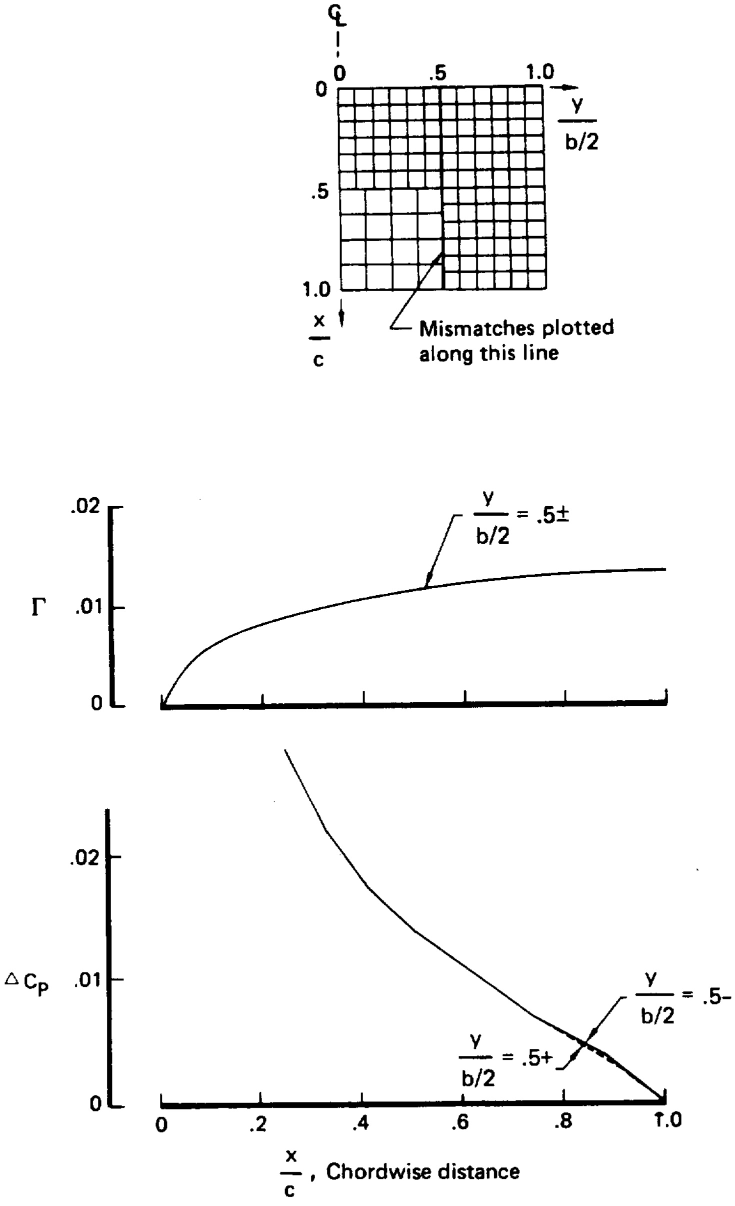

Figure 17. — (Concluded)

importance to the global properties of the flow and in all cases, it is virtually continuous across the network junctions. The pressure mismatch across the edge $\frac{2y}{b} = 0.5$ is small in both cases. The pressure mismatch across the leading edge of network IV is small in the case of N = 2, although there is a slight anomaly at about $\frac{2y}{b} = 0.3$. The pressure mismatch across this edge in the case N = 4 shows the clear lack of opposing control points. Here, continuity of pressure is not enforced at any point on the edge and the only stabilizing influence is from adjacent panel center control points. The discontinuity appears to be confined to the network edge, but until more data is available, it is recommended that density refinements be made so that all edge control points of the coarsely paneled networks be opposed by edge control points adjacent finely paneled networks.

6.3.5 THIN RECTANGULAR WING WITH VARYING SPANWISE GAPS

In figure 18, we display spanwise lift distributions for a square wing separated from its image by varying spanwise gaps. A 10 x 10 uniformly spaced paneling arrangement was employed and symmetry was exploited. The purpose here was to examine the ability of the present method (and in particular, the edge control point boundary conditions) to account for the nonuniform convergence of the lift distribution as the right and left halves of an AR 2 rectangular wing were brought together.

At a separation distance greater than 10, each half was for all practical purposes, an isolated square wing as evidenced by the symmetric spanwise lift distribution. As the separation distance decreased, the presence of the image wing was felt and the lift distribution away from the inboard edge began approaching that of an aspect ratio 2 wing. However, as long as the method perceived a gap, the load at the inboard edge continued to vanish in confirmity with the requirements of potential flow. At a separation distance of 10^{-4}, the method was unable to continue the limiting process, probably because the inboard paneling was simply too coarse to account for the severe local behavior. At a separation distance of 10^{-10}, the method believes the halves to be joined, but the edge control point boundary condition equations (section C.3) of appendix C) are still computed from the actual separated geometry resulting in some anomalies. At a separation distance of 10^{-14}, these anomalies disappear and the lift distribution of figure 16d is achieved. This example illustrates that in potential flow, a gap which is negligible physically, can have an enormous effect on the solution. The present method seems to account for such an effect, although numerical limitations exist for very small gaps.

6.3.6 THIN T-TAIL

In this example, a thin T-Tail configuration at 0.01 radians angle of attack and yaw was analyzed to test the functioning of the edge control point boundary conditions for nonplanar configurations. A square wing was used for each of the three components of the T-Tail. Each wing was simulated with a doublet/analysis network (type 2 with continuous spline) to which was abutted a doublet/wake network (type 8 with continuous spline). Since T-Tail comparison data were unavailable, two different panel configurations were run, the first with 25 uniformly spaced panels per component and the second with 81 uniformly spaced panels per component. Panel center boundary conditions were of type equation (C.3) with $c_U = 1$, $c_L = 0$ and $\beta_n = 0$. The resultant spanwise pressure distributions at half chord are displayed in figure 19a and the spanwise load distributions together with force and moment coefficients are shown in figure 19b. Agreement between the data of the coarse and fine panelings

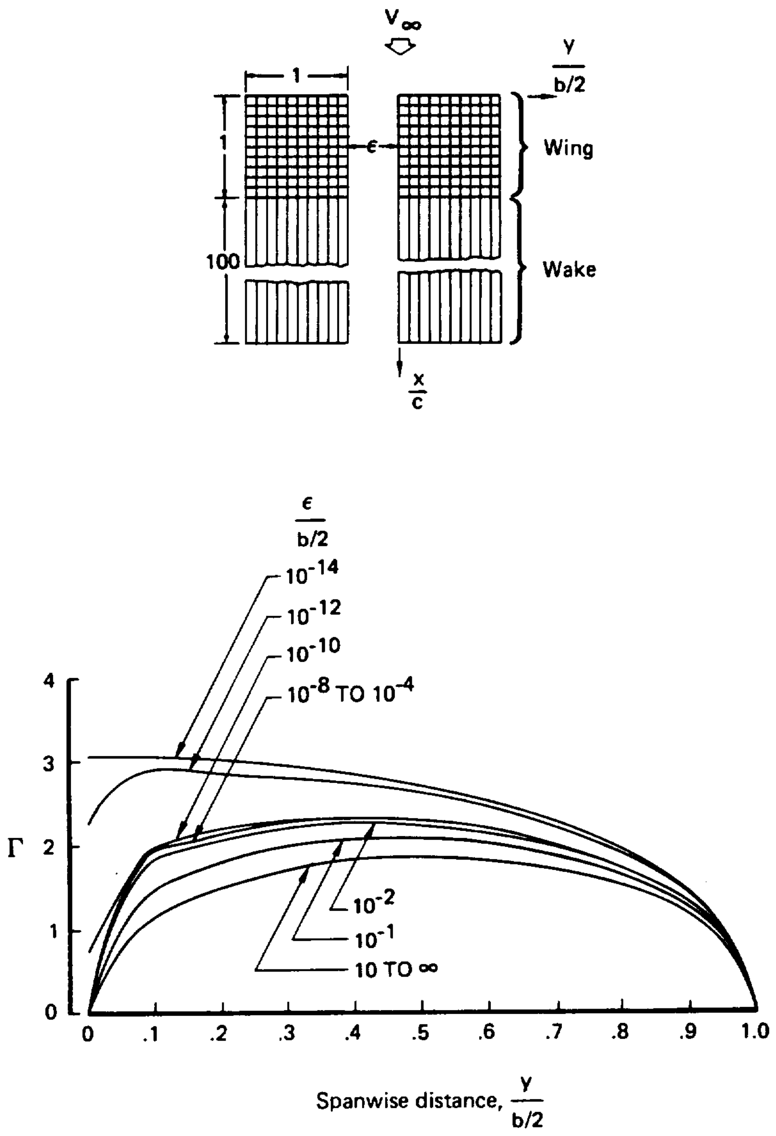

Figure 18. — Nonuniform Limiting Behavior of Sectional Lift Distribution vs. Spanwise Separation Distance, α = 1 Radian

(a) SPANWISE PRESSURE DISTRIBUTION

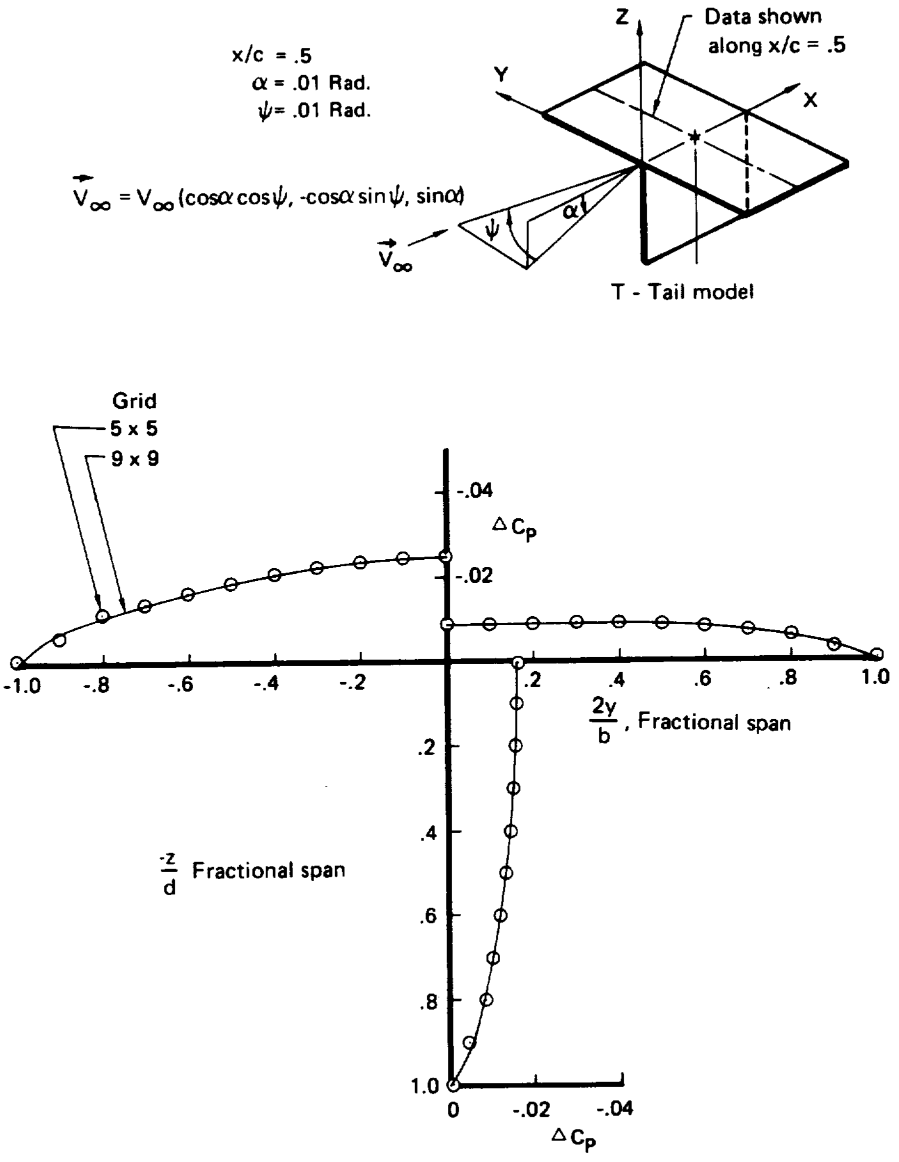

Figure 19. — T - TAIL

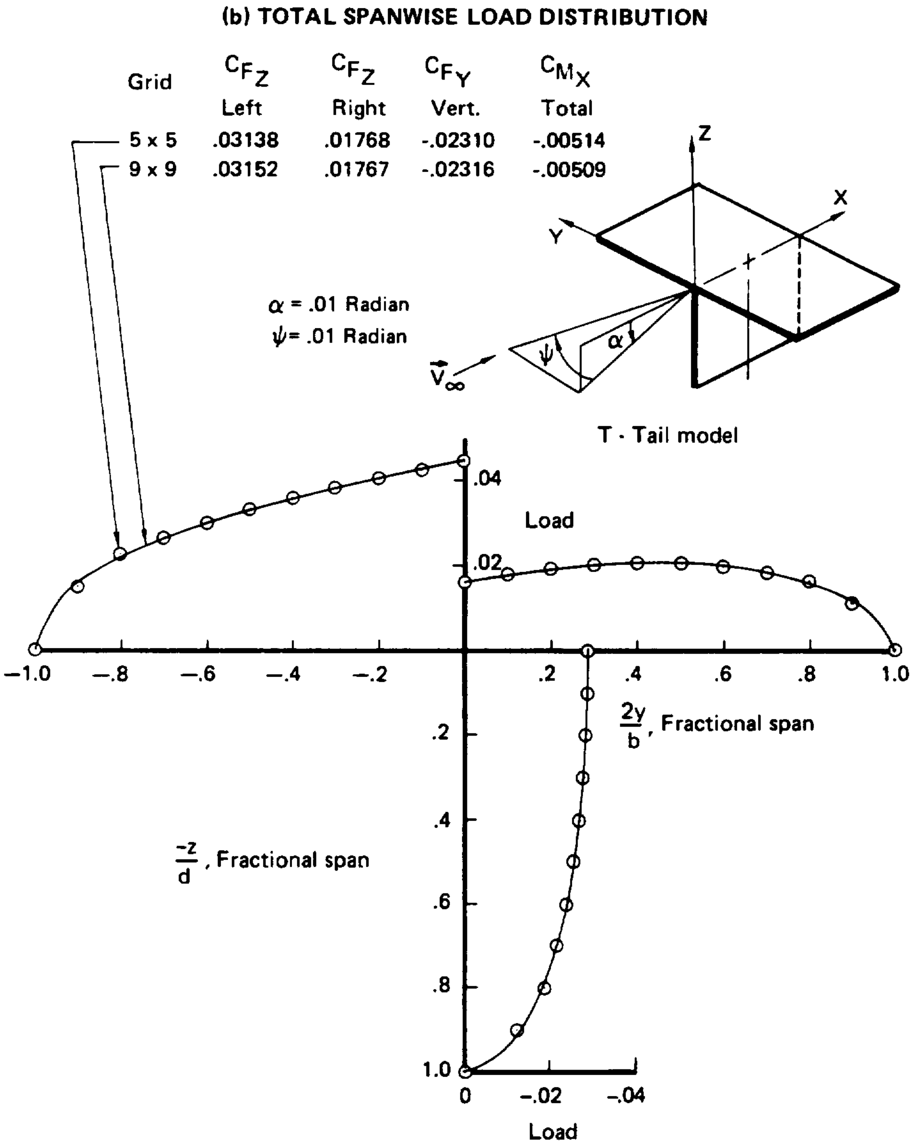

(b) TOTAL SPANWISE LOAD DISTRIBUTION

Grid	C_{F_Z} Left	C_{F_Z} Right	C_{F_Y} Vert.	C_{M_X} Total
5 x 5	.03138	.01768	-.02310	-.00514
9 x 9	.03152	.01767	-.02316	-.00509

Figure 19. — (Concluded)

is good. The pressure and load distributions have the right character. In particular, the discontinuity in ΔC_p across the junction of the horizontal components is matched by the ΔC_p of the vertical component at the junction. (This follows from the definition of ΔC_p and the fact that the upper surface C_p distribution is continuous across the junction of the horizontal component.) The same property is true of the total load distribution. At present, leading edge suction terms are not included in force and moment calculation; hence, only those coefficients not significantly affected are displayed. The magnitudes and signs appear, in our judgment, to be correct.

6.4 COMBINED SOURCE/ANALYSIS AND DOUBLET/ANALYSIS NETWORKS

6.4.1 WING-BODY ANALYSIS

In figure 20, we present aerodynamic data for a symmetric wing-body configuration at 10° angle of attack. The fuselage is a body of revolution of thickness ratio 0.11. The wing is symmetric, 10% thick, and of an aspect ratio 5.6 with a leading edge sweep of 47°. The configuration was first analyzed by the method of reference 6, using 936 flat, constant-strength source panels on the standard wing and body surfaces, accompanied by 12 lifting elements. (This represents a typical number of panels used for wing/body applications with this method.)

The paneling employed by the present method is depicted in figure 20a and comprises 160 surface panels. The first such network contained all body panels forward of the wing. The second and third networks contained all body panels above and below the wing, respectively. The fourth network contained all body panels aft of the wing. The body was represented by four source/analysis networks with a total of 96 panels. The wing surface was represented by a 64 panel source/analysis network as shown. An internal lifting system (not shown) was used to create lift. The lifting system was composed of four networks. The first was a 32 panel doublet/analysis network on the camber surface of the wing with stream surface (impermeability) boundary conditions. The second was a 4 panel type 8 (doublet/wake, No. 1) network, emanating from the wing trailing edge. The third was an eight panel type 8 (doublet/wake No. 1) network inside the body, extending the internal lifting system to the centerline. The fourth was a one panel type 10 (doublet/wake No. 2) network extending the trailing edge wake to the centerline. The continuous spline was used for all four lifting system networks.

Spanwise load distribution comparisons are plotted in figure 20b and chordwise pressure distribution comparisons are plotted in figure 20c. In addition lift, moment, and drag coefficients are compared in figure 20b. All three coefficients agree well with the reference values; however, the drag coefficient agreement must be considered fortuitous in view of the extremely sparse wing leading and trailing edge paneling. The calculation of accurate drag coefficients by integrating panel pressures generally requires a greater concentration of panels near the leading edge and trailing edge than the calculation of accurate lift and moment coefficients. It should also be pointed out that the drag values computed by the method of reference 6 should not be considered as a valid standard, since that method has never been shown to produce reliable drag values from integrated surface pressures.

(a) PANELING

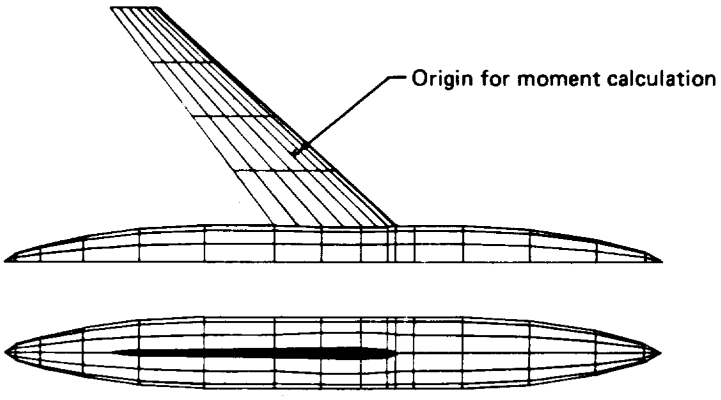

(b) SPANWISE LOAD DISTRIBUTION

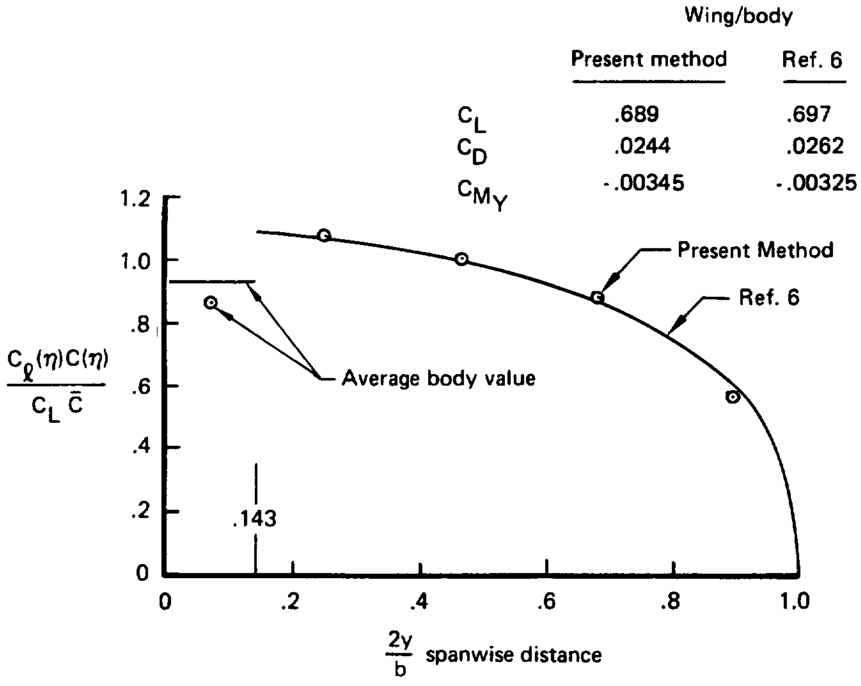

	Wing/body Present method	Wing/body Ref. 6
C_L	.689	.697
C_D	.0244	.0262
C_{M_Y}	-.00345	-.00325

Figure 20. — Wing Body Analysis

(c) WING PRESSURES

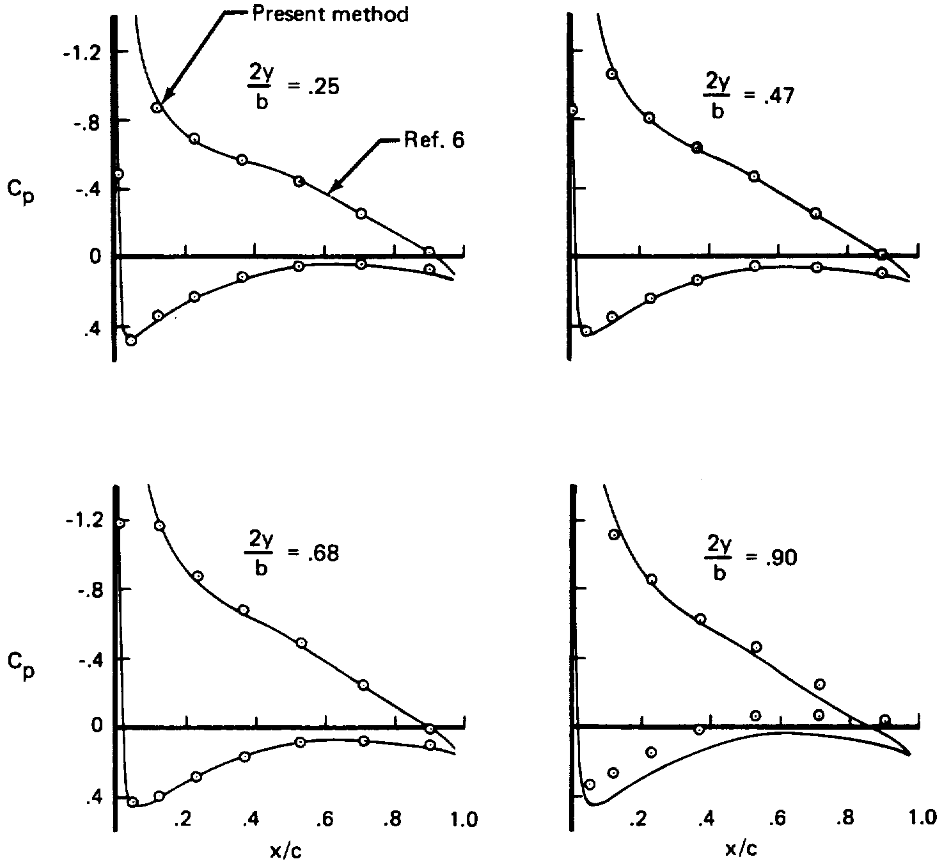

Figure 20. — (Concluded)

The spanwise load distribution agreement is good, although there is a slight discrepancy in average body lift. (The average body load was obtained by subtracting the total wing load from the total configuration load. The result was divided by the total load and distributed uniformly over the body span fraction. No precise span loading distribution for the body could be calculated because the body panel columns were not located along constant span stations.) Wing pressure agreement is excellent at the three inboard span stations. The disagreement in lower surface pressures at the outboard span stations is due to higher spanwise velocity components predicted by the present method. The reference method is known to underestimate spanwise velocities near wing tips, However, the discrepancy may also be due in part, to the width of the outboard panels employed in the present analysis.

6.4.2 THICK WING ANALYSIS WITH FIVE DIFFERING BOUNDARY VALUE PROBLEM FORMULATIONS

In section 4.2, we described a variety of boundary value formulations for solving a flow problem where part of the boundary of the fluid domain also bounded an adjacent domain. It was noted there that an infinite number of different source and doublet distributions on this part of the boundary could all produce the desired flow in the fluid domain. In this example, we show results generated by the present method, illustrating this point. Specifically, we analyze the wing of figure 21(a) in five different ways. The wing has an Æ 2 rectangular panform and a symmetric, 11% thick Boeing TR17 airfoil section. A 0.1 radian angle of attack is assumed. Analysis of the wing by the method of reference 6 using 624 constant strength panels on the wing surface and 144 constant strength doublet panels for the internal lifting system produced the reference solution data of figures 21(b) and 21(c). The wing tip was left open for the reference calculation, an aspect that can affect in an unpredictable manner, the pressures near the tip, due to the possibility of inflow or outflow from the tip. The moment coefficient C_{M_Y} is calculated about the leading edge.

The panel layout used for the five applications of the present method is displayed in figure 21(a). Each wing network employed in these applications comprises the lower, upper or camber wing surface and contains four panel columns spanwise and 12 panel rows chordwise. The tip was paneled in only one instance and a network containing two panel columns and 12 panel rows was used for this purpose. A four panel type 8 network was used to represent the wake in each case. The five methods of analysis are described in the following five paragraphs.

1. The first analysis performed was similar to that of the reference method. Source/analysis networks were placed on the wing upper and lower surfaces and a doublet/analysis network was placed on the wing camber surface (fig. 9). All three wing networks were assigned zero normal flow panel center boundary conditions. For each source network, these conditions were applied on the side of the surface exposed to the exterior flow. Resultant aerodynamic data is compared to that of the reference method in figure 22. The data generally agrees well. As a check of the force coefficients of the reference method, this analysis was again performed with twice as many panels, resulting in values $C_L = 0.261$, $C_{M_Y} = -0.0549$, $C_D = 0.0128$.

(a) WING PANELING

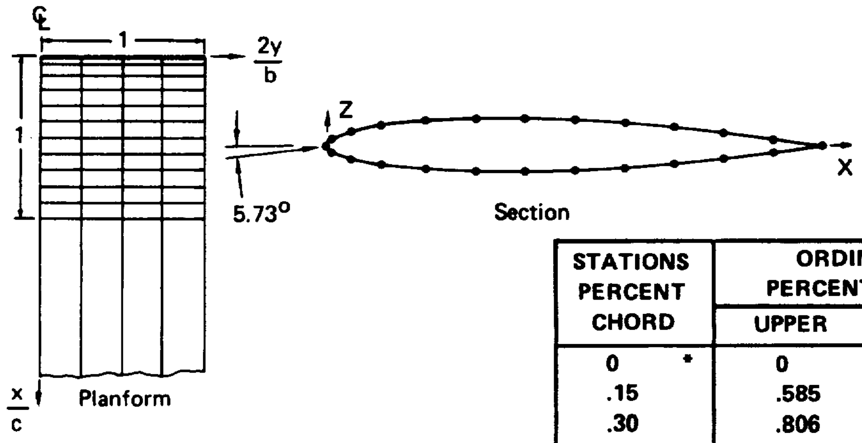

(b) SPANWISE CIRCULATION (REFERENCE SOLUTION)

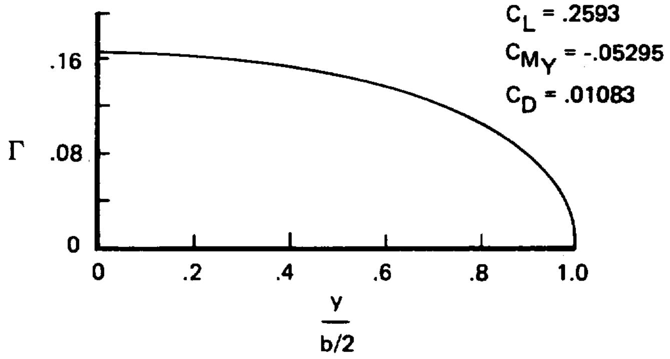

(c) SECTION PRESSURES (REFERENCE SOLUTION)

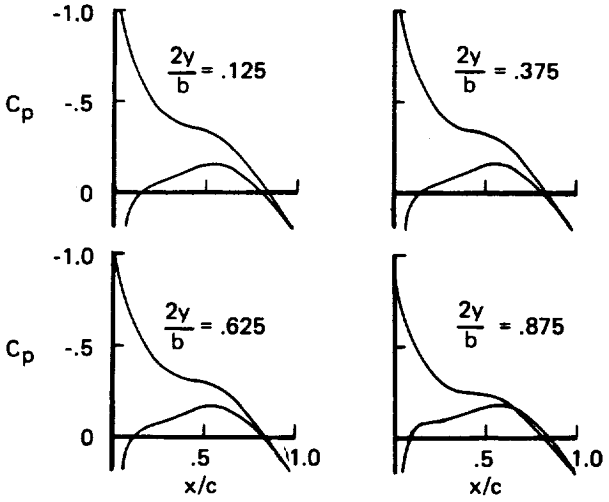

STATIONS PERCENT CHORD	ORDINATES PERCENT CHORD	
	UPPER	LOWER
0 *	0	0
.15	.585	- .585
.30	.806	- .806
.60	1.103	- 1.103
1.0 *	1.392	- 1.392
1.5	1.679	- 1.679
2.5	2.135	- 2.135
4.0 *	2.667	- 2.667
6.0	3.216	- 3.216
8.0	3.644	- 3.644
10.0 *	3.986	- 3.986
12.5	4.325	- 4.325
15.0	4.589	- 4.589
17.5	4.799	- 4.799
20. *	4.969	- 4.969
25.	5.222	- 5.222
30. *	5.396	- 5.396
35.	5.507	- 5.507
40. *	5.556	- 5.556
45.	5.534	- 5.534
50. *	5.429	- 5.429
55.	5.228	- 5.228
60. *	4.923	- 4.923
65.	4.510	- 4.510
70. *	3.992	- 3.992
75.	3.381	- 3.381
80. *	2.699	- 2.699
85.	1.977	- 1.977
90. *	1.256	- 1.256
92.5	.914	- .914
95.0	.592	- .592
97.5	.301	- .301
100. *	.050	- .050
LE Radius = 1.20% Chord TE Radius = .0548% Chord		
$\frac{t}{c}$ = 11.1%	$\frac{h}{c}$ = 0%	ϵ_{te} = 11.3°

* POINTS SELECTED FOR PANEL CORNER POINTS

Figure 21. — Æ 2 Thick Wing

(a) SPANWISE CIRCULATION

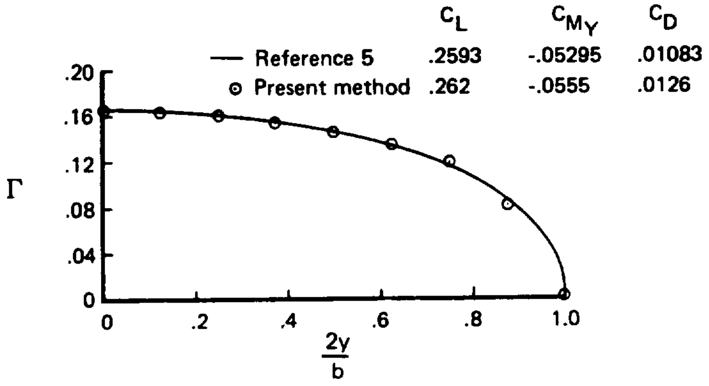

(b) SECTION PRESSURES

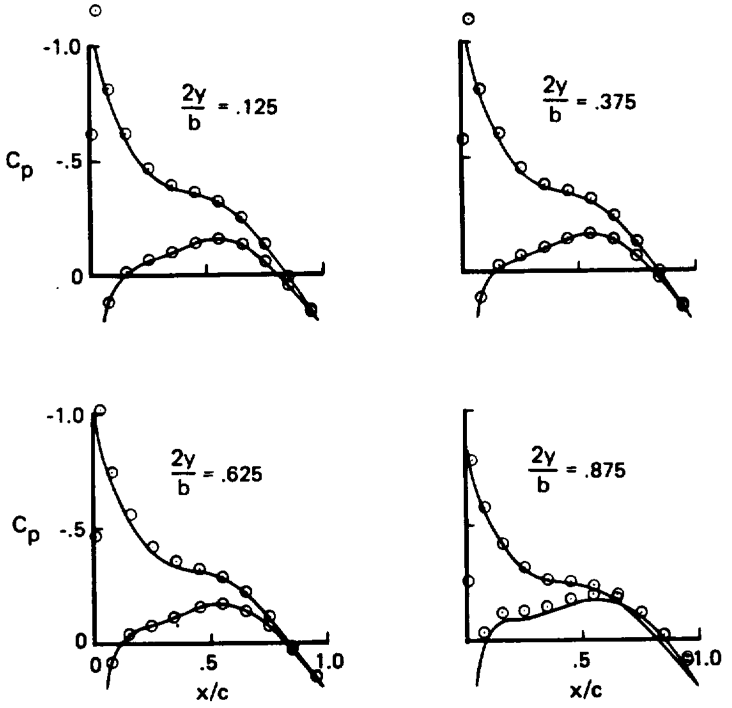

Figure 22. — Æ 2 Thick Wing Analysis #1

2. The second analysis performed used a formulation similar to that in reference 11. Both source and doublet/analysis networks were placed on the wing upper and lower surfaces, (fig. 8). Boundary conditions requiring zero perturbation potential on the interior side of the wing surface were assigned to doublet panel control points (type equation (C.11) with $k_U = 0$, $k_L = 1$ and $\beta_\phi = 0$). Boundary conditions requiring source strength to be equal to the negative of the normal component of freestream velocity were assigned to source panel control points (type equation (C.3) with $c_A = 0$, $c_D = 1$, $\beta_n = -\vec{V}_\infty \cdot n$). The latter boundary conditions in conjunction with zero perturbation flow in the wing interior cause the wing to be a stream surface in the exterior flow. Because of the crude leading edge paneling and to a lesser extent, the open tip, the specification of zero perturbation potential at doublet control points did not produce precisely zero perturbation flow in the wing interior near the leading and tip edges. Consequently, the wing was not quite a stream surface in the exterior flow. This did not seem to make a great deal of difference, however, since most of the resultant aerodynamic data (fig. 23) agrees well with the reference data. The disagreement in drag and moment coefficients may be due to a slight error in the way the pilot program calculates pressure coefficients when source and doublet panels are superimposed (see app. F). This error would affect primarily leading edge pressures.

3. The third analysis performed reversed the formulation of the first analysis placing doublet/analysis networks on the upper and lower wing surfaces and a source analysis network on the camber surface (fig. 11). Zero normal flow panel center boundary conditions were applied to the doublet networks. Boundary conditions requiring the perturbation potential to be zero were applied at all control points of the source/analysis network. Resultant aerodynamic data are displayed in figure 24. As an interesting note, the source strength on the internal source/analysis network turned out to be equal to the slope of the wing thickness.

4. The fourth analysis performed used doublet/analysis networks only. Doublet/analysis networks were placed on the wing upper and lower surfaces and assigned zero normal flow panel center boundary conditions. The resultant spanwise circulation data were excellent, but the resultant pressure distributions were grossly in error and could only be improved by increasing panel density. Indirect boundary conditions similar to those of the second analysis were then substituted. Here, zero total potential on the interior side of the wing surface was specified at panel center control points in an attempt to force zero total velocity (stagnation) in the wing interior. (This would, in turn, cause the wing to be a stream surface in the external flow because normal velocity is continuous across a doublet surface as proven on page 170 of ref. 1.) Stagnation was achieved near the centerline, but rather large velocities were present outboard and these were eliminated by paneling the tip. Stagnant flow inside the wing implies that the total velocity on the exterior wing surface is equal to the surface gradient of the doublet strength (see eq. (C.10)). Although stagnation was not quite achieved in the wing interior, the exterior velocities were calculated from doublet strength gradient anyway, resulting in slightly more accurate values of C_p than those produced by actual exterior surface velocities calculated in the usual way. Resultant aerodynamic data are displayed in figure 25.

(a) SPANWISE CIRCULATION

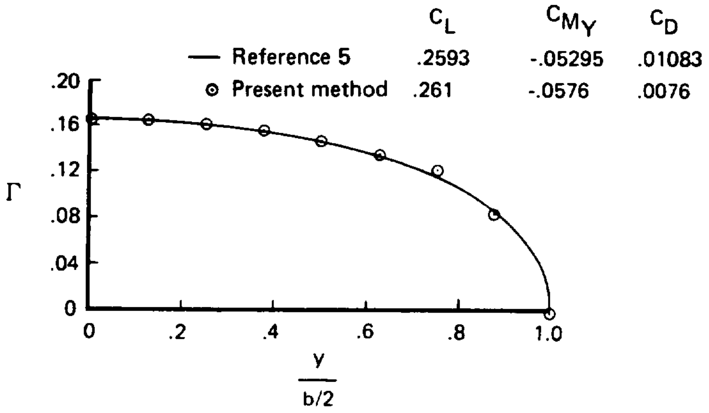

(b) SECTION PRESSURES

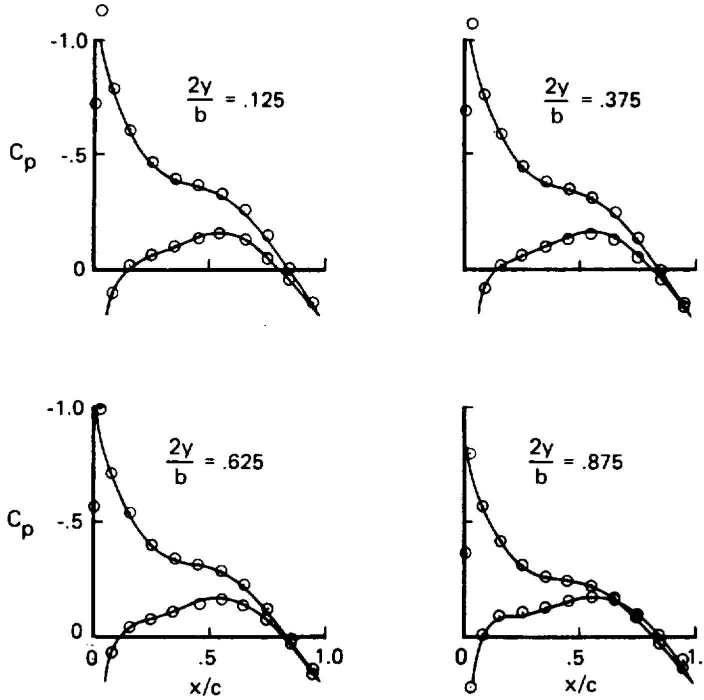

Figure 23. — Æ 2 Thick Wing Analysis #2

(a) SPANWISE CIRCULATION

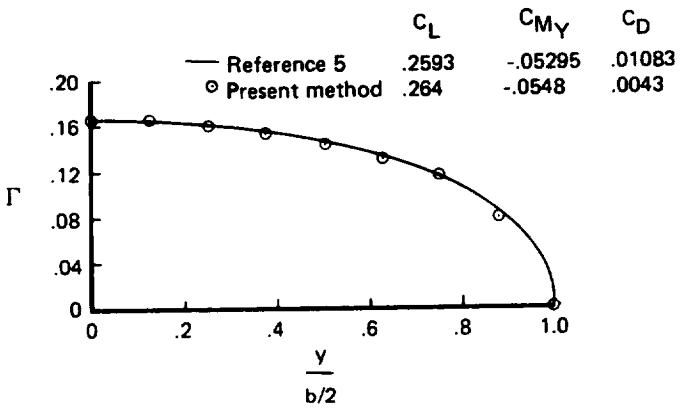

(b) SECTION PRESSURES

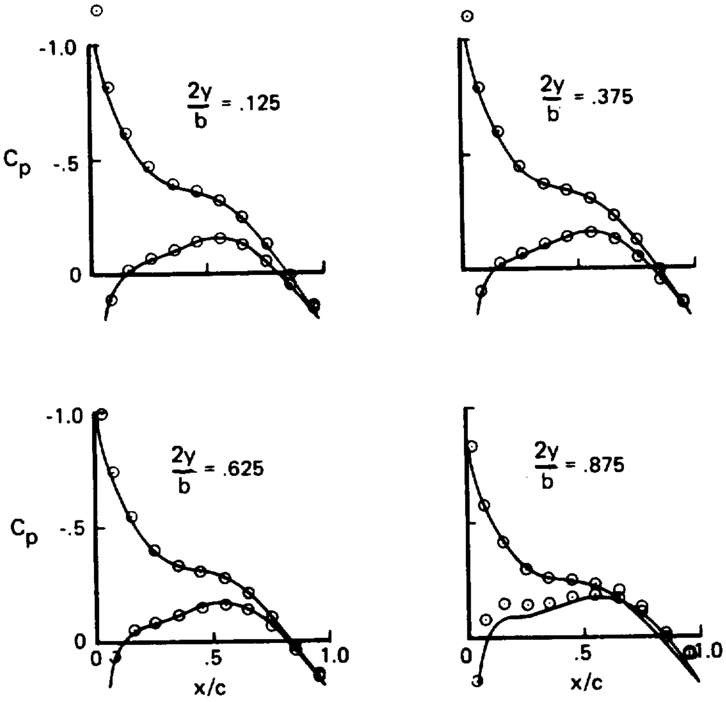

Figure 24. — Æ 2 Thick Wing Analysis #3

(a) SPANWISE CIRCULATION

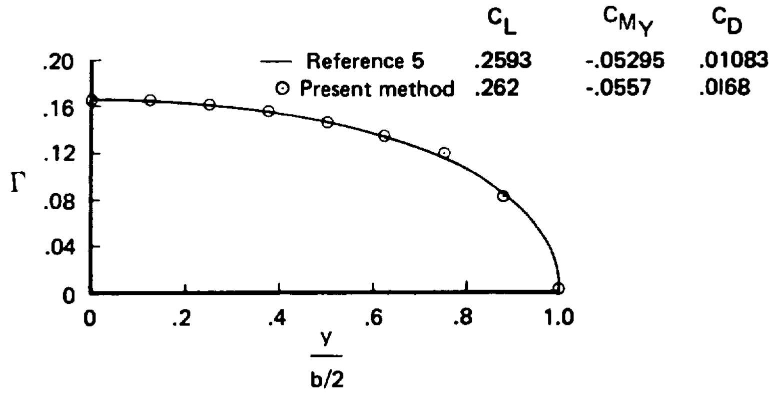

(b) SECTION PRESSURES

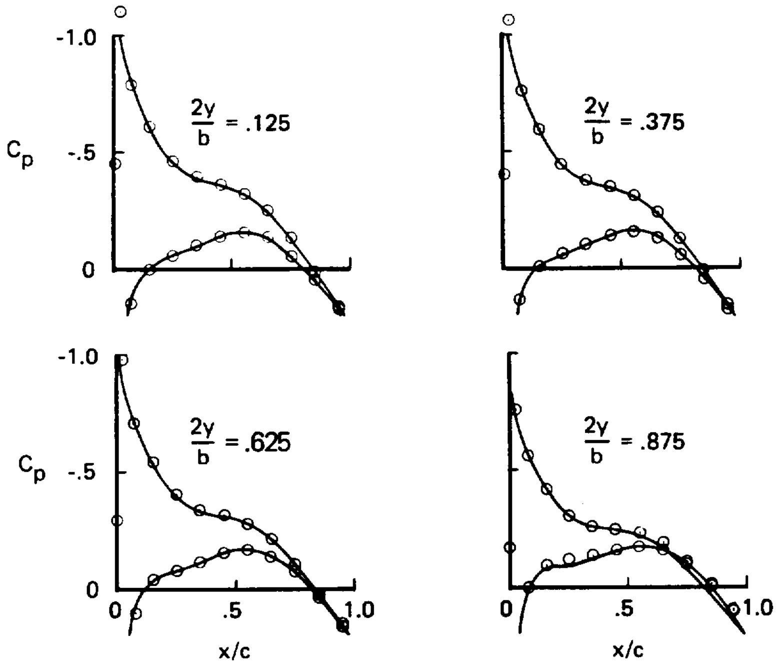

Figure 25. — Æ 2 Thick Wing Analysis #4

5. The fifth analysis performed used linearized boundary conditions and linearized geometry (chapter 17, ref. 18). Source/analysis and doublet/analysis networks were placed on the wing camber surface, which in this case was the x-y plane. As in the third analysis, boundary conditions requiring source strength to be equal to the slope of the wing thickness were applied to all control points of the source/analysis network. Boundary conditions of type equations (C.7) with $c_A = 1$ and $c_D = 0$ were assigned to each doublet panel control point. To be consistent with linear theory, the freestream was directed along the planform centerline and angle of attack effects were achieved by specifying $\beta_n = -0.1$ at these control points. In addition, pressure coefficients were calculated using the linearized formula $C_p = -2 \frac{\partial \phi}{\partial x}$. This resulted in values of ΔC_p which were unaffected by the presence of the source network. Hence, lift and moment coefficients as well as spanwise circulation (fig. 26) do not reflect thickness effects and agree with the data of figure 16. The primary effect of the source network in this case was to change the average of the upper and lower surface values of C_p to reflect thickness. For a pure thin wing, the upper and lower surface values of C_p would have equal magnitudes and opposite signs. There is not a great deal of difference in the results produced by the first four analyses and without further study, it is difficult to favor any particular formulation. In fact, the choice of a formulation could very well depend on the specific application at hand. For example, a requirement for surface streamline tracing would clearly favor the use of formulations No. 2 and No. 4, where potential and velocities can be computed everywhere on the surface from the value and gradient of doublet strength. (Incidentally, this latter fact would allow somewhat more accurate integration of force and moment coefficients since the effect of the variation of pressure within a panel may be included in the calculation.) For extremely coarse panelings formulation, No. 1 is probably the most stable and accurate method of analysis, but it requires extra boundary conditions inside a lifting body. (However, the internal lifting system can be quite crude. For most wings, the use of only three panel rows chordwise does not appreciably degrade results.)

6.5 SOURCE/DESIGN NETWORKS

6.5.1 DESIGN OF ARBITRARY AIRFOIL

Figure 27 shows an application of the type 5 (source/design No. 2) network to a two-dimensional airfoil design problem. A NACA 65-010 symmetric airfoil at zero angle of attack was chosen as the nominal configuration. The arbitrary problem selected was a redesign of the airfoil between 20% and 90% chord producing zero C_p there. Analysis of the NACA 65-010 airfoil was accomplished by means of three source/analysis networks placed between 0% and 20% chord, 20% and 90% chord and 90% and 100% chords, respectively, as shown in figure 27a. (Panels were elongated in the crossflow direction to approximate two-dimensional flow.) The resultant pressure distribution is displayed in figure 27b and is virtually identical to that given in reference 21. The center network was then replaced by the type 5 (source/design No. 2) network with tangential velocities of freestream magnitude as boundary conditions. Together with the closure condition (eq. 11) these boundary conditions produced a

(a) SPANWISE CIRCULATION

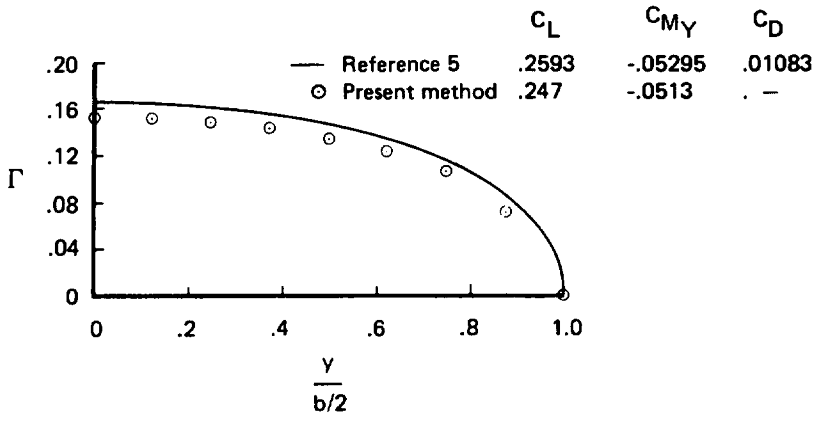

(b) SECTION PRESSURES

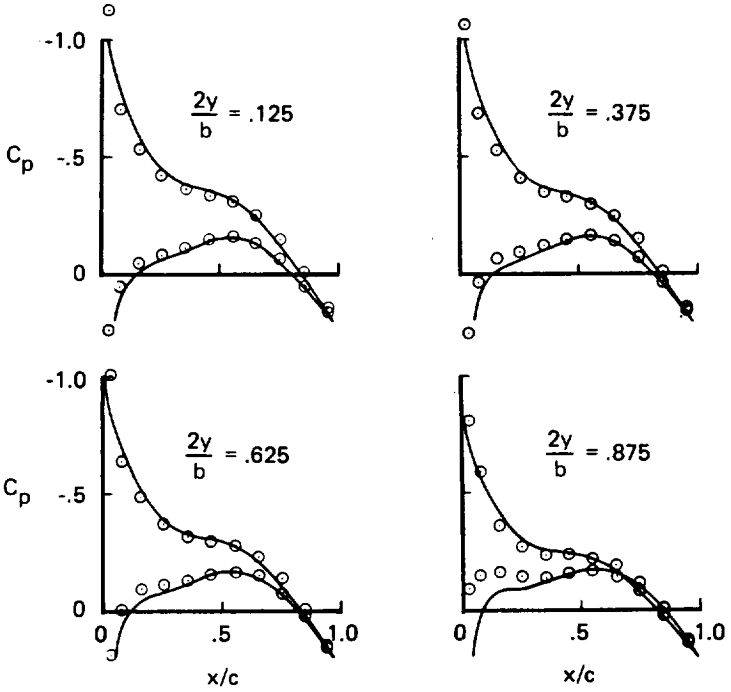

Figure 26. — Æ 2 Thick Wing Analysis #5

(a) GEOMETRY

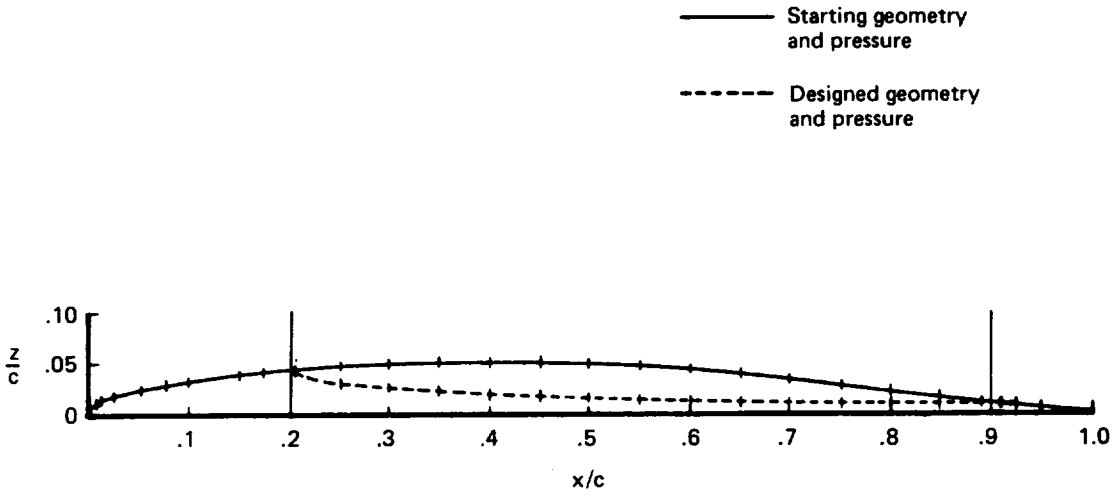

(b) PRESSURE DISTRIBUTION

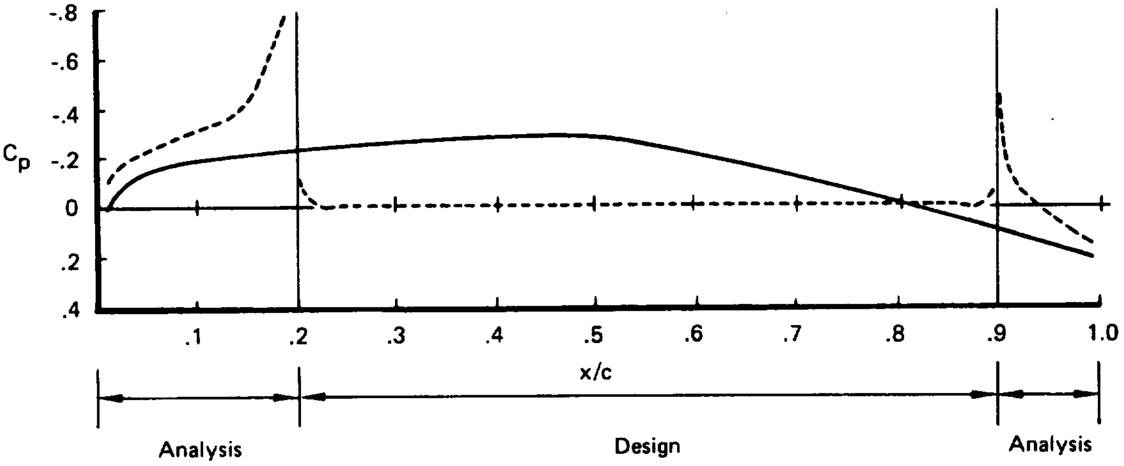

Figure 27. — Design of Arbitrary Airfoil

flow with nonzero normal velocities at control points of the design network. The network panels were then relofted to eliminate the normal flow. This was done by sequentially moving each point a suitable distance in the positive or negative z direction, starting with the second point of the center network and continuing aft. The distance is determined by the requirement that the unit normal of each updated panel be orthogonal to the velocity vector computed at the panel center prior to the update. In theory, the closure condition will ensure that the last point of the network will not be moved at all, thereby, maintaining continuity in geometry between the center design network and the aft analysis network. Because of the numerical discretization involved in the procedure, a slight gap may appear, in which case the whole design network is rotated about the initial corner point to achieve exact closure. Three iterations produced the reasonably converged geometry displayed in figure 27a. Analysis of this geometry produced the pressure distribution in figure 27b, which is close to that specified.

6.5.2 REDESIGN OF TR 17 AIRFOIL

A similar, but more practical application of the type 5 (source/design No. 2) network is shown in figure 28. Here, a Boeing TR17 symmetric airfoil (11% thick) was modified to produce a different aft loading at 0° angle of attack. An analysis of the original airfoil section produced the pressure distribution plotted in figure 28b. The desired upper surface pressure distribution aft of 50% chord is also shown. In order to avoid the sharp discontinuities in pressure of the previous example, the upper surface geometry was allowed to vary aft of 30% chord and the original pressure distribution was specified between 30% and 50% chord. The design procedure used was identical to that of the previous example with the exception of the addition of an internal (doublet/analysis) lifting system and wake to allow for a lifting solution. Analysis of the designed section after one iteration indicated convergence.

6.5.3 FULL AIRFOIL DESIGN

Figure 29 shows a test of the type 5 (source/design No. 2) network on a full airfoil design problem. A circle was arbitrarily selected as a nominal airfoil. A 34 panel source/design No. 2 network was placed on the airfoil surface and assigned tangential velocities of an 18% thick, 3% cambered Karman-Trefftz airfoil as panel center boundary conditions. The closure condition (eq. 11) was also enforced and a lifting system composed of the usual internal doublet/analysis No. 1 network was employed to account for possible lift. The resultant flow produced nonzero normal velocities at source panel control points and these components were eliminated by relofting the airfoil panels in the same manner as the example in paragraph 6.5.1. The internal lifting system was relofted to the new camber line. The first iteration, shown in figure 29a, indicates the unsophisticated nature of the loft procedure used. No damping was employed, i.e., the geometry was allowed to assume the position predicted, even though the perturbation clearly violated linearity assumptions. The existence of a region of crossover at the leading edge did not cause the failure of subsequent iterations even though boundary conditions were applied on the interior side of the surface in this region. This is because sources alone were used to represent the airfoil surface and the specified tangential components of velocity automatically applied to both sides of the surface. At the fifth iteration, the crossover was finally eliminated and the geometry rapidly converged. The airfoil produced on the ninth iteration is displayed in figure 29a and is almost indistinguishable from that of the true Karman-Trefftz airfoil. An analysis of this geometry with the source/design network replaced by a source/analysis network produced the C_p distribution shown in figure 29b which is close to that desired.

(a) GEOMETRY

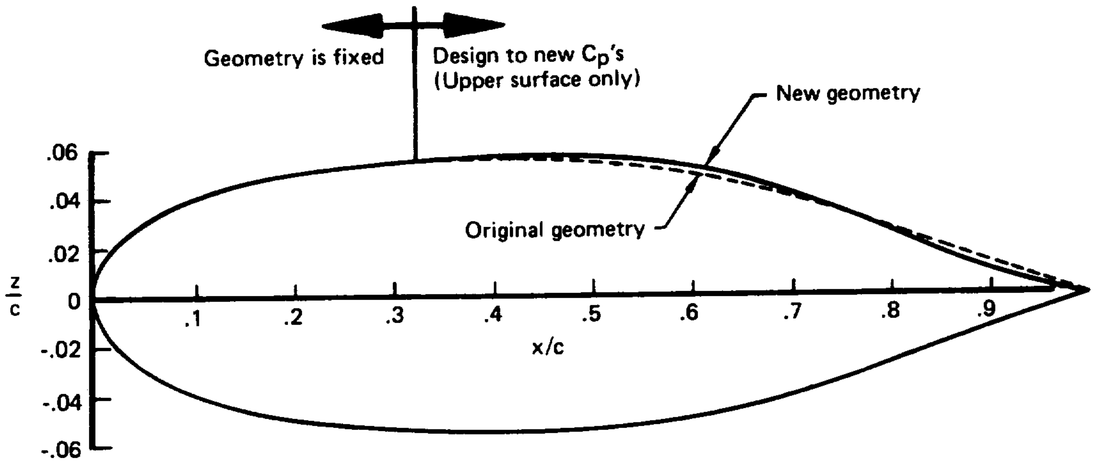

(b) PRESSURE DISTRIBUTION

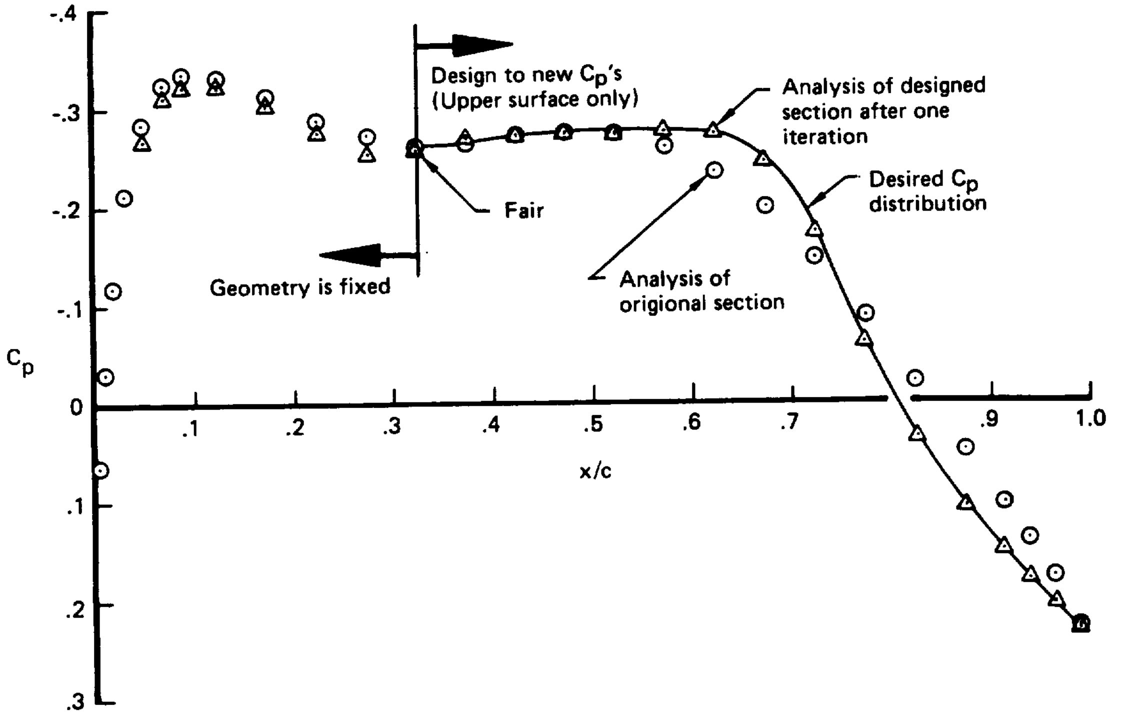

Figure 28. – Redesign of TR 17 Airfoil

(a) GEOMETRY

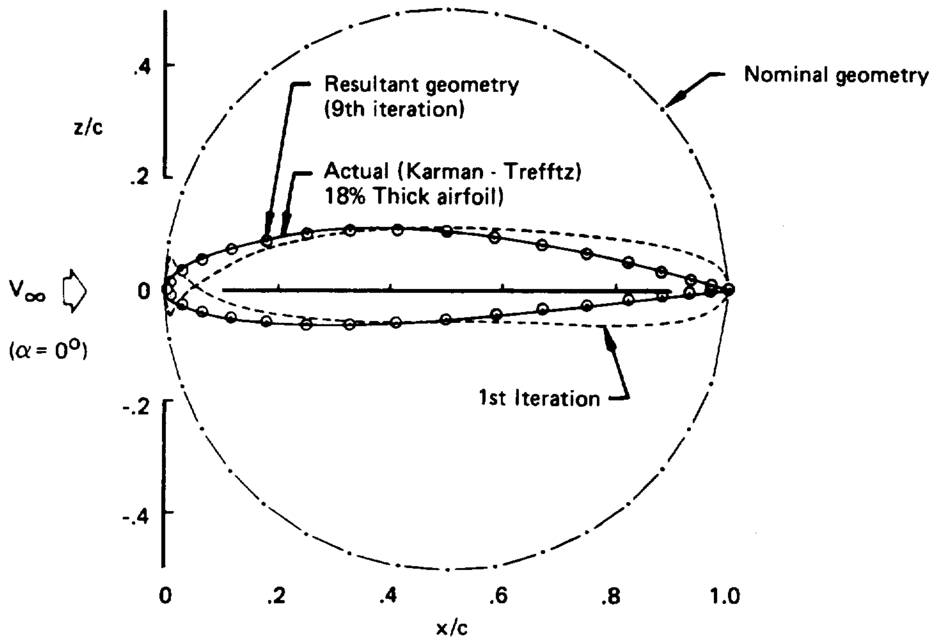

(b) PRESSURE DISTRIBUTION

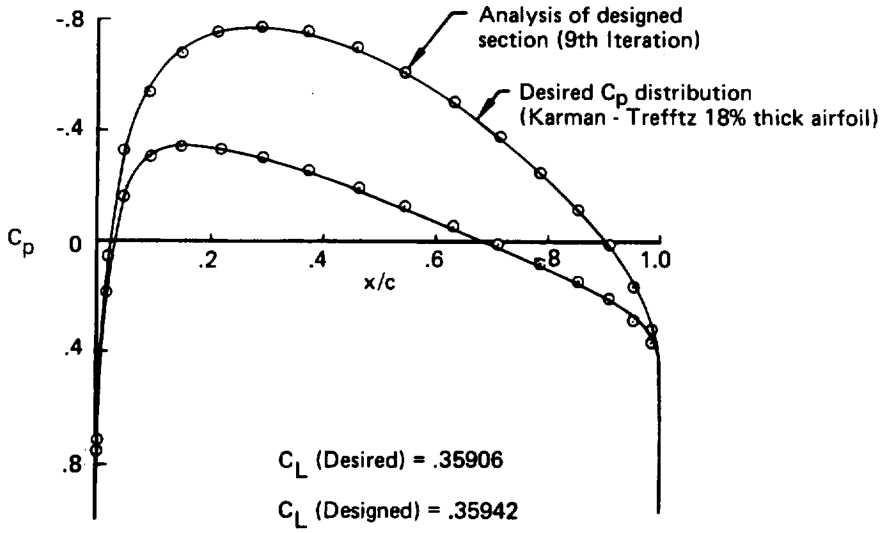

Figure 29. – Full Airfoil Design

6.5.4 WING DESIGN

Figure 30 shows a three-dimensional test of a type 5 (source/design No. 2) network. Paneling of the wing-body model used for the test is displayed in figure 30a. For economy, the model is somewhat abbreviated; nevertheless, the wing has camber, dihedral, and twist. The purpose of the test was to determine if the source/design network in conjunction with a geometry lofting routine could reproduce the original geometry from a perturbed geometry, using as boundary conditions the pressure distribution of the original wing. Analysis of the original geometry produced the wing pressures at four span stations displayed in figure 30b. The network arrangement and boundary conditions were identical to those of the example in section 6.4.1, except that the wing upper surface aft of the leading edge was simulated with a separate source/analysis network. A perturbed wing geometry was achieved by compressing the wing upper surface approximately 30% at four span stations as shown in figure 30c. The configuration was reanalyzed, producing the modified wing pressures in figure 30b. The upper surface source/analysis network with modified geometry was then replaced with a type 5 (source/design No. 2) network. The design boundary conditions applied to panel center control points of this network were of type equation (C.4) with $\vec{t}_L = 0$, $\vec{t}_U$ = the unit vector in the direction of the modified geometry tangential velocities and β_t = the magnitudes of the original geometry velocities. A closure condition of type equation (C.17) with $c_U = 1$, $c_L = 0$ was applied to all four panel columns. The resultant flow produced velocities with nonzero normal components. The design sheet was then relofted to eliminate these components. For this purpose, all grid points at the design sheet edges except those at the wing tip were held fixed. The remaining grid points were allowed to move normal to the wing mean surfaces. The relofting was accomplished using the method of least squares, whereby a function was minimized with respect to a set of free parameters. The payoff was of the form

$$\text{PAYOFF} = \frac{1}{2} \sum_{\substack{\text{panel}\\ \text{centers}}} (\vec{V} \cdot \hat{n})^2$$

where $\vec{V}$ is the total velocity vector at a typical source/design network panel center, resulting from solution of the flow problem. The dependence of each panel center unit normal $\hat{n}$ on the four panel corner points is given in equation (A.1). Let us assume that $\vec{P}_i$ is such a corner point, and that $\hat{z}$ is a unit vector normal to the wing mean surface at $\vec{P}_i$. Then if $\vec{P}_i$ is one of the corner points allowed to move, we assume $\vec{P}_i(\lambda_i) = \vec{P}_i(0) + \lambda_i \hat{z}$, where $\vec{P}_i(0)$ is the location of $\vec{P}_i$ before relofting. λ_i is then a parameter to be optimized in driving PAYOFF to a minimum. Many standard computational techniques are available for finding the minimum of PAYOFF with respect to all the parameters λ_i. The particular technique employed in this case was a damped Newton–Raphson method (chapter 10 of ref. 22).

Two iterations of this design procedure produced a geometry almost identical to the original geometry as shown in figure 30c. The difference between the first and second iterations was relatively small. Resultant pressure distributions for the designed geometry are displayed in figure 30b. At each lofting step, the payoff function was driven to a value very close to zero by unique values of the free parameters. This indicated that the closure conditions performed their function well. It also indicated the necessity of fixing the inboard edge grid points of the design network.

(a) PANELING OF DESIGN MODEL

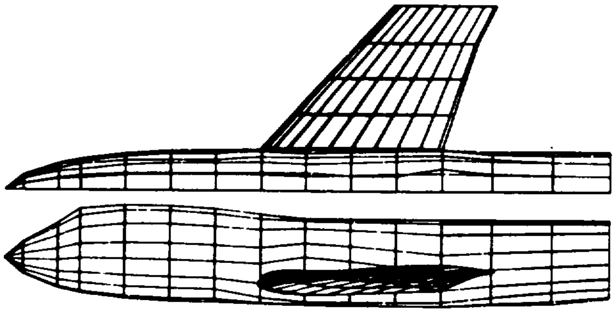

(b) WING-PRESSURE PROFILES—ANALYSIS MODE

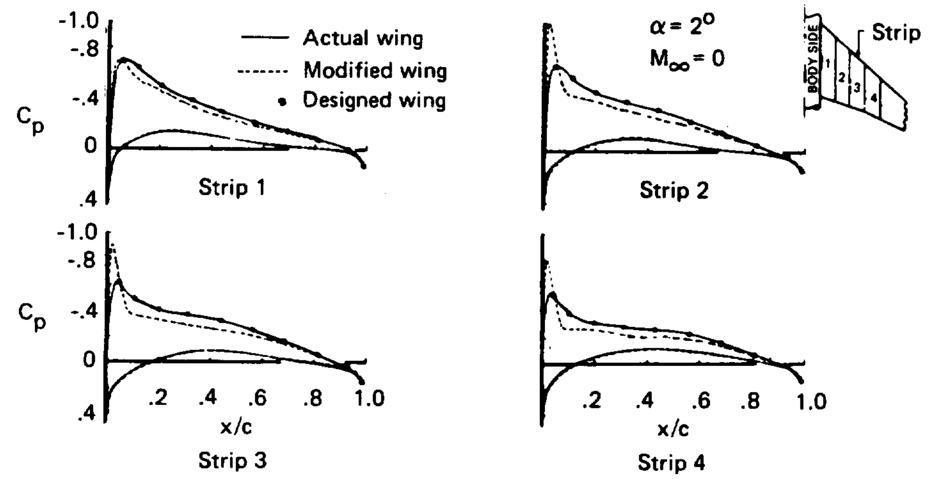

(c) WING GEOMETRY

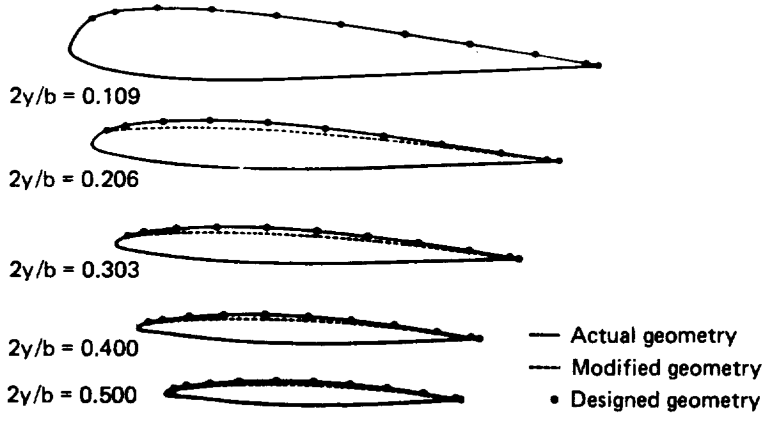

Figure 30. — Wing Design

6.5.5 SPHERE DESIGN

Figure 31 shows the application of a type 5 (source/design No. 2) network to an axisymmetric design problem. A sphere was analyzed with a type 1 (source/analysis) network. Symmetry was exploited so that only the right half of the sphere was modeled. Nine panel rows and columns were used for a total of 81 panels. The panel columns were defined by equally spaced lines of longitude with respect to poles at $x = \pm 1$ and the panel rows were defined by equally spaced x coordinates.

Application of equation (C.3) with the usual impermeability option ($c_U = 1, c_L = 0, \beta_n = 0$) produced tangential velocities agreeing well with exact velocities distribution $V/V_\infty = 1.5\sqrt{1 - X^2}$. The middle of the sphere was then chopped as shown in figure 31a and the resultant geometry was analyzed with three source/analysis networks, the first comprising the first two panel rows, the second comprising the middle five rows (chopped section), and the third comprising the last two panel rows. The resultant velocity distribution is displayed in figure 31b. The middle source/analysis network was then replaced by a type 5 source/design network with the tangential velocity distribution of the original sphere specified at panel center control points. The closure condition (C.17) with $c_U = 1, c_L = 0$ was enforced on all panel columns. The resultant flow produced nonzero normal velocities at each panel center control point which were eliminated by the least square lofting technique of the previous example. In this case, grid points were allowed to move in a radial direction with respect to the x-axis. Only the front and aft edges of the design network were held fixed. Three iterations of this procedure produced a geometry indistinguishable from that of the original sphere.

(a) GEOMETRY (X–Y PLANE CUT)

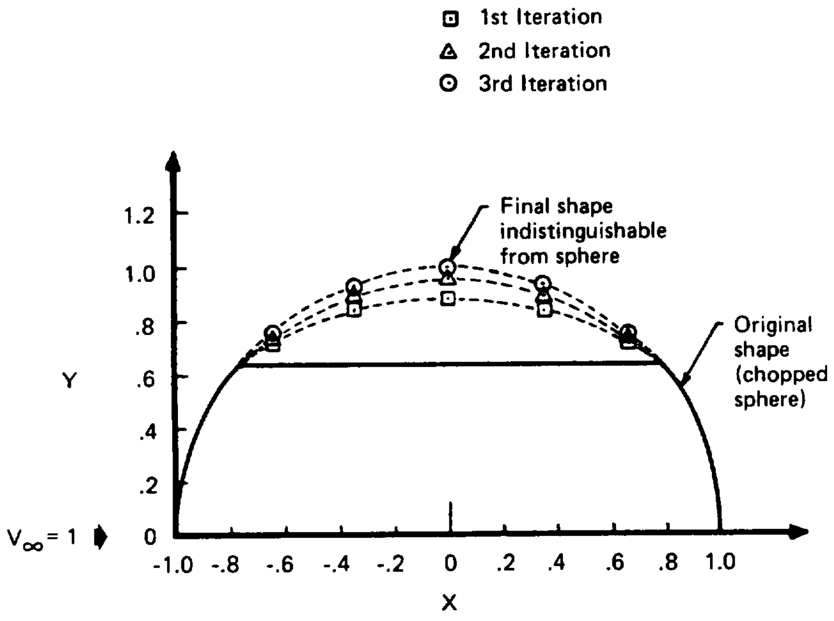

(b) TANGENTIAL VELOCITY

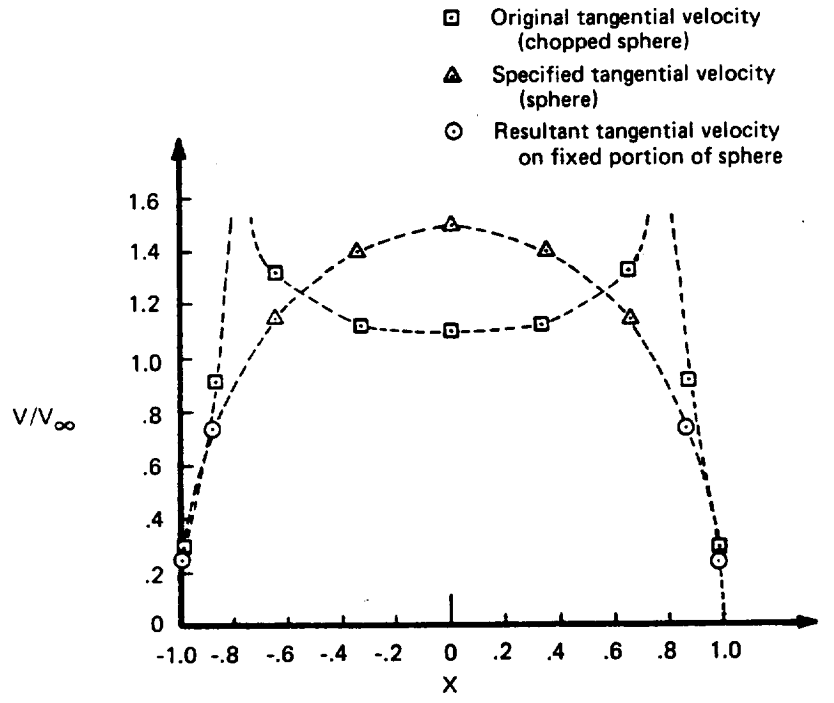

Figure 31. — Sphere Design

6.6 DOUBLET/DESIGN NETWORKS

6.6.1 LEADING EDGE SEPARATION

Figure 32 shows the application of a type 4 (doublet/design No. 1) network to the analysis of separated flow off the leading edge of a sharp-edged thin delta wing. This network was used to represent the free vortex sheet shed from the leading edge as shown in figure 32(a). The wing itself was modeled with a 30 panel type 1 (doublet/analysis) network. A simple kinematic model of the vortex core was simulated with a type 8 (doublet/wake No. 1) network. Other type 8 networks (not shown) were employed to represent wakes extending downstream from the wing and leading edge sheets.

Analysis boundary conditions of type equation (C.3) with $c_U = 1$, $c_L = 0$, $\beta_n = 0$ where specified on the wing. A sophisticated iteration procedure was used to achieve the design-type condition of zero pressure jump across the sheet as well as the requirement that the sheet be a stream surface (refer to equations (5) and (8) of section 4.1). This procedure used a quasi-Newton scheme to simultaneously drive pressure and normal flow residuals to zero; however, at each iteration step, the effective design boundary conditions at free sheet panel centers were of type equation (C.8) with

$$\vec{t}_A = \vec{\nabla}\mu_o , \quad \vec{t}_D = \vec{V}_{A_o} , \quad \beta_t = -\frac{1}{2} V_\infty^2 \Delta C_{p_o}$$

the subscript (0) denoting existing values. These conditions follow from the formula for C_p given by equations (F.1), from which it is easy to show that the jump in C_p across a sheet (ΔC_p) is given by $\Delta C_p = -2\ (\vec{V}_A \cdot \vec{V}_D)/V_\infty^2$ where $\vec{V}_A$ and $\vec{V}_D$ are given by equations (C.5) and (C.6) respectively. From equation (C.10), we see that for a doublet sheet $\Delta C_p = -2\ (V_A \cdot \vec{\nabla}\mu)/V_\infty^2$. Then $-\frac{1}{2}/V_\infty^2\ (\Delta C_p + \Delta C_{p_o}) = (\vec{V}_{Ao} \cdot \vec{\nabla}\mu_o) + (\vec{V}_A - \vec{V}_{Ao}, \vec{\nabla}\mu - \vec{\nabla}\mu_o)$, and the result follows by setting $\Delta C_p = 0$ and neglecting the last term on the right, because it is of second order in the changes from the existing values. Boundary conditions of type equation (2) were specified at the control points along the free sheet edge adjoining the wing to enforce a Kutta condition there.

Free sheet corner points (not attached to the wing) were allowed to vary in planes perpendicular to the centerline to satisfy the stream surface requirement. The variation was defined by fixing panel edge lengths in those planes and assigning slope angles as free parameters.

Figure 32(b) shows detailed pressure distributions for a thin delta wing of aspect ratio 1.4559 at a 14° angle of attack. Upper and lower surface pressure distributions agree with the experimental data from ref. 23 in spite of the sparse wing paneling. Figure 33 displays results for a thin delta wing of aspect ratio 1. Normal force coefficients at four angles of attack are plotted in figure 33(a) and they agree well with the experimental data of Peckham (ref. 24) and theoretical results from the leading edge suction analogy of Polhamus (ref. 25). A typical load distribution is plotted in figure 33(b) and it agrees well with experimental data.

(a) PANELING OF DELTA WING AND VORTEX SHEET

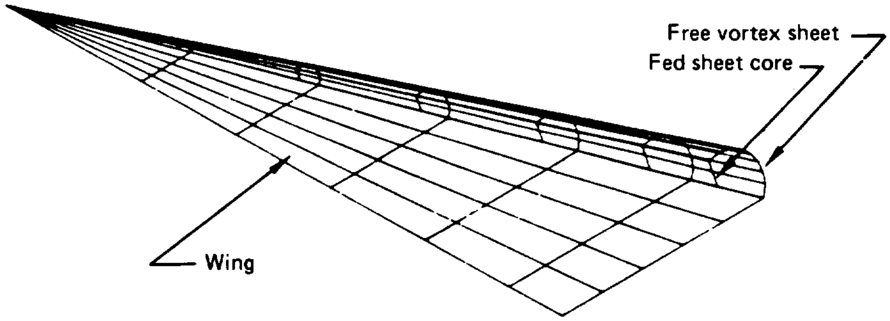

(b) SURFACE PRESSURE DISTRIBUTION OF DELTA WING

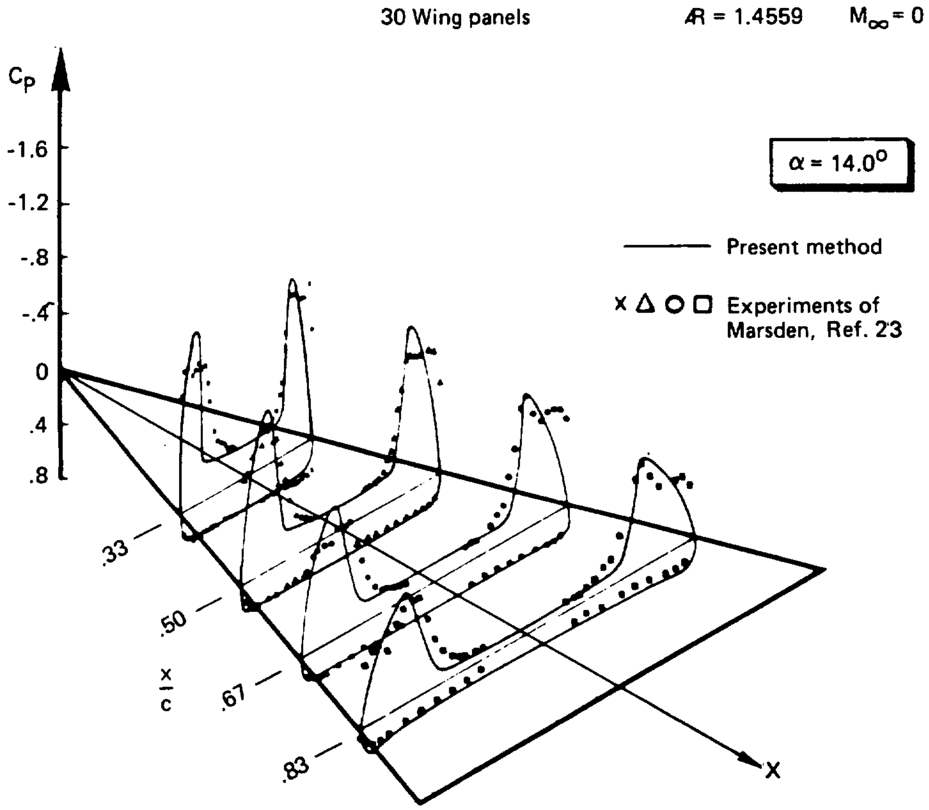

Figure 32. — AR 1.4559 Delta Wing with Leading Edge Separation

(a) NORMAL FORCE COEFFICIENT AT VARIOUS α

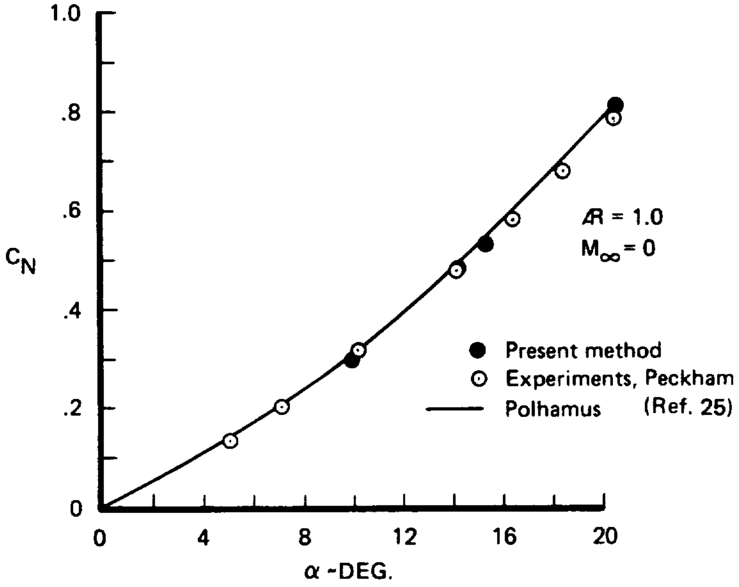

(b) TYPICAL LOAD DISTRIBUTION

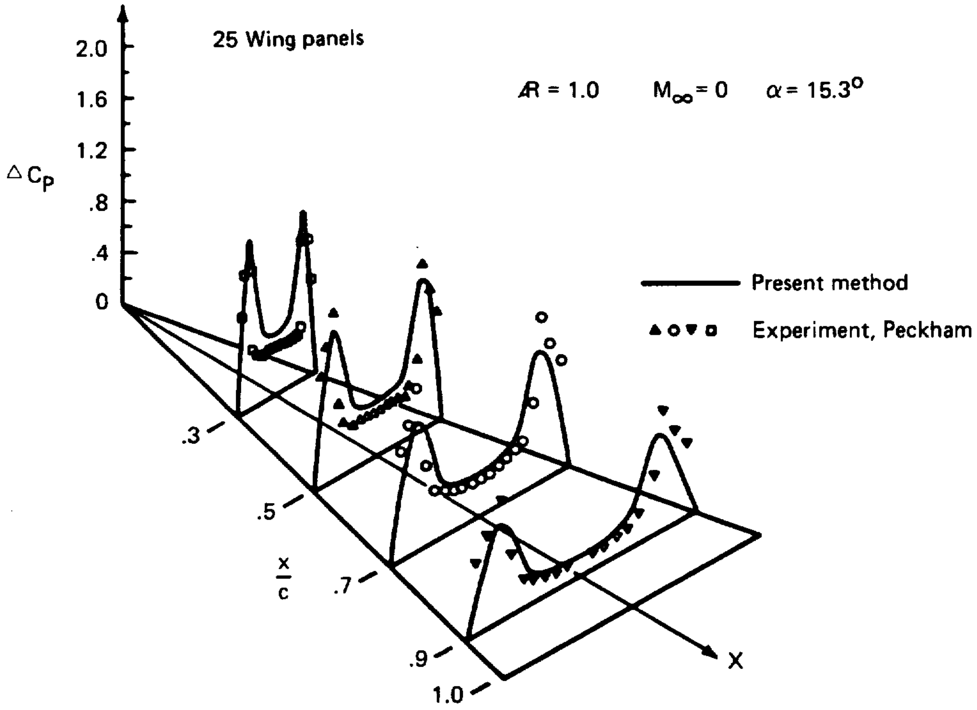

Figure 33. — Æ 1 Delta Wing with Leading Edge Separation

6.7 NUMERICAL EFFICIENCY

Enough information is currently available to surmise that the computing costs associated with the present use of curved panels and locally varying singularity strengths are quite comparable on a panel by panel basis with those of first order panel methods. (In terms of total computing cost per problem the present method has clear advantages because of the reduced number of panels required.)

Computing costs depend primarily on central processing (CP) time and mass storage use (IO). Although IO costs are important, they are little affected by the use of higher order panels and singularities. To be sure, additional geometry and singularity defining quantities must be stored for each panel, but IO costs usually depend more on mass storage access requests than the quantity of data stored per record. For cases with less than a certain number of panels (about 750 in our case) the IO costs of a well-optimized program are usually small compared to CP costs. For cases with greater than this number of panels, the IO costs of solving the influence coefficient equations are dominant.

For an influence coefficient program CP costs behave according to the rough formula,

$$\text{Cost} = C_1 n + C_2 n^2 + C_3 n^3 \tag{18}$$

where n is the number of panels. The linear term on the right is associated with the computation of panel geometry, singularity strength and control point defining quantities as well as the calculation of output. The quadratic term corresponds to the computation of the influence coefficients and the cubic term is associated with solving the influence coefficient equation set. The severity of the cubic term can sometimes be reduced through the use of iterative techniques, but the diagonal dominance required for convergence is difficult to ensure for truly arbitrary configurations with interacting components. The quadratic term is somewhat too severe to represent the behavior of the CP time for generating influence coefficients when n is in the usual range of interest. This is because pure increases in panel density are accompanied by a higher proportion of efficient far field calculations. Nevertheless, the quadratic assumption is sufficient for the present analysis.

The coefficient C_1 is considerably greater for the present method than for first order techniques. With the exception of output calculations, the linear terms dominate only when $n < 25$ and by the time $n = 60$, they contribute less than 10% of the total cost. However, for multiple freestream directions, the output calculations can represent up to 25% of the total CP costs even when $n = 500$. This is because the present pilot code calculates an enormous quantity of output—primarily for diagnostic purposes. Presumably, a production program would not require such extravagance.

The coefficient C_3 is unaffected by the use of higher order panels and singularities. Current projections indicate the cubic terms become dominant when $n > 1000$, so that the cost advantage of using a higher order method is clear for large cases. Here, however, we must note that the effective value of n increases for networks with edge control points. In most cases to which current first order techniques are applied, the edge control point equations are somewhat uncoupled from the total equation set, although advantage is not derived from this fact in the pilot program. The reason for this uncoupling is that the edge control point boundary conditions effectively control singularity matching across network edges (app. c) and therefore, each such boundary condition equation depends only on a few unknown singularity parameters in the neighborhood of the network edge.

For problems with moderate numbers of panels ($50 < n < 1000$), the quadratic term of equation (18) is dominant. The calculation of influence coefficients is the area where some higher order methods would ordinarily be expected to incur substantial penalty. For the present method, this is not the case; primarily because the contributions of higher order terms can be expressed as simple combinations of lower order terms. Table 1 shows near field influence coefficient calculation time comparisons between the present method and two first order methods–those of references 6 and 26. Table 2 shows analogous data for intermediate and far field calculations. Reformulation of the pilot code for the curved panel option has not yet been accomplished. The near field flat panel source calculation of the present method is faster than that of TEA 230, although computation of higher order terms requires about 10 more operations. Actually CP time is only roughly proportional to operation count and such a variation falls well within the range expected for different codes. The same is true of the source intermediate and far field calculations. The times displayed in table 1 and 2 correspond to the computation of the potential and velocity at a field point induced by a singularity distribution on a panel. There is also an additional cost for transforming the resultant velocities to global coordinates. Moreover, for the present method, there is a further cost of distributing the influence coefficients to the singularity parameters. The net additional cost for the present method is approximately 0.24 milliseconds per source influence coefficient and 0.58 milliseconds per doublet influence coefficient. These costs diminish the effectiveness of the far field computations in the present pilot code; however, they can be recovered for the important source/analysis network by implementing the third recommendation of section 7.2.

In figure 34, we show CP time comparisons between the highly optimized TEA 230 program and the pilot code of the present method. The range of CP times for a given number of singularity parameters reflects variations due to source and doublet and to near field and far field ratios. TEA 230 appears to be about 30% faster on the average on a panel for panel basis. It is estimated that for a well-polished version of the present method, this advantage could be reduced to 15%.

Table 1. — Near Field AIC Calculation Time Comparisons

AIC	Panel geometry	CDC 6600 Time (milliseconds)	
		Source	Doublet
1. Present method (original formulation)	Flat Curved	8. 13.	15. 29.
2. Present method (reformulation of recursions, etc.)	Flat Curved	4.2 6.1	6.3 9.
3. Present method (reformulation of code)†	Flat Curved	.91 —	1.41 —
4. TEA 230 (Ref. 6)	Flat	.94	1., 14.*
5. Flexstab (Ref. 26)	Flat	Not easily isolated	5.4**

†Funded by Boeing IR & D

*Linearly varying vortex

**Constant strength vortex

Table 2. — Intermediate / Far Field AIC Calculation Time Comparisons

AIC	Panel geometry	CDC 6600 Time (milliseconds)			
		Source		Doublet	
		Far field	Int. field	Far field	Int. field
1. Present method (original formulation)	Flat Curved	.6 .6	.9 .9	.7 .7	1.8 1.8
2. Present method (reformulation of recursions, etc.)	Flat Curved	.09 .09	.54 .54	.26 .26	.72 .72
3. Present method (reformulation of code)†	Flat Curved	.09 .09	.54 .54	.26 .26	.72 .72
4. TEA 230 (Ref. 6)	Flat	.16	.26	Not comparable	
5. Flexstab (Ref. 26)	Flat		Not comparable		

†Funded by Boeing IR & D

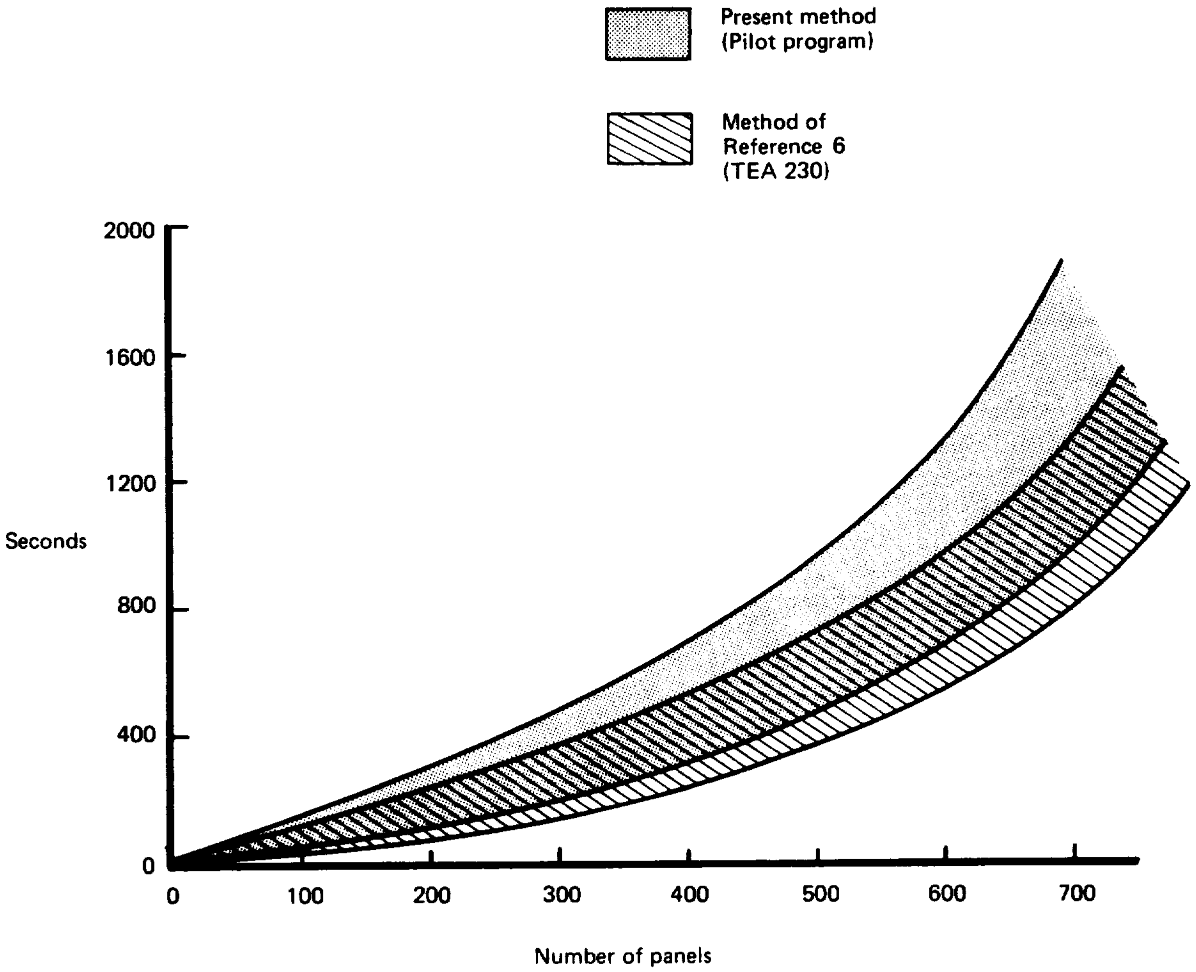

Figure 34. – Central Processor Time Comparisons; CDC 6600

7.0 CONCLUDING REMARKS

7.1 CONCLUSIONS

An advanced panel method for solving boundary value problems associated with the analysis and design of arbitrary configurations in subsonic potential flow has been presented. Theory and computed results indicate the method has the necessary characteristics for widespread acceptance by the user community. These characteristics include the following:

1. Generality: The method is capable of solving a wide range of analysis and design boundary value problems. In particular, the method can handle virtually all analysis problems to which current panel techniques are applied. The added feature of combined analysis and design provides a capability that is extremely powerful for an extensive variety of applications. Most design problems involve the aerodynamic design of one or more components of a configuration in the presence of others whose geometrical shapes are fixed. The present method provides this capability along with the limiting cases of pure design or analysis.

2. Flexibility: The method offers the user a variety of modeling options as well as a straightforward means of implementing those most suited to a specific application. For economical analysis and design, all the usual thin surface approximations are available. For more accurate results, exact boundary conditions may be applied on actual configuration surfaces. Here, a variety of surface singularity distributions are available. The efficient source-alone option may be employed on nonlifting portions of the configuration. Components which shed vorticity can be modeled with combined source and doublet surfaces or source surfaces accompanied by interior doublets or doublet surfaces accompanied by interior sources. The shed vorticity can be fixed in location and direction or designed to satisfy pressure jump and stream surface requirements. These and other options are easily implemented through the use of standard networks to simulate arbitrary boundary surfaces. Aside from modeling versatility, the method offers substantial paneling flexibility. No restrictions appear necessary on panel shape or orientation so long as density is sufficient for the accuracy desired.

3. Stability and Accuracy: For well-posed boundary value problems, the present method has been demonstrated to be numerically stable and accurate even under extremely adverse conditions. It displays a marked insensitivity to paneling layout and achieves acceptable accuracy with relatively sparse panel densities. Convergence to highly accurate results occurs at moderate panel densities.

4. Efficiency: On a panel-by-panel basis, the present method appears capable of the same efficiency as that enjoyed by existing first order techniques. On a case-by-case basis, the present method has significant advantages because of the reduced number of panels required. These advantages become overwhelming for cases involving complex configurations.

7.2 RECOMMENDATIONS

During the development of the present method, a number of improvements were discovered but not implemented because they did not sufficiently bear on establishing feasibility. Nonetheless, these improvements could have significant impact on any production-oriented version of the method and therefore we sketch the more important ones below.

1. Curvature expansion: The curvature expansion of equation (D.18) is valid for any field point, although it is used only for near field calculations. More efficient expansions are available for this case. As an example, we have

$$\frac{1}{R} \approx \frac{1}{\sqrt{\left[(1 - ha)\,\xi - (1 + ha)x\right]^2 + \left[(1 - hb)\eta - (1 + hb)y\right]^2 + h^2}}$$

   when (x,y) is in close proximity to Σ. By a suitable linear transformation, this approximation reduces to the flat panel expression with corresponding simplifications to equations (D.22), (D.28), (D.32) and (D.34). Here, curvature is simulated by modifications to the panel shape and field point location.

2. Near Field Influence Coefficient Calculation: One of the mitigating factors in the use of higher order singularity splines is that the complexity of the near field influence coefficient calculation need not grow at the rate one might expect. This is because the increased continuity of the splines across panel edges allows the elimination of many canceling line integrals. (Refer to sec. D.5 of app. D). At present, no advantage is derived from the fact.

3. Projection Algorithm: For the construction of the higher order panel surface representations and singularity distributions, an orthogonal tangent plane projection algorithm is currently used. (Refer to eq. (A.9) and (B.5), (B.2) and (B.3.) Because of the tendency of the user community to violate hypothesis (A.23), a length and azimuth preserving projection would be better. For example, the standard projection could be altered by scaling the distance from the projected point to the origin so that it is the same as the distance from the original point to the origin.

4. Curvature: At the present time, violation of the curvature restriction (A.21) is ignored. It would be better to incorporate this constraint into the least square panel surface fit algorithm so that it is satisfied automatically. At the same time, provision should be made for better curvature definition in cases with sparse paneling, e.g., extra grid points at panel centers.

5. Specification of Singularity Strength: The specification of source or doublet strength at a control point now requires an influence coefficient equation, although the equation usually amounts to direct specification of an element of the solution vector. Such an equation should be eliminated from the full equation set before solution. In the case of the continuous doublet/analysis spline wherein the values of the singularity parameters do not directly correspond to singularity strength, the network boundary condi-

tion equations for any such network still uncouple from the full set and can be solved prior to the full solution. This reduction can also be applied to certain situations where doublet strength gradient is specified at panel center control points of a design type network.

6. Superimposed Doublet and Source Panels: In the present numerics, superimposed doublet and source networks are treated independently even when paneling is identical. There are clear advantages to identifying superimposed panels in the geometry definition, influence coefficient calculation and force computation procedures. These advantages are best exploited by defining new network types with combined source and doublet splines and duplicate control points.

7. Force and Moment Calculations: The force and moment calculations of appendix F should be generalized to include momentum transfer terms for cases involving permeable surfaces and edge delta function terms for cases involving thin surface approximations. These generalizations are already under study in connection with the work of reference 17.

8. Panel Center Boundary Condition Generalization: In connection with certain design problems, it appears desirable to require that the pressure at a given control point be equal to that at another control point. More generally, it appears desirable to allow boundary conditions which relate quantities at any number of control points. The closure condition (eq. (C.17) is already a boundary condition of this type. Another example is the slotted wind tunnel wall boundary condition, i.e., $k^2\phi + \frac{\partial \phi}{\partial n} = k^2\phi_o + \frac{\partial \phi_o}{\partial n}$ where ϕ_o and $\frac{\partial \phi_o}{\partial n}$ are evaluated upstream of the slotted wall section. The well-posed nature of the resultant boundary value problems is open to question, but preliminary experiments indicate that such boundary conditions can work very well in practice. The necessary modifications to equations (C.3) and (C.4) are straightforward.

9. **Grid Layout Generalization.** The requirement that grid points and panels be arranged in rows and columns limits the ability to vary panel density in complex configurations. Clearly our least square definitions of panel geometry and singularity strength do not require such an arrangement and a more general panel identification logic is highly desirable.

10. Design Procedure Generalization: Of all the design procedures described in the examples of section 6, that of reference 17 appears to offer the most potential for practical design. Here, the problem of designing a stream surface to support a given pressure distribution is attacked as an optimization problem in which a payoff consisting of a weighted sum of residuals is minimized using sophisticated iteration techniques. The residuals include deviations in both pressure and normal flow and the optimizing variables are the singularity parameters as well as the parameters controlling surface perturbations. The pressure specification and stream surface lofting problems are coupled in this formulation, but this has the advantage of allowing trade studies. For example, inequality or equality constraints can be applied to the surface perturbation parameters, resulting in either an acceptable or unacceptable degradation in the specified pressure distribution. Moreover, residuals of certain specified functions of pressure (forces and moments) can be weighted and added to the payoff function.

APPENDIX A
GEOMETRY DEFINITION

A.1 INTRODUCTION

In this appendix, we shall define how a surface is constructed which approximates the true surface (i.e., analytically defined input surface) for the purpose of achieving a numerical solution to the flow problem. We assume that the overall configuration has been partitioned into networks. In the interior of each network, the true surface is assumed to have continuous position, slope and curvature. Any discontinuities in these quantities, as far as the true configuration surface is concerned, must therefore, occur at network edges. We assume that a discrete representation of the true network surface is provided by a grid of corner points $\vec{P}(I,J)$; $I = 1,M$ and $J = 1,N$ where the elements of the position vector of $\vec{P}$ are resolved in a global (x,y,z) coordinate system. A planar schematic of these points is shown in figure A.1. The grid layout is shown as rectangular for convenience only. For example, the wing corner points of figure 15a form an $M = 9$ by $N = 7$ grid. For each point J identifies the column of points to which it belongs and I identifies the row. The grid is assumed to be sufficiently dense that the portion of the true network surface lying between four adjacent corner points does not deviate significantly from their average plane (to be discussed later). Moreover, we assume that the projection of the four corner points onto their average plane defines a quadrilaterial which at most degenerates into a triangle. (We, therefore, require at least three of every four adjacent corner points of a grid to be distinct.) The construction of an approximate surface or panel S lying between four adjacent corner points of the grid is the subject of the next two sections.

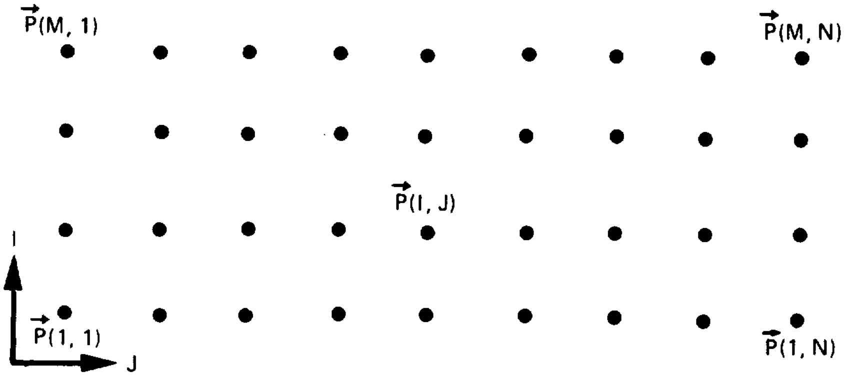

Figure A.1. – Schematic of Corner Point Grid

A.2 FLAT PANEL APPROXIMATION

Consider four adjacent corner points $\vec{P}(I,J)$, $\vec{P}(I,J+1)$, $\vec{P}(I+1,J+1)$ and $\vec{P}(I+1,J)$ and relabel these points as $\vec{P}1$, $\vec{P}2$, $\vec{P}3$ and $\vec{P}4$ respectively. In this section, we will construct a first order approximation S to the true surface of the network lying between $\vec{P}1$, $\vec{P}2$, $\vec{P}3$ and $\vec{P}4$. At the same time, we will define a local orthogonal coordinate system on S for later use.

Let the orthogonal unit vectors $\hat{\xi}$, $\hat{\eta}$ and $\hat{\zeta}$ be defined as:

$$\hat{\xi} = \frac{\left[\vec{P}_1 + \vec{P}_4 - \vec{P}_2 - \vec{P}_3\right]}{\left|\left[\vec{P}_1 + \vec{P}_4 - \vec{P}_2 - \vec{P}_3\right]\right|}$$

$$\hat{\zeta} = \hat{\xi} \otimes \frac{\left[\vec{P}_1 + \vec{P}_2 - \vec{P}_3 - \vec{P}_4\right]}{\left|\left[\vec{P}_1 + \vec{P}_2 - \vec{P}_3 - \vec{P}_4\right]\right|}$$

$$\hat{\eta} = \hat{\zeta} \otimes \hat{\xi} \tag{A.1}$$

where $\otimes$ denotes the vector cross product.

Let the average point $\vec{P}_o$ be defined by

$$\vec{P}_o = \frac{1}{4}\left[\vec{P}_1 + \vec{P}_2 + \vec{P}_3 + \vec{P}_4\right] \tag{A.2}$$

The plane passing through $\vec{P}_o$ with normal $\hat{\zeta}$ is defined being the average plane of the points $\vec{P}_1$, $\vec{P}_2$, $\vec{P}_3$ and $\vec{P}_4$. This plane is average in the sense that it also passes through the midpoints of the line segments joining $\vec{P}_1$ and $\vec{P}_2$, $\vec{P}_2$ and $\vec{P}_3$, $\vec{P}_3$ and $\vec{P}_4$, $\vec{P}_4$ and $\vec{P}_1$ as shown in figure A.2. To see this, we note that it is sufficient to prove that $\hat{\zeta} \cdot (\vec{P}_M - \vec{P}_o) = 0$ where $\vec{P}_M$ is one of the midpoints, i.e., $\vec{P}_M = \frac{1}{2}(\vec{P}_i + \vec{P}_{i+1})$. By direct substitition, one can show that for any i, $\vec{P}_M - \vec{P}_o = \pm(\vec{P}_1 + \vec{P}_4 - \vec{P}_2 - \vec{P}_3)$ or $\pm(\vec{P}_1 + \vec{P}_2 - \vec{P}_3 - \vec{P}_4)$. The result then follows from (A.1), (A.2) and the well known fact that for any vector $\vec{a}$ and $\vec{b}$, $\vec{a} \cdot (\vec{a} \otimes \vec{b}) = 0$.

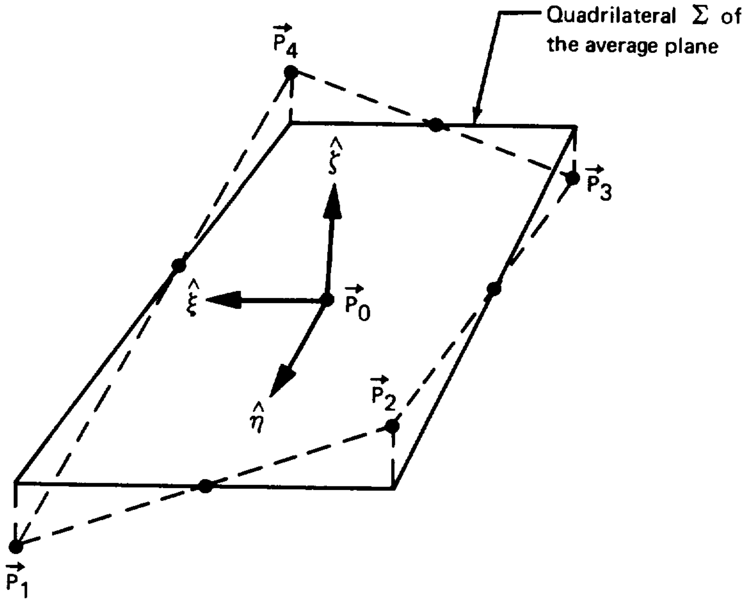

Figure A.2. – Average Plane of Four Adjacent Corner Points

Note that the average plane of four arbitrary points is not unique and depends on the order assigned the points. Also note the cyclical order assigned the points above is such that the normals $\hat{\zeta}$ of all the panels lie on the same side of the network surface.

The points formed by the intersection of the average plane with the perpendiculars from $\vec{P}_1$, $\vec{P}_2$, $\vec{P}_3$ and $\vec{P}_4$ onto the average plane define a plane quadrilateral Σ whose boundary consists of the straight line segments joining these projections in cyclical order (see fig. A.2.). The panel Σ is taken to be the surface S which approximates the true surface. The coordinate directions of the local coordinate system associated with S are taken to be the $\hat{\xi}$, $\hat{\eta}$ and $\hat{\zeta}$ directions, however, the origin is chosen as the centroid $\vec{P}_c$ of the panel Σ, rather than the average point $\vec{P}_0$. This choice makes little difference numerically, but is made to facilitate comparisons with earlier codes such as TEA 230, which also have origins at the panel centroid. The centroid $\vec{P}_c$ may be computed as follows:

Define

$$\vec{P}_5 = \vec{P}_1 \tag{A.3}$$

and

$$\left.\begin{aligned} \xi_i &= (\vec{P}_i - \vec{P}_o) \cdot \hat{\xi} \\ \eta_i &= (\vec{P}_i - \vec{P}_o) \cdot \hat{\eta} \end{aligned}\right\} \quad i = 1, \ldots 5$$

Then

$$\vec{P}_c = \vec{P}_o + \frac{1}{3D} \sum_{i=1}^{4} D_i \left[(\xi_i + \xi_{i+1}) \, \hat{\xi} + (\eta_i + \eta_{i+1}) \, \hat{\eta} \right] \qquad \text{(A.4)}$$

where

$$D_i = \frac{1}{2} (\xi_i \, \eta_{i+1} - \eta_i \, \xi_{i+1})$$

and

$$D = \sum_{i=1}^{4} D_i$$

With this choice of local coordinates, any point $\vec{P}$ with components (x,y,z) in the global system is the same as the point $\vec{Q}$ with components (ξ, η, z) resolved in the local system if and only if

$$\overline{Q} = \overline{A} \left(\overline{P} - \overline{P}_c \right) \qquad \text{(A.5)}$$

i.e.,

$$\begin{pmatrix} \xi \\ \eta \\ \zeta \end{pmatrix} = \begin{pmatrix} A_{11} & A_{12} & A_{13} \\ A_{21} & A_{22} & A_{23} \\ A_{31} & A_{32} & A_{33} \end{pmatrix} \begin{pmatrix} x - x_c \\ y - y_c \\ z - z_c \end{pmatrix}$$

where (x_c, y_c, z_c) are the global coordinates of the centroid $\vec{P}_c$.

Here, $\bar{A}$ is the 3 x 3 orthogonal matrix,

$$\bar{A} = \begin{pmatrix} \{\hat{\xi}^T\} \text{——} \\ \{\hat{\eta}^T\} \text{——} \\ \{\hat{\zeta}^T\} \text{——} \end{pmatrix} \tag{A.6}$$

(where $\{\hat{\xi}\}$, $\{\hat{\eta}\}$ and $\{\hat{\zeta}\}$ are the column vectors containing the x, y and z components of the unit vectors $\hat{\xi}$, $\hat{\eta}$ and $\hat{\zeta}$, respectively, and T denotes transpose.) We also note the inverse transformation, i.e.,

$$\bar{P} = \bar{A}^T \bar{Q} + \bar{P}_c \tag{A.7}$$

In general, the flat panel approximation to the network surface described above possesses discontinuities in position and slope along panel edges. However, because of our assumptions about the smoothness of the true network surface, these discontinuities become small relative to panel size as the grid density increases.

For a somewhat coarse grid, these discontinuities as well as deviations from the true surface can be large, relative to panel size; moreover, the effect of local curvature on the local flow is lost. For these reasons, a curved panel approximation has been devised and is described in the following section.

A.3 CURVED PANEL APPROXIMATION

In this section, we will construct a second order approximation to the true surface of the network lying between $\vec{P}_1, \vec{P}_2, \vec{P}_3$ and $\vec{P}_4$. Our smoothness assumptions about the true network surface imply that for a sufficiently fine grid, the portion of the true surface lying between $\vec{P}_1, \vec{P}_2, \vec{P}_3$ and $\vec{P}_4$ can be approximated by a parabolic panel S whose shape depends only on local grid points. The panel S may be defined in a variety of ways, but we select the following. Using the local (ξ, η, ζ) coordinate system constructed in section (A.2), we assume S may be represented in the approximate form

$$\zeta(\xi, \eta) = \zeta_o + \zeta_\xi \xi + \zeta_\eta \eta + \frac{1}{2} \zeta_{\xi\xi} \xi^2 + \zeta_{\xi\eta} \xi\eta + \frac{1}{2} \zeta_{\eta\eta} \eta^2 \tag{A.8}$$

The coefficients $(\zeta_o, \zeta_\xi, \zeta_\eta, \zeta_{\xi\xi}, \zeta_{\xi\eta}, \zeta_{\eta\eta})$ are then obtained by fitting S to a set of points Π which is composed of the corner points $\vec{P}_1, \vec{P}_2, \vec{P}_3$ and $\vec{P}_4$, as well as every grid point adjacent to these points. The fit is accomplished by the method of weighted least squares. To be specific, we minimize the quantity

$$R = \frac{1}{2} \sum_k w_k \left(\zeta(\xi_k, \eta_k) - \zeta_k \right)^2 \tag{A.9}$$

where (ξ_k, η_k, ζ_k) are the known coordinates of a point $\vec{P}_k$ in Π. The weights W_k are chosen to be unity, unless $\vec{P}_k$ happens to be a corner point of S, in which case W_k is chosen large (nominally 10^8). With this choice, S very nearly passes through its corner points. If we let $\overline{C}$ be the column vector with components $(\zeta_o, \zeta_\xi, \zeta_\eta, \zeta_{\xi\xi}, \zeta_{\xi\eta}, \zeta_{\eta\eta})$ and $\overline{V}_k$ the column vector with components $(1, \xi_k, \eta_k, \frac{1}{2}\xi_k^2, \xi_k\eta_k, \frac{1}{2}\eta_k^2)$, then $\zeta(\xi_k,\eta_k) = \overline{V}_k^T C_k$, and minimizing R with respect to the components of $\overline{C}$ yields

$$\underset{(6 \times 1)}{\overline{C}} = \Bigg[\sum_k \underset{(6 \times 6)}{W_k \overline{V}_k \overline{V}_k^T} \Bigg]^{-1} \sum_k \underset{(6 \times 1)}{W_k \zeta_k \overline{V}_k} \tag{A.10}$$

(Here the superscript -1 denotes matrix inverse.)

Once the coefficients in $\overline{C}$ have been obtained the expression (A.8) for the surface S can be simplified by a suitable transformation of coordinates. If the coefficient $\zeta_{\xi\eta}$ is nonzero, the $\xi\eta$ term may be eliminated by a rotation of the (ξ, η, ζ) coordinate system about the ζ axis through the angle $\psi \epsilon \, [-\pi/4, \pi/4]$ where

$$\psi = \sin^{-1} \left[\lambda \sqrt{\frac{1}{2} \left| 1 - \frac{|\zeta_{\xi\xi} - \zeta_{\eta\eta}|}{\sqrt{4\zeta^2_{\xi\eta} + (\zeta_{\xi\xi} - \zeta_{\xi\eta})^2}} \right|} \right] \tag{A.11}$$

and

$$\lambda = \begin{cases} 1 & \text{if} \quad \zeta_{\xi\eta}\left(\zeta_{\xi\xi} - \zeta_{\eta\eta}\right) \geqslant 0 \\ -1 & \text{otherwise} \end{cases}$$

This defines a primed local coordinate system such that a point $\vec{P}$ having coordinates (x,y,z) in the global system is the same as a point $\vec{Q}$ having coordinates (ξ', η', ζ') in the primed local system if and only if

$$\overline{Q} = \overline{A}' \left(\overline{P} - \overline{P}_c\right) \tag{A.12}$$

where

$$\overline{A}' = \overline{D}\overline{A}$$

Here $\overline{A}$ and $\overline{P}_c$ are defined in section (A.2) and

$$\overline{D} = \begin{pmatrix} \cos\psi & \sin\psi & 0 \\ -\sin\psi & \cos\psi & 0 \\ 0 & 0 & 1 \end{pmatrix}$$

In the primed local coordinate system S has the representation

$$\zeta' = \zeta_o + d\xi' + e\eta' + a\xi'^2 + b\eta'^2 \qquad \text{(A.13)}$$

where

$$a = \frac{1}{2}(\zeta_{\xi\xi}\cos^2\psi + 2\zeta_{\xi\eta}\cos\psi\sin\psi + \zeta_{\eta\eta}\sin^2\psi)$$
$$b = \frac{1}{2}(\zeta_{\xi\xi}\sin^2\psi - 2\zeta_{\xi\eta}\cos\psi\sin\psi + \zeta_{\eta\eta}\cos^2\psi)$$
$$d = \zeta_\xi\cos\psi + \zeta_\eta\sin\psi$$
$$e = -\zeta_\xi\sin\psi + \zeta_\eta\cos\psi$$

If $a \neq 0$, the term linear in ξ' may be eliminated by a translation of the origin of the (ξ', η', ζ') coordinate system to the point

$$\xi' = \frac{-d}{2a}, \quad \eta' = 0, \quad \zeta' = 0 \qquad \text{(A.14)}$$

If $b \neq 0$, the term linear in η' may be eliminated in a similar fashion. If $a = 0$, then the term linear in ξ' may be eliminated by a rotation of the (ξ', η', ζ') coordinate system about the $\hat{\eta}$ axis through an angle $\alpha \epsilon [-\pi/2, \pi/2]$, where

$$\alpha = \sin^{-1}\left(\frac{d}{\sqrt{1+d^2}}\right) \qquad \text{(A.15)}$$

If $b = 0$, the term linear in η' may be eliminated similarly by a rotation about the $\hat{\xi}$ axis.

If a is nonzero but much smaller than d, equation (A.14) translates the origin of the (ξ', η', ζ') coordinate system far away from the panel causing eventual numerical difficulties. The transformation (A.15) however, is a mere coordinate system rotation and clearly to be preferred. If this transformation is used when $a \neq 0$, the expression for S in the resultant (ξ'', η'', ζ'') coordinate system will have no linear ξ'' term as desired, but will have quadratic terms involving ζ''. These quadratic terms are actually of higher order in δ (see eq. (A.21)) and can be ignored if the grid is sufficiently fine or removed iteratively otherwise. To remove the quadratic terms involving ζ'', iteratively we use the following procedure. We define a double primed local coordinate system in a manner similar to that suggested above, such that a point $\vec{P}$ having components (x,y,z) in the global system is the same as a point $\vec{Q}$ having components (ξ'', η'', ζ'') in the double primed local system if and only if

$$\bar{Q} = \bar{A}''(\bar{P} - \bar{P}_c) \text{ or } \begin{Bmatrix} \xi'' \\ \eta'' \\ \zeta'' \end{Bmatrix} = [\bar{A}''] \begin{Bmatrix} x - x_c \\ y - y_c \\ z - z_c \end{Bmatrix} \tag{A.16}$$

where

$$\bar{A}'' = \bar{E}\bar{A}'$$

and

$$\bar{E} = \begin{pmatrix} 1 & 0 & 0 \\ 0 & \cos\beta & \sin\beta \\ 0 & -\sin\beta & \cos\beta \end{pmatrix} \begin{pmatrix} \cos\alpha & 0 & \sin\alpha \\ 0 & 1 & 0 \\ -\sin\alpha & 0 & \cos\alpha \end{pmatrix}$$

$$= \begin{pmatrix} \cos\alpha & 0 & \sin\alpha \\ -\sin\beta\sin\alpha & \cos\beta & \sin\beta\cos\alpha \\ -\cos\beta\sin\alpha & -\sin\beta & \cos\beta\cos\alpha \end{pmatrix}$$

and

$$\alpha = \sin^{-1}\left(\frac{d}{\sqrt{1 + d^2}}\right) \quad ; \alpha \epsilon [-\pi/2, \pi/2]$$

$$\beta = \sin^{-1}\left(\frac{e}{\sqrt{1 + d^2 + e^2}}\right) \quad ; \beta \epsilon [-\pi/2, \pi/2]$$

(The matrix $\bar{E}$ represents the composition of the coordinate transformations for eliminating d and then the resultant e.) We then replace the original (ξ, η, ζ) local coordinate system with the (ξ'', η'', ζ'') system and repeat the construction from equation (A.8) on. If the procedure fails to converge the flat panel approximation of section (A.2) must be used. (This contingency has never been necessary.) For a sufficiently fine grid, the procedure will converge rapidly so that shortly a coordinate system will be obtained in which d and e type terms in equation (A.13) will be essentially zero and no quadratic terms in ζ will be present. The local coordinate system for which this occurs is then defined by the transformation of equation (A.12) where now

$$\bar{A}' = \left(\bar{D}_n\bar{E}_{n-1}\bar{D}_{n-1}\cdots\bar{E}_1\bar{D}_1\right)\bar{A} \tag{A.17}$$

and $\bar{D}_i$, $\bar{E}_i$ are the $\bar{D}$ and $\bar{E}$ matrices for the ith iteration.

The coefficient ζ_o of equation (A.13) may be eliminated by a translation for the (ξ', η', ζ') coordinate system to the point

$$\vec{R}_o = \vec{P}_c + \zeta_o\hat{\zeta}' \tag{A.18}$$

We then obtain a final local (ξ, η, ζ) coordinate system defined by the transformation from global to local coordinates,

$$Q = \bar{A}\left(\bar{P} - \bar{R}_o\right) \tag{A.19}$$

where $\bar{A}$ is now the matrix $\bar{A}'$, defined in (A.17) and $\vec{R}_o$ is defined by (A.18). In this coordinate system, S has the representation

$$\zeta(\xi, \eta) = a\xi^2 + b\eta^2 \tag{A.20}$$

The domain of (ξ, η) here is again the quadralateral Σ defined by projecting the corner points $\vec{P}_1$, $\vec{P}_2$, $\vec{P}_3$ and $\vec{P}_4$ onto the (ξ, η) plane (see fig. D.1). Equation (A.20) represents a considerable simplification over equation (A.8) and leads to substantial economics in the calculation of influence coefficients (app. D).

This completes the construction of the second order approximation to S. In section (A.1), we made the assumption that the grid was sufficiently dense that the true surface lying between four adjacent corner points did not deviate significantly from their average plane. This assumption implies that the coefficients a and b are limited in magnitude. We formalize this limitation as follows. Let

$$\delta = \frac{1}{2}\,\underset{(\xi,\eta)\in\Sigma}{\text{Max}}\left\{\sqrt{a^2\xi^2 + b^2\eta^2}\right\} \tag{A.21}$$

Then we require

$$\delta << 1 \tag{A.22}$$

Define this diameter d of S by

$$d = 2 \max_{(\xi, \eta) \in \Sigma} \left\{ \sqrt{\xi^2 + \eta^2} \right\}$$

and the height ω of S by

$$\omega = \max_{(\xi, \eta) \in \Sigma} \left\{ |\zeta(\xi, \eta)| \right\}$$

It can be shown that δ is an upper bound for ω/d; hence, equation (A.22) implies that the ratio of the height of S to its diameter is small. Equation (A.20) can always be ensured by a sufficiently fine grid. As a practical matter, we have adopted

$$\delta < .066 \tag{A.23}$$

as a "rule of thumb" governing panel density. For a two dimensional cylinder, equation (A.23) would imply a maximum of 30° subtended angle per panel or a minimum of 12 total panels.

Although it is not sufficient, equation (A.22) helps to guarantee that S is a close approximation to the true surface. It also allows the expansion and subsequent integration in closed form of the induced velocity kernels. Moreover, it is doubtful that our assumed linear or quadratic distributions of singularity strength on S would be adequate for more highly curved panels.

APPENDIX B
SINGULARITY STRENGTH DEFINITION

B.1 INTRODUCTION

In section 4.2 it was noted that equation (13) represents an explicit solution to any of the boundary value problems described in section 4.1, once the source strength distribution $\sigma(Q)$ and doublet strength distribution $\mu(Q)$ are determined such that the specified boundary conditions are satisfied.

In this appendix we shall describe how an approximation to the true network singularity distribution is defined for the purpose of achieving a numerical solution to the flow problem. The true singularity distribution will be approximated by a truncated Taylor's series on each panel. Such a representation is valid on any interior part of the network providing the paneling there is sufficiently fine. It is less valid at a network edge where the true singularity distribution may become unbounded, in which case some error on panels adjacent to the edge will be unavoidable regardless of panel density. The approximation here as well as in the network interior can be improved by using a higher order distribution than currently employed by first order methods (which use constant source and doublet distributions). The next logical step as far as sources are concerned is to use a linearly varying source distribution on each panel. The order of doublet distribution consistent with such a source distribution is quadratic. This can be seen from equation (C.10) which shows that it is the gradient of doublet strength which performs a function similar to that of a source, i.e., it creates a jump in a certain tangential component of velocity across a singularity surface. Hence, the gradient of doublet strength should also be linear, following that the doublet strength itself must be quadratic.

In this report, we will consider only a linear singularity distribution on source panels and a quadratic distribution on doublet panels. There may be an advantage in using even higher order distributions, but as pointed out in reference 13, it would then be necessary to consider a higher order panel geometry definition for the sake of consistency. Specifically, we assume that the singularity strength λ at a point (ξ, η, ζ) on a panel S is given by

Source: $$\lambda(\xi, \eta, \zeta) = \sigma(\xi, \eta) = \sigma_o + \sigma_\xi \xi + \sigma_\eta \eta \qquad \text{(B.1)}$$

Doublet: $$\lambda(\xi, \eta, \zeta) = \mu(\xi, \eta)$$

$$= \mu_o + \mu_\xi \xi + \mu_\eta \eta + \frac{1}{2} \mu_{\xi\xi} \xi^2 + \mu_{\xi\eta} \xi\eta + \frac{1}{2} \mu_{\eta\eta} \eta^2 \qquad \text{(B.2)}$$

Here (ξ, η, ζ) are local panel coordinates as defined by equation (A.19).

The unknown source and doublet coefficients (which may also be referred to as degrees of freedom) on the right sides of equations (B.1) and (B.2) respectively, are not assumed independent; rather they are linear combinations of an independent set of singularity parameters $\lambda_1, \lambda_2, \lambda_3, \ldots \lambda_{MAX}$ whose values are to be determined from application of the boundary conditions. The complete set of these singularity parameters will be denoted as Λ. In otherwords, for each panel S we have

$$\bar{C} = \bar{B}\bar{\lambda} \tag{B.3}$$

where $\bar{C}$ is the column vector of either the source or doublet coefficients and $\bar{\lambda}$ is a column vector whose elements λ_k form a subset of Λ. In the next section we describe; 1) how the set Λ is chosen for each type of network, 2) how the vector $\bar{\lambda}$ is chosen for a panel, and 3) how the rectangular matrix $\bar{B}$ is determined. (For a source panel $\bar{B}$ has dimensions $3 \times N_S$; for a doublet panel $\bar{B}$ has dimensions $6 \times N_D$. N_S and N_D are the size of $\bar{\lambda}$ for source and doublet panels respectively and depend on the network type and on the location of the panel within the network.)

B.2 CALCULATION OF DISTRIBUTION COEFFICIENTS

The singularity parameters Λ are chosen to be the source or doublet singularity strengths $\lambda(\xi, \eta, \zeta)$ at a set of discrete points Ω on the network surface. The choice of Ω for the various types of networks employed is shown schematically in figure B.1.

The circles represent points in Ω. The intersections of the lines correspond to grid points of the network, i.e., panel corner points (see fig. A.1). A circle at one of these intersections therefore represents a grid point. A circle midway between two adjacent intersections represents the average of the corresponding two grid points. Finally, a circle centrally located among four adjacent intersections represents the average of the four corresponding grid points. Here the average $\vec{P}^*$ of N points $\vec{P}_1, \vec{P}_2, \ldots \vec{P}_N$ is defined by

$$\vec{P}^* = (\vec{P}_1 + \vec{P}_2 + \ldots + \vec{P}_N)/N \tag{B.4}$$

and this definition holds even if some of the $\vec{P}_i$ are identical. Technically, some of the points of Ω may not lie on any panel of the network since in general the panels defined in appendix A may not contain the grid corner points and/or midpoints; however, this is of no consequence since only the projections of the points in Ω onto planes tangent to the panel surfaces are employed in future computations. The reasons for the choice of singularity parameter locations for various networks will be discussed in connection with control point locations in appendix C.4. We also note here that even numbered networks are doublet networks and odd numbered networks are source networks. There are no type 7 and 9 networks.

The singularity parameters in Λ are ordered using the row index M = 1, 2, . . . I as an inner index and column index N = 1, 2, . . . J as an outer index in a manner similar to a doubly indexed dimensioned variable in FORTRAN. The singularity parameters in Λ corresponding to two or more points of Ω which physically coincide due to triangular panels, are identified in the ordering. This device can be used even when points do not coincide to create networks with fewer degrees of freedom than those in figure B.1. For example, the two wake networks are obtained in this manner from the type 6 (doublet/analysis) network. The first is designated type 8 (doublet/wake #1) and is obtained by identifying all parameters in each column with the parameter at the head of the column. The second is designated type 10 (doublet/wake No. 2) and is obtained by identifying all parameters with the first parameter.

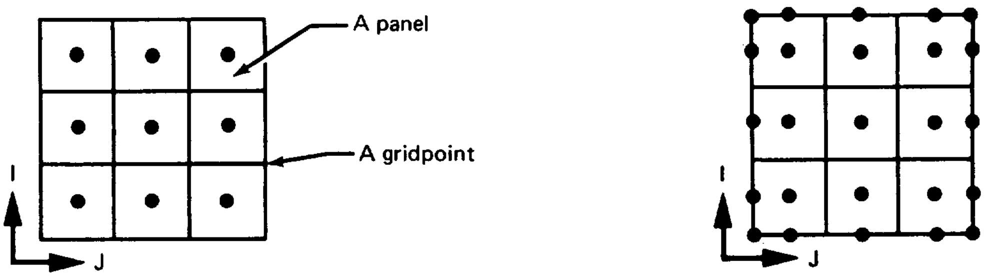

Type 1 (Source/analysis)

Type 2 (Doublet/analysis)

Type 3 (Source/design No. 1)

Type 4 (Doublet/design No. 1)

Type 5 (Source/design No. 2)

Type 6 (Doublet/design No. 2)

Type 8 (Doublet/wake No. 1)

Type 10 (Doublet/wake No. 2)

Figure B.1. — Schematic of Singularity Parameter Location

We now define the vector $\bar{\lambda}$ of equation (B.3) for an arbitrary panel S. The components of $\bar{\lambda}$ are the parameters $\lambda_k \epsilon \Lambda$ corresponding to points $P_k \epsilon \Omega$ which belong to S or else are adjacent to points belonging to S. For this purpose a point $P \epsilon \Omega$ is considered to belong to a panel if it is the average point of one or more of the panel's corner points. (Hence some points in Ω belong to more than one panel.) Also, a point $Q \epsilon \Omega$ is considered adjacent to a point P belonging to S if each of its I and J indices differ by one at the most.

The matrix $\bar{B}$ is obtained as the result of fitting the distribution of equation (B.1) or equation (B.2) to the singularity parameters of $\bar{\lambda}$ by the method of least squares. To be specific we minimize the quantity

$$R = \frac{1}{2} \sum_k W_k \left[\lambda(\xi_k, \eta_k, \zeta_k) - \lambda_k\right]^2 \tag{B.5}$$

with respect to the degrees of freedom in equation (B.1) or (B.2). In equation (B.5) the sum is over the N components of λ_k which belong to S, and (ξ_k, η_k, ζ_k) are the coordinates of the corresponding points $P_k \epsilon \Omega$ expressed in the local coordinate system of the panel S. The weights W_k are chosen to be unity unless $\vec{P}_k$ happens to belong to S in which case W_k is chosen large (nominally 10^8). If we let $\bar{C}$ be the vector having the coefficients (degrees of freedom) of $\lambda(\xi, \eta, \zeta)$ as its components and $\bar{V}_k$ the vector with components $(1, \xi_k, \eta_k)$ in the case of a source distribution or

$$\left(1, \xi_k, \eta_k, \frac{1}{2}\xi_k^2, \xi_k\eta_k, \frac{1}{2}\eta_k^2\right)$$

in the case of a doublet distribution, then the quantity R is minimized with respect to the coefficients when

$$\bar{C} = \left[\sum_k W_k \bar{V}_k \bar{V}_k^T\right]^{-1} \sum_k W_k \lambda_k \bar{V}_k \tag{B.6}$$

Comparison with equation (B.3) reveals that

$$\bar{B} = \bar{B}_1^{-1} \bar{B}_2 \tag{B.7}$$

where

$$\bar{B}_1 = \sum_k W_k \bar{V}_k \bar{V}_k^T \tag{B.8}$$

and $\bar{B}_2$ is the N column matrix whose kth column is $W_k \bar{V}_k$.

Thus, for each panel S, the coefficients in equation (B.1) and (B.2) are expressed in terms of the λ_k belonging to the panel.

B.3 CONTINUOUS DOUBLET/ANALYSIS DISTRIBUTION

The network singularity distributions defined in the previous section are basically splines although they lack the continuity characteristics usually associated with splines. Ideally, source strength and doublet strength and gradient should be continuous across panel edges. This is because discontinuities in source strength and doublet gradient across a panel edge induce logarithmically unbounded velocities there, and a discontinuity in doublet strength induces a jump in potential at the edge as well as a velocity which becomes unbounded as the inverse of the distance to the edge (see app. D.5). The problem with such flow anomalies is that flow boundary conditions imposed at control points close to these anomalies will concentrate on eliminating the anomalies in order to produce finite flow. The only way the flow anomalies can be eliminated is by greater continuity of the source and doublet splines; hence, the boundary conditions will interact with the splines rather than control the finite flow in an appropriate manner. The weak flow anomalies produced by source and doublet gradient discontinuities are of little consequence to boundary conditions applied at panel centers; however, the strong flow anomalies produced by discontinuities in doublet strength can be of concern where panel center control points lie close to panel edges, as might be the case when the upper surface of a thin wing has different panel spacing than the lower surface.

The least square procedure employed in the previous section does produce virtual continuity of doublet strength in regions where paneling is sufficient. In regions such as thin wing leading edges where the singularity strength gradients are large and the paneling is usually too coarse for the quadratic approximations to hold discontinuities do arise. It must be remembered that discontinuities in doublet strength correspond to jumps in potential which are not reflected in the gradient of the potential. Hence, calculation of velocities from the gradient of the doublet strength, as in example 4 of section 5.4.2, as well as the calculation of ΔC_p for infinitely thin wings in many examples of section 5, can be erroneous without taking into account the fact that the variation of potential may be "lumped" at panel edges. This can be done after solution, i.e., after the singularity parameters are known. It is then possible to average doublet values along common panel edges creating a unique definition of doublet strength along grid lines. The distribution of doublet strength on any panel may then be modified by fitting the distribution coefficients to the values on the panel perimeter in a weighted least square sense. This refinement has been implemented in the pilot code and is responsible for more accurate values of C_p in cases involving the least square doublet/analysis spline of the previous section where panel density is sparse, however, in view of the preceding paragraph it would be far more desirable to construct a doublet spline with inherent continuity across panel edges.

It is virtually impossible to construct a quadratically accurate doublet spline with exact continuity across all panel edges of a network when the distribution on a panel has only six degrees of freedom (equation (B.2)). The best we can do is achieve continuity at certain points along panel edges, e.g., at corner points. The type 4 (doublet/design no. 1) network is continuous at panel corner points and does a good job on the inverse problem, i.e., obtaining potential from gradient data.

In this section we will develop an alternate spline for the type 2 (doublet/analysis) network with sufficient continuity to yield more accurate velocity data at panel centers in cases where panel density is sparse.

There are many ways to construct a doublet/analysis spline which is continuous at corner points. However, we wish to preserve certain desirable characteristics of the type 2 least square spline of the previous section. In particular we want the quadratic distribution on a panel to depend linearly on local singularity parameters only, on the nine parameters in an immediate neighborhood. Continuity at corner points then requires that a corner point value of the spline depend on the four adjacent singularity parameters only. This eliminates the choice of point values of the spline for singularity parameters as in the previous section, since four point values cannot in general be interpolated to obtain a fifth by a second order accurate formula. On the other hand, the following choice of singularity parameters does allow the second order accurate determination of corner point values by four adjacent parameters in the case where grid lines are straight. On any panel S we define the associated panel center singularity parameter in terms of the local doublet distribution by the formula

$$\lambda = \frac{1}{4} \sum_{i=1}^{4} \left[\mu\left(\xi_i, \eta_i\right) + \frac{1}{2} \vec{\nabla}\mu\left(\xi_i, \eta_i\right) \cdot \left(\vec{P}_{i+2} - \vec{P}_i\right) \right] \tag{B.9}$$

Here

$$\vec{P}_i = \vec{P}_i(\xi_i, \eta_i, \zeta_i)$$

is the ith panel corner point as shown in figure (B.2) with $\vec{P}_5 = \vec{P}_1$ and $\vec{P}_6 = \vec{P}_2$. The distribution $\mu(\xi, \eta)$ is defined by equation (B.2) and $\vec{\nabla}\mu(\xi, \eta)$ is the surface gradient of μ defined by the formula

$$\vec{\nabla}\mu(\xi, \eta) = \left[\mu_\xi(\xi, \eta) ,\ \mu_\eta(\xi, \eta) ,\ 0 \right] \tag{B.10}$$

where

$$\mu_\xi(\xi, \eta) = \mu_\xi + \mu_{\xi\xi}\xi + \mu_{\xi\eta}\eta$$

and

$$\mu_\eta(\xi, \eta) = \mu_\eta + \mu_{\xi\eta}\xi + \mu_{\eta\eta}\eta$$

Any network edge singularity parameter can be defined by equation (B.9) as well by allowing S to collapse to the panel edge or corner associated with the parameter (see fig. B.1). For example, if $\vec{P}_1$ is a network corner point, then the appropriate expression for the singularity parameter λ at $\vec{P}_1$ is obtained by sending $\vec{P}_2$, $\vec{P}_3$ and $\vec{P}_4$ to $\vec{P}_1$; hence, from equation (B.9)

$$\lambda \text{ at } \vec{P}_1 = \mu(\xi_1, \eta_1) \tag{B.11}$$

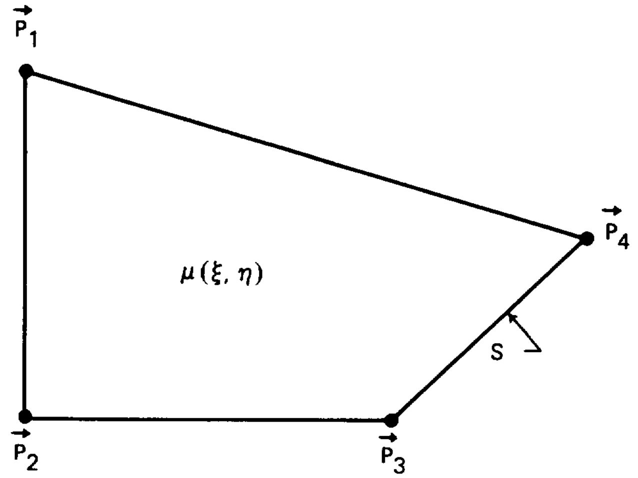

Figure B.2. – Panel Schematic for Singularity Parameter Definition

If $\vec{P}_1$ and $\vec{P}_2$ are network edge grid points, then the appropriate expression for the singularity parameter λ at the midpoint of $\vec{P}_1$ and $\vec{P}_2$ is obtained by sending $\vec{P}_3$ to $\vec{P}_2$ and $\vec{P}_4$ to $\vec{P}_1$; hence, from equation (B.9)

$$\lambda \text{ at } \frac{1}{2}\left(\vec{P}_1 + \vec{P}_2\right) = \frac{1}{2}\left[\mu\left(\xi_1, \eta_1\right) + \frac{1}{2}\vec{\nabla}\mu\left(\xi_1, \eta_1\right) \cdot \left(\vec{P}_2 - \vec{P}_1\right)\right] + \frac{1}{2}\left[\mu\left(\xi_2, \eta_2\right) + \frac{1}{2}\vec{\nabla}\mu\left(\xi_2, \eta_2\right) \cdot \left(\vec{P}_1 - \vec{P}_2\right)\right] \tag{B.12}$$

Since $\mu(\xi, \eta)$ is quadratic along the line joining $\vec{P}_1$ and $\vec{P}_2$ the expressions in square brackets on the right side of equation (B.12) can be shown to be equal so that

$$\begin{aligned} \lambda \text{ at } \frac{1}{2}\left(\vec{P}_1 + \vec{P}_2\right) &= \mu\left(\xi_1, \eta_1\right) + \frac{1}{2}\vec{\nabla}\mu\left(\xi_1, \eta_1\right) \cdot \left(\vec{P}_2 - \vec{P}_1\right) \\ &= \mu\left(\xi_2, \eta_2\right) + \frac{1}{2}\vec{\nabla}\mu\left(\xi_2, \eta_2\right) \cdot \left(\vec{P}_1 - \vec{P}_2\right) \end{aligned} \tag{B.13}$$

The last expression is closely associated with the definition of the singularity parameters used to solve the one-dimensional quadratic interpolation problem. Assume we wish to interpolate values $\mu_0, \mu_1, \ldots\ldots \mu_{n+1}$ defined at the points ξ_k, $k = 0, 1, \ldots n+1$ where

$$\xi_0 = x_0, \xi_1 = \frac{1}{2}\left(x_0 + x_1\right), \xi_2 = \frac{1}{2}\left(x_1 + x_2\right), \ldots, \xi_{n+1} = x_n$$

as shown in figure B.3. It is possible to define a function $\mu(x)$ such that 1) $\mu(x)$ is quadratic on each interval $\left[x_{i-1}, x_i\right]$, $i = 1, 2, \ldots n$; 2) $\mu(x)$ is continuous and $\mu'(x) = \frac{d\mu(x)}{dx}$ is continuous on the full domain $\left[x_o, x_n\right]$; and 3) $\mu(x)$ interpolates the values μ_k, $k = 0, 1, \ldots, n+1$. Moreover, the $\mu(x)$ with such properties is unique.

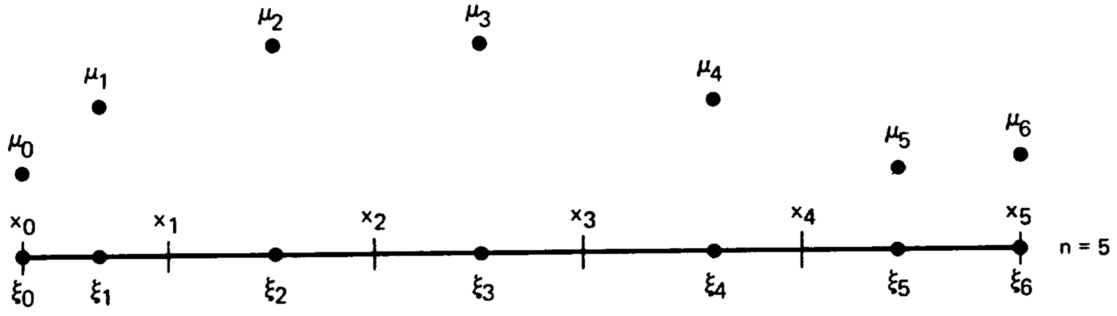

Figure B.3. – One Dimensional Quadratic Interpolation

To find $\mu(x)$ we first define the singularity parameters λ_k as

$$\begin{aligned} \lambda_k &= \mu_k - \frac{1}{8}\left(x_k - x_{k-1}\right)^2 \mu''_k \;, k = 1, 2, \ldots n \\ \lambda_o &= \mu_o \\ \lambda_{n+1} &= \mu_{n+1} \end{aligned} \tag{B.14}$$

where μ''_k is $\dfrac{d^2\mu(x)}{dx^2}$ evaluated at ξ_k. Since $\mu(x)$ is quadratic on $\left[x_{k-1}, x_k\right]$ it is possible to show that

$$\begin{aligned} \lambda_k &= \mu\left(x_{k-1}\right) + \frac{1}{2}\mu'\left(x_{k-1}\right)\left(x_k - x_{k-1}\right) \\ &= \mu\left(x_k\right) + \frac{1}{2}\mu'\left(x_k\right)\left(x_{k-1} - x_k\right) \end{aligned} \tag{B.15}$$

This formula can be used when k = 0 and k = n + 1 by defining $x_{-1} \equiv x_o$ and $x_{n+1} \equiv x_n$. It is then easy to show that

$$\mu\left(x_k\right) = \frac{\left(x_k - \xi_k\right)\lambda_{k+1} + \left(\xi_{k+1} - x_k\right)\lambda_k}{\xi_{k+1} - \xi_k} \;, \mu'\left(x_k\right) = \frac{\lambda_{k+1} - \lambda_k}{\xi_{k+1} - \xi_k} \;; k = 1, 2, \ldots n \tag{B.16}$$

Equation (B.16) has the following interpretation; plot the λ_k in place of the μ_k and connect the values with straight lines. Then μ and μ' at x_k are the value and slope at x_k of the straight line segment connecting λ_k and λ_{k+1}. From equation (B.16) we can obtain the coefficients of the quadratic doublet distribution in each interval in terms of the λ_k. We have

$$\mu_k(x) = \mu_k + \mu_k' \left(x - \xi_i\right) + \frac{1}{2}\mu_k'' \left(x - \xi_k\right)^2, \quad x \in \left[x_{k-1}, x_k\right] \tag{B.17}$$

where

$$\begin{pmatrix} \mu_k \\ \mu_k' \\ \mu_k'' \end{pmatrix} = \begin{pmatrix} \frac{1}{4}\frac{d_2}{d_1} & 1 - \frac{d_2}{4}\left(\frac{1}{d_3} + \frac{1}{d_1}\right) & \frac{1}{4}\frac{d_2}{d_3} \\ -\frac{1}{2d_1} & \frac{1}{2}\left(\frac{1}{d_1} - \frac{1}{d_3}\right) & \frac{1}{2d_3} \\ \frac{1}{d_2 d_1} & -\frac{1}{d_2}\left(\frac{1}{d_3} + \frac{1}{d_1}\right) & \frac{1}{d_2 d_3} \end{pmatrix} \begin{pmatrix} \lambda_{k-1} \\ \lambda_k \\ \lambda_{k+1} \end{pmatrix} \tag{B.18}$$

and

$$d_1 = \left(\xi_k - \xi_{k-1}\right), \quad d_2 = \left(x_k - x_{k-1}\right), \quad d_3 = \left(\xi_{k+1} - \xi_k\right).$$

Note that the coefficients depend only on the singularity parameters belonging to the interval and its immediately adjacent intervals. The λ_k can be obtained in terms of the μ_k by solving an equation set consisting of $\lambda_o = \mu_o$, $\lambda_{n+1} = \mu_{n+1}$ and the first equation of (B.18) for every interval, using a tridiagonal equation solution algorithm.

The definition of equation (B.9) is an attempt to generalize equation (B.15) for the case of a surface spline. As in the one dimensional case, the next task is to determine the corner point values of doublet strength and gradient. Given any corner point $\vec{P}(I, J)$ of the network, we define a local (ξ, η, ζ) coordinate system with origin at the corner point and with the (ξ, η) plane approximately tangent to the true network surface. The $\hat{\xi}, \hat{\eta}, \hat{\zeta}$ unit vectors are defined as follows:

$$\hat{\xi} = \frac{\left(\vec{P}_{33} - \vec{P}_{31}\right) + 2\left(\vec{P}_{23} - \vec{P}_{21}\right) + \left(\vec{P}_{13} - \vec{P}_{11}\right)}{\left|\left(\vec{P}_{33} - \vec{P}_{31}\right) + 2\left(\vec{P}_{23} - \vec{P}_{21}\right) + \left(\vec{P}_{13} - \vec{P}_{11}\right)\right|}$$

$$\hat{\zeta} = \hat{\xi} \otimes \frac{\left(\vec{P}_{31} - \vec{P}_{11}\right) + 2\left(\vec{P}_{32} - \vec{P}_{12}\right) + \left(\vec{P}_{33} - \vec{P}_{13}\right)}{\left|\left(\vec{P}_{31} - \vec{P}_{11}\right) + 2\left(\vec{P}_{32} - \vec{P}_{12}\right) + \left(\vec{P}_{33} - \vec{P}_{13}\right)\right|} \tag{B.19}$$

$$\hat{\eta} = \hat{\zeta} \otimes \hat{\xi}$$

Here $\vec{P}_{22}$ is the point $\vec{P}(I, J)$ and the other $\vec{P}_{ij}$ are the eight adjacent corner points defined by

$$
\begin{aligned}
\vec{P}_{11} &= \vec{P}(I-1, J-1) \\
\vec{P}_{21} &= \vec{P}(I, J-1) \\
\vec{P}_{31} &= \vec{P}(I+1, J-1) \\
\vec{P}_{12} &= \vec{P}(I-1, J) \\
\vec{P}_{32} &= \vec{P}(I+1, J) \\
\vec{P}_{13} &= \vec{P}(I-1, J+1) \\
\vec{P}_{23} &= \vec{P}(I, J+1) \\
\vec{P}_{33} &= \vec{P}(I+1, J+1)
\end{aligned}
\tag{B.20}
$$

(If any index exceeds a grid point row or column limit it is assumed to be replaced by that limit.) These corner points are shown schematically in figure (B.4) along with the four relevant singularity parameters.

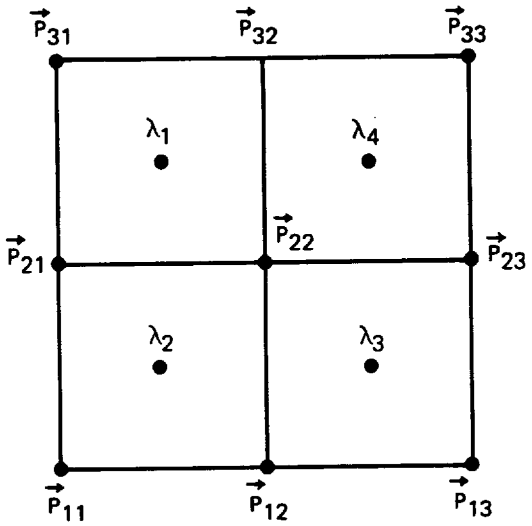

Figure B.4. — Corner Point Schematic for Spline Corner Point Value Determination at the Corner Point P_{22} Common to Four Panels

Let μ_c and $\vec{\nabla}\mu_c$ be the doublet strength and gradient at the origin $\vec{P}_{22}$. These quantities are then to be determined in terms of the four λ_i, by minimizing the function

$$\begin{aligned} R = \frac{1}{2} \sum_{i=1}^{4} W^2 \Big\{ & \mu_c + \frac{1}{4} \vec{\nabla}\mu_c \cdot \left(\vec{S}_i + \vec{S}_{i+1} + \vec{d}_i \right) \\ & + \frac{1}{4} \left[a_1 \xi_i \xi_{i+1} + a_2 \left(\xi_i \eta_{i+1} + \eta_i \xi_{i+1} \right) + a_3 \eta_i \eta_{i+1} \right] - \lambda_i \Big\}^2 \\ & + \frac{1}{2} W_\xi{}^2 a_1{}^2 + W_\xi W_\eta a_2{}^2 + \frac{1}{2} W_\eta{}^2 a_3{}^2 \end{aligned} \qquad (B.21)$$

with respect to

$$\mu_c,\ \vec{\nabla}\mu_c,\ a_1,\ a_2 \text{ and } a_3$$

Here

$$\vec{S}_1 = \vec{P}_{32} - \vec{P}_{22},\quad \vec{S}_2 = \vec{P}_{21} - \vec{P}_{22},\quad \vec{S}_3 = \vec{P}_{12} - \vec{P}_{22},\quad \vec{S}_4 = \vec{P}_{23} - \vec{P}_{22},\quad \vec{S}_5 = \vec{S}_1 \qquad (B.22)$$

and

$$\vec{d}_1 = \vec{P}_{31} - \vec{P}_{22},\quad \vec{d}_2 = \vec{P}_{11} - \vec{P}_{22},\quad \vec{d}_3 = \vec{P}_{13} - \vec{P}_{22},\quad \vec{d}_4 = \vec{P}_{33} - \vec{P}_{22},\quad \vec{d}_5 = \vec{d}_1$$

and

$$\left(\xi_i, \eta_i, \zeta_i \right) = \vec{S}_i$$

The weight W is nominally chosen as 10^4. The weight W_ξ is chosen as the square of the ξ component of the $\vec{S}_i$ and $\vec{d}_i$ with largest magnitude, the weight W_η is chosen similarly. The choice of R in equation (B.21) is motivated by an attempt to obtain $\mu_c, \vec{\nabla}\mu_c$ by fitting a quadratic distribution to $\lambda_1, \lambda_2, \lambda_3, \lambda_4$ with a_1, a_2, a_3 being the second order coefficients. Such a fit has two degrees of freedom, however, if $\vec{S}_1$ is parallel to $\vec{S}_3$ and $\vec{S}_2$ is parallel to $\vec{S}_4$, these degrees of freedom affect the second order coefficients only and the values of μ_c and $\vec{\nabla}\mu_c$ are determined uniquely by the λ_i.

The function R is minimized by values of $\mu_c, \vec{\nabla}\mu_c, a_1, a_2, a_3$ which can be obtained from a formula similar to equation (B.6), i.e.,

$$\left\{\begin{array}{l}\mu_c\\ \mu_{\xi c}\\ \mu_{\eta_c}\\ a_1\\ a_2\\ a_3\end{array}\right\} = \begin{bmatrix}\text{Known Matrix}\\ \text{Determined Solely From}\\ \text{Geometry of } \vec{P}_{ij}\end{bmatrix} \left\{\begin{array}{l}\lambda_1\\ \lambda_2\\ \lambda_3\\ \lambda_4\end{array}\right\} \tag{B.23}$$

As in the one-dimensional case, once the dependence of all corner point values and gradients on the network singularity parameters has been found the panel distributions $\mu(\xi, \eta)$ may be calculated. Return to figure (B.2) and equation (B.2). The six coefficients of $\mu(\xi, \eta)$ in equation (B.2) are determined as follows. We require that the distribution actually attain the corner point values just computed, i.e.,

$$\mu\left(\xi_i, \eta_i\right) = \mu_i \quad ; \quad i = 1, \ldots 4 \tag{B.24}$$

where μ_i is the value of μ_c at $\vec{P}_i$ we also require that equation (B.9) hold for the panel center singularity parameter and any network edge singularity parameter associated with the panel. All remaining degrees of freedom (if any) are then eliminated by requiring that

$$\vec{\nabla}\mu\left(\xi_i, \eta_i\right) = \vec{\nabla}\mu_i \quad ; \quad i = 1, \ldots 4 \tag{B.25}$$

hold in a least square sense, where $\vec{\nabla}\mu_i$ is the value of $\vec{\nabla}\mu_c$ at $\vec{P}_i$. Specifically, for a panel in the network interior, the six coefficients of $\mu(\xi, \eta)$ are obtained by minimizing the function

$$\begin{aligned} R = \frac{1}{2}\sum_{i=1}^{4}\Bigg\{ & W^2\left[\mu\left(\xi_i, \eta_i\right) - \mu_i\right]^2 + W_\xi^{\,2}\left[\mu_\xi\left(\xi_i, \eta_i\right) - \mu_{\xi_i}\right]^2 \\ & + W_\eta^{\,2}\left[\mu_\eta\left(\xi_i, \eta_i\right) - \mu_{\eta_i}\right]^2 \\ & + W^2\left[\lambda - \frac{1}{4}\sum_{i=1}^{4}\mu\left(\xi_i, \eta_i\right) - \frac{1}{2}\vec{\nabla}\mu\left(\xi_i, \eta_i\right) \cdot \left(\vec{P}_{i+2} - \vec{P}_i\right)\right]^2 \end{aligned} \tag{B.26}$$

with respect to

$$\mu_o,\ \mu_\xi,\ \mu_\eta,\ \mu_{\xi\xi},\ \mu_{\xi\eta},\ \mu_{\eta\eta}$$

where μ_{ξ_i} and μ_{η_i} are the ξ and η components of $\vec{\nabla}\mu_i$, and λ is the panel center singularity parameter. The weight W is nominally chosen as 10^4. The weights W_ξ and W_η are chosen as the maximum values of $|\xi_i|$ and $|\eta_i|$ respectively. Only the panel center singularity parameter defining equation is displayed on the right side, but for network edge panels the associated network edge singularity parameter defining equations should also be included. Note that for network corner panels the doublet distribution can only achieve specified corner point values and singularity parameters in a least square sense. The procedure for minimizing R is similar to that used to derive equation (B.6) and the result is a B matrix to replace that of equation (B.3). The vector $\overline{C}$ is again the coefficients of equation (B.2) and the vector $\overline{\lambda}$ consists of the singularity parameters which belong to S or immediately adjacent panels. The 6 x N_D matrix B again depends only on the geometry of the corner points of S and those of its immediately adjacent panels.

APPENDIX C
CONTROL POINT DEFINITION AND BOUNDARY CONDITION SPECIFICATION

In this appendix we describe the selection of a set Γ of control points on a network. (By definition control points are points at which boundary conditions are applied, i.e., points at which the integral equations or auxiliary conditions of the problem hold exactly.) In addition, we describe the form in which the boundary conditions may be specified.

C.1 CONTROL POINT LOCATION

The set Γ for each network is shown schematically in figure C.1. (There are no type 7 and 9 networks.)

The circles represent points in Γ. As in figure B.1 the intersections of the lines correspond to grid points of the network and the squares correspond to panels. Circles located on edges or at intersections correspond to the same network locations as in figure B.1—at least for the present. However, a circle in the middle of a square (which we call a panel center control point) denotes the origin of the local coordinate system (see app. A) of the corresponding panel rather than the average of the four adjacent corner points. The points in Γ may be ordered using the row index as an inner index and the column index as an outer index. For this purpose points which coincide with previous points are deleted. Hence, Γ and Λ have the same size for network types where Λ and Ω are schematically similar, i.e., types 1, 2, 8, and 10. This may not be the case with the design networks when triangular panels are present. We do not specifically exclude triangular panels from design networks, but we do require that the presence of triangular panels result in sets Γ and Λ of identical size. For example, the collapse of an entire edge of a type 4 network would be permissible.

Once Γ has been ordered, it is necessary to withdraw the control points on the network edges slightly to avoid numerical difficulties associated with infinite self-induced velocities (see app. D.5). The displacement is accomplished in the following manner. First, assume the control point $\vec{P}$ is one of the four corner grid points of the network. Without loss of generality, we can assume $\vec{P} = \vec{P}(1, 1)$ (see fig. A.1). Let $\hat{N}$ be the unit normal at $\vec{P}$ of the panel containing $\vec{P}$. The control point $\vec{P}$ is then redefined by the formula

$$\vec{P} = \vec{P}(1, 1) + \alpha\left(\hat{D}_1 + \hat{D}_2\right) \tag{C.1}$$

where

$$\vec{D}_1 = \hat{N} \otimes \left[\vec{P}(1, 2) - \vec{P}(1, 1)\right]$$

$$\vec{D}_2 = \hat{N} \otimes \left[\vec{P}(1, 1) - \vec{P}(2, 1)\right]$$

$$\hat{D}_1 = \vec{D}_1 \Big/ \left|\vec{D}_1\right|$$

$$\hat{D}_2 = \vec{D}_2 \Big/ \left|\vec{D}_2\right|$$

$$\alpha = \epsilon\left(\left|\vec{D}_1\right| + \left|\vec{D}_2\right|\right)$$

Type 1 (Source/analysis)

Type 2 (Doublet/analysis)

Type 3 (Source/design No. 1)

Type 4 (Doublet/design No. 1)

Type 5 (Source/design No. 2)

Type 6 (Doublet/design No. 2)

Type 8 (Doublet/wake No. 1)

Type 10 (Doublet/wake No. 2)

Figure C.1. — Schematic of Control Point Locations

Here ϵ is a small number (nominally $1/4 \times 10^{-5}$). If either $\vec{P}(1, 2)$ or $\vec{P}(2, 1)$ coincides with $\vec{P}(1, 1)$ we replace it by $\vec{P}(2, 2)$.

Next assume the control point $\vec{P}$ is located at the edge of the network midway between two grid points. Without loss of generality we can assume $\vec{P} = \frac{1}{2} (\vec{P}(1, 1) + \vec{P}(1, 2))$. Again, let $\hat{N}$ be the unit normal of the panel containing $\vec{P}$. The control point $\vec{P}$ is then redefined by the formula

$$\vec{P} = \frac{1}{2} \left[\vec{P}(1, 1) + \vec{P}(1, 2) \right] + \alpha \hat{D}_1 \tag{C.2}$$

where

$$\vec{D}_1 = \hat{N} \otimes \left[\vec{P}(1,1) - \vec{P}(1, 2) \right]$$

$$\hat{D}_1 = \vec{D}_1 \Big/ \left| \vec{D}_1 \right|$$

$$\alpha = \epsilon \left| \vec{D}_1 \right|$$

Here ϵ is a small number (nominally 10^{-5}). If $\vec{P}(1, 1)$ coincides with $\vec{P}(1, 2)$ the displacement procedure of equation (C.1) is used.

Note that the displaced network edge control points do not necessarily lie on their respective panel surfaces. However, this causes no problems since induced velocities at these points are computed in a special way taking into account only edge induced effects. (See the discussion in equations (C.16) and (C.18).)

C.2 PANEL CENTER BOUNDARY CONDITIONS

In this section we describe the form of the boundary condition equations at panel center control points. We first consider boundary conditions involving velocities where the equations may take the form

$$c_U \left(\hat{n} \cdot \vec{V}_U \right) + c_L \left(\hat{n} \cdot \vec{V}_L \right) = \beta_n \qquad \left(\text{specify } c_U, c_L, \beta_n \right) \tag{C.3}$$

$$\left(\vec{t}_U \cdot \vec{V}_U \right) + \left(\vec{t}_L \cdot \vec{V}_L \right) = \beta_t \qquad \left(\text{specify } \vec{t}_U, \vec{t}_L, \beta_t \right) \tag{C.4}$$

Here $\vec{V}_U$ is the total upper surface velocity (perturbation plus free stream) and $\vec{V}_L$ is the total lower surface velocity. By upper surface we mean the side of the panel surface on which lies the positive ζ axis of the local coordinate system. The lower surface is the other side. The unit vector $\hat{n}$ is the upper surface normal and $\vec{t}_U$ and $\vec{t}_L$ are surface tangent vectors. (Arbitrary vectors may be specified but they are projected onto the tangent plane of the panel at the control point before application.) Conditions of type (C.3) are employed on analysis networks while conditions of type (C.4) are used on design networks. These conditions cover problems involving both interior and exterior flows as well as thin sheets.

To explain the application of the equations (C.4) and (C.3) we first consider a panel of the boundary surface B which bounds D on one side only (e.g., the wing section shown in fig. 21). Without loss of generality we can assume this side is the upper side. Lower surface velocities are then irrelevant and we may assume $c_U = 1, c_L = 0$ in equation (C.3) and $|\vec{t}_U| = 1$ and $\vec{t}_L = 0$ in equation (C.4). Analysis boundary conditions then reduce to the specification of β_n, the fluid velocity normal to the panel at the control point. For example, conditions of type (C.3) with $c_U = 1, c_L = 0, \beta_n = 0$ are the usual analysis boundary conditions on impermeable surfaces. On the other hand, both the unit tangent vector $\vec{t}$ and the velocity component β_t in the direction $\vec{t}_U$ must be specified for design conditions. Often $\vec{t}_U$ is selected to be the stream direction at the control point obtained from analyzing the flow about the existing geometry and β_t is the desired velocity magnitude to be produced by a perturbed geometry.

Next, let us consider a portion of the boundary surface which bounds D on both sides (e.g., the model of fig. 19). In order to control the flow on both sides, the surface must conceptually be represented by superimposed source and doublet networks. Without loss of generality we can assume the orientation of both networks is the same regarding upper and lower surface designations. We also assume that the paneling for both networks is identical so that a pair of boundary conditions is applied at each center control point location. This pair may consist of two analysis, one analysis, and one design or two design type boundary conditions. To study these combinations it is convenient to define a set of boundary conditions equivalent to (C.4) and (C.3). For this purpose we define an "average" velocity by

$$\vec{V}_A = \frac{1}{2}\left(\vec{V}_U + \vec{V}_L\right) \tag{C.5}$$

and a "difference" velocity by

$$\vec{V}_D = \vec{V}_U - \vec{V}_L \tag{C.6}$$

Then (C.4) and (C.3) are equivalent to

$$c_A\left(\hat{n} \cdot \vec{V}_A\right) + c_D\left(\hat{n} \cdot \vec{V}_D\right) = \beta_n \qquad \left(\text{specify } c_A, c_D, \beta_n\right) \tag{C.7}$$

$$\left(\vec{t}_A \cdot \vec{V}_A\right) + \left(\vec{t}_D \cdot \vec{V}_D\right) = \beta_t \qquad \left(\text{specify } \vec{t}_A, \vec{t}_D, \beta_t\right) \tag{C.8}$$

respectively, where

$$c_A = c_U + c_L \qquad \vec{t}_A = \vec{t}_U + \vec{t}_L$$

$$c_D = \frac{1}{2}\left(c_U - c_L\right) \qquad \vec{t}_D = \frac{1}{2}\left(\vec{t}_U - \vec{t}_L\right)$$

Equivalence is established by noting the inverse transformation, i.e.,

$$\begin{aligned} \vec{V}_U &= \vec{V}_A + \frac{1}{2}\vec{V}_D \\ \vec{V}_L &= \vec{V}_A - \frac{1}{2}\vec{V}_D \\ c_U &= \frac{1}{2}c_A + c_D \\ c_L &= \frac{1}{2}c_A - c_D \\ \vec{t}_U &= \frac{1}{2}\vec{t}_A + \vec{t}_D \\ \vec{t}_L &= \frac{1}{2}\vec{t}_A - \vec{t}_D \end{aligned} \tag{C.9}$$

Let us first consider the case where both boundary conditions are of analysis type, i.e., of the form (C.7). If the boundary value problem is well posed, the boundary conditions must be independent and consistent, hence, without loss of generality we can assume that one condition controls the normal component of the average velocity (i.e., $c_D = 0$) and the other controls the normal component of the difference velocity (i.e., $c_A = 0$). In theory, it doesn't matter which boundary condition is associated with the source panel control point or doublet panel control point. However, in the present numerical development (i.e., in the existing pilot code logic) a distinction must be made. The present development calculates the influence coefficients for $\vec{V}_A$ directly (see app. D.3) but obtains those for $\vec{V}_D$ by using the formula

$$\vec{V}_D = \sigma\hat{n} + \vec{\nabla}\mu \tag{C.10}$$

which follows from equations (15), (16), and (B.10).

Here σ is source strength and $\vec{\nabla}\mu$ the doublet strength gradient at the control point. Because of the logical structure of the present method (in which network independence is maintained) only the first term on the right side of equation (C.10) is considered for a source panel control point and only the second term is considered for a doublet panel control point. It is then essential that the boundary condition controlling the normal component of the difference velocity (i.e., $c_A = 0$) be associated with the source panel control point since only for a source panel control point is this component computed correctly. (Note $\hat{n} \cdot \vec{\nabla}\mu = 0$, see equation (B.10).)

A similar situation exists in the case of one analysis boundary condition (type (C.7)) and one design boundary condition (type (C.8)). Here the analysis boundary condition must be associated with the source panel control point and the design boundary condition with the doublet panel control point. The case of two design boundary conditions is slightly different since it is no longer possible to assume without loss of generality that one boundary condition controls a tangential component of $\vec{V}_A$ and the other a tangential component of $\vec{V}_D$. Such an assumption is not too restrictive since one can probably achieve any general design result of this type by controlling the tangential components of $\vec{V}_A$ and $\vec{V}_D$ separately. At any rate, it is clear that under such an assumption the source panel boundary condition should be used to control $\vec{V}_A$ and the doublet panel boundary condition should be used to control $\vec{V}_D$.

As a final note, equation (C.10) implies that a surface across which normal velocity is continuous may be represented by a doublet network alone. On the other hand, a surface across which tangential velocity is continuous may be represented by a source network together with a doublet network of constant strength. The latter network is unnecessary if there is no jump in potential across the surface.

Next, we consider specification of potential at panel center control points where the boundary condition equation may take the form

$$k_U\phi_U + k_L\phi_L = \beta_\phi \qquad \left(\text{specify } k_U, k_L, \beta_\phi\right) \tag{C.11}$$

Here ϕ_U and ϕ_L are the upper and lower surface values of perturbation potential respectively. Boundary conditions imposed by equation (C.11) are design (Dirichlet) conditions, but differ from those imposed by equation (C.4) in that scalars rather than components of vectors are specified. For this reason the symmetrically defined singularity parameter and control point locations of network types 1 and 2 are most suitable for applying these conditions. To avoid constructing additional design networks with identical properties we simply use these network types substituting equation (C.11) for (C.4).

The application of equation (C.11) is obvious from our earlier discussion. We note only the analogues to equations (C.5), (C.6), (C.7), (C.9), and (C.10). We have

$$\phi_A = \frac{1}{2}(\phi_U + \phi_L), \quad \phi_D = \phi_U - \phi_L \tag{C.12}$$

$$\phi_U = \phi_A + \frac{1}{2}\phi_D, \quad \phi_L = \phi_A - \frac{1}{2}\phi_D \tag{C.13}$$

and

$$k_A\phi_A + k_D\phi_D = \beta\phi \quad \left(\text{specify } k_A, k_D, \beta_\phi\right) \tag{C.14}$$

where

$$k_A = k_U + k_L$$

$$k_D = \frac{1}{2}\left(k_U - k_L\right)$$

$$k_U = \frac{1}{2} k_A + k_D$$

$$k_L = \frac{1}{2} k_A - k_D$$

Finally, we have from equation (15)

$$\phi_D = \mu \tag{C.15}$$

C.3 NETWORK EDGE BOUNDARY CONDITIONS

Boundary condition equations of type (C.7) with $c_A = 1$, $c_D = 0$ and $\beta_n = 0$ are automatically imposed at all edge control points of the doublet/analysis network. Because of the singular behavior of the velocity induced by a finite doublet distribution at a panel edge, this boundary condition in effect controls the continuity properties of the distribution across the edge. To give an example we note (from equation (D.141)) that near the common edge of two smoothly adjoining doublet networks the downwash (normal velocity) is given by

$$\left(\vec{V}_A \cdot \hat{n}\right) = \frac{1}{4\pi}\left(\frac{2\Delta\mu}{\eta} + 2\Delta\mu'\log(|\eta|) + \text{regular terms}\right) \tag{C.16}$$

where η is the tangential coordinate perpendicular to the edge, $\Delta\mu$ is the jump in doublet strength across the edge and $\Delta\mu'$ is the jump in the derivative of doublet strength in the direction perpendicular to the edge. A control point placed near the edge requiring that downwash be finite will tend to make $\Delta\mu$ vanish (because of the strong antisymmetric singularity $\frac{1}{\eta}$), i.e., μ continuous across the edge. A similar control point on the opposing panel of the adjoining network will, in addition, force $\Delta\mu'$ to vanish (because of the weaker symmetric singularity $\log(|\eta|)$), thereby establishing continuity of μ'.

Because of small, unintended discontinuities in geometry between panels of adjacent networks due to the approximate nature of the surface fit technique, such singularity matching cannot be accomplished dependably if $\vec{V}_A$ is computed in an exact manner. (See section 6.3.5 for the effect of geometry gaps on doublet strength matching.) Consequently, a special algorithm is used. This algorithm considers only velocities induced by panel edges adjacent to the control point. Moreover, the algorithm computes an edge induced velocity as if the edge were the straight line joining the corresponding two grid points rather than the actual panel edge. This means that two doublet network edges are considered physically joined from a potential flow standpoint if and only if the rectilinear curves formed by connecting their edge grid points coincide. Unintended discontinuities in surface slope between adjacent panels of two abutting networks can also occur because of the approximate nature of the surface fit algorithm. However, the effects of such an error remain quite local in character and no special modification is required.

The edge boundary conditions for the remaining doublet networks are the same as for the doublet/analysis network and they control continuity of μ and/or μ' as well. As discussed in section 4.1 these edge conditions are fundamental to the boundary value problem for design networks and fulfill the auxiliary conditions of type equation (12). Network type 4 assumes inflow on the left and lower edges whereas network type 6 assumes inflow on the lower edge and outflow on the upper edge. The wake network types 8 and 10 are special design networks used in place of a regular doublet/design network when a reasonable guess of the direction of velocity is deemed sufficient. (A common use is for the representation of vortex wakes.)

Auxiliary conditions corresponding to equation (11) can be substituted for the continuity boundary conditions at the edge control point heading each panel column in networks type 4 and 6. These conditions take the form

$$\iint_C c_U\left(\hat{n} \cdot \vec{V}_U\right) + c_L\left(\hat{n} \cdot \vec{V}_L\right) dS = 0 \qquad \text{(C.17)}$$

where the integration extends over a panel column and c_U and c_L are specified. The integral is evaluated by summing over each panel in the column the product of the panel area and the integrand evaluated at the panel center control point. The networks are assumed to be paneled with columns aligned along streamlines. In practice this requirement may be relaxed considerably, and only a general streamwise alignment appears necessary. Technically, new network types should be assigned for application of these closure conditions; but to avoid constructing additional design network with identical properties we simply use types 4 and 6 with the above mentioned modification.

The edge boundary conditions for the source/design networks 3 and 5 perform the same functions as those for 4 and 6. For application of equation (12) a different numerical device is used which takes advantage of the fact that a finite strength source panel induces an infinite tangential component of velocity at its edges. To give an example we note from equation (D.121) that near the edge of two smoothly adjoining source networks the tangential component of velocity perpendicular to the edge is given by

$$\left(\vec{V}_A \cdot \hat{t}\right) = \frac{1}{4\pi}\left(-2\Delta\sigma \log\left(|\eta|\right) + \text{regular terms}\right) \qquad \text{(C.18)}$$

where $\hat{t}$ is the unit tangent vector perpendicular to the edge, η is the coordinate in this direction measured from the edge and $\Delta\sigma$ is the jump in source strength across the edge. A control point placed near the edge requiring that $(\vec{V}_A \cdot \hat{t})$ be finite will tend to make $\Delta\sigma$ vanish, i.e., source strength continuous across the edge. This in turn will accomplish equation (12). The same special algorithms for evaluating $\vec{V}_A$ for doublet edge control points are used here. Finally, equation (C.17) is applied in the identical manner for network types 3 and 5 as for network types 4 and 6 when closure is preferred.

In the case where specification of potential is substituted for specification of normal velocity at center control points of network type 2, potential is also specified at all edge control points.

C.4 RATIONALE FOR CONTROL POINT/SINGULARITY PARAMETER LOCATIONS

The set Ω of singularity parameter locations and the set Γ of control point locations for various network types are shown schematically in figures B.1 and C.1 respectively. Let us first consider the type 1 (source/analysis) network. We note the following: 1) The sets Γ and Ω are schematically the same for this network (although the precise point locations are slightly different); 2) The points in Γ (or Ω) are symmetrically located with respect to the network grid point schematic; and 3) The points in Γ and Ω are located at the panel centers.

The locating of the points of Γ at panel centers is quite reasonable in view of the discussion at the beginning of section B.3. Both the panel geometry and singularity splines are analytic at panel centers, and moreover, the panel centers are the points which are farthest from the flow anomalies induced by discontinuities in geometry and singularity strength at panel edges. The locating of the points of Ω at panel centers is acceptable from two points of view. First, Ω and Γ have the same size leading to the same number of equations as unknowns. Secondly, there are a sufficient number of local singularity parameters (i.e., singularity parameters belonging to a given panel and its immediately adjacent neighbors) to determine the three coefficients of the panel source distribution via the method of least squares. The smallest set of local singularity parameters occurs for each of the corner panels in a network and the four local parameters in the set are sufficient to determine three coefficients.

The fact that the points of Γ and Ω are symmetrically located is reasonable considering the allowable boundary condition types for this network. These boundary conditions can involve ϕ or $\frac{\partial \phi}{\partial n}$ only, and hence, involve no preferred direction on the network surface as opposed to design boundary conditions which involve directional derivatives of ϕ.

The fact that the points of Γ and Ω are identical is among other things due to considerations of spline stability. As with any other application of splines, we desire that our source and doublet splines be stable relative to the type of boundary conditions applied. This means that small changes in the boundary conditions should result in similarly small changes in the singularity parameters. For given sets Γ and Ω the spline may be stable with respect to one type of boundary condition but not another. Also, for a given set Ω and a given type of boundary condition, the spline may be stable for certain control point locations but not others. A discussion of spline stability is beyond the scope of this report (see e.g., ref. 27); however, the source/analysis spline can be shown to be stable with respect to application of $\frac{\partial \phi}{\partial n}$ boundary conditions at panel centers, using equation (C.10). From experience, it also appears to be stable with respect to the application of ϕ boundary conditions at panel centers.

The rationale for locating the points of the sets Γ and Ω in the case of the (doublet/analysis) type 2 network is the same as for the (source/analysis) network. The addition of network edge singularity parameters is due primarily to the quadratic order of the doublet distribution on each panel. We note that the six coefficients of such a distribution could not be determined from the four local singularity parameters in the case of a network corner panel, were the source/analysis spline to be used. With the singularity parameter arrangement shown in figure (B.1) for the doublet/analysis network type, the local set of singularity parameters for every panel contains nine singularity parameters which is more than adequate to determine six distribution coefficients by the method of weighted least squares. The corresponding addition of edge control points to Γ keeps the number of control points equal to the number of singularity parameters and allows for doublet strength and gradient matching across network edges. It can be shown using equation (C.15) that the arrangement of points in Γ and Ω in the case of the doublet/analysis network type is stable relative to the application of ϕ boundary conditions. From experience, it also appears stable relative to the application of $\frac{\partial\phi}{\partial n}$ type boundary conditions on a surface bounded by the fluid domain on both sides.

The control points for network types 3, 4, 5, and 6 are not symmetrically located due to the directional nature of design type boundary conditions. The discussion corresponding to figure 4 indicates the necessity of defining "auxiliary" boundary conditions at edge points of a design network where inflow is anticipated. For network types 3 and 4 we assume inflow across the bottom and left side edge (relative to the schematic displayed in fig. C.1); for network type 5 we assume inflow across the bottom edge only; and for network type 6 we assume inflow across all but the top edges. The network interior control points are located at panel centers for the same reason as in the case of the analysis networks. Spline stability relative to design type boundary conditions then requires that the singularity parameter points be located at grid corner points in the case of the network types 3 and 4, and at edge midpoints in the case of the interior parameters for network types 5 and 6. In each case the number of singularity parameters equals the number of control points.

The wake type networks 8 and 10 are in reality the design type network number 6 where the boundary condition has already been applied directly to the spline, resulting in fewer degrees of freedom. The type 8 network is obtained by applying to all type 6 control points, except for those along the bottom edge, the design type boundary condition that $\vec{\nabla}\mu$ be zero in the panel column direction. (Assuming that the panel column direction corresponds roughly to the freestream direction such a boundary condition implies that the $\Delta Cp = 0$ where Cp is computed using the linearized formula.) By integration we see that such a boundary condition implies that all singularity parameters in each column of the type 6 singularity spline will be equal to the value of the singularity parameter at the head of the column (i.e., at the bottom edge of the schematic). Performing such singularity parameter identification results in the type 8 network. The remaining control points and singularity parameters are used for doublet strength and derivative matching (see sec. C.3). The type 10 network is obtained by requiring in addition that $\vec{\nabla}\mu$ be zero in the row direction along the first (bottom) row of control points, which can be achieved by identifying all singularity parameters in that row with the first. This results in a network where doublet strength is constant everywhere. Such a network creates a jump in potential but no jump in velocity (see equations (C.10) and (C.15)). In contrast, the type 8 network creates a jump in the component of velocity perpendicular to the column direction.

APPENDIX D
PANEL INFLUENCE COEFFICIENT GENERATION

D.1 INTRODUCTION

In this appendix we shall calculate the potential and velocity induced by a source or doublet distribution on a curved panel. As shown in figure (D.1), let S be the curved panel surface, Σ its tangent plane projection, Q a point on S, $\hat{n}$ the normal to S at $\vec{Q}$, and $\vec{P}$ a field point.

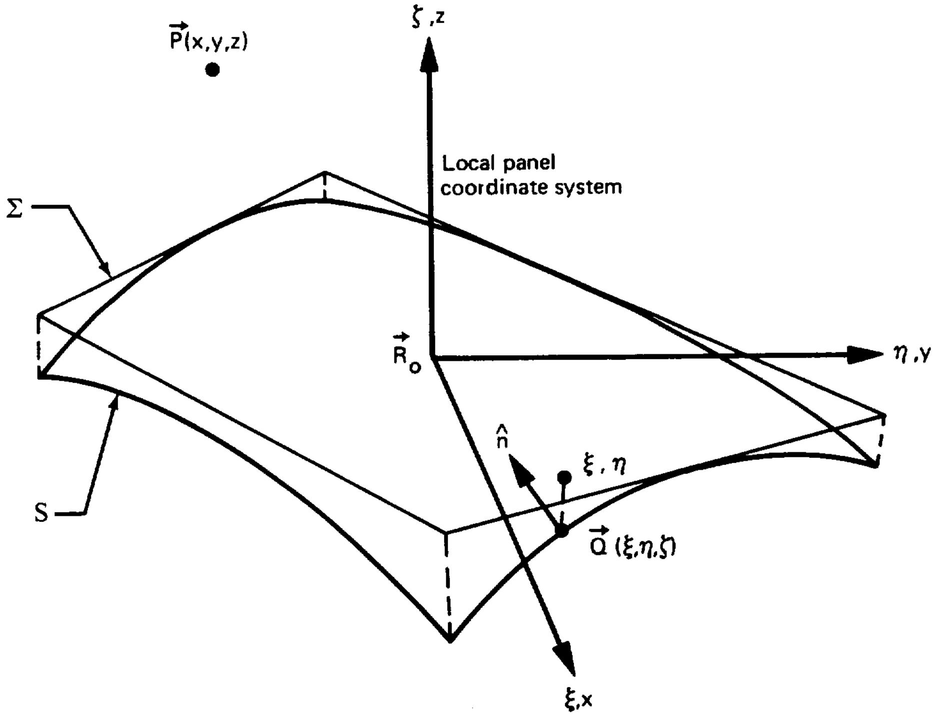

Figure D.1. – Field Point/Panel Geometry

The perturbation potential ϕ at $\vec{P}$ induced by a source distribution of strength σ on S is defined by

$$\phi = \iint_S \sigma \left(\frac{-1}{4\pi R}\right) dS \tag{D.1}$$

where

$$\vec{R} = (\xi - x, \eta - y, \zeta - z) = \vec{Q} - \vec{P} \tag{D.2}$$

and

$$R = |\vec{R}| = \sqrt{(\xi - x)^2 + (\eta - y)^2 + (\zeta - z)^2}$$

The perturbation potential ϕ at $\vec{P}$ induced by a doublet distribution of strength μ on S with doublet axis in the $\hat{n}$ direction is obtained by taking the directional derivative of $\frac{1}{4\pi R}$ in the $\hat{n}$ direction:

$$\phi = \iint_S \mu \, \hat{n} \cdot \vec{\nabla}_Q \left(\frac{1}{4\pi R} \right) dS$$

$$= \iint_S \mu \left(\frac{-\vec{R} \cdot \hat{n}}{4\pi R^3} \right) dS \qquad \text{(D.3)}$$

The perturbation velocity $\vec{v}$ induced at $\vec{P}$ by a source or doublet distribution on S is defined by

$$\vec{v} = \vec{\nabla} \phi \qquad \text{(D.4)}$$

We assume that the surface S is defined by equation (A.20):

$$\zeta = a\xi^2 + b\eta^2, \ (\xi, \eta) \epsilon \Sigma \qquad \text{(D.5)}$$

We also assume that S does not deviate significantly from Σ, more precisely that

$$\delta << 1 \qquad \text{(D.6)}$$

where

$$\delta = \frac{1}{2} \underset{(\xi, \eta) \epsilon \Sigma}{\text{Max}} \left\{ \sqrt{a^2\xi^2 + b^2\eta^2} \right\} \qquad \text{(D.7)}$$

(Nominally, we assume $\delta < .066$ see equation (A.23).)

The distribution of singularity strength on S is assumed to be linear in the case of a source panel and quadratic in the case of a doublet panel. To be specific we assume

$$\sigma = \sigma_0 + \sigma_\xi \xi + \sigma_\eta \eta, \quad (\xi, \eta) \epsilon \Sigma \qquad \text{(D.8)}$$

and

$$\mu = \mu_0 + \mu_\xi \xi + \mu_\eta \eta + \frac{1}{2}\mu_{\xi\xi}\xi^2 + \mu_{\xi\eta}\xi\eta + \frac{1}{2}\mu_{\eta\eta}\eta^2, \quad (\xi, \eta) \in \Sigma \tag{D.9}$$

which are the same as equations (B.1) and (B.2) respectively.

D.2 EVALUATION OF SOURCE AND DOUBLET INTEGRALS FOR AN ARBITRARY FIELD POINT

Let us first consider the evaluation of source potential defined by equation (D.1). Evaluation of source velocity and doublet potential and velocity will be quite similar. The first step in the evaluation procedure is to transfer the integral over S to the equivalent integral over Σ. (See discussion of fig. (A.2) for a precise definition of the plane quadrilateral Σ.) We have

$$\phi = \iint_\Sigma \sigma \left(\frac{-1}{4\pi R}\right) \sec\left(\hat{\zeta}, \hat{\eta}\right) d\xi d\eta \tag{D.10}$$

From equation (D.5) we obtain

$$\hat{n} = \frac{1}{\sqrt{1 + 4a^2\xi^2 + 4b^2\eta^2}} \quad (-2a\xi, -2b\eta, 1) \tag{D.11}$$

and

$$\sec\left(\hat{\zeta}, \hat{\eta}\right) = \sqrt{1 + 4a^2\xi^2 + 4b^2\eta^2} \tag{D.12}$$

Substitution of equations (D.2), (D.8) and (D.12) into (D.10) yields an explicit integral for ϕ. However, the integral cannot be evaluated in closed form as it stands. By employing the hypothesis that δ^2 is negligible compared to unity (hypothesis (D.6)) the integrand can be approximated by terms that are integrable in closed form. A uniform approximation to sec $(\hat{\zeta}, \hat{\eta})$ can be obtained by noting that

$$4a^2\xi^2 + 4b^2\eta^2 \leqslant 16\delta^2 \tag{D.13}$$

hence

$$\sec\left(\hat{\zeta}, \hat{\eta}\right) \approx 1 \tag{D.14}$$

A uniform approximation to $1/R$ is somewhat more difficult to obtain since this factor is singular. Let $(x_0, y_0, 0)$ be the point on Σ closest to $(x, y, 0)$ (see fig. D.2) and set

$$z_0 = \zeta(x_0, y_0), \quad h = z - z_0, \quad \text{and } r = \sqrt{(\xi - x)^2 + (\eta - y)^2} \tag{D.15}$$

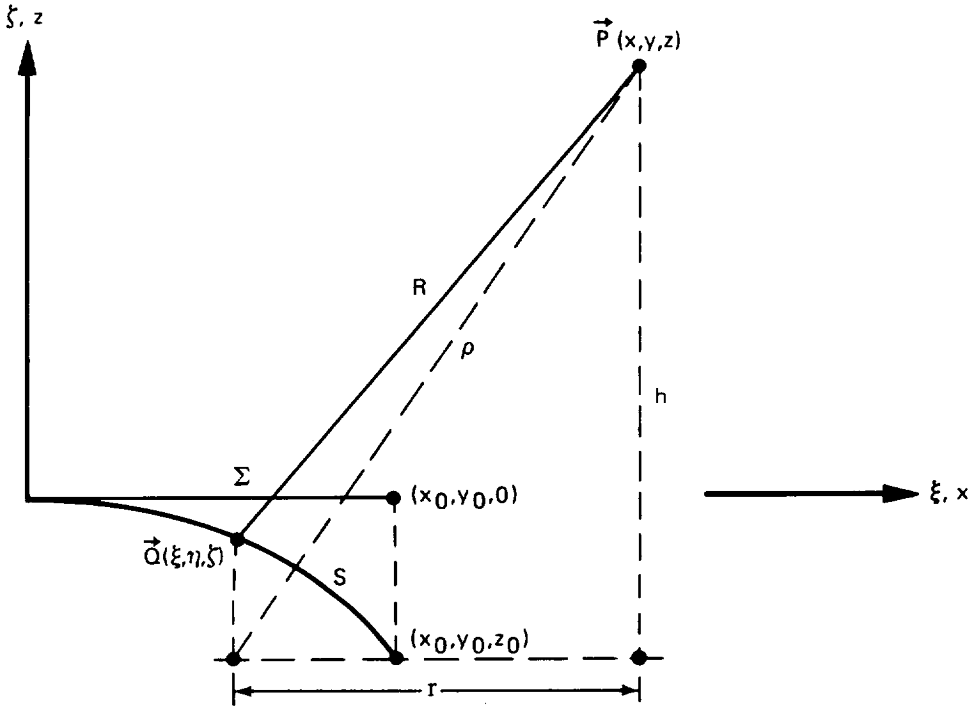

Figure D.2. – Geometry for Curvature Approximation

Then

$$R = \sqrt{\left(r^2 + h^2\right) - 2h\left(\zeta - z_0\right) + \left(\zeta - z_0\right)^2}$$

$$= \sqrt{r^2 + h^2} \cdot \sqrt{1 + \frac{-2h(\zeta - z_0) + (\zeta - z_0)^2}{r^2 + h^2}} \tag{D.16}$$

Let

$$\epsilon = \max_{(\xi, \eta)\,\epsilon\,\Sigma} \left\{ \frac{|\zeta - z_0|}{r} \right\} \tag{D.17}$$

Then

$$\left|\frac{-2h(\zeta - z_0)+(\zeta - z_0)^2}{r^2 + h^2}\right| \leqslant \frac{2\epsilon rh + \epsilon^2 r^2}{r^2 + h^2} \leqslant \epsilon + \epsilon^2 \tag{D.18}$$

Therefore, if ϵ^2 is everywhere negligible equation (D.16) yields

$$\frac{1}{R} \approx \frac{1}{\rho} + \frac{h(\zeta - z_0)}{\rho^3}, \quad \rho = \sqrt{r^2 + h^2} \tag{D.19}$$

But

$$\begin{aligned}
\epsilon &= \underset{(\xi,\eta)\in\Sigma}{\text{Max}} \left\{\frac{|\zeta(\xi,\eta) - \zeta(x_0, y_0)|}{r}\right\} \\
&= \underset{(\xi,\eta)\in\Sigma}{\text{Max}} \left\{\frac{\left|a(\xi + x_0)(\xi - x_0) + b(\eta + y_0)(\eta - y_0)\right|}{r}\right\} \\
&\leqslant \underset{(\xi,\eta)\in\Sigma}{\text{Max}} \left\{\sqrt{a^2(\xi + x_0)^2 + b^2(\eta + y_0)^2} \cdot \frac{\sqrt{(\xi - x_0)^2 + (\eta - y_0)^2}}{r}\right\} \\
&\leqslant \underset{(\xi,\eta)\in\Sigma}{\text{Max}} \left\{\sqrt{a^2(\xi + x_0)^2 + b^2(\eta + y_0)^2} \cdot 2\right\} \\
&\leqslant 8\delta
\end{aligned} \tag{D.20}$$

A much better bound on ϵ is available when (x, y) is several panel diameters away from Σ and the assumption that δ^2 is negligible becomes unnecessary. However, in this case a far field expansion will be used to obtain an efficient approximation to the right side of equation (D.10). Note that the panel curvature effect is contained in the second term on the right side of (D.19), this term being zero for a flat panel.

Substituting equations (D.8), (D.14) and (D.19) into (D.10) and rearranging them, we obtain, after considerable algebraic manipulation:

$$\phi = \sigma(x, y)\, I(1, 1) + \sigma_x(x, y)\; I(2, 1) + \sigma_y(x, y)\; I(1, 2) \tag{D.21}$$

where

$$\begin{aligned} \sigma(x, y) &= \sigma_0 + \sigma_\xi x + \sigma_\eta y \\ \sigma_x(x, y) &= \sigma_\xi \\ \sigma_y(x, y) &= \sigma_\eta \end{aligned} \tag{D.22}$$

Note that $\sigma_x(x, y)$ and $\sigma_y(x, y)$ are constant, although formal dependence on x and y has been displayed to emphasize the shift in the origin of the Taylor's series expansion to the point (x, y).

Here

$$\begin{aligned} I(M, N) = -\frac{1}{4\pi} \Big\{ H(M, N, 1) &+ a\big[hH(M + 2, N, 3) + 2xhH(M + 1, N, 3)\big] \\ &+ b\big[hH(M, N + 2, 3) + 2yhH(M, N + 1, 3)\big] \\ &+ c\big[hH(M, N, 3)\big] \Big\} \end{aligned} \tag{D.23}$$

where

$$c = ax^2 + by^2 - z_0 \tag{D.24}$$

and

$$H(M, N, K) = \iint_\Sigma \frac{(\xi - x)^{M-1} (\eta - y)^{N-1}}{\left(\sqrt{(\xi - x)^2 + (\eta - y)^2 + h^2}\right)^K} \, d\xi \, d\eta \tag{D.25}$$

The H integrals will be evaluated in the next section. The leading term in the righthand side of equation (D.23) is due to the leading term on the righthand side of equation (D.19) and thus corresponds to a flat panel. The remaining terms having coefficients of a, b, and c are due to the second term on the right side of equation (D.19) and constitute panel curvature effects.

To find $\vec{v}$, equation (D.21) can be differentiated. For this purpose z_0 may be treated as constant, although formally z_0 depends on x and y because $(x_0, y_0, 0)$ depends on x and y, being the point on Σ closest to (x, y, 0). However, the derivatives of z_0 with respect to x and y either cancel each other or are negligible because of hypothesis (D.6). The derivatives of the H integrals then are simple combinations of the H integrals themselves, i.e.,

$$\frac{\partial}{\partial x} H(M, N, K) = -(M-1)\, H(M-1, N, K) + KH(M+1, N, K+2)$$

$$\frac{\partial}{\partial y} H(M, N, K) = -(N-1)\, H(M, N-1, K) + KH(M, N+1, K+2)$$

$$\frac{\partial}{\partial z} H(M, N, K) = -KhH(M, N, K+2) \tag{D.26}$$

It turns out to be easier to calculate $\vec{v}$ by differentiating equation (D.10) to obtain $\vec{v} = \iint\limits_{\Sigma} \sigma \left(\frac{\vec{R}}{4\pi R^3}\right) \sec(\hat{\zeta}, \hat{\eta})\; d\xi d\eta$ and using a generalized form of equation (D.19), that is

$$\frac{1}{R^K} \approx \frac{1}{\rho^K} + \frac{Kh(\zeta - z_0)}{\rho^{K+2}} \quad , \quad \rho = \sqrt{r^2 + h^2} \tag{D.27}$$

Equation (D.27) can be obtained by raising equation (D.19) to the K power and expanding the righthand side by the binomial theorem. In either case we obtain

$$\vec{v} = \sigma(x, y)\, \vec{J}(1, 1) + \sigma_x(x, y)\, \vec{J}(2, 1) + \sigma_y(x, y)\, \vec{J}(1, 2) \tag{D.28}$$

where

$$\vec{J}(M, N) = \left[J_x(M, N),\;\; J_y(M, N),\;\; J_z(M, N)\right] \tag{D.29}$$

i. e., $v_x = \sigma(x, y)\, J_x(1, 1) + \sigma_x(x, y)\, J_x(2, 1) + \sigma_y(x, y)\, J_x(1, 2)$, etc.

and

$$
\begin{aligned}
J_x(M, N) = -\frac{1}{4\pi} \Big\{ & H(M+1, N, 3) + a\big[3hH(M+3, N, 5) + 6xhH(M+2, N, 5)\big] \\
& + b\big[3hH(M+1, N+2, 5) + 6yhH(M+1, N+1, 5)\big] \\
& + c\big[3hH(M+1, N, 5)\big]\Big\} \\
J_y(M, N) = -\frac{1}{4\pi} \Big\{ & H(M, N+1, 3) + a\big[3hH(M+2, N+1, 5) + 6xhH(M+1, N+1, 5)\big] \\
& + b\big[3hH(M, N+3, 5) + 6yhH(M, N+2, 5)\big] \\
& + c\big[3hH(M, N+1, 5)\big]\Big\} \\
J_z(M, N) = -\frac{1}{4\pi} \Big\{ & -hH(M, N, 3) + a\big[H(M+2, N, 3) - 3h^2H(M+2, N, 5) \\
& + 2xH(M+1, N, 3) - 6xh^2H(M+1, N, 5)\big] \\
& + b\big[H(M, N+2, 3) - 3h^2H(M, N+2, 5) \\
& + 2yH(M, N+1, 3) - 6yh^2H(M, N+1, 5)\big] \\
& + c\big[H(M, N, 3) - 3h^2H(M, N, 5)\big]\Big\}
\end{aligned}
$$

Doublet potential and velocity can be evaluated similarly using equations (D.3), (D.11) and (D.27).

However, the assumption (D.14) is unnecessary since $\sec(\hat{\xi}, \hat{\eta})$ does not appear in the product $\hat{n}dS$. We obtain

$$
\begin{aligned}
\phi = {} & \mu(x, y)\, I(1, 1) + \mu_x(x, y)\, I(2, 1) + \mu_y(x, y)\, I(1, 2) \\
& + \frac{1}{2}\mu_{xx}(x, y)\, I(3, 1) + \mu_{xy}(x, y)\, I(2, 2) + \frac{1}{2}\mu_{yy}(x, y)\, I(1, 3) \qquad \text{(D.30)}
\end{aligned}
$$

where

$$
\begin{aligned}
\mu(x, y) &= \mu_0 + \mu_\xi x + \mu_\eta y + \frac{1}{2}\mu_{\xi\xi}x^2 + \mu_{\xi\eta}xy + \frac{1}{2}\mu_{\eta\eta}y^2 \\
\mu_x(x, y) &= \mu_\xi + \mu_{\xi\xi}x + \mu_{\xi\eta}y \\
\mu_y(x, y) &= \mu_\eta + \mu_{\xi\eta}x + \mu_{\eta\eta}y \\
\mu_{xx}(x, y) &= \mu_{\xi\xi} \\
\mu_{xy}(x, y) &= \mu_{\xi\eta} \\
\mu_{yy}(x, y) &= \mu_{\eta\eta} \qquad \text{(D.31)}
\end{aligned}
$$

and

$$
\begin{aligned}
I(M, N) = \frac{1}{4\pi}\Big\{ & hH(M, N, 3) + a\Big[H(M + 2, N, 3) + 3h^2H(M + 2, N, 5) + 6xh^2H(M + 1, N, 5)\Big] \\
& + b\Big[H(M, N + 2, 3) + 3h^2H(M, N + 2, 5) + 6yh^2H(M, N + 1, 5)\Big] \\
& + c\Big[- H(M, N, 3) + 3h^2H(M, N, 5)\Big]\Big\} \qquad \text{(D.32)}
\end{aligned}
$$

As in equation (D.23), the terms containing a, b, and c as coefficients are the effects of panel curvature.

We also obtain

$$
\begin{aligned}
\vec{v} = {} & \mu(x, y)\,\vec{J}(1, 1) + \mu_x(x, y)\,\vec{J}(2, 1) + \mu_y(x, y)\,\vec{J}(1, 2) \\
& + \frac{1}{2}\mu_{xx}(x, y)\,\vec{J}(3, 1) + \mu_{xy}(x, y)\,\vec{J}(2, 2) + \frac{1}{2}\mu_{yy}(x, y)\,\vec{J}(1, 3) \qquad \text{(D.33)}
\end{aligned}
$$

where

$$\vec{J}(M, N) = \Big[J_x(M, N),\ J_y(M, N),\ J_z(M, N)\Big] \qquad \text{(D.34)}$$

and

$$\begin{aligned}
J_x(M, N) = \frac{1}{4\pi} \Big\{ & 3hH(M + 1, N, 5) + a\Big[3H(M + 3, N, 5) - 2H(M + 1, N, 3) \\
& + 15h^2H(M + 3, N, 7) - 2xH(M, N, 3) + 30\,xh^2H(M + 2, N, 7)\Big] \\
& + b\Big[3H(M + 1, N + 2, 5) + 15h^2H(M + 1, N + 2, 7) + 30\,yh^2H(M + 1, N + 1, 7)\Big] \\
& + c\Big[-3H(M + 1, N, 5) + 15h^2H(M + 1, N, 7)\Big]\Big\}
\end{aligned}$$

$$\begin{aligned}
J_y(M, N) = \frac{1}{4\pi} \Big\{ & 3hH(M, N + 1, 5) + a\Big[3H(M + 2, N + 1, 5) + 15h^2H(M + 2, N + 1, 7) \\
& + 30xh^2H(M + 1, N + 1, 7)\Big] + b\Big[3H(M, N + 3, 5) - 2H(M, N + 1, 3) \\
& + 15h^2H(M, N + 3, 7) - 2yH(M, N, 3) + 30yh^2H(M, N + 2, 7)\Big] \\
& + c\Big[-3H(M, N + 1, 5) + 15h^2H(M, N + 1, 7)\Big]\Big\}
\end{aligned}$$

$$\begin{aligned}
J_z(M, N) = \frac{1}{4\pi} \Big\{ & H(M, N, 3) - 3h^2H(M, N, 5) + a\Big[3hH(M + 2, N, 5) \\
& - 15h^3H(M + 2, N, 7) + 12xhH(M + 1, N, 5) - 30xh^3H(M + 1, N, 7)\Big] \\
& + b\Big[3hH(M, N + 2, 5) - 15h^3H(M, N + 2, 7) + 12yhH(M, N + 1, 5) \\
& - 30yh^3H(M, N + 1, 7)\Big] + c\Big[9hH(M, N, 5) - 15h^3H(M, N, 7)\Big]\Big\}
\end{aligned}$$

D.3 CALCULATION OF H INTEGRALS

In this section we shall compute in closed form each of the integrals

$$H(M, N, K) = \iint_{\Sigma} \frac{(\xi - x)^{M-1} (\eta - y)^{N-1}}{\rho^K} d\xi d\eta \qquad (D.35)$$

$$\rho = \sqrt{(\xi - x)^2 + (\eta - y)^2 + h^2}$$

for M = 1, MXQ ; N = 1, MXQ – M + 1 ; K = 1, MXK, 2.

Note that M and N both vary from 1 to MXQ in such a manner that $M + N - 1 \leqslant MXQ$. The index K varies from 1 to MXK in steps of 2, which means that K is odd. The following values of MXQ and MXK are evident from the previous section.

Panel Type	MXQ	MXK	
Source Potential (Flat Panel)	2	1	
Source Velocity (Flat Panel)	3	3	
Doublet Potential (Flat Panel)	3	3	
Doublet Velocity (Flat Panel)	4	5	
Source Potential (Curved Panel)	4	3	
Source Velocity (Curved Panel)	5	5	
Doublet Potential (Curved Panel)	5	5	
Doublet Velocity (Curved Panel)	6	7	(D.36)

For the range of indices above, some H(M, N, K) become divergent as the field point $\vec{P}(x, y, z)$ approaches the panel surface S. This is because h approaches zero as $\vec{P}$ approaches S, and therefore ρ becomes zero when the integration variables (ξ η) take on the field point values of (x, y). Note that the singularity occurs as $\vec{P}$ approaches S even though the integration variables range over Σ. For further analysis see the discussion following equations (D.52) and (D.105).

The integrals H(M, N, K) may be computed with the aid of the following algebraic recursion relations. From the definitions of H(M, N, K) and ρ we can easily derive the following identity:

$$H(M + 2, N, K) + H(M, N + 2, K) + h^2 H(M, N, K) = H(M, N, K - 2) \qquad (D.37)$$

A second recursion relation can be obtained by considering the identity

$$\iint_{\Sigma} \frac{\partial}{\partial \xi} \left[\frac{(\xi - x)^{M-2} (\eta - y)^{N-1}}{\rho^{K-2}}\right] d\xi d\eta = (M-2)\, H(M-2, N, K-2) - (K-2)\, H(M, N, K)$$

Integrating the left side by parts we obtain:

$$(K-2)\, H(M, N, K) = (M-2)\, H(M-2, N, K-2) - \sum_{1}^{4} \nu_{\xi}\, F(M-1, N, K-2), \qquad (D.38)$$

and by interchanging the roles of ξ and η:

$$(K-2)\, H(M, N, K) = (N-2)\, H(M, N-2, K-2) - \sum_{1}^{4} \nu_{\eta}\, F(M, N-1, K-2) \qquad (D.39)$$

The summations on the right sides of equations (D.38) and (D.39) are over all four sides of Σ.

Here $\hat{\nu}$ is the unit outer normal of the side L (see fig. (D.3)) and F(M, N, K) is the line integral for side L, defined by

$$F(M, N, K) = \int_{L} \frac{(\xi - x)^{M-1} (\eta - y)^{N-1}}{\rho^{K}}\, d\ell\,, \quad \rho = \sqrt{(\xi - x)^2 + (\eta - y)^2 + h^2} \qquad (D.40)$$

The procedure for evaluating F integrals will be described following equation (D.53). The fundamental integrals are H(1, 1, 3) and F(1, 1, 1). Once these two integrals are evaluated, the remaining H and F integrals can be evaluated from recursion relations. The details of the evaluation of H(1, 1, 3) are given in section G.1 of appendix G, and F(1, 1, 1) is given by equation (D.60). Assuming the F integrals and H(1, 1, 3) are known, the recursion relations (D.37), (D.38) and (D.39) may be recombined (app. G.2) to yield the efficient procedure, given below, for calculating the H integrals. Because some of the H integrals are singular on S it is actually necessary to consider three slightly different procedures depending upon the relationship of the field point $\vec{P}$ to the panel S. Define d_H to be the minimum distance of the point (x, y) to the perimeter of Σ. If δ_h is some small number (nominally chosen as 0.01) we have the following three computational procedures.

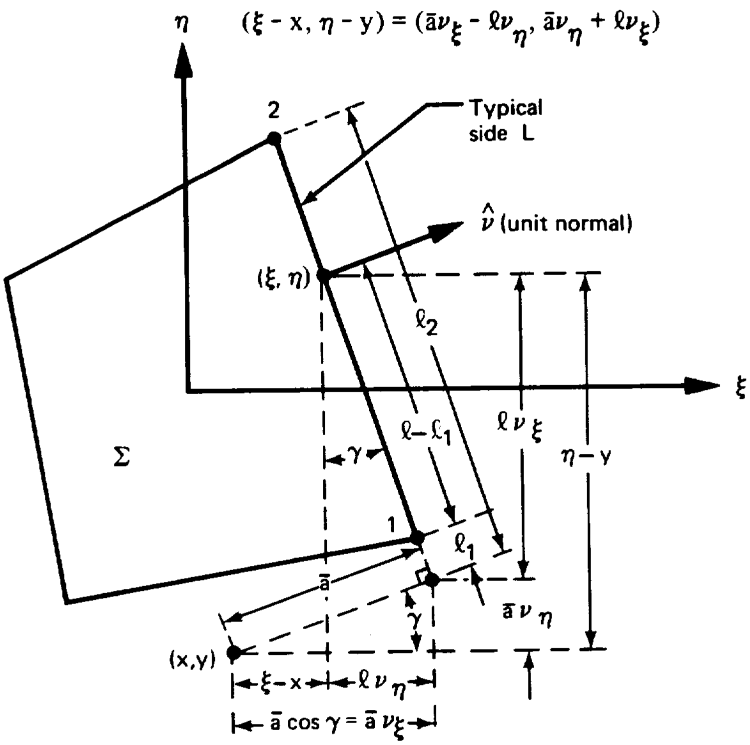

Figure D.3. – Quadrilateral Geometry

Procedure 1: $|h| \geqslant \delta_h d_H$, (i.e., $\vec{P}$ is not "too near" the plane of Σ). When the following eight steps are performed in the order given, all the H(M, N, K)'s will be obtained for the MXQ and MXK given by equation (D.36).

1.

$$H(1, 1, 1) = -|h| \sum_{1}^{4} \tan^{-1}\left[\bar{a}\left(\ell_2 c_1 - \ell_1 c_2\right),\ c_1 c_2 + \bar{a}^2 \ell_1 \ell_2\right] + \sum_{1}^{4} \bar{a} F(1, 1, 1) \quad \text{(D.41)}$$

where the $\tan^{-1}$ terms are from H(1, 1, 3) (see equation (G.24), and where

$$c_1 = g^2 + |h| \sqrt{\ell_1^2 + g^2}, \quad c_2 = g^2 + |h| \sqrt{\ell_2^2 + g^2}, \quad g = \sqrt{\bar{a}^2 + h^2}$$

Here $\tan^{-1}(y, x)$ is defined by $\phi = \tan^{-1}(\sin\phi, \cos\phi)$, $\epsilon[-\pi, \pi]$, and is the same as the ATAN2 function of FORTRAN. The sum is over the four sides of Σ.

2.

$$H(1,1,K) = \frac{1}{(K-2)\,h^2}\left[(K-4)\,H(1,1,K-2) + \sum_1^4 \bar{a}F(1,1,K-2)\right];$$

$$K = 3, MXK, 2. \tag{D.42}$$

3.

$$H(2,N,1) = \frac{1}{(N+1)}\left[h^2 \sum_1^4 \nu_\xi F(1,N,1) + \sum_1^4 \bar{a}F(2,N,1)\right];$$

$$N = 1, MXQ - 1. \tag{D.43}$$

4.

$$H(1,N,1) = \frac{1}{N}\left[-h^2(N-2)\,H(1,N-2,1) + h^2 \sum_1^4 \nu_\eta F(1,N-1,1)\right.$$

$$\left. + \sum_1^4 \bar{a}F(1,N,1)\right]; \quad N = 2, MXQ \tag{D.44}$$

Note that when N = 2, H(1, N – 2, 1) need not be computed since it is multiplied by zero. The same holds for similar terms in steps 5 and 6.

5.

$$H(M,N,1) = \frac{1}{(M+N-1)}\left[-h^2(M-2)\,H(M-2,N,1) + h^2 \sum_1^4 \nu_\xi F(M-1,N,1)\right.$$

$$\left. + \sum_1^4 \bar{a}F(M,N,1)\right]; \; M = 3, MXQ \text{ and } N = 1, MXQ - M + 1 \tag{D.45}$$

6.

$$H(1, N, K) = \frac{1}{(K - 2)} \left[(N - 2)\, H(1, N - 2, K - 2) - \sum_{1}^{4} \nu_{\eta} F(1, N - 1, K - 2) \right] ;$$

N = 2, MXQ and K = 3, MXK, 2 (D.46)

7.

$$H(2, N, K) = \frac{1}{(K - 2)} \left[- \sum_{1}^{4} \nu_{\xi} F(1, N, K - 2) \right] ;$$

N = 1, MXQ – 1 and K = 3, MXK, 2 (D.47)

8.

$$H(M, N, K) = - H(M - 2, N + 2, K) - h^2 H(M - 2, N, K) + H(M - 2, N, K - 2);$$

M = 3, MXQ and N = 1, MXQ - M + 1 and K = 3, MXK, 2 (D.48)

Procedure 2: $|h| < \delta_h d_H$ and $(x, y, 0) \notin \Sigma$, (i.e., $\vec{P}$ is "near" the plane of Σ but outside the boundary of Σ). In this case the recursion defined by equation (D.42) cannot be used because h may be zero or close to zero. Hence, H(1, 1, K) for $K \geq 3$ must be computed by some other means. Note that if H(1, 1, K) were known for some large value of K, then the recursion of equation (D.42) could be reversed and H(1, 1, K) could be computed for successively lower values of K. This is what is done in steps 1 and 2 below. The justification for step 1 is contained in appendix (G.8).

1. Set

$$H(1, 1, NHK + MXK) = 0.0 \tag{D.49}$$

where NHK is a positive integer (nominally taken to be 16), and

2. Compute

$$H(1, 1, K - 2) = \frac{1}{(K - 4)} \left[h^2 (K - 2)\, H(1, 1, K) - \sum_{1}^{4} \bar{a} F(1, 1, K - 2) \right] \tag{D.50}$$

for K = NHK + MXK, 3, – 2

3. All the remaining steps in Procedure 2 (steps 3 through 8) are the same as for Procedure 1.

Procedure 3: $|h| < \delta_h d_H$ and $(x, y, 0) \in \Sigma$, (i.e., $\vec{P}$ is "near" the plane of Σ and within the boundary of Σ).

Define

$$H^*(M, N, K) = H(M, N, K) - 2\pi\nu(M, N, K)\,|h|^{M+N-K} \tag{D.51}$$

where

$$\nu(M, N, K) = \begin{cases} 0 \text{ if } M \text{ or } N \text{ is even} \\ \dfrac{\overbrace{[1 \cdot 1 \cdot 3 \cdot 5 \ldots |M-2|]}^{1 \text{ for } M = 1}\ \overbrace{[1 \cdot 1 \cdot 3 \cdot 5 \ldots |N-2|]}^{1 \text{ for } N = 1}}{[(K-2)(K-4)(K-6) \ldots (K-M-N)]} \text{ otherwise.} \end{cases} \tag{D.52}$$

and K is odd.

Then it may be shown (app. G.7) that H^* obeys the same recursions as H (except for the initial condition (D.41) which is irrelevant for procedure 2), and is continuous with respect to the field point $\vec{P}$ when $(x, y, 0) \epsilon \Sigma$. Hence H^* may be computed using procedure 2 (see app. G.8).

Once H^* has been calculated H may be obtained from equation (D.51). Care must be taken when $M + N < K$ with M and N odd. H^* is continuous in the interior of S but equation (D.51) shows that H is singular there when $M + N < K$ with singular part $2\pi\nu\,(M, N, K)\,|h|^{M+N-K}$. Upon solving (D.51) for H and substituting into our previous formula for potential and velocity, the only terms involving ν that don't cancel each other are of the form $\nu Th/|h|$, where T is continuous. Such terms are responsible for jump discontinuities in potential and velocity across S. Recall from appendix C that the potential and velocity at a panel can be expressed as upper and lower values or as average and difference values (e.g., see equations (C.5) and (C.6)). The terms $\nu Th/|h|$ make no contribution to average values since they are positive on one side of the panel and negative with equal magnitude on the other side. Hence, for simplicity we choose to evaluate the average value of potential and velocity on S when $h = 0$ (numerically when $|h| < \delta_0 d_H$ where δ_0 is nominally chosen as 10^{-8}). This involves no loss of generality since the difference values can be computed directly from equations (C.10) and (C.15), hence, upper and lower surface values can be easily computed from equations (C.9) and (C.13). As a practical matter, the desired evaluation will be accomplished simply by replacing $h/|h|$ everywhere it appears by signh, where

$$\text{signh} = \begin{cases} +1 & \text{if } h > 0 \\ -1 & \text{if } h < 0 \\ 0 & \text{if } h = 0 \text{ (numerically } |h| < \delta_0 d_H). \end{cases}$$

Note that when $h = 0$, all terms involving $h/|h|$ will disappear, with the result that average values are calculated.

We now evaluate the integrals F(M, N, K) for the indices M, N, K required by the H evaluation procedures. It is apparent that we need only the following F integrals.

$$\begin{aligned} &F(1,1,K) \ ; \ K = 1, MXFK, 2 \\ &F(M,N,1) \ ; \ M = 1, MXQ \quad \text{and} \quad N = 1, MXQ - M + 1 \\ &F(1,N,K) \ ; \ N = 2, MXQ \quad \text{and} \quad K = 3, MXK - 2, 2 \end{aligned} \tag{D.53}$$

where

$$MXFK = \begin{cases} MXK - 2 \text{ if } |h| \geqslant \delta_h d_H & \text{(procedure 1)} \\ NHK + MXK - 2 \text{ if } |h| < \delta_h d_H & \text{(procedure 2)} \end{cases} \tag{D.54}$$

These integrals may be obtained with the aid of three recursion relations. We have the following two identities.

$$F(M+2,N,K) + F(M,N+2,K) + h^2 F(M,N,K) = F(M,N,K-2) \tag{D.55}$$

and

$$\nu_\xi F(M+1,N,K) + \nu_\eta F(M,N+1,K) = \bar{a} F(M,N,K) \tag{D.56}$$

Equation (D.55) is the analogue of equation (D.37), and equation (D.56) follows from the equation in figure D.2 A third identity is obtained by considering the expression

$$E(\xi,\eta) = \frac{(\xi - x)^{M-1} (\eta - y)^{N-1}}{\rho^{K-2}}$$

where $\rho(\xi, \eta)$ is given by equation (D.40). From figure D.2 we see that $(\xi - x)$ and $(\eta - y)$ are functions only of ℓ along typical side L since $\bar{a}$ is constant. Thus, we can write

$$\frac{dE}{d\ell} = \frac{\partial E}{\partial(\xi - x)} \frac{\partial(\xi - x)}{\partial \ell} + \frac{\partial E}{\partial(\eta - y)} \frac{\partial(\eta - y)}{\partial \ell}$$

or

$$\int_{\ell_1}^{\ell_2} \frac{dE}{d\ell} d\ell = -\nu_\eta \int_{\ell_1}^{\ell_2} \frac{\partial E}{\partial(\xi - x)} d\ell + \nu_\xi \int_{\ell_1}^{\ell_2} \frac{\partial E}{\partial(\eta - y)} d\ell$$

Performing the indicated operations yields

$$-(M-1)\,\nu_\eta F(M-1, N, K-2) + (N-1)\,\nu_\xi F(M, N-1, K-2)$$

$$+(K-2)\,\nu_\eta F(M+1, N, K) - (K-2)\,\nu_\xi F(M, N+1, K) = E(M, N, K-2) \qquad \text{(D.57)}$$

where

$$E(M, N, K) = \left.\frac{(\xi - x)^{M-1}\,(\eta - y)^{N-1}}{\rho^K}\right|_1^2$$

$$\rho = \sqrt{(\xi - x)^2 + (\eta - y)^2 + h^2} \qquad \text{(D.58)}$$

The quantities E(M, N, K) may be evaluated directly or else recursively with the aid of the formula

$$P(I) = \left(x_2 + x_1\right) P(I-1) - x_1 x_2 P(I-2) \qquad \text{(D.59)}$$

where

$$P(I) \equiv A_2 x_2^{I-1} - A_1 x_1^{I-1}$$

(See app. G.4.)

The recursion relations (D.55), (D.56) and (D.57) may be recombined to yield the efficient procedure for evaluating the required F integrals below. (See app. G.3.) Again, the singular behavior of some of the F integrals (near the edges of S) requires a special case. Let us define d_F to be the minimum distance of the field point $\vec{P}(x, y, z)$ to the perimeter of S. Then if δ_g is some small number (nominally chosen as 0.01) we have the following two procedures (see app. G.3).

Procedure 4: $g \geqslant \delta_g d_F$, (i.e., $\vec{P}$ is not "too near" the perimeter of S).

1. $$F(1, 1, 1) = \int_{\ell_1}^{\ell_2} \frac{d\ell}{\sqrt{g^2 + \ell^2}} = \ln\left(\sqrt{\ell^2 + g^2} + \ell\right) \Big|_1^2$$

$$= \begin{cases} \ln\left(\dfrac{\sqrt{\ell_2{}^2 + g^2} + \ell_2}{\sqrt{\ell_1{}^2 + g^2} + \ell_1}\right); \; \ell_1, \ell_2 \geqslant 0 \\[2ex] \ln\left(\dfrac{\sqrt{\ell_1{}^2 + g^2} - \ell_1}{\sqrt{\ell_2{}^2 + g^2} - \ell_2}\right); \; \ell_1, \ell_2 < 0 \\[2ex] \ln\left(\dfrac{\left(\sqrt{\ell_1{}^2 + g^2} - \ell_1\right)\left(\sqrt{\ell_2{}^2 + g^2} + \ell_2\right)}{g^2}\right); \; \ell_2 \geqslant 0, \ell_1 < 0 \end{cases} \qquad \text{(D.60)}$$

where $g^2 \equiv \bar{a}^2 + h^2$. Note that $\rho = \sqrt{g^2 + \ell^2}$.

Here we have used three different (but equal) expressions for the evaluation of F(1, 1, 1) in order to avoid possible round off problems from cancellation of negative and positive numbers in the argument of the natural logarithm.

2. $$F(1, 1, K) = \frac{1}{g^2(K - 2)} \left[(K - 3)\, F(1, 1, K - 2) - \nu_\eta\, E(2, 1, K - 2)\right] + \nu_\xi\, E(1, 2, K - 2)];$$

K = 3, MXFK, 2. (MXFK is defined in equation (D.54). (D.61)

3. a. If $|\nu_\eta| \leqslant |\nu_\xi|$

(i) $$F(1, N, 1) = \frac{1}{(N - 1)} \Big[(2N - 3)\, \bar{a}\nu_\eta F(1, N - 1, 1) - (N - 2)\left(\bar{a}^2 + \nu_\xi{}^2 h^2\right) F(1, N - 2, 1) + \nu_\xi E(1, N - 1, -1)\Big] ;$$

N = 2, MXQ (D.62)

(ii)

$$F(M, N, 1) = \frac{-\nu_\eta}{\nu_\xi} F(M-1, N+1, 1) + \frac{\bar{a}}{\nu_\xi} F(M-1, N, 1);$$

$$M = 2, MXQ \text{ and } N = 1, MXQ - M + 1 \tag{D.63}$$

b. If $|\nu_\xi| \leqslant |\nu_\eta|$

(i)

$$F(M, 1, 1) = \frac{1}{(M-1)} \Big[(2M-3)\,\bar{a}\nu_\xi F(M-1, 1, 1) - (M-2)\left(\bar{a}^2 + \nu_\eta{}^2 h^2\right) F(M-2, 1, 1) - \nu_\eta E(M-1, 1, -1) \Big]$$

$$M = 2, MXQ \tag{D.64}$$

(ii)

$$F(M, N, 1) = \frac{-\nu_\xi}{\nu_\eta} F(M+1, N-1, 1) + \frac{\bar{a}}{\nu_\eta} F(M, N-1, 1);$$

$$N = 2, MXQ \quad \text{and} \quad M = 1, MXQ - N + 1 \tag{D.65}$$

4.
$$F(1, 2, K) = \nu_\eta \bar{a}\, F(1, 1, K) - \frac{\nu_\xi}{(K - 2)}\, E(1, 1, K - 2)$$
$$K = 3, MXK - 2, 2 \qquad \text{(D.66)}$$

5.
$$F(1, N, K) = 2\bar{a}\nu_\eta F(1, N - 1, K) - \left(\bar{a}^2 + \nu_\xi{}^2 h^2\right) F(1, N - 2, K)$$
$$+ \nu_\xi{}^2 F(1, N - 2, K - 2) \; ;$$
$$N = 3, MXQ \quad \text{and } K = 3, MXK - 2, 2 \qquad \text{(D.67)}$$

Procedure 5: $g < \delta_g d_F$, (i.e., $\vec{P}$ is close to the perimeter of S).

1.
$$F(1, 1, MXFK + NFK) = 0 \qquad \text{(See app. G.8)} \qquad \text{(D.68)}$$

where NFK is a positive integer (nominally taken as 16)

2.
$$F(1, 1, K - 2) = \frac{1}{(K - 3)} \left[g^2(K - 2)\ F(1, 1, K) + \nu_\eta E(2, 1, K - 2) - \nu_\xi E(1, 2, K - 2)\right] ;$$
$$K = MXFK + NFK, 5, 2 \qquad \text{(D.69)}$$

3. F (1, 1, 1) as well as other F integrals may be computed in the same manner as for procedure 4.

This completes the calculation of the H integrals.

D.4 EVALUATION OF SOURCE AND DOUBLET INTEGRALS FOR A DISTANT FIELD POINT

If the field point $\vec{P}$ is a large distance from S the approximation (D.18) may be replaced by an approximation based on this fact. Let

$$P = |\vec{P}| \quad \text{and} \quad Q = |\vec{Q}| \tag{D.70}$$

Then

$$\frac{1}{R} = \frac{1}{\sqrt{P^2 - 2\left(\vec{P} \cdot \vec{Q}\right) + Q^2}} = \frac{1}{P} \frac{1}{\sqrt{1 + \dfrac{-2\left(\vec{P} \cdot \vec{Q}\right) + Q^2}{P^2}}} \tag{D.71}$$

Let

$$\epsilon = \frac{1}{P} \underset{(\xi, \eta) \epsilon \Sigma}{\text{Max}} \{Q\} \tag{D.72}$$

Then

$$\left| \frac{-2\left(\vec{P} \cdot \vec{Q}\right) + Q^2}{P^2} \right| \leqslant 2\epsilon + \epsilon^2 \tag{D.73}$$

Hence, if

$$\epsilon << 1 \tag{D.74}$$

we have

$$\frac{1}{R^K} \approx \frac{1}{P^K} + \frac{K\left(\vec{P} \cdot \vec{Q}\right)}{P^{K+2}} - \frac{K}{2} \frac{1}{P^{K+2}} \left[Q^2 - (K+2) \frac{\left(\vec{P} \cdot \vec{Q}\right)^2}{P^2} \right] \tag{D.75}$$

Only the first three terms of the binominal expansion are displayed (monopole, dipole, and quadrapole). In practice this expansion is used only when ϵ is less than 1/5. All three terms are used unless ϵ is less than 1/8 in which case only the first two terms are required.

Substituting (D.75) into (D.10) and using hypothesis (D.6) we obtain for the source potential

$$\phi = \sigma_0 I(1, 1) + \sigma_\xi I(2, 1) + \sigma_\eta I(1, 2) \tag{D.76}$$

Here

$$I(M, N) = -\frac{1}{4\pi}\left\{\frac{1}{P}(E1) + \frac{1}{P^2}\left(\vec{E2}\cdot\hat{P}\right) + \frac{1}{P^3}\left[-\frac{1}{2}E3 + \frac{3}{2}\left(\hat{P}\cdot\bar{E4}\hat{P}\right)\right]\right\} \tag{D.77}$$

where

$$E1 = C(M, N) \tag{D.78}$$

$$\vec{E2} = \left[C(M + 1, N),\ C(M, N + 1),\ aC(M + 2, N) + bC(M, N + 2)\right] \tag{D.79}$$

$$E3 = C(M + 2, N) + C(M, N + 2) \tag{D.80}$$

$$\bar{E4} = \begin{pmatrix} C(M + 2, N) & C(M + 1, N + 1) & aC(M + 3, N) + bC(M + 1, N + 2) \\ C(M + 1, N + 1) & C(M, N + 2) & aC(M + 2, N + 1) + bC(M, N + 3) \\ aC(M + 3, N) + bC(M + 1, N + 2) & aC(M + 2, N + 1) + bC(M, N + 3) & 0 \end{pmatrix} \tag{D.81}$$

$$\hat{P} = \frac{\vec{P}}{P} \tag{D.82}$$

and

$$C(M, N) = \iint_{\Sigma} \xi^{M-1} \eta^{N-1} \, d\xi \, d\eta \tag{D.83}$$

In computing the elements of the matrix $\overline{E}4$ hypothesis (D.6) has been employed. The integrals C(M, N) will be computed later (see equation (D.94)). The induced source velocity may be obtained by differentiating equation (D.76), and is given by

$$\vec{v} = \sigma_0 \vec{J}(1, 1) + \sigma_\xi \vec{J}(2, 1) + \sigma_\eta \vec{J}(1, 2) \tag{D.84}$$

where

$$\vec{J}(M, N) = -\frac{1}{4\pi}\left\{\frac{-1}{P^2}\left(E1\hat{P}\right) + \frac{1}{P^3}\left[\overrightarrow{E2} - 3\left(\overrightarrow{E2} \cdot \hat{P}\right)\hat{P}\right]\right.$$
$$\left. + \frac{1}{P^4}\left[\frac{3}{2} E3\hat{P} - \frac{15}{2}\left(\hat{P} \cdot \overline{E}4\hat{P}\right)\hat{P} + 3\overline{E}4\hat{P}\right]\right\} \tag{D.85}$$

A similar expansion may be obtained for the doublet induced potential and velocity. Substituting the approximation (D.75) into equation (D.3) and using hypothesis (D.6) we obtain,

$$\phi = \mu_0 I(1, 1) + \mu_\xi I(2, 1) + \mu_\eta I(1, 2) + \frac{1}{2}\mu_{\xi\xi} I(3, 1) + \mu_{\xi\eta} I(2, 2) + \frac{1}{2}\mu_{\eta\eta} I(1, 3) \tag{D.86}$$

Here

$$I(M, N) = \frac{1}{4\pi}\left\{\frac{1}{P^2}\left(\overrightarrow{E2} \cdot \hat{P}\right) + \frac{1}{P^3}\left[- E3 + 3\left(\hat{P} \cdot \overline{E}4\hat{P}\right)\right]\right\} \tag{D.87}$$

where

$$\overrightarrow{E2} = \left[- 2aC(M + 1, N), \; - 2bC(M, N + 1), \; C(M, N)\right] \tag{D.88}$$

$$E3 = - aC(M + 2, N) - bC(M, N + 2) \tag{D.89}$$

and

$$\bar{E}4 = \begin{pmatrix} -2aC(M+2,N) & -(a+b)C(M+1,N+1) & \frac{1}{2}C(M+1,N) \\ -(a+b)\,C(M+1,N+1) & -2bC(M,N+2) & \frac{1}{2}C(M,N+1) \\ \frac{1}{2}C(M+1,N) & \frac{1}{2}C(M,N+1) & \begin{matrix} aC(M+2,N) \\ +\,bC(M,N+2) \end{matrix} \end{pmatrix} \qquad \text{(D.90)}$$

Note that these expressions differ from the $\overrightarrow{E2}$, E3 and $\bar{E}4$ given above for the source.

Again, hypothesis (D.6) has been used in the computation of the matrix $\bar{E}4$. The induced velocity may be obtained by differentiating equation (D.86) and is given by

$$\vec{v} = \mu_0\,\vec{J}(1,1) + \mu_\xi\,\vec{J}(2,1) + \mu_\eta\,\vec{J}(1,2) + \frac{1}{2}\mu_{\xi\xi}\,\vec{J}(3,1) + \mu_{\xi\eta}\,\vec{J}(2,2) + \frac{1}{2}\mu_{\eta\eta}\,\vec{J}(1,3) \qquad \text{(D.91)}$$

Here

$$\vec{J}(M,N) = \frac{1}{4\pi}\left\{\frac{1}{P^3}\left[\overrightarrow{E2} - 3\left(\overrightarrow{E2}\cdot\hat{P}\right)\hat{P}\right] + \frac{1}{P^4}\left[3E3\,\hat{P} - 15\left(\hat{P}\cdot\bar{E}4\hat{P}\right)\hat{P} + 6\bar{E}4\hat{P}\right]\right\} \qquad \text{(D.92)}$$

Note that the quadrapole term of expansion (D.75) is not used for doublet panel induced potential and velocity. This is primarily because of the complexity of this term and the resultant fact that evaluation of this term is only marginally more efficient than evaluation of doublet velocity and potential from the formulas of the previous sections.

The computation of the C(M, N) integrals of equation (D.78) follows from the computation of the H integrals of section (D.3) by noting that C(M, N) = H(M, N, 0) with x = y = 0. The range for the indices M and N is the same as that for the H integrals, i.e.,

$$M = 1, MXQ; \quad N = 1, MXQ - M + 1 \qquad \text{(D.93)}$$

where MXQ is given in (D.36). Setting K = 2 and x = y = 0 in equations (G.42) and (G.43) and adding these equations, we obtain

$$(M+N)\,C(M,N) = \sum_{1}^{4}\left[\nu_\xi\,F(M+1,N,0) + \nu_\eta\,F(M,N+1,0)\right]$$

Upon substituting equation (D.56) on the right we obtain

$$C(M, N) = \frac{1}{(M + N)} \sum_{1}^{4} \bar{a}G(M, N); \quad M = 1, MXQ \quad \text{and} \quad N = 1, MXQ - M + 1 \tag{D.94}$$

where

$$\begin{aligned} G(M, N) &= F(M, N, 0) \text{ (evaluated at } x = y = 0) \\ &= \int_L \xi^{M-1} \eta^{N-1} \, d\ell; \quad M = 1, MXQ \quad \text{and} \quad N = 1, MXQ - M + 1 \end{aligned} \tag{D.95}$$

The integrals G(M, N) may be obtained with the aid of two recursion relations. By setting $K = 0$ and $x = y = 0$ in equation (D.56) we have

$$\nu_\xi G(M + 1, N) + \nu_\eta G(M, N + 1) = \bar{a}G(M, N) \tag{D.96}$$

By setting $K = 2$ and $x = y = 0$ in equation (D.57) we obtain

$$-(M - 1)\,\nu_\eta G(M - 1, N) + (N - 1)\,\nu_\xi G(M, N - 1) = D(M, N) \tag{D.97}$$

where

$$\begin{aligned} D(M, N) &= E(M, N, 0) \text{ (evaluated at } x = y = 0) \\ &= \xi^{M-1} \eta^{N-1} \Big|_1^2 \end{aligned} \tag{D.98}$$

The quantities D(M, N) may be evaluated directly or else recursively with the aid of equation (D.59) (see app. G.5). The recursion relations (D.96) and (D.97) may be recombined to yield an efficient procedure for evaluating the G integrals. (see app. G.5).

Procedure 6:

1. a. If $|\nu_\eta| \leqslant |\nu_\xi|$

$$\text{(i) } G(1, N) = \frac{1}{N\nu_\xi} D(1, N + 1) : \quad N = 1, MXQ \tag{D.99}$$

(ii)

$$G(M, N) = -\frac{\nu_\eta}{\nu_\xi} G(M-1, N+1) + \frac{\bar{a}}{\nu_\xi} G(M-1, N) ;$$

$$M = 2, MXQ \quad \text{and} \quad N = 1, MXQ - M + 1 \tag{D.100}$$

b. If $|\nu_\xi| < |\nu_\eta|$

(i)

$$G(M, 1) = -\frac{1}{M\nu_\eta} D(M+1, 1);\ M = 1, MXQ \tag{D.101}$$

(ii)

$$G(M, N) = -\frac{\nu_\xi}{\nu_\eta} G(M+1, N-1) + \frac{\bar{a}}{\nu_\eta} G(M, N-1);$$

$$N = 2, MXQ \quad \text{and} \quad M = 1, MXQ - N + 1 \tag{D.102}$$

This completes the evaluation of the source and doublet potential and velocity for a distant field point.

D.5 BEHAVIOR OF INDUCED POTENTIAL AND VELOCITIES

In this section we shall study the behavior of the potential and velocity induced by source and doublet panels. We shall restrict our attention to flat panels since the addition of curvature produces no qualitative change in behavior. First, consider the potential ϕ induced by a flat source panel. Setting a and b zero in equations (D.10), (D.15) and (D.16) we obtain

$$\phi = \iint_\Sigma \sigma \left(\frac{-1}{4\pi R}\right) d\xi d\eta \tag{D.103}$$

where

$$R = \sqrt{(\xi - x)^2 + (\eta - y)^2 + h^2} = \rho$$

and

$$h = z$$

We note from (D.103) that ϕ is regular everywhere in finite space except perhaps on Σ. From equation (D.75) we see that near infinity

$$\phi = -\frac{1}{4\pi} \iint_{\Sigma} \sigma d\xi d\eta \cdot \frac{1}{P} + 0\left(\frac{1}{P^2}\right) \tag{D.104}$$

Since ϕ vanishes as $1/P$ near $P = \infty$, ϕ is regular at infinity as well. To examine the behavior of ϕ near Σ we use equations (D.20) and (D.22) with $a = b = 0$.

Then

$$\begin{aligned} \phi = \sigma(x, y)&\left[-\frac{1}{4\pi}H(1, 1, 1)\right] \\ &+ \sigma_x(x, y)\left[-\frac{1}{4\pi}H(2, 1, 1)\right] + \sigma_y(x, y)\left[\frac{-1}{4\pi}H(1, 2, 1)\right] \end{aligned} \tag{D.105}$$

Appendix G.6 shows that h^J H(M, N, K) is continuous near Σ and equal to zero on Σ if $J + M + N > K$, and h^J H(M, N, K) is bounded there if $J + M + N = K$. Consequently, ϕ is continuous everywhere, in particular on Σ.

From equation (D.103) we have

$$\vec{v} = \vec{\nabla}\phi = \iint_{\Sigma} \sigma\left(\frac{-\vec{R}}{4\pi R^3}\right) d\xi d\eta \tag{D.106}$$

Equation (D.106) shows $\vec{v}$ is regular everywhere in finite space except perhaps on Σ. From equation (D.104), we see that near infinity

$$\vec{v} = \frac{1}{4\pi} \iint_{\Sigma} \sigma d\xi d\eta \cdot \frac{\vec{P}}{P^3} + O\left(\frac{1}{P^3}\right) \tag{D.107}$$

so that $\vec{v} = 0(1/P^3)$ if total source strength is zero and $\vec{v} = 0(1/P^2)$ otherwise.

The behavior of $\vec{v}$ near Σ will now be examined. For this purpose one can use equations (D.27) and (D.28) with $a = b = 0$. However, it is more instructive to derive an alternate expression for $\vec{v}$. Differentiating equation (D.103) with respect to x we obtain

$$\frac{\partial\phi}{\partial x} = \iint_{\Sigma} \sigma \frac{\partial}{\partial x}\left(\frac{-1}{4\pi R}\right) d\xi d\eta = \iint_{\Sigma} \sigma \frac{\partial}{\partial \xi}\left(\frac{1}{4\pi R}\right) d\xi d\eta \tag{D.108}$$

Integrating by parts we obtain

$$\frac{\partial\phi}{\partial x} = -\iint\limits_{\Sigma} \frac{\partial\sigma}{\partial\xi}\left(\frac{1}{4\pi R}\right) d\xi d\eta + \sum_{1}^{4} \int\limits_{L} \sigma\left(\frac{\nu_\xi}{4\pi R}\right) d\ell \tag{D.109}$$

Similarly

$$\frac{\partial\phi}{\partial y} = -\iint\limits_{\Sigma} \frac{\partial\sigma}{\partial\eta}\left(\frac{1}{4\pi R}\right) d\xi d\eta + \sum_{1}^{4} \int\limits_{L} \sigma\left(\frac{\nu_\eta}{4\pi R}\right) d\ell \tag{D.110}$$

Finally

$$\frac{\partial\phi}{\partial z} = \iint\limits_{\Sigma} \sigma\left(\frac{h}{4\pi R^3}\right) d\xi d\eta \tag{D.111}$$

Combining all three equations we have

$$\vec{v} = \left(\frac{\partial\phi}{\partial x}, \frac{\partial\phi}{\partial y}, \frac{\partial\phi}{\partial z}\right) = \vec{v}_A + \sum_{1}^{4} \vec{v}_B + \vec{v}_C \tag{D.112}$$

where

$$\vec{v}_A = -\iint\limits_{\Sigma} \left(\frac{\partial\sigma}{\partial\xi}, \frac{\partial\sigma}{\partial\eta}, 0\right)\left(\frac{1}{4\pi R}\right) d\xi d\eta \tag{D.113}$$

$$\vec{v}_B = \int\limits_{L} \left(\nu_\xi, \nu_\eta, 0\right) \sigma\left(\frac{1}{4\pi R}\right) d\ell \tag{D.114}$$

$$\vec{v}_C = \iint\limits_{\Sigma} (0, 0, 1)\, \sigma\left(\frac{h}{4\pi R^3}\right) d\xi d\eta \tag{D.115}$$

(Note that $\vec{v}_A$ here is not the same quantity as the average velocity of equation (C.5).)

First consider the vector $\vec{v}_A$. From equations (D.113), (D.8), (D.22), (D.25), and (D.15) we have

$$\vec{v}_A = \left[\sigma_x(x, y), \sigma_y(x, y), 0\right]\left[\frac{-1}{4\pi} H(1, 1, 1)\right] \tag{D.116}$$

Again H(1, 1, 1) is continuous everywhere, hence $\vec{v}_A$ is continuous everywhere.

Consider $\vec{v}_B$ for a typical side L of Σ. Note first that if L is a common edge of Σ and an adjacent panel across which source strength is continuous and the surface slopes are continuous (i.e., $(\nu_\xi, \nu_\eta, 0)$ of L = $-(\nu_\xi, \nu_\eta, 0)$ of the adjacent panel) then the behavior of $\vec{v}_B$ is irrelevant since $\vec{v}_B$ is cancelled by the same component of the adjacent panel induced velocity. In any event, the behavior of $\vec{v}_B$ can be established as follows. From equations (D.114), (D.22), (D.15), and (D.40) we have

$$\vec{v}_B = (\nu_\xi, \nu_\eta, 0)\left[\sigma(x, y)\frac{F(1, 1, 1)}{4\pi} + \sigma_x(x, y)\frac{F(2, 1, 1)}{4\pi} + \sigma_y(x, y)\frac{F(1, 2, 1)}{4\pi}\right] \tag{D.117}$$

In appendix G.6 we show that $g^J F(M, N, K)$ is continuous everywhere if $J + M + N > K + 1$. Therefore, any discontinuity in $\vec{v}_B$ must arise from F(1, 1, 1). Again, from equation (D.40) F(1, 1, 1) is continuous everywhere except possibly on L, where g = 0. From equation (D.60) we derive the following asymptotic formulas for F(1, 1, 1) as $\vec{P}$ approaches a point $\vec{P}_L \in L$.

$$F(1, 1, 1) \sim \begin{cases} \ln(1/g^2) \ ; & \vec{P}_L \text{ in the interior of L (at } \ell) \\ \ln(1/\rho) \ ; & \ell_1 \cdot \ell_2 \geqslant 0 \text{ and } \vec{P}_L \text{ at endpoint of L} \\ \ln(\rho/g^2) \ ; & \ell_2 \cdot \ell_1 < 0 \text{ and } \vec{P}_L \text{ at endpoint of L} \end{cases} \tag{D.118}$$

Here $\rho = |\vec{P} - \vec{P}_L| = \sqrt{g^2 + \ell^2}$. We see that $\vec{v}_B$ has a logarithmic singularity on L which is proportional to local source strength.

Finally, we obtain from equations (D.115), (D.22) and (D.25) that

$$\vec{v}_C = (0, 0, 1)\left[\sigma(x, y)\frac{hH(1, 1, 3)}{4\pi} + \sigma_x(x, y)\frac{hH(2, 1, 3)}{4\pi} + \sigma_y(x, y)\frac{hH(1, 2, 3)}{4\pi}\right] \tag{D.119}$$

Any possible discontinuity in $\vec{v}_C$ must arise from the term $\frac{hH(1, 1, 3)}{4\pi}$ and can only occur on Σ. From equation (G.24) we have

$$\frac{hH(1, 1, 3)}{4\pi} = \frac{1}{4\pi}\left(\frac{h}{|h|}\right)\sum_{1}^{4}\tan^{-1}\left[\bar{a}(\ell_2 c_1 - \ell_1 c_2),\ c_1 c_2 + \bar{a}^2 \ell_1 \ell_2\right] \qquad \text{(D.120)}$$

One can show (see sec. G.1 of app. G) that the sum of arctangents on the right is continuous everywhere except on the perimeter of Σ where it remains bounded. Moreover, when $h \rightarrow 0$ this sum approaches the value 2π inside Σ and 0 outside Σ. Consequently, as $h \rightarrow 0$, $\frac{hH(1, 1, 3)}{4\pi}$ approaches 0 outside Σ, 1/2 on the upper surface of Σ and -1/2 on the lower surface of Σ. $\frac{hH(1, 1, 3)}{4\pi}$ is defined to be zero on Σ (actually when $(x, y) \in \Sigma$ and $|h| < \delta_0 d_H$ where δ_0 is nominally chosen as 10^{-8}) and this results in the computation of an average velocity on Σ as discussed in section D.3. The discontinuities of $\vec{v}_C$ are essentially the same except for the proportionality factor $\sigma(x, y)$. Note that this behavior gives the first term on the righthand side of equation (C.10).

The behavior of $\vec{v}$ in finite space can be summarized as follows. The normal component of $\vec{v}$ is bounded everywhere but discontinuous on Σ. As the field point approaches the source panel plane, this component is zero outside Σ, equal to 1/2 local source strength on the upper side of Σ and -1/2 local source strength on the lower side of Σ. (This component is defined to be zero on Σ.) The tangential components of $\vec{v}$ are continuous everywhere except on each edge L of Σ. As the field point $\vec{P}$ approaches a point $\vec{P}_L$ in the interior of L, $\vec{v}$ has the following singular behavior due to the characteristics of $\vec{v}_B$:

$$\vec{v} \sim \frac{-2\sigma \log(g)\, \hat{\ell} \oplus \hat{n}}{4\pi} \qquad \text{(D.121)}$$

Here σ is the source strength at $\vec{P}_L$, $\hat{n}$ is the normal to Σ at $\vec{P}_L$, $\hat{\ell}$ is a unit vector along L such that $\hat{\ell} \otimes \hat{n}$ points out of Σ and g is the distance from $\vec{P}$ to the line containing L. If $\vec{P}$ approaches a point $\vec{P}_L$ at a corner of Σ, the singular behavior of $\vec{v}$ is derived by summing the singular contributions of the two intersecting edges. These contributions are described by the right side of equation (D.121) with but slight modification to the factor $-2 \log(g)$ arising from the alternate expressions of equation (D.118).

Next we consider the potential ϕ induced by a flat doublet panel. Setting a and b zero in equation (D.3) we have

$$\phi = \iint_{\Sigma} \mu \left(\frac{h}{4\pi R^3}\right) d\xi d\eta \qquad \text{(D.122)}$$

We note from (D.122) that ϕ is regular everywhere in finite space except perhaps on Σ. From equation (D.75) we see that near infinity

$$\phi = \frac{1}{4\pi} \iint_{\Sigma} \mu d\xi d\eta \cdot \frac{h}{P^3} + O\left(1/P^3\right) \qquad \text{(D.123)}$$

so that ϕ is regular at infinity as well.

To examine the behavior of ϕ near Σ we use equations (D.33) and (D.34) with a = b = 0. Then

$$\phi = \mu(x, y) \left[\frac{h}{4\pi} H(1, 1, 3)\right] + \mu_x(x, y) \left[\frac{h}{4\pi} H(2, 1, 3)\right]$$

$$+ \mu_y(x, y) \left[\frac{h}{4\pi} H(1, 2, 3)\right] + \frac{1}{2} \mu_{xx}(x, y) \left[\frac{h}{4\pi} H(3, 1, 3)\right]$$

$$+ \mu_{xy}(x, y) \left[\frac{h}{4\pi} H(2, 2, 3)\right] + \frac{1}{2} \mu_{yy}(x, y) \left[\frac{h}{4\pi} H(1, 3, 3)\right] \qquad \text{(D.124)}$$

Any possible discontinuity in ϕ must arise from the first term on the right. We have already analyzed $\frac{hH(1, 1, 3)}{4\pi}$ in connection with equation (D.120). Consequently, we can say that ϕ is bounded in a neighborhood of Σ. Moreover, as the field point approaches the doublet panel plane ϕ is zero outside Σ equal to 1/2 local doublet strength on the upper surface and -1/2 local doublet strength on the lower surface of Σ. (ϕ is defined as zero on Σ.)

From equation (D.122) we have $\vec{v} = \vec{\nabla}\phi = \iint_{\Sigma} \mu \left[\frac{(0, 0, 1)}{4\pi R^3} + \frac{3h\vec{R}}{4\pi R^5}\right] d\xi d\eta$ (D.125)

Equation (D.125) shows that $\vec{v}$ is regular everywhere in finite space except perhaps on Σ. From equation (D.123) we see that near infinity

$$\vec{v} = \frac{1}{4\pi} \iint_{\Sigma} \mu d\xi d\eta \cdot \left[\frac{(0, 0, 1)}{P^3} - \frac{3h\vec{P}}{P^5}\right] + O\left(\frac{1}{P^4}\right) \qquad \text{(D.126)}$$

so that $\vec{v} = 0(1/P^4)$ if total doublet strength is zero and $\vec{v} = 0(1/P^3)$ otherwise.

The behavior of $\vec{v}$ near Σ will now be examined. Differentiating equation (D.122) with respect to x we have

$$\frac{\partial\phi}{\partial x} = \iint\limits_{\Sigma} \mu \frac{\partial}{\partial x}\left(\frac{h}{4\pi R^3}\right) d\xi d\eta = -\iint\limits_{\Sigma} \mu \frac{\partial}{\partial \xi}\left(\frac{h}{4\pi R^3}\right) d\xi d\eta$$

$$= -\int\limits_{L} \mu \left(\frac{h}{4\pi R^3}\right)\nu_\xi d\ell + \iint\limits_{\Sigma} \frac{\partial\mu}{\partial\xi}\left(\frac{h}{4\pi R^3}\right) d\xi d\eta \tag{D.127}$$

Similarly

$$\frac{\partial\phi}{\partial y} = -\int\limits_{L} \mu \left(\frac{h}{4\pi R^3}\right) \nu_\eta d\ell + \iint\limits_{\Sigma} \frac{\partial\mu}{\partial\eta}\left(\frac{h}{4\pi R^3}\right) d\xi d\eta \tag{D.128}$$

Finally

$$\frac{\partial\phi}{\partial z} = \iint\limits_{\Sigma} \mu \frac{\partial}{\partial h}\left(\frac{h}{4\pi R^3}\right) d\xi d\eta$$

$$= -\iint\limits_{\Sigma} \mu \left[\frac{\partial}{\partial\xi}\left(\frac{(\xi - x)}{4\pi R^3}\right) + \frac{\partial}{\partial\eta}\left(\frac{(\eta - y)}{4\pi R^3}\right)\right] d\xi d\eta$$

$$= -\int\limits_{L} \mu \left[\frac{(\xi - x)}{4\pi R^3}\nu_\xi + \frac{(\eta - y)}{4\pi R^3}\nu_\eta\right] d\ell$$

$$+ \iint\limits_{\Sigma} \left[\frac{\partial\mu}{\partial\xi}\frac{(\xi - x)}{4\pi R^3} + \frac{\partial\mu}{\partial\eta}\frac{(\eta - y)}{4\pi R^3}\right] d\xi d\eta$$

$$= -\int\limits_{L} \mu \frac{\bar{a}}{4\pi R^3} d\ell - \iint\limits_{\Sigma} \left[\frac{\partial\mu}{\partial\xi}\frac{\partial}{\partial\xi}\left(\frac{1}{4\pi R}\right) + \frac{\partial\mu}{\partial\eta}\frac{\partial}{\partial\eta}\left(\frac{1}{4\pi R}\right)\right] d\xi d\eta$$

$$= -\int\limits_{L} \mu \frac{\bar{a}}{4\pi R^3} d\ell - \int\limits_{L} \left[\frac{\partial\mu}{\partial\xi}\nu_\xi + \frac{\partial\mu}{\partial\eta}\nu_\eta\right]\frac{1}{4\pi R} d\ell$$

$$+ \iint\limits_{\Sigma} \left[\frac{\partial^2\mu}{\partial\xi^2} + \frac{\partial^2\mu}{\partial\eta^2}\right]\frac{1}{4\pi R} d\xi d\eta \tag{D.129}$$

Combining all three equations we have

$$\vec{v} = \left(\frac{\partial\phi}{\partial x}, \frac{\partial\phi}{\partial y}, \frac{\partial\phi}{\partial z}\right) = \vec{v}_A + \sum_1^4 \vec{v}_B + \sum_1^4 \vec{v}_C + \vec{v}_D \tag{D.130}$$

where

$$\vec{v}_A = \iint_\Sigma (0, 0, 1)\left[\frac{\partial^2\mu}{\partial\xi^2} + \frac{\partial^2\mu}{\partial\eta^2}\right]\frac{1}{4\pi R}\, d\xi d\eta \tag{D.131}$$

$$\vec{v}_B = \int_L (-h\nu_\xi, -h\nu_\eta, -\bar{a})\ \mu \frac{1}{4\pi R^3}\, d\ell \tag{D.132}$$

$$\vec{v}_C = \int_L (0, 0, -1)\left[\frac{\partial\mu}{\partial\xi}\nu_\xi + \frac{\partial\mu}{\partial\eta}\nu_\eta\right]\frac{1}{4\pi R}\, d\ell \tag{D.133}$$

$$\vec{v}_D = \iint_\Sigma \left(\frac{\partial\mu}{\partial\xi}, \frac{\partial\mu}{\partial\eta}, 0\right)\frac{h}{4\pi R^3}\, d\xi d\eta \tag{D.134}$$

(Note that $\vec{v}_D$ is not the same as the difference velocity of equation (C.6).)

First consider the vector $\vec{v}_A$. From equations (D.131), (D.9), (D.25), and (D.31) we have

$$\vec{v}_A = (0, 0, 1)\left[\mu_{xx}(x, y) + \mu_{yy}(x, y)\right]\left[\frac{1}{4\pi}\, H(1, 1, 1)\right] \tag{D.135}$$

Again H(1, 1, 1) is continuous everywhere, hence $\vec{v}_A$ is continuous everywhere.

Next consider $\vec{v}_B$ for a typical side L of Σ. Note first that if L is a common edge of Σ and an adjacent panel across which doublet strength is continuous then the behavior of $\vec{v}_B$ is irrelevant since $\vec{v}_B$ is cancelled by the same component of the adjacent panel induced velocity. In any event the behavior of $\vec{v}_B$ can be established as follows. From its definition $\vec{v}_B$ is clearly continuous except possibly on L. To examine the behavior of $\vec{v}_B$ on L we have from equations (D.132), (D.9), (D.31), and (D.40) that

$$\vec{v}_B = \left(\frac{-h\nu_\xi}{g}, \frac{-h\nu_\eta}{g}, \frac{-\bar{a}}{g} \right) \left[\mu(x, y) \frac{gF(1, 1, 3)}{4\pi} \right.$$

$$+ \mu_x(x, y) \frac{gF(2, 1, 3)}{4\pi} + \mu_y(x, y) \frac{gF(1, 2, 3)}{4\pi}$$

$$\left. + \frac{1}{2} \mu_{xx}(x, y) \frac{gF(3, 1, 3)}{4\pi} + \mu_{xy}(x, y) \frac{gF(2, 2, 3)}{4\pi} + \frac{1}{2} \mu_{yy}(x, y) \frac{F(1, 3, 3)}{4\pi} \right] \tag{D.136}$$

The direction of $\vec{v}_B$ is the unit vector

$$\left(\frac{-h\nu_\xi}{g}, \frac{-h\nu_\eta}{g}, \frac{-\bar{a}}{g} \right) = \frac{\hat{\ell} \otimes \left(\vec{P}_L - \vec{P} \right)}{|\hat{\ell} \otimes \left(\vec{P}_L - \vec{P} \right)|} \tag{D.137}$$

Here $\hat{\ell}$ is the unit vector $(-\nu_\eta, \nu_\xi, 0)$ along L and $\vec{P}_L$ is the closest point on L to $\vec{P}$. The magnitude of $\vec{v}_B$ is the term in the square brackets on the right side of equation (D.136). The second and third terms are bounded and the last three terms are continuous in a neighborhood of L. However, the first term is unbounded as $\vec{P}$ approaches L. From equation (D.61) we have the following asymptotic formulas for the coefficient of $\mu(x, y)$ as $\vec{P}$ approaches $\vec{P}_L$ and L.

$$gF(1, 1, 3) \sim \begin{cases} \dfrac{2}{g} \; ; \; \vec{P}_L \text{ in the interior of L} \\[2ex] \dfrac{g}{\rho^2} \left[\dfrac{1}{1 + \sqrt{1 - g^2/\rho^2}} \right] ; \; \ell_1 \cdot \ell_2 \geqslant 0 \text{ and } \vec{P}_L \text{ at endpoint of L} \\[2ex] \dfrac{1}{g} \left[1 + \sqrt{1 - g^2/\rho^2} \right] ; \; \ell_1 \cdot \ell_2 < 0 \text{ and } \vec{P}_L \text{ at endpoint of L} \end{cases} \tag{D.138}$$

Consequently $\vec{v}_B$ becomes unbounded as the reciprocal of the distance from $\vec{P}$ to L.

Next we consider $\vec{v}_C$ for a typical side L of Σ. Note first that if L is a common edge of Σ and an adjacent panel across which the derivative of μ perpendicular to L and surface slope are continuous then the behavior of $\vec{v}_C$ is irrelevant since $\vec{v}_C$ is cancelled by the same component of the adjacent panel induced velocity. $\vec{v}_C$ is clearly continuous except perhaps on L. From equations (D.133), (D.9), (D.31), and (D.40) we have

$$\vec{v}_C = (0, 0, -1) \left\{ \left[\mu_x(x, y)\, \nu_\xi + \mu_y(x, y)\, \nu_\eta\right] \frac{F(1, 1, 1)}{4\pi} \right.$$

$$+ \left[\mu_{xx}(x, y)\, \nu_\xi + \mu_{xy}(x, y)\, \nu_\eta\right] \frac{F(2, 1, 1)}{4\pi}$$

$$\left. + \left[\mu_{xy}(x, y)\, \nu_\xi + \mu_{yy}(x, y)\, \nu_\eta\right] \frac{F(1, 2, 1)}{4\pi} \right\} \tag{D.139}$$

Any discontinuity in $\vec{v}_C$ must come from the factor F(1, 1, 1). The asymptotic behavior of this function is displayed in equation (D.118). We see then that the normal component of $\vec{v}_C$ has a logarithmic singularity on L proportional to the local derivative of μ in a direction perpendicular to L.

Finally, we consider $\vec{v}_D$. Clearly $\vec{v}_D$ is continuous except perhaps on Σ. From equations (D.134), (D.9), (D.31), and (D.24), we have

$$\vec{v}_D = \left[\mu_x(x, y),\ \mu_y(x, y),\ 0\right] \left[\frac{hH(1, 1, 3)}{4\pi}\right]$$

$$+ \left[\mu_{xx}(x, y),\ \mu_{xy}(x, y),\ 0\right] \left[\frac{hH(2, 1, 3)}{4\pi}\right]$$

$$+ \left[\mu_{xy}(x, y),\ \mu_{yy}(x, y),\ 0\right] \left[\frac{hH(1, 2, 3)}{4\pi}\right] \tag{D.140}$$

The quantities hH(2, 1, 3) and hH(1, 2, 3) are continuous everywhere, however, $\frac{hH(1, 1, 3)}{4\pi}$ is discontinuous on Σ as discussed previously (equation (D.120)). The behavior of $\vec{v}_D$ is essentially the same except for a proportionality factor $\vec{\nabla}\mu(x, y)$.

The behavior of $\vec{v}$ in finite space can be summarized as follows. $\vec{v}$ is continuous everywhere in finite space except perhaps on Σ. As a field point $\vec{P}$ approaches a point $\vec{P}_\Sigma$ in the interior of Σ the normal component of $\vec{v}$ is continuous at P_Σ but the tangential components approach $1/2\vec{\nabla}\mu$ at $\vec{P}_\Sigma$ if $\vec{P}$ approaches Σ from above and $-1/2\vec{\nabla}\mu$ at $\vec{P}_\Sigma$ if $\vec{P}$ approaches Σ from below. (The tangential components of $\vec{v}$ are defined to be 0 on Σ so that they are zero everywhere in the plane of Σ.) Note that it is this behavior that gives the second term on the righthand side of equation (C.10).

As a field point $\vec{P}$ approaches a point $\vec{P}_L$ in the interior of an edge L of Σ, $\vec{v}$ has the following singular behavior due to the characteristics of $\vec{v}_B$ and $\vec{v}_C$ discussed above:

$$\vec{v} \sim \frac{2\mu}{4\pi g} \hat{\ell} \otimes \hat{g} + \frac{2\hat{\ell} \bullet (\hat{n} \otimes \vec{\nabla} \mu)}{4\pi} \log(g)\, \hat{n} + \text{bounded terms} \tag{D.141}$$

Here μ is doublet strength and $\vec{\nabla}\mu$ doublet gradient at $\vec{P}_L$. $\hat{n}$ is the unit normal to Σ at $\vec{P}_L$, $\hat{\ell}$ is a unit vector along L such that $\hat{\ell} \otimes \hat{n}$ points out of Σ and $\vec{g} = g\hat{g}$ is the vector from $\vec{P}$ to the closest point on the line containing L. If $\vec{P}$ approaches a point $\vec{P}_L$ at a corner of Σ, the asymptotic behavior of $\vec{v}$ is derived by summing the contributions of the two intersecting edges. These contributions are described by the right side of equation (D.141) with but slight modification to the factors 2/g and 2 log(g), arising from the alternate forms in equations (D.138) and (D.118) respectively.

D.6 DERIVATION OF BOUNDARY VALUE PROBLEM INFLUENCE COEFFICIENT EQUATIONS

In section D.2 we derived the expressions for perturbation potential and velocity due to source or doublet panels. These expressions are in terms of the panel singularity distribution coefficients of equations (D.8) and (D.9). Before boundary conditions can be imposed, these expressions must be re-expressed in terms of the unknown singularity parameters $\bar{\lambda}$ of appendix B. In this section we describe how this is done for the specific case of the velocities due to a doublet/analysis network.

From equations (D.33) and (D.31) we obtain

$$\vec{v} = \lfloor \vec{J} \rfloor \begin{Bmatrix} \mu_o \\ \mu_\xi \\ \mu_\eta \\ \mu_{\xi\xi} \\ \mu_{\xi\eta} \\ \mu_{\eta\eta} \end{Bmatrix} \tag{D.142}$$

where

$$\lfloor \vec{J} \rfloor = \left[\begin{array}{c:c:c:c:c:c} \vec{J}(1,1) & x\vec{J}(1,1) & y\vec{J}(1,1) & \frac{1}{2}x^2\vec{J}(1,1) & xy\vec{J}(1,1) & \frac{1}{2}y^2\vec{J}(1,1) \\ & +\vec{J}(2,1) & +\vec{J}(1,2) & +x\vec{J}(2,1) & +y\vec{J}(2,1) & +y\vec{J}(1,2) \\ & & & +\frac{1}{2}\vec{J}(3,1) & +x\vec{J}(1,2) & +\frac{1}{2}\vec{J}(1,3) \\ & & & & +\vec{J}(2,2) & \end{array} \right]$$

Using equation (D.34), the scalar form of equation (D.142) is

$$\begin{Bmatrix} \vec{v}_x \\ \vec{v}_y \\ \vec{v}_z \end{Bmatrix} = \left[\begin{array}{c:c:c} J_x(1,1) & x\,J_x(1,1) + J_x(2,1) & \\ J_y(1,1) & x\,J_y(1,1) + J_y(2,1) & \text{----etc.----} \\ J_z(1,1) & x\,J_z(1,1) + J_z(2,1) & \end{array}\right] \begin{Bmatrix} \mu_o \\ \mu_\xi \\ \mu_\eta \\ \mu_{\xi\xi} \\ \mu_{\xi\eta} \\ \mu_{\eta\eta} \end{Bmatrix} \tag{D.143}$$

Equation (D.142) gives the velocity at field point i (i.e., at x_i, y_i, z_i) due to the doublet distribution

$$\mu(\xi,\eta) = \mu_0 + \mu_\xi\,\xi + \mu_\eta\eta + \frac{1}{2}\,\mu_{\xi\xi}\,\xi^2 + \mu_{\xi\eta}\,\xi\eta + \frac{1}{2}\,\mu_{\eta\eta}\,\eta^2$$

associated with a particular panel. If we label this panel as panel number k, we rewrite equation (D.142) as

$$\vec{v}_i^{\,k} = \lfloor \vec{J} \rfloor_k \begin{Bmatrix} \mu_o \\ \vdots \\ \mu_{\eta\eta} \end{Bmatrix}_k \tag{D.144}$$

From appendix B, recall that the six unknown doublet strength coefficients $\mu_0 \rightarrow \mu_{\eta\eta}$ for panel k are expressed in terms of a subset of the unknown doublet singularity parameters $\overline{\lambda}$; denote this subset as λ_j. From equations (B.3) and (B.6) we have

$$\begin{array}{ccccc} 6\text{x}1 & & 6\text{x}N_D & & N_D\text{x}1 \\ \begin{Bmatrix} \mu_o \\ \vdots \\ \mu_{\eta\eta} \end{Bmatrix}_k & = & \left[\,\bar{B}\,\right]_k & & \left\{\lambda_j\right\}_k \end{array} \tag{D.145}$$

where N_D is the number of doublet singularity parameters associated with panel k. Equations (D.144) and (D.145) give

$$\vec{v}_{i(j)}^{\;k} = \lfloor \vec{J} \rfloor_k \;\; [\bar{B}]_k \;\; \{\lambda_j\}_k \tag{D.146}$$

where the subscript (j) is used to indicate that the velocity due to the single panel k depends on several singularity parameters λ_j.

Now imagine that the network contains nine panels (e.g., as in the type 2 schematic of figure B.2). Then the velocity at point i due to these nine panels, and the free-stream velocity $\vec{V}_\infty$, is

$$\vec{v}_i = \vec{V}_\infty + \sum_{k=1}^{9} \vec{v}_{i(j)}{}^k = \vec{V}_i(\lambda) \qquad \text{(D.147)}$$

where $\vec{V}_i(\lambda)$ denotes that the velocity is now in terms of all the singularity parameters associated with the network. For the case of figure B.2, type 2, there are 25 singularity parameters.

Next, let the field point i be one of the 25 control points on the network (see fig. C.1, type 2). Imposing the boundary condition $\vec{V}_i \cdot \hat{n}_i = 0$ (where $\hat{n}_i$ is the unit normal at control point i) at each of these control points gives

$$\sum_{k=1}^{25} \vec{v}_{i(j)}{}^k \cdot \hat{n}_i = -\vec{V}_\infty \cdot \hat{n}_i \qquad i = 1, \ldots 25 \qquad \text{(D.148)}$$

When cast in matrix form, equation (D.148) becomes

$$\overset{25 \times 25}{\left[A_{ij}\right]} \begin{Bmatrix} \lambda_1 \\ \vdots \\ \lambda_{25} \end{Bmatrix} = - \begin{Bmatrix} \vec{V}_\infty \cdot \hat{n}_1 \\ \vdots \\ \vec{V}_\infty \cdot \hat{n}_{25} \end{Bmatrix} \qquad \text{(D.149)}$$

Each row i of the aerodynamic influence coefficient matrix $[A_{ij}]$ represents a boundary condition imposed at one of the 25 control points. Each column j corresponds to one of the 25 singularity parameters in $\{\lambda\}$. The matrix $[A_{ij}]$ is constructed one row (control point) at a time. For each row, one cycles through the panels and enters the contributions of each panel to the appropriate columns of $[A_{ij}]$.

For more than a single network, the procedure is exactly the same except that the matrices in equation (D.149) expand in size so as to incorporate all the panels, all the singularity parameters, and all the control points of every network. The general form of equation (D.149) is then

$$\overset{M \times M}{[\bar{A}]} \; \overset{M \times 1}{\{\bar{\lambda}\}} = \overset{M \times 1}{\{\bar{b}\}} \qquad \text{(D.150)}$$

where M is the total number of singularity parameters (and control points) for all the networks. Hence $\{\bar{\lambda}\}$ can be solved for, and then the resulting velocities can be calculated from equation (D.147). (The value $k = 9$ appearing in equation (D.147) would be replaced with the total number of panels in all the networks.) Knowing the velocities, the pressures, forces and moments are then computed as shown in appendix F.

APPENDIX E
EQUATION SOLUTION

In this appendix we give a brief description of the numerical method used in the pilot code to solve the influence coefficient equation set. This equation set is denoted in matrix form by

$$\overline{A}\overline{X} = \overline{B} \tag{E.1}$$

where $\overline{A}$ is an NxN matrix of coefficients, $\overline{B}$ is an NxM matrix of righthand sides and $\overline{X}$ is an NxM matrix of unknowns. The method assumes that the matrix $\overline{A}$ resides in mass storage in such a manner that each row is a record which can be accessed in a sequential manner only. The matrix $\overline{B}$ is also assumed to be stored in the same way and once the matrix $\overline{X}$ has been computed it is likewise stored in the same way.

For large values of N, the data transfers to and from mass storage during solution became excessive if the row storage format is retained. Hence, the method begins by reformatting the $\overline{A}$ and $\overline{B}$ matrices in block form. Specifically, the matrices $\overline{A}$ and $\overline{B}$ are partitioned into blocks (e.g., fig. E.1)

$$\overline{A} = \overline{A}_{ij} \; ; \quad i = 1, n \quad \text{and} \quad j = 1, n \tag{E.2}$$

$$\overline{B} = \overline{B}_{ij} \; ; \quad i = 1, n \quad \text{and} \quad j = 1, m \tag{E.3}$$

which are stored as randomly accessible records. The values of n and m are determined by the available central memory.

The Crout decomposition algorithm is then used to solve equation (E.1). This algorithm employs the substitution

$$\overline{L}\overline{U} = \overline{A} \tag{E.4}$$

to obtain

$$\overline{L}\overline{Y} = \overline{B} \tag{E.5}$$

where

$$\overline{U}\overline{X} = \overline{Y} \tag{E.6}$$

The matrix $\overline{L}$ is lower triangular and $\overline{U}$ is upper triangular normalized by ones along the diagonal. The decomposition of equation (E.4) is accomplished as follows. The matrices $\overline{L}$ and $\overline{U}$ must satisfy the relationship

$$\sum_{k=1}^{N} \ell_{ik} u_{kj} = a_{ij} \tag{E.7}$$

$$\underset{\bar{A}}{\left[\begin{array}{c|c|c} \bar{A}_{11} & \bar{A}_{12} & \bar{A}_{13} \\ \hline \bar{A}_{21} & \bar{A}_{22} & \bar{A}_{23} \\ \hline \bar{A}_{31} & \bar{A}_{32} & \bar{A}_{33} \end{array}\right]} \qquad \underset{\bar{B}}{\left[\begin{array}{c|c} \bar{B}_{11} & \bar{B}_{12} \\ \hline \bar{B}_{21} & \bar{B}_{22} \\ \hline \bar{B}_{31} & \bar{B}_{32} \end{array}\right]}$$

Figure E.1. – Partition of Left and Right Hand Side Matrices Into Blocks where ℓ_{ij}, u_{ij}, a_{ij} are the elements in the ith row and jth jolumn of $\overline{L}$, $\overline{U}$ and $\overline{A}$ respectively. From this equation we obtain

$$\ell_{ij} = a_{ij} - \sum_{k=1}^{j-1} \ell_{ik} u_{kj} \; ; \qquad i \geqslant j \tag{E.8}$$

and

$$u_{ij} = \left(a_{ij} - \sum_{k=1}^{i-1} \ell_{ik} u_{kj} \right) \Big/ \ell_{ii} \; ; \quad i < j \tag{E.9}$$

Since $\overline{A}$ is physically stored as its component submatrices $\overline{A}_{ij}$, the operations of equations (E.8) and (E.9) are actually performed by forming the submatrices

$$\overline{C}_{ij} = \overline{A}_{ij} - \sum_{k=1}^{\min(i,j)-1} \overline{L}_{ik} \overline{U}_{kj} \tag{E.10}$$

and then solving

$$\overline{L}_{ij} \overline{U}_{jj} = \overline{C}_{ij} \qquad \text{for} \qquad \overline{L}_{ij} \qquad \text{when} \qquad i > j, \tag{E.11}$$

$$\overline{L}_{ii} \overline{U}_{ij} = \overline{C}_{ij} \qquad \text{for} \qquad \overline{U}_{ij} \qquad \text{when} \qquad i < j \tag{E.12}$$

and decomposing

$$\overline{C}_{ii} = \overline{L}_{ii} \overline{U}_{ii} \qquad \text{when} \qquad i = j \tag{E.13}$$

The forward substitution of equation (E.5) is accomplished as follows. The matrix $\overline{Y}$ must satisfy the relationship

$$\sum_{k=1}^{i} \ell_{ij} y_{kj} = b_{ij} \tag{E.14}$$

so that

$$y_{ij} = \left(b_{ij} - \sum_{k=1}^{i-1} \ell_{ik} y_{kj} \right) \Big/ \ell_{ii} \tag{E.15}$$

where y_{ij}, b_{ij} are the elements in the ith row and jth column of $\overline{Y}$ and $\overline{B}$, respectively. The block operation is performed by first forming

$$\bar{D}_{ij} = \bar{B}_{ij} - \sum_{k=1}^{i-1} \bar{L}_{ik} \bar{Y}_{kj} \qquad \text{(E.16)}$$

and then solving

$$\bar{L}_{ii} \bar{Y}_{ij} = \bar{D}_{ij} \qquad \text{(E.17)}$$

by forward substitution.

The backward substitution of equation (E.6) is accomplished as follows. The solution $\bar{X}$ must satisfy the relationship

$$\sum_{k=1}^{n} u_{ik} x_{kj} = y_{ij} \qquad \text{(E.18)}$$

where x_{ij} is the element in the ith row and jth column of $\bar{X}$. Since

$$u_{ii} = 1 \ , \qquad \text{(E.19)}$$

we have

$$x_{ij} = y_{ij} - \sum_{k=i+1}^{n} u_{ik} x_{kj} \qquad \text{(E.20)}$$

The corresponding block operation is performed by first forming

$$\bar{E}_{ij} = \bar{Y}_{ij} - \sum_{k=i+1}^{n} \bar{U}_{ik} \bar{X}_{kj} \qquad \text{(E.21)}$$

and then solving

$$\bar{U}_{ii} \bar{X}_{ij} = \bar{E}_{ij} \qquad \text{(E.22)}$$

by backward substitution.

The present method does in-block partial pivoting. The pivoting is established during the in-core decomposition step. That is the quantity

$$\bar{C}_{ii} = \bar{A}_{ii} - \sum_{k=1}^{i-1} \bar{L}_{ik} \bar{U}_{ki} \qquad \text{(E.23)}$$

if formed without any pivoting considerations. The decomposition of $\overline{C}_{ii}$ is performed with pivoting, that is

$$\overline{C}_{ii} = \overline{P}_i \overline{L}_{ii} \overline{U}_{ii} \tag{E.24}$$

where $\overline{P}_i$ is the identity matrix with row interchanges corresponding to the required pivoting. At this point, the identical row swaps in $\overline{L}_{ij}$ for $j < i$ and $\overline{B}_{ij}$ for $j = 1$, m could be performed. However, this is not done. Instead, $\overline{P}_i$ is stored as a vector describing the row swaps required to generate $\overline{P}_i$ from the identity matrix. Each time $\overline{L}_{ii}$ is used to perform forward substitutions, the swaps dictated by this vector are first performed on the righthand side.

The method used to detect singularities in the system uses discontinuity of the pivot elements to flag the singularity. Each proposed pivot element is compared in absolute value to the minimum previously accepted pivot element. If the proposed element is much less in magnitude, a singularity is declared. While this method is adequate for the detection of obvious singularities (row identically zero, two rows the same, etc.), it does not adequately detect ill-conditioned problems. An additional check is provided to detect ill-conditioned systems. The method approximates error growth by the following scheme. Let

$$a_{ij,\,0} = a_{ij} \tag{E.25}$$

and

$$a_{ij,\,k} = a_{ij,\,k-1} - a_{ik,\,k-1} - a_{ik,\,k-1}\, a_{kj,\,k-1} / a_{kk,\,k-1} \tag{E.26}$$

The relative error e is approximated by

$$e = \max_{\substack{1 \leq k \leq N \\ i,j > k}} \left[k(k+1) \frac{|a_{ij,\,k}|}{|a_{kk,\,k}|} \right] \times 10^{-14} \tag{E.27}$$

The quotient $a_{ij,\,k}/a_{kk,\,k}$ is the ratio of the remaining matrix elements at elimination step k divided by the kth pivot. The product of this ratio with the growth term $(k + 1)\,k$ gives the error growth ratio. The assumed initial error is 10^{-14}. A singularity is flagged when e exceeds 10^{-6}.

APPENDIX F
COMPUTATION OF AERODYNAMIC QUANTITIES

In this appendix we describe the manner in which certain local and global quantities of aerodynamic interest are computed. Our point of departure is the computation of the average total velocity $\vec{V}_A$ at each panel center control point along with the distribution of singularity strength on each panel. From the singularity distribution the total difference velocity $\vec{V}_D$ may be calculated from equation (C.10) and then the total upper surface velocity $\vec{V}_U$ and total lower surface velocity $\vec{V}_L$ may be computed from equation (C.9). (However, note the discussion following equation (C.10) which implies that in the case of a source panel superimposed on a doublet panel the normal difference velocity is computed correctly only at the source panel control point, whereas the tangential difference velocity is computed correctly only at the doublet panel control point.)

The two velocities $\vec{V}_U$ and $\vec{V}_L$ are of most interest in aerodynamic applications and all aerodynamic quantities are computed separately for each type of velocity. Hence, let $\vec{V}$ be one of these velocities. We then define a pressure coefficient C_p at each panel center control point by the formula

$$C_p = 1 - \left(\vec{V} \cdot \vec{V}\right) / \left(\vec{V}_\infty \cdot \vec{V}_\infty\right) \tag{F.1}$$

where $\vec{V}_\infty$ is the freestream velocity. (Because of limitations in the existing pilot code logic the computed C_p will be in error for control points on superimposed source and doublet sheets, however, in the usual case of small or zero normal velocities the value of C_p at the doublet control points will be quite accurate).

A linear distribution of C_p on each panel can be calculated from the values of C_p at the control points. The method used is identical to that for computing the linear source distribution of network type number 1 (see app. B). On any panel S, we then have

$$C_p(\xi, \eta) = C_{p_o} + C_{p_\xi} \xi + C_{p_\eta} \eta \tag{F.2}$$

The force coefficient vector $\vec{C}_F$ on S is defined by

$$\vec{C}_F = \frac{1}{S_R} \iint_S C_p \hat{n} \, ds \tag{F.3}$$

where S_R is a specified reference area.

Substituting (F.2) into (F.3) and using (D.30) and (D.12) we obtain the following expression for $\vec{C}_F$ in local coordinates,

$$\vec{C}_F = \frac{1}{S_R} \iint\limits_{\Sigma} \left(C_{p_o} + C_{p_\xi}\, \xi + C_{p_\eta}\, \eta \right) (-2a\xi, -2b\eta, 1)\, d\xi d\eta$$

$$= \frac{1}{S_R}\, C_{p_o} \left[-2aC(2,1), -2bC(1,2), C(1,1) \right]$$

$$+ \frac{1}{S_R}\, C_{p_\xi} \left[-2aC(3,1), -2bC(2,2), C(2,1) \right] + \frac{1}{S_R}\, C_{p_\eta} \left[-2aC(2,2), -2bC(1,3), C(1,2) \right] \tag{F.4}$$

where C(M, N) is defined by equation (D.83) and computed in appendix D, section 4. ($\vec{C}_F$ may be expressed in global coordinates via a premultiplication by $\bar{A}^T$ where $\bar{A}$ is the transformation matrix defined in equation (A.17).) The sum of the force coefficient vectors for each panel in a network yields a force coefficient for the whole network. The force coefficient vectors for any collection of networks can be combined to yield a force coefficient vector for the configuration represented by that collection. This force coefficient vector can then be resolved into components along $\vec{V}_\infty$ (drag) and perpendicular to $\vec{V}_\infty$ (lift and side force).

The moment coefficient C_M at a point $\vec{R}_R$ about an axis $\hat{t}_R$ is defined by

$$C_M = \frac{1}{S_R T_R}\, \hat{t}_R \cdot \iint\limits_{S} \left(\vec{R} - \vec{R}_R \right) \otimes \hat{n}\, C_p\, dS \tag{F.5}$$

where T_R is a reference length and $\vec{R}$ is the integration point on S. Equation (F.5) is equivalent to

$$C_M = \frac{1}{T_R}\, \hat{t}_R \cdot \left[\vec{C}_E + \left(\vec{R}_o - \vec{R}_R \right) \otimes \vec{C}_F \right] \tag{F.6}$$

where $\vec{R}_o$ is the center of the local coordinate system on S. Here $\vec{C}_E$ is defined by

$$\vec{C}_E = \frac{1}{S_R} \iint\limits_{S} \vec{Q} \otimes \hat{n}\, C_p\, dS \tag{F.7}$$

where

$$\vec{Q} = \vec{R} - \vec{R}_o$$

$\vec{C}_E$ may be computed in local coordiantes in the same manner as $\vec{C}_F$, i.e.,

$$
\begin{aligned}
\vec{C}_E &= \frac{1}{S_R} \iint\limits_{\Sigma} \left(C_{p_o} + C_{p_\xi}\, \xi + C_{p_\eta}\, \eta \right) \left[\left(\xi, \eta, a\xi^2 + b\eta^2 \right) \otimes \left(-2a\xi, -2b\eta, 1 \right) \right] d\xi d\eta \\
&= \frac{1}{S_R} \iint\limits_{\Sigma} \left(C_{p_o} + C_{p_\xi}\, \xi + C_{p_\eta}\, \eta \right) \left[\left(\eta, -\xi, 2(a-b)\, \xi\, \eta \right) \right] d\xi d\eta \\
&= \frac{1}{S_R}\, C_{p_o} \left[C(1, 2), -C(2, 1),\ 2(a-b)\ C(2, 2) \right] \\
&\quad + \frac{1}{S_R}\, C_{p_\xi} \left[C(2, 2),\ -C(3, 1),\ 2(a-b)\, C(3, 2) \right] \\
&\quad + \frac{1}{S_R}\, C_{p_\eta} \left[C(1, 3),\ -C(2, 2),\ 2(a-b)\, C(2, 3) \right] \qquad \text{(F.8)}
\end{aligned}
$$

Here we have neglected terms of second order in a and b on account of hypothesis (D.6). The vector $\vec{C}_E$ may be expressed in global coordinates in the same way as $\vec{C}_F$.

APPENDIX G
DERIVATION OF RESULTS GIVEN WITHOUT PROOF IN APPENDIX D

In Appendix D, several results were given without proof. This was done in order to emphasize the procedures required to generate the influence coefficients. In this appendix we provide the proofs and derivations that are missing from Appendix D.

G.1. EVALUATION OF H(1, 1, 3)

In section (D.3), H(1, 1, 3) was referred to as the fundamental H integral, since all the other H (M, N, K) integrals are obtained from it and F(1, 1, 1) by the recursions given in procedures 1, 2, 3, 4, and 5. In this section, we give a detailed derivation of the closed form integration for H(1, 1, 3), and then describe the behavior of hH(1, 1, 3).

From equations (D.25), (D.15) and (D.16), we have

$$H(1,1,3) = \iint_{\Sigma} \frac{d\xi d\eta}{\rho^3} \tag{G.1}$$

where

$$\rho = \sqrt{r^2 + h^2}$$

$$r = \sqrt{(\xi - x)^2 + (\eta - y)^2}$$

$$h = z - z_0 \tag{G.2}$$

are illustrated in figure D.2. In equation (G.1), the integration is over the flat surface $d\Sigma = d\xi d\eta$ and h is a constant as far as the integration is concerned. Changing to polar coordinates, equation (G.1) becomes

$$H(1,1,3) = \sum_{i=1}^{4} \int_{\phi_i}^{\phi_{i+1}} \left[\int_0^r \frac{rdr}{\left(r^2 + h^2\right)^{3/2}} \right] d\phi \tag{G.3}$$

where the upper limit on r extends to the boundary of Σ. The geometry of the situation is shown in figure G.1, where (x, y, 0) is the perpendicular projection of the field point P onto the plane z = 0. The case shown is where the projection of P lies outside the boundary

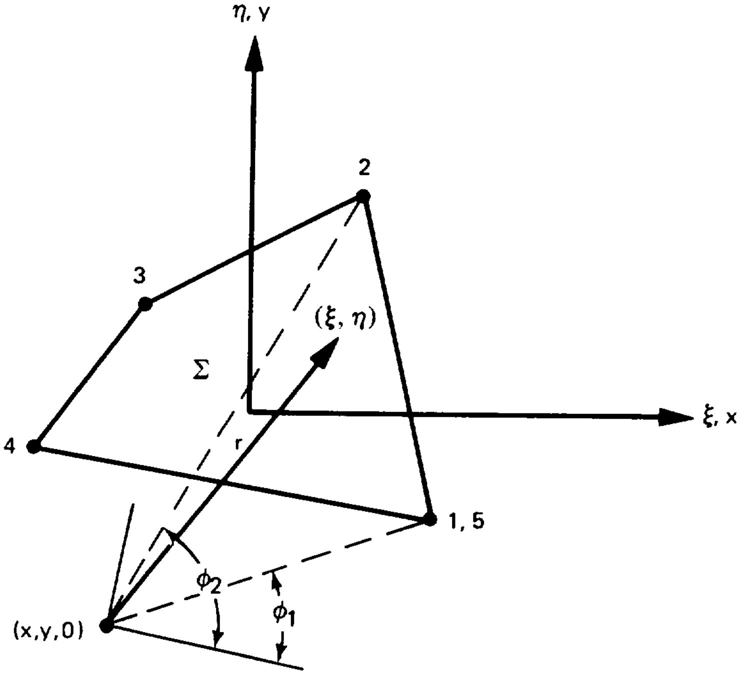

Figure G.1. – Geometry Relating to Equation (G.3)

of Σ. The "extra" contribution in the sum $\sum_{i=1}^{3}$ due to $r \notin \Sigma$ is cancelled by the final sweep in ϕ from corner point 4 to corner point 5. Performing the r - integration yields

$$H(1, 1, 3) = \sum_{i=1}^{4} \int_{\phi_i}^{\phi_{i+1}} \left[\frac{1}{|h|} - \frac{1}{\sqrt{r^2 + h^2}} \right] d\phi \qquad \text{(G.4)}$$

The next step is to convert equation (G.4) to a line integral along the boundary of Σ. To do this, consider figure G.2 (which is based on figure D.3).

Along typical side L of the boundary, $r^2 = \bar{a}^2 + \ell^2$ and the variable of integration ϕ is related to ℓ as follows:

$$\cos\phi = \frac{\bar{a}}{\sqrt{\ell^2 + \bar{a}^2}} \,, \quad \sin\phi = \frac{\ell \,\mathrm{sign}\,(\bar{a})}{\sqrt{\ell^2 + \bar{a}^2}}$$

$$\tan\phi = \ell / \bar{a} \,, \qquad d\phi = \frac{\bar{a}\,d\ell}{\ell^2 + \bar{a}^2} \qquad \text{(G.5)}$$

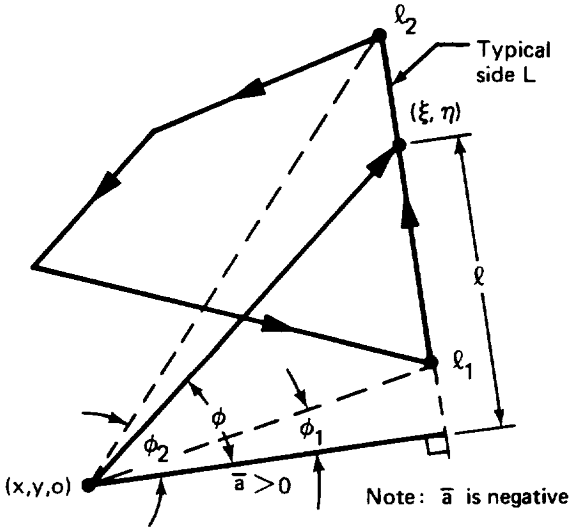

Note: $\bar{a}$ is negative for $\phi_1 > 90°$

Figure G.2. – Geometry Relating to Equation (G.6).

Thus, equation (G.4) becomes

$$H(1,1,3) = \sum_{i=1}^{4} \int_{\ell_i}^{\ell_{i+1}} \left(\frac{1}{|h|} - \frac{1}{\sqrt{\ell^2 + g^2}} \right) \frac{\bar{a}\, d\ell}{\left(\ell^2 + \bar{a}^2\right)} \qquad \text{(G.6)}$$

where $|h|$ and $\bar{a}$*are constants as far as the integration on ℓ is concerned, and

$$g^2 = \bar{a}^2 + h^2 \qquad \text{(G.7)}$$

---

*Note: $|\bar{a}|$ is the perpendicular distance from (x, y, 0) to side L (or its extension); thus, there is a different $\bar{a}$ for each side of Σ (see fig. G.8).

Separating equation (G.6) into its two parts gives

$$H(1, 1, 3) = \sum_{i=1}^{4} \left(\frac{\bar{a}}{|h|} I_1 - \bar{a} I_2 \right) \tag{G.8}$$

where

$$I_1 = \int_{\ell_i}^{\ell_{i+1}} \frac{d\ell}{\ell^2 + \bar{a}^2} = \frac{1}{|\bar{a}|} \tan^{-1} \left(\frac{\ell}{|\bar{a}|} \right) \Bigg|_{\ell_i}^{\ell_{i+1}} \tag{G.9}$$

and

$$I_2 = \int_{\ell_i}^{\ell_{i+1}} \frac{d\ell}{\left(\ell^2 + \bar{a}^2\right) \sqrt{\ell^2 + g^2}} = \frac{1}{|\bar{a}| \cdot |h|} \tan^{-1} \left(\frac{|h|\, \ell}{|\bar{a}| \sqrt{\ell^2 + g^2}} \right) \Bigg|_{\ell_i}^{\ell_i + 1} \tag{G.10}$$

Note: The integral denoted by I_2 may be found in reference 28 (page 49, line 3).

Using these last two results, equation (G.8) becomes

$$H(1, 1, 3) = \frac{1}{|h|} \sum_{i=1}^{4} \left(\frac{\bar{a}}{|\bar{a}|} \beta \right) \Bigg|_{\ell_i}^{\ell_{i+1}} \tag{G.11}$$

where

$$\beta = \tan^{-1} \left(\frac{\ell}{|\bar{a}|} \right) - \tan^{-1} \left(\frac{|h|\, \ell}{|\bar{a}| \sqrt{\ell^2 + g^2}} \right) \tag{G.12}$$

In this form, four arc tangents must be computed for each side of Σ.

To make for more efficient computations, the two arc tangents in equation (G.12) are combined into a single arc tangent.

$$\beta = \tan^{-1} \frac{|\bar{a}|\, \ell \left(\sqrt{\ell^2 + g^2} - |h|\right)}{\bar{a}^2 \sqrt{\ell^2 + g^2} \; + \; \ell^2 |h|}$$

$$= \tan^{-1} \frac{|\bar{a}|\, \ell}{g^2 + |h| \sqrt{\ell^2 + g^2}} \qquad \text{(G.13)}$$

With the aid of the following sketch,

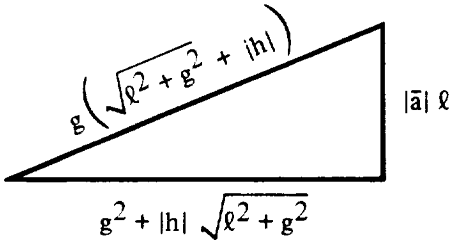

and the relation

$$\frac{m}{|m|} \tan^{-1} |m| = \tan^{-1} m \qquad \text{(G.14)}$$

we obtain

$$H(1, 1, 3) = \frac{1}{|h|} \sum_{i=1}^{4} \beta \Big|_{\ell_i}^{\ell_{i+1}} \qquad \text{(G.15)}$$

where

$$\sin \beta = \frac{\bar{a}\,\ell}{g\left(\sqrt{\ell^2 + g^2} + |h|\right)}$$

$$\cos \beta = \frac{g^2 + |h| \sqrt{\ell^2 + g^2}}{g\left(\sqrt{\ell^2 + g^2} + |h|\right)}$$

$$\tan \beta = \frac{\bar{a}\,\ell}{g^2 + |h| \sqrt{\ell^2 + g^2}} \tag{G.16}$$

An additional efficiency is gained by combining the difference $\beta_{i+1} - \beta_i$ into a single arc tangent. For simplicity, consider only a single side of Σ, with endpoints $i = 1$ and $i + 1 = 2$.

Then

$$\beta_2 - \beta_1 = \tan^{-1}\left(\frac{\bar{a}\ell_2}{c_2}\right) - \tan^{-1}\left(\frac{\bar{a}\ell_1}{c_1}\right) \tag{G.17}$$

where

$$c_1 = g^2 + |h|\, s_1 \qquad s_1 = \sqrt{\ell_1{}^2 + g^2}$$

$$c_2 = g^2 + |h|\, s_2 \qquad s_2 = \sqrt{\ell_2{}^2 + g^2} \tag{G.18}$$

Equation (G.17) reduces to

$$\beta_2 - \beta_1 = \tan^{-1}\left(\frac{\bar{a}\left(\ell_2 c_1 - \ell_1 c_2\right)}{c_1 c_2 + \bar{a}^2 \ell_1 \ell_2}\right) \tag{G.19}$$

and equation (G.15) becomes

$$H(1,1,3) = \frac{1}{|h|} \sum_{j=1}^{4} \left(\beta_2 - \beta_1\right)_j$$

$$= \frac{1}{|h|} \sum_{j=1}^{4} \tan^{-1} \left(\frac{\bar{a}\left(\ell_2 c_1 - \ell_1 c_2\right)}{c_1 c_2 + \bar{a}^2 \ell_1 \ell_2} \right)_j \qquad \text{(G.20)}$$

where the sum is over the four sides of Σ and the subscripts 1 and 2 are now taken as the first and second endpoints of each side j.

Computing equations (G.19) and (G.20) with the single argument FORTRAN ATAN external function returns values of $\beta_2 - \beta_1$ in the range $\left(-\frac{\pi}{2}, \frac{\pi}{2}\right)$. To use the double argument ATAN2 external function, so as to obtain values of $\beta_2 - \beta_1$ in the range $(-\pi, \pi)$, we must also compute $\sin(\beta_2 - \beta_1)$ and $\cos(\beta_2 - \beta_1)$. These quantities are obtained from equations (G.16), using the difference formulas for sin and cos. The result is

$$\sin\left(\beta_2 - \beta_1\right) = \frac{\bar{a}\left(\ell_2 c_1 - \ell_1 c_2\right)}{g^2 d_1 d_2}$$

$$\cos\left(\beta_2 - \beta_1\right) = \frac{c_1 c_2 + \bar{a}^2 \ell_1 \ell_2}{g^2 d_1 d_2} \qquad \text{(G.21)}$$

where

$$d_1 = s_1 + |h|$$

$$d_2 = s_2 + |h| \qquad \text{(G.22)}$$

Equation (G.20) is then rewritten as

$$H(1,1,3) = \frac{1}{|h|} \sum_{1}^{4} \tan^{-1} \left[\sin\left(\beta_2 - \beta_1\right),\ \cos\left(\beta_2 - \beta_1\right)\right] \qquad \text{(G.23)}$$

If $g^2 d_1 d_2 \neq 0$, equation (G.23) can be written as

$$H(1,1,3) = \frac{1}{|h|} \sum_{1}^{4} \tan^{-1}\left[\bar{a}\left(\ell_2 c_1 - \ell_1 c_2\right),\ c_1 c_2 + \bar{a}^2 \ell_1 \ell_2\right] \tag{G.24}$$

which is the form appearing in equation (D.41).

The quantity $g = \sqrt{\bar{a}^2 + h^2}$ is illustrated in figure G.3 for $(x, y, 0) \notin \Sigma$. Recall from equations (D.15) that $h = z - z_0$ where $z_0 = a x_0^2 + b y_0^2$ and (x_0, y_0) is the point on Σ closest to $(x, y, 0)$.

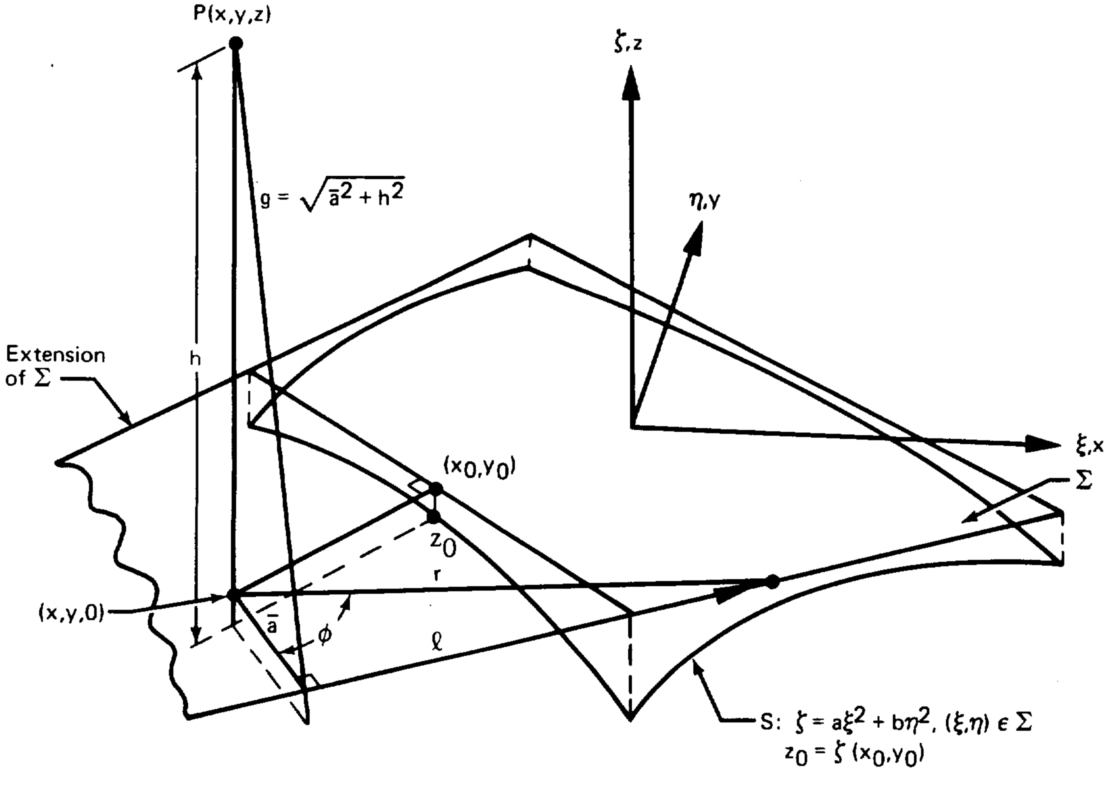

Figure G.3. – The Quantity $g = \sqrt{\bar{a}^2 + h^2}$ for $(x,y,o) \notin \Sigma$

Figure G.4 shows $g = \sqrt{\bar{a}^2 + h^2}$ for the case $(x, y, 0) \in \Sigma$; here, $g = 0$ if P is a point on the edge of S, S being defined by $\zeta = a\xi^2 + b\eta^2$, $(\xi, \eta) \in \Sigma$. [(The quantity $s = \sqrt{g^2 + \ell^2}$ is also shown in figure G.4 since it will be referred to later (in eq. G.33)].

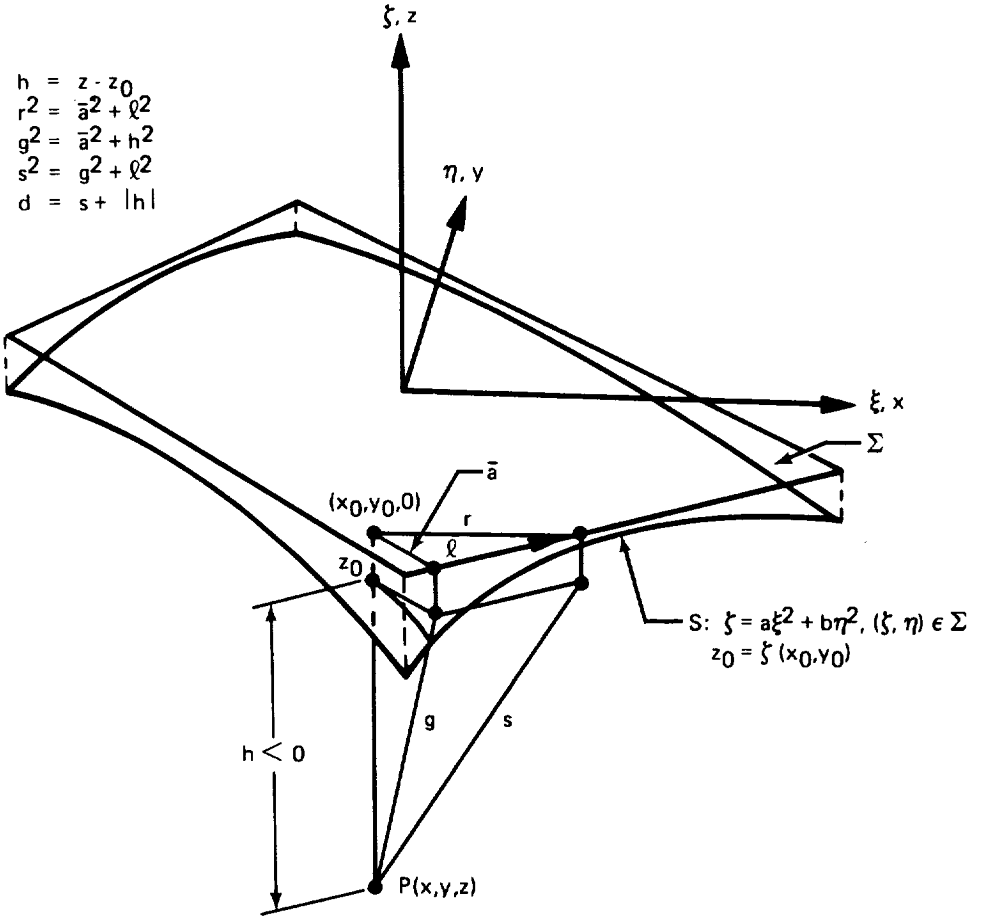

Figure G.4. – The Quantity $g = \sqrt{\bar{a}^2 + h^2}$ *for* $(x,y,0) \in \Sigma$.

For $g = 0$, both $\bar{a}$ and h are zero. Although $H(1, 1, 3)$ is singular for $h = 0$, $hH(1, 1, 3)$ is not, and it is $hH(1, 1, 3)$ that appears in the influence coefficient equations. For the flat panel, this can be seen directly from equations (D.119), (D.124) and (D.140); for the curved panel the corresponding equations are (D.28), (D.30) and (D.33), respectively. An alternate form for equations (G.21) can be obtained which handles the $g = 0$ case provided $\ell_1 \ell_2 > 0$. This is shown next.

With considerable algebraic manipulation, the g^2 term can be removed from the denominator of equations (G.21). The result is

$$d_1 d_2 \sin\left(\beta_2 - \beta_1\right) = \bar{a}\left[\left(\ell_2 - \ell_1\right) + \frac{|h|\left(\ell_2^2 - \ell_1^2\right)}{\left(\ell_2 s_1 + \ell_1 s_2\right)}\right]$$

$$d_1 d_2 \cos\left(\beta_2 - \beta_1\right) = g^2 + |h|\left(s_1 + s_2\right) + \ell_1 \ell_2 + \frac{h^2\left(g^2 + \ell_1^2 + \ell_2^2\right)}{\left(s_1 s_2 + \ell_1 \ell_2\right)} \qquad \text{(G.25)}$$

For $(x, y, 0) \notin \Sigma$, e.g., as shown in figures G.2 and G.3, the origin of ℓ is on an extension of L rather than on L itself. Hence, ℓ_1 and ℓ_2 are both of the same sign and $\ell_1 \ell_2 > 0$. For this condition, the terms $\ell_2 s_1 + \ell_1 s_2$ and $s_1 s_2 + \ell_1 \ell_2$ appearing in the denominator of equations (G.25) are never zero (even for $g = 0$) and $d_1 d_2$ is also positive ($d_1 d_2 = \ell_1 \ell_2$ for $g = 0$). Thus, equations (G.25) present no computational difficulties for any field point P satisfying $(x, y, 0) \notin \Sigma$.

To summarize, hH(1, 1, 3) is given by equation (G.23) in terms of the arguments $\sin(\beta_2 - \beta_1)$ and $\cos(\beta_2 - \beta_1)$. For $(x, y, 0) \in \Sigma$ but *not* on an edge of S ($g \neq 0$), the arguments are those given in equation (G.24). For $(x, y, 0) \notin \Sigma$, equation (G.24) is still valid provided $g \neq 0$; for this case however, equation (G.23) with arguments given by equations (G.25) is preferred since these arguments are valid for any g. Thus, equations (G.23) – (G.25) cover all cases except when P is on an edge of S. This case is considered next.

Consider figure G.5 which shows the field point P approaching Q at an edge of S, along a fixed direction given by θ. The pertinent geometric quantities g, $\bar{a}$, and h are shown for two positions of the field point. As P moves to P′ to Q along θ = constant, G moves to G′ to Q and

$$\begin{aligned} h &\rightarrow h' \rightarrow 0 \\ \bar{a} &\rightarrow \bar{a}' \rightarrow 0 \\ g &\rightarrow g' \rightarrow 0 \end{aligned} \qquad \text{(G.26)}$$

Now consider equation (G.16) viz.,

$$\tan\beta = \frac{\bar{a}\ell}{g^2 + |h|\sqrt{\ell^2 + g^2}} \qquad \text{(G.27)}$$

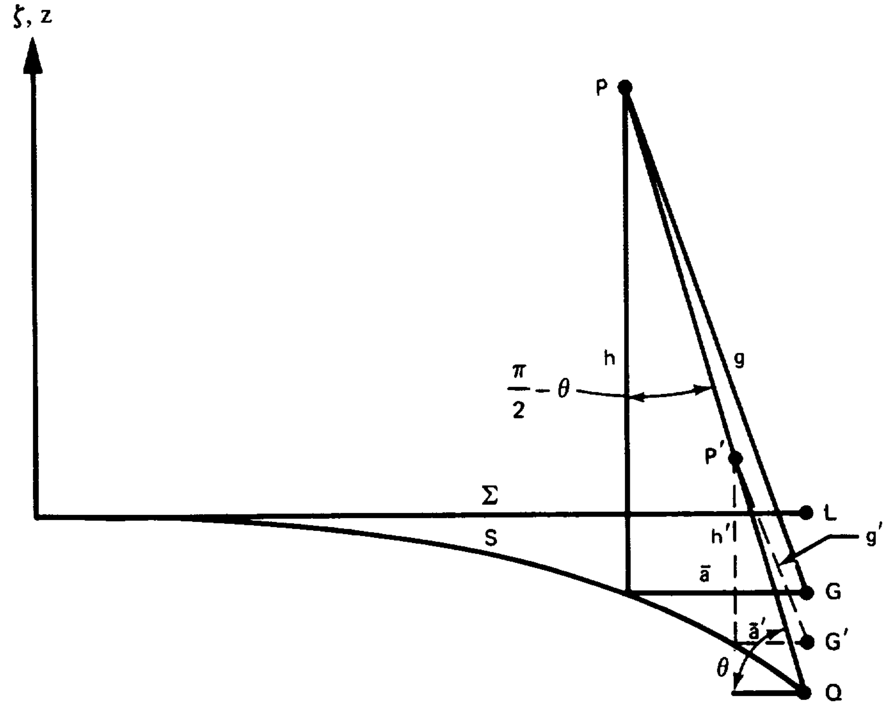

Figure G.5. — P Approaching Q Along a Constant Direction θ

As g → 0 due to P → Q along θ = constant, equation G.27 becomes

$$\tan\beta \rightarrow \frac{\bar{a}}{|h|}\,\frac{\ell}{|\ell|} \tag{G.28}$$

From figure G.5, we see that the ratio ā/h is equal to $\tan\left(\frac{\pi}{2} - \theta\right)$ when P reaches Q. Equation (G.28) however, contains $\frac{\bar{a}}{|h|}$, so we must distinguish between the case where P approaches Q from above, i.e., $h > 0$, and the case where P approaches Q from below, i.e., $h < 0$. These two cases are shown in figure G.6 along with the corresponding angles θ_u and θ_ℓ which are both defined over the interval $(0, \pi)$.

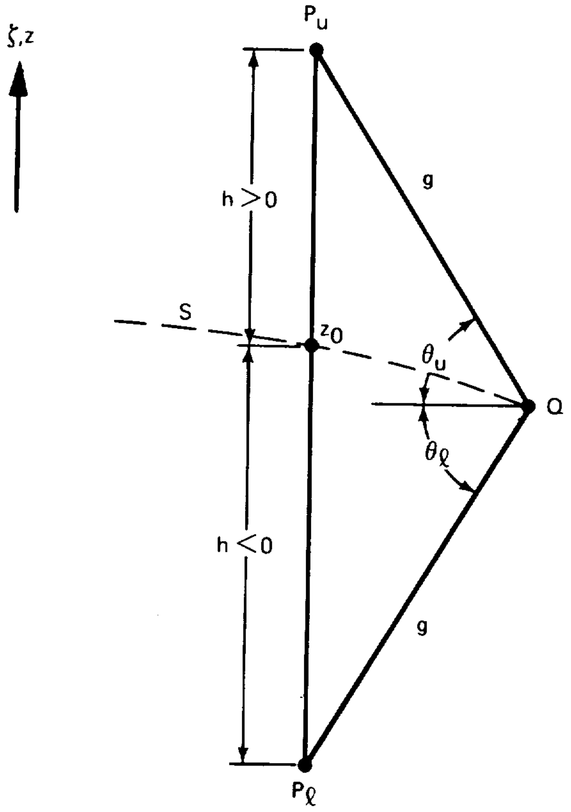

Figure G.6. – P Approaching Q From Opposite Sides of S.

With θ now considered to be either θ_u or θ_ℓ we can then write

$$\tan(\pi / 2 - \theta) = \frac{\bar{a}}{|h|} \quad , \qquad 0 \leqslant \theta \leqslant \pi \qquad \text{(G.29)}$$

Thus, equation (G.28) becomes

$$\tan\beta \rightarrow \text{sign}(\ell) \tan\left(\frac{\pi}{2} - \theta\right) \qquad \text{(G.30)}$$

Evaluating this at the two endpoints of L, viz, at ℓ_1 and ℓ_2, and noting that ℓ_2 is positive and ℓ_1 is negative for P at some point on the interior of the edge of S, gives

$$\beta_2 - \beta_1 \rightarrow \pi - 2\theta \quad , \qquad 0 \leqslant \theta \leqslant \pi \qquad \text{(G.31)}$$

where θ is either θ_u or θ_ℓ.

Substituting this for one of the sides in equation (G.20) gives

$$hH(1, 1, 3) = \frac{h}{|h|}\left[\sum_{3\text{ sides}} \tan^{-1}\left(\frac{\bar{a}(\ell_2 c_1 - \ell_1 c_2)}{c_1 c_2 + \bar{a}^2 \ell_1 \ell_2}\right) + (\pi - 2\theta)\right] \tag{G.32}$$

where the last term is for the side at which P is on the edge of S.

Equation (G.31) shows that for P being a point on the edge of S, the value $\beta_2 - \beta_1$ for that edge depends on the direction of approach. Thus, as stated in section D.5, the sum of the arc tangent terms making up hH(1, 1, 3) is bounded, but not continuous for P on an edge of S (or Σ for a flat panel); that is, the value of hH(1, 1, 3) is indeterminate. This difficulty is avoided for the network edge control points by withdrawing these control points slightly from the edge as described in appendix C.

Finally, we determine the character of hH(1, 1, 3) for the case h = 0, but P is not on an edge of S. For $(x, y, 0) \in \Sigma$, this places P at a point on the interior of S. Thus, referring to figure G.7, we want to see how hH(1, 1, 3) behaves as P approaches the point z_0.

First, write equation (G.16) in terms of the angles α and $\tilde{\theta}$ defined in figure G.7, viz.,

$$\tan\alpha = \frac{\ell}{g} \quad , \quad \cos\alpha = \frac{g}{s}$$

$$\sin\tilde{\theta} = \frac{|h|}{g} \quad , \quad \cos\tilde{\theta} = \frac{\bar{a}}{g} \quad , \quad 0 \leqslant \tilde{\theta} \leqslant \pi \tag{G.33}$$

where $\tilde{\theta}$ is taken as either $\tilde{\theta}_u$ or $\tilde{\theta}_\ell$ in the same fashion as θ_u and θ_ℓ of figure G.6. So, equation (G.16) becomes

$$\tan\beta = \left(\frac{\ell}{g}\right) \cdot \frac{\bar{a}/g}{1 + \frac{|h|}{g}\sqrt{1 + (\ell/g)^2}}$$

$$= (\tan\alpha) \cdot \frac{\cos\tilde{\theta}}{1 + \sin\tilde{\theta}\sqrt{1 + \tan^2\alpha}}$$

$$= (\tan\alpha) \cdot \left(\frac{\cos\alpha\cos\tilde{\theta}}{\cos\alpha + \sin\tilde{\theta}}\right) \tag{G.34}$$

For the case shown in figure G.7, viz., $(x, y, 0) = (x_0, y_0, 0) \in \Sigma$, we see that $\tilde{\theta}$ goes to zero as h goes to zero and that α takes on the same value as ϕ. Hence, equation (G.34) becomes

$$\tan\beta \Big|_{\substack{h \to 0 \\ (x,y,0)\in\Sigma}} = \tan\phi \qquad \text{(G.35)}$$

This result is valid for each side of Σ, so with the aid of figure G.8 we see that equation (G.20) yields

$$hH(1,1,3) \Big|_{\substack{h \to 0 \\ (x,y,0)\in\Sigma}} = \frac{h}{|h|} \sum_{j=1}^{4} \left(\phi_2 - \phi_1\right)_j = 2\pi \frac{h}{|h|} \qquad \text{(G.36)}$$

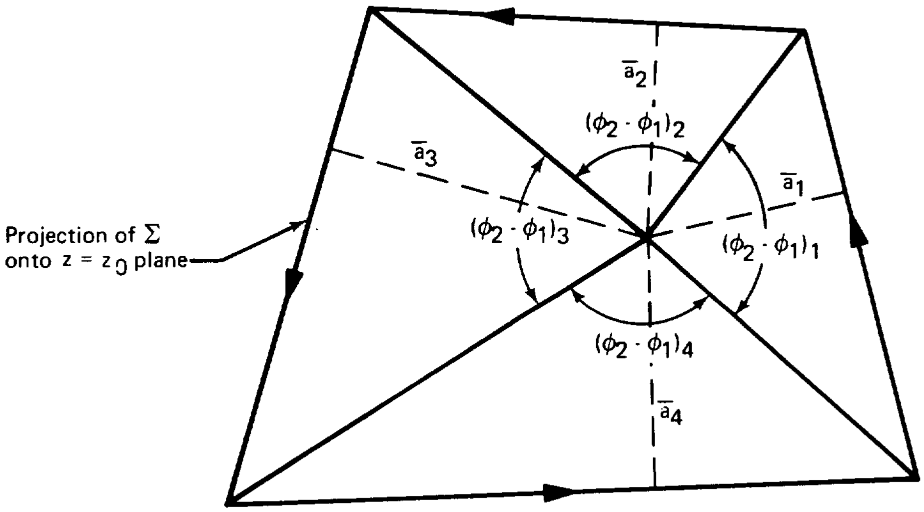

Figure G.8. – Geometric Interpretation of Equation (G.36)

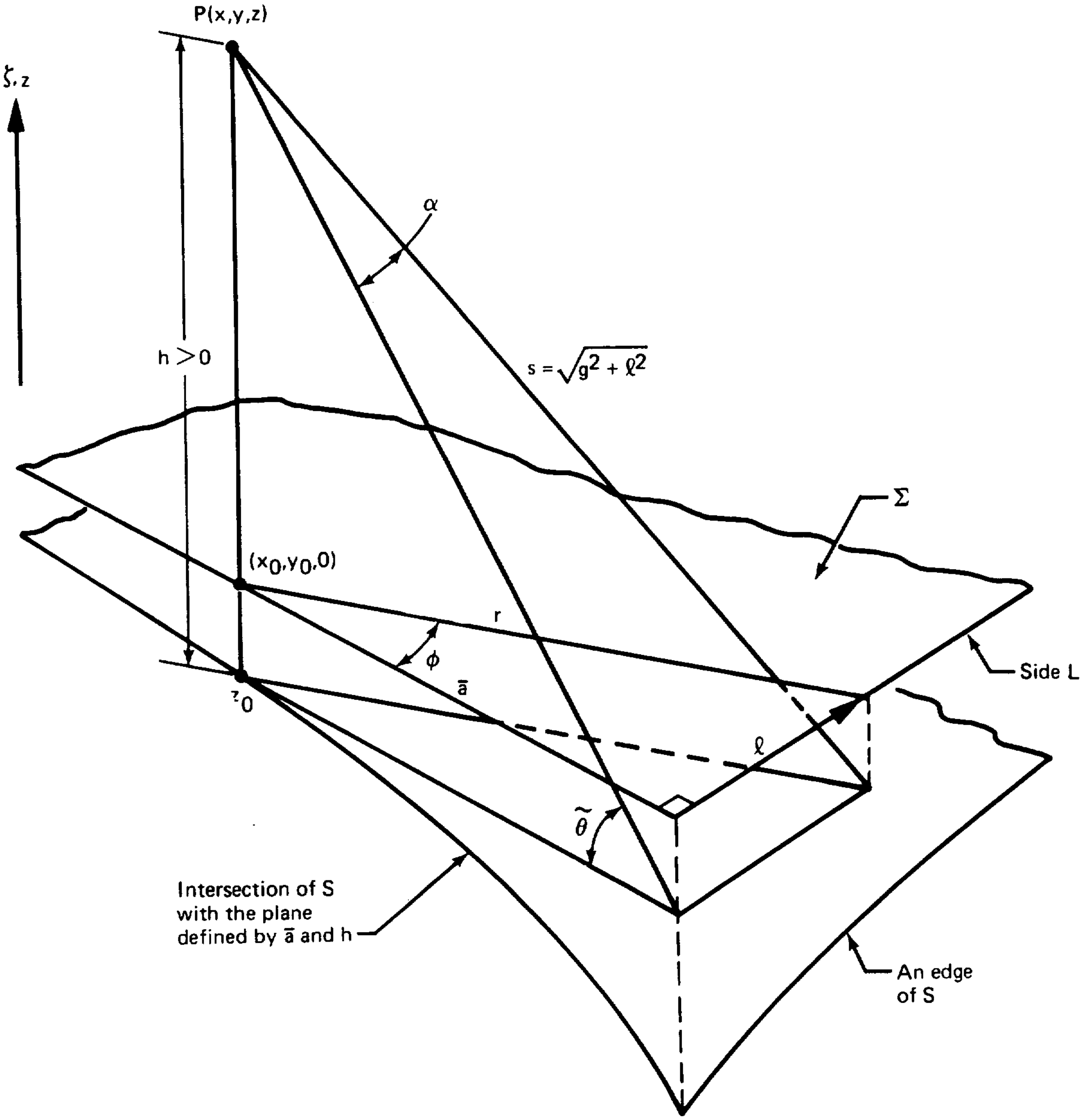

Figure G.7. – Field Point P Approaching the Point z_0 on the Interior of S

If the point P(x, y, z) is located such that $(x, y, 0) \notin \Sigma$, e.g., as in figure G.3, the $\tilde{\theta}$'s for the four sides of Σ do not all go to zero when h goes to zero. This is shown in figure G.9. (Note that the lengths $\bar{a}_j$ are in the plane $z = z_0$ whereas the actual $\bar{a}_j$ are defined in the plane $z = 0$, see figure G.3.) The side "facing" the point (x, y, z_0) is called side one. We see that $\tilde{\theta}_1$ is greater than $\pi/2$ and the $\tilde{\theta}$'s for the remaining sides are less than $\pi/2$. Thus, as h goes to zero, $\tilde{\theta}_1 \to \pi$ and $\tilde{\theta}_j \to 0$ for j = 2, 3, 4. Substituting these values for $\tilde{\theta}$ into equation (G.34) gives

$$\tan\beta \,\Bigg|_{\substack{h \to 0 \\ (x, y, 0) \notin \Sigma}} = \begin{cases} -\tan\phi & \text{for} \quad \text{side 1} \\ +\tan\phi & \text{for} \quad \text{sides 2, 3, 4} \end{cases} \tag{G.37}$$

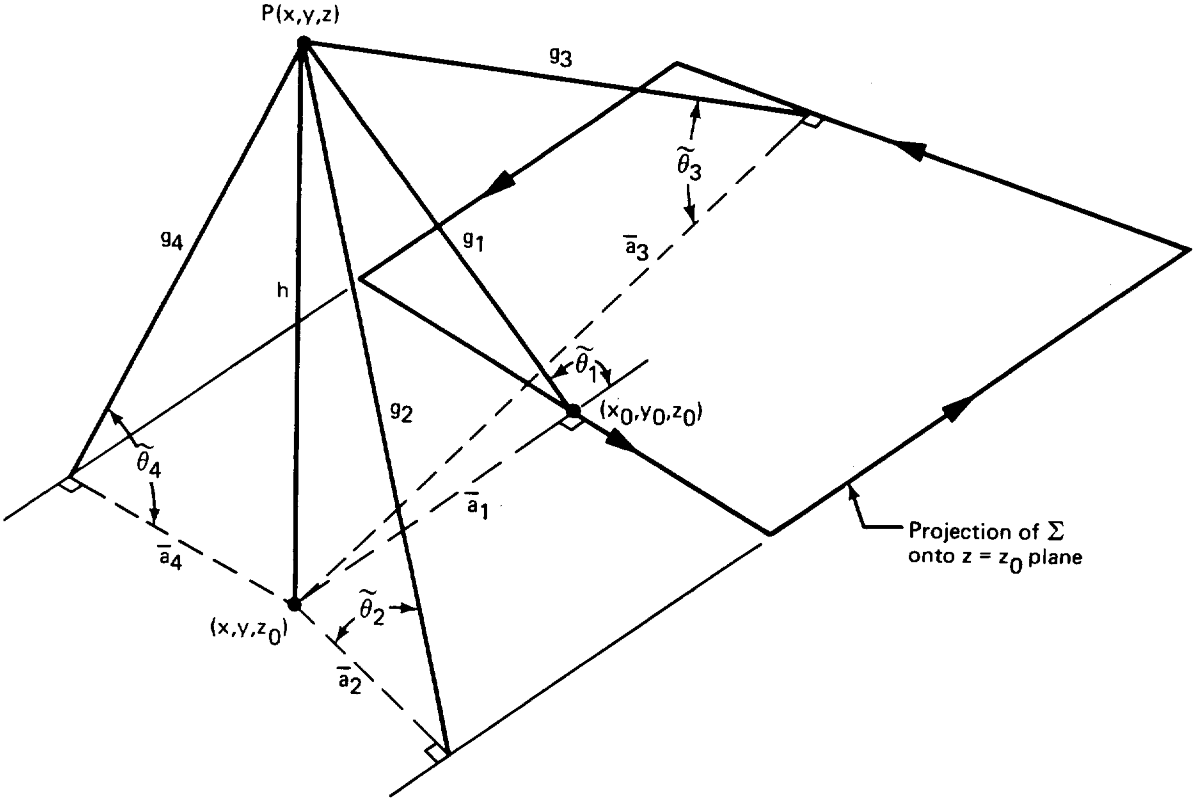

Figure G.9. – The Case $h \to 0$ for $(x,y,0) \notin \Sigma$

Equation (G.20) then becomes

$$hH(1,1,3)\Bigg|_{\substack{h\to 0\\(x,y,0)\notin\Sigma}} = \frac{h}{|h|}\left[-\left(\phi_2-\phi_1\right)_{\substack{\text{side}\\1}} + \sum_{j=2}^{4}\left(\phi_2-\phi_1\right)_j\right] \tag{G.38}$$

From figure G.10, we see that

$$\left(\phi_2-\phi_1\right)_{\substack{\text{side}\\1}} = \Gamma \qquad \text{(clockwise)}$$

$$\sum_{j=2}^{4}\left(\phi_2-\phi_1\right)_j = \Gamma \qquad \text{(counterclockwise)} \tag{G.39}$$

so

$$hH(1,1,3)\Bigg|_{\substack{h\to 0\\(x,y,0)\notin\Sigma}} = 0 \tag{G.40}$$

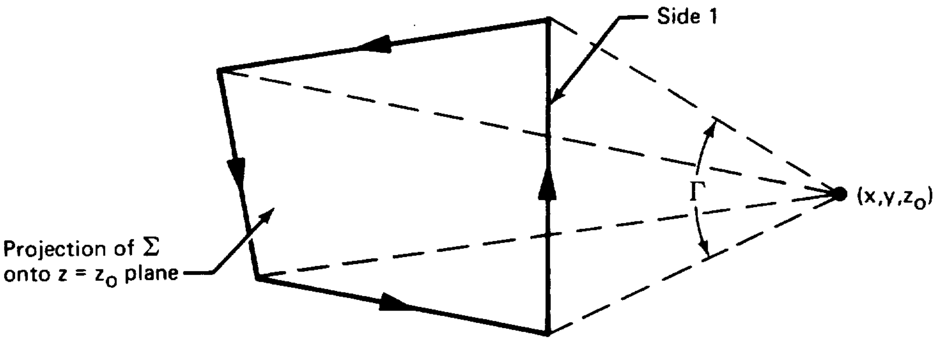

Figure G.10. – Geometric Interpretation of Equations (G.38) – (G.40)

Taken together, equations (G.36) and (G.40) give

$$hH(1,1,3)\Big|_{h \to 0} = \begin{cases} 2\pi \dfrac{h}{|h|} & , \quad (x, y, 0) \in \Sigma \\ 0 & , \quad (x, y, 0) \notin \Sigma \end{cases} \tag{G.41}$$

provided P is not on an edge of S (recall equation (G.32)). This result holds for either a curved or a flat panel. For a flat panel, S becomes Σ, and $h = 0$ corresponds to the plane $z = 0$ (which contains Σ). The effect of the $hH(1, 1, 3)$ jump property (across S) on the source velocity, and on the doublet velocity and potential, is discussed in section D.5 for the flat panel case.

G.2 PROCEDURE 1 RECURSIONS: EQUATIONS (D.41) → (D.48)

The equations given in procedure 1 are obtained from recombinations of equations (D.37), (D.38), (D.39), and (D.56). These four equations are repeated here for convenience

$$H(M + 2, N, K) + H(M, N + 2, K) + h^2H(M, N, K) = H(M, N, K - 2) \tag{D.37}$$

$$(K - 2)\, H(M, N, K) = (M - 2)\, H(M - 2, N, K - 2) - \sum_1^4 \nu_\xi\, F(M - 1, N, K - 2), \tag{D.38}$$

$$(K - 2)\, H(M, N, K) = (N - 2)\, H(M, N - 2, K - 2) - \sum_1^4 \nu_\eta\, F(M, N - 1, K - 2) \tag{D.39}$$

$$\nu_\xi F(M + 1, N, K) + \nu_\eta F(M, N + 1, K) = \bar{a}F(M, N, K) \tag{D.56}$$

Our first task is to put the recursions (D.37), (D.38) and (D.39) into normal form, i.e., derive three equivalent recursions in each of which only one index varies. To do this we replace M by M + 2 in equation (D.38) and N by N + 2 in equation (D.39) to obtain

$$(K - 2)\, H(M + 2, N, K) = M\, H(M, N, K - 2) - \sum_1^4 \nu_\xi\, F(M + 1, N, K - 2) \tag{G.42}$$

and

$$(K - 2)\, H(M, N + 2, K) = N\, H(M, N, K - 2) - \sum_1^4 \nu_\eta\, F(M, N + 1, K - 2) \tag{G.43}$$

Substituting H(M + 2, N, K) from (G.42) and H(M, N + 2, K) from (G.43) into equation (D.37) and rearranging we obtain

$$(K - 2)\, h^2\, H(M, N, K) = (K - M - N - 2)\; H(M, N, K - 2)$$

$$+ \sum_1^4 \nu_\xi\, F(M + 1, N, K - 2) + \sum_1^4 \nu_\eta\, F(M, N + 1, K - 2)$$

Substituting D.56, we obtain a recursion which involves variations in the K index only:

$$(K - 2)\, h^2\, H(M, N, K) = (K - M - N - 2)\, H(M, N, K - 2) + \sum_1^4 \bar{a}\, F(M, N, K - 2) \qquad (G.44)$$

Substituting H(M, N, K) from equation (D.38) into (G.44) and rearranging we obtain

$$(K - M - N - 2)\, H(M, N, K - 2) = (M - 2)\, h^2\, H(M - 2, N, K - 2)$$

$$- h^2 \sum_1^4 \nu_\xi\, F(M - 1, N, K - 2) - \sum_1^4 \bar{a}\, F(M, N, K - 2).$$

Replacing K by K +2 we obtain a recursion which involves variations in the M index only:

$$(K - M - N)\, H(M, N, K) = (M - 2)\, h^2\, H(M - 2, N, K)$$

$$- h^2 \sum_1^4 \nu_\xi\, F(M - 1, N, K) - \sum_1^4 \bar{a}\, F(M, N, K) \qquad (G.45)$$

Interchanging the roles of M and N, and ν_ξ and ν_η, we obtain a recursion which involves variations in the N index only:

$$(K - M - N)\, H(M, N, K) = (N - 2)\, h^2\, H(M, N - 2, K)$$

$$- h^2 \sum_1^4 \nu_\eta\, F(M, N - 1, K) - \sum_1^4 \bar{a}\, F(M, N, K). \qquad (G.46)$$

Now it is an easy matter to derive equations (D.41) through (D.48). Setting M = N = 1 in equation (G.44) yields equation (D.42). Setting K = 3 in addition and substituting H(1, 1, 3) from equation (G.24) yields equation (D.41). Equation (D.43) is obtained by setting K = 1 and M = 2 in equation (G.45). Here we note that the first term on the right of (G.45) has a zero coefficient, hence H(0, N, 1) is not needed. Equation (D.44) is obtained by setting M = 1 and K = 1 in equation (G.46). Equation (D.45) is obtained by setting K = 1 in equation (G.45). Equation (D.46) is obtained by setting M = 1 in equation (D.39). Equation (D.47) is the result of setting M = 2 in equation (D.39). Finally, equation (D.48) is simply a rearrangement of the terms of equation (D.37).

G.3 PROCEDURE 4 RECURSIONS: EQUATIONS (D.61) → (D.67)

The equations given in Procedure 4 are obtained from recombinations of equations (D.55), (D.56) and (D.57). These three equations are repeated here for convenience.

$$F(M+2, N, K) + F(M, N+2, K) + h^2 F(M, N, K) = F(M, N, K-2) \tag{D.55}$$

$$\nu_\xi F(M+1, N, K) + \nu_\eta F(M, N+1, K) = \bar{a} F(M, N, K) \tag{D.56}$$

$$\begin{aligned} &-(M-1)\nu_\eta F(M-1, N, K-2) + (N-1)\nu_\xi F(M, N-1, K-2) \\ &\quad + (K-2)\nu_\eta F(M+1, N, K) - (K-2)\nu_\xi F(M, N+1, K) = E(M, N, K-2) \end{aligned} \tag{D.57}$$

Our first task is to put the recursions (D.55), (D.56) and (D.57) into useful form, i.e., derive equivalent recursions which will allow systematic evaluation. To do this we solve equations (D.56) and (D.57) for the unknowns F(M + 1, N, K) and F(M, N + 1, K) using the fact that $\nu_\xi^2 + \nu_\eta^2 = 1$ and obtain

$$\begin{aligned} F(M+1, N, K) = \frac{1}{(K-2)} \Big[&(K-2)\nu_\xi \bar{a} F(M, N, K) + (M-1)\nu_\eta^2 F(M-1, N, K-2) \\ &- (N-1)\nu_\xi\nu_\eta F(M, N-1, K-2) + \nu_\eta E(M, N, K-2)\Big] \end{aligned} \tag{G.47}$$

and

$$\begin{aligned} F(M, N+1, K) = \frac{1}{(K-2)} \Big[&(K-2)\nu_\eta \bar{a} F(M, N, K) - (M-1)\nu_\xi\nu_\eta F(M-1, N, K-2) \\ &+ (N-1)\nu_\xi^2 F(M, N-1, K-2) - \nu_\xi E(M, N, K-2)\Big] \end{aligned} \tag{G.48}$$

Replacing M by M + 1 in (G.47), and N by N + 1 in (G.48) we obtain

$$\begin{aligned} F(M+2, N, K) = \frac{1}{(K-2)} \Big[&(K-2)\nu_\xi \bar{a} F(M+1, N, K) + M\nu_\eta^2 F(M, N, K-2) \\ &- (N-1)\nu_\xi\nu_\eta F(M+1, N-1, K-2) + \nu_\eta E(M+1, N, K-2)\Big] \end{aligned} \tag{G.49}$$

$$F(M, N+2, K) = \frac{1}{(K-2)} \Big[(K-2)\,\nu_\eta\,\bar{a}\,F(M, N+1, K) - (M-1)\,\nu_\xi \nu_\eta\,F(M-1, N+1, K-2) + N\nu_\xi^2\,F(M, N, K-2) - \nu_\xi\,E(M, N+1, K-2)\Big] \quad (G.50)$$

Adding equations (G.49) and (G.50) and noting that $\nu_\xi^2 + \nu_\eta^2 = 1$:

$$\begin{aligned} &F(M+2, N, K) + F(M, N+2, K) \\ &= \frac{1}{(K-2)} \Big\{(K-2)\,\bar{a}\,\Big[\nu_\xi\,F(M+1, N, K) + \nu_\eta\,F(M, N+1, K)\Big] \\ &\quad + (N+M-1)\,F(M, N, K-2) \\ &\quad - (N-1)\,\nu_\eta \Big[\nu_\xi\,F(M+1, N-1, K-2) + \nu_\eta\,F(M, N, K-2)\Big] \\ &\quad - (M-1)\,\nu_\xi \Big[\nu_\xi\,F(M, N, K-2) + \nu_\eta\,F(M-1, N+1, K-2)\Big] \\ &\quad + \nu_\eta\,E(M+1, N, K-2) - \nu_\xi\,E(M, N+1, K-2)\Big\} \end{aligned} \quad (G.51)$$

The term on the left side of (G.51) is equal to F(M, N, K - 2) - h^2 F(M, N, K) from equation (D.55). The terms in square brackets on the right side of (G.51) can be reduced via equation (D.56). For the first square bracket we use (D.56) directly. For the second, we replace N by N - 1 and K by K - 2. For the third, we replace M by M - 1 and K by K - 2. Making the substitutions and rearranging, we obtain the following recursion on K:

$$\begin{aligned} F(M, N, K) = \frac{1}{g^2\,(K-2)} \Big[&(K-M-N-1)\,F(M, N, K-2) \\ &+ (N-1)\,\bar{a}\,\nu_\eta\,F(M, N-1, K-2) \\ &+ (M-1)\,\bar{a}\,\nu_\xi\,F(M-1, N, K-2) - \nu_\eta\,E(M+1, N, K-2) \\ &+ \nu_\xi\,E(M, N+1, K-2)\Big] \end{aligned} \quad (G.52)$$

Next we solve equation (D.56) for F(M + 1, N, K) and for F(M, N + 1, K):

$$F(M+1, N, K) = \frac{\bar{a}}{\nu_\xi}\,F(M, N, K) - \frac{\nu_\eta}{\nu_\xi}\,F(M, N+1, K) \quad (G.53)$$

and

$$F(M, N+1, K) = \frac{\bar{a}}{\nu_\eta}\,F(M, N, K) - \frac{\nu_\xi}{\nu_\eta}\,F(M+1, N, K) \quad (G.54)$$

Replacing M by M + 1 in equation (G.53) we have

$$F(M+2, N, K) = \frac{\bar{a}}{\nu_\xi} F(M+1, N, K) - \frac{\nu_\eta}{\nu_\xi} F(M+1, N+1, K). \tag{G.55}$$

Next we substitute the expression for F(M + 1, N, K) given by (G.53) into the first term on the right side of (G.55) and the expression for F(M + 1, N + 1, K) given by (G.53) with N replaced by N + 1 into the second term on the right side of (G.55) to obtain:

$$\begin{aligned} F(M+2, N, K) = \frac{1}{\nu_\xi^2} \Big[& \bar{a}^2 F(M, N, K) \\ & - 2\bar{a}\,\nu_\eta F(M, N+1, K) + \nu_\eta^2 F(M, N+2, K) \Big] \end{aligned} \tag{G.56}$$

Finally, we solve equation (D.55) for F(M + 2, N, K) and substitute the result into the left side of (G.56). Upon rearrangement we obtain

$$\begin{aligned} F(M, N+2, K) = {} & 2\,\bar{a}\,\nu_\eta F(M, N+1, K) \\ & - (\bar{a}^2 + \nu_\xi^2 h^2) F(M, N, K) + \nu_\xi^2 F(M, N, K-2) \end{aligned} \tag{G.57}$$

Interchanging the roles of M and N, and ν_ξ and ν_η, we have the symmetric result:

$$\begin{aligned} F(M+2, N, K) = {} & 2\bar{a}\,\nu_\xi F(M+1, N, K) \\ & - (\bar{a}^2 + \nu_\eta^2 h^2) F(M, N, K) + \nu_\eta^2 F(M, N, K-2) \end{aligned} \tag{G.58}$$

We need one more result. Replacing N by N – 1 in equation (G.47) we have

$$\begin{aligned} (K-2) F(M, N, K) = {} & (K-2)\,\nu_\eta\,\bar{a}\,F(M, N-1, K) \\ & - (M-1)\,\nu_\xi \nu_\eta F(M-1, N-1, K-2) \\ & + (N-2)\,\nu_\xi^2 F(M, N-2, K-2) \\ & - \nu_\xi E(M, N-1, K-2) \end{aligned} \tag{G.59}$$

The second and third terms on the right side of (G.59) can be transformed into expressions involving K rather than K – 2 using equation (D.55). For the second term, we replace M by M – 1 and N by N – 1 in (D.55) and for the third term we replace N by N – 2 in (D.55). Upon substitution into (G.59) we obtain:

$$
\begin{aligned}
(K-2)\,F(M,N,K) = {} & (K-2)\,\nu_\eta\,\bar{a}\,F(M,N-1,K) - (M-1)\,\nu_\xi\nu_\eta\,F(M+1,N-1,K) \\
& - (M-1)\,\nu_\xi\nu_\eta\,F(M-1,N+1,K) \\
& - (M-1)\,\nu_\xi\nu_\eta\,h^2\,F(M-1,N-1,K) \\
& + (N-2)\,\nu_\xi^2\,F(M+2,N-2,K) \\
& + (N-2)\,\nu_\xi^2\,F(M,N,K) \\
& + (N-2)\,\nu_\xi^2 h^2\,F(M,N-2,K) \\
& - \nu_\xi\,E(M,N-1,K-2)
\end{aligned}
\tag{G.60}
$$

Next we replace N by N - 1 in equation (G.53) and substitute the result into the second term on the right of (G.60). In addition, we replace M by M - 1 in equation (G.54) and substitute the result into the third term on the right of (G.60). Finally, we replace N by N - 2 in equation (G.56) and substitute the result into the fifth term on the right of (G.60). Making these substitutions and rearranging, we obtain:

$$
\begin{aligned}
F(M,N,K) = \frac{1}{(K-M-N+1)} \Big[& (K-M-2N+3)\,\bar{a}\nu_\eta\,F(M,N-1,K) \\
& + (N-2)\,(\bar{a}^2 + \nu_\xi^2 h^2)\,F(M,N-2,K) \\
& - (M-1)\,\bar{a}\nu_\xi\,F(M-1,N,K) \\
& - (M-1)\,\nu_\xi\nu_\eta h^2\,F(M-1,N-1,K) \\
& - \nu_\xi\,E(M,N-1,K-2) \Big]
\end{aligned}
\tag{G.61}
$$

Interchanging the roles of M and N, and ν_ξ and ν_η we obtain

$$
\begin{aligned}
F(M,N,K) = \frac{1}{(K-M-N+1)} \Big[& (K-2M-N+3)\,\bar{a}\nu_\xi\,F(M-1,N,K) \\
& + (M-2)\,(\bar{a}^2 + \nu_\eta^2\,h^2)\,F(M-2,N,K) \\
& - (N-1)\,\bar{a}\nu_\eta\,F(M,N-1,K) \\
& - (N-1)\,\nu_\xi\nu_\eta h^2\,F(M-1,N-1,K) \\
& + \nu_\eta\,E(M-1,N,K-2) \Big]
\end{aligned}
\tag{G.62}
$$

Notice the + sign in the last term on the right side of (G.62) as compared with the - sign in the analogous term of (G.61). This is because the left side of equation (D.57) undergoes a change of sign when M and N, and ν_ξ and ν_η are interchanged, hence our formulas will be correct if we replace E by $-E$ whenever such an interchange is made

Now we are prepared to derive equations (D.61) through (D.67). Equation (D.61) is obtained from equation (G.52) by setting $M = N = 1$. Equation (D.62) is obtained from equation (G.61) by setting $M = K = 1$. Equation (D.63) is simply a rearrangement of equation (D.56) with $K = 1$. Equation (D.64) is obtained from equation (G.62) by setting $N = K = 1$. Equation (D.65) is simply a rearrangement of equation (D.56) with $K = 1$. Equation (D.66) is obtained from equation (G.61) by setting $M = 1$ and $N = 2$. Finally, equation (D.67) is obtained from equation (G.57) by setting $M = 1$ and replacing N by $N - 2$.

G.4 PROCEDURE FOR EVALUATING THE E FUNCTIONS

The E functions are defined by equation (D.58) which we repeat here for convenience:

$$E(M, N, K) = \frac{(\xi - x)^{M-1} (\eta - y)^{N-1}}{\rho^K} \Bigg|_1^2 , \quad \rho = \sqrt{(\xi - x)^2 + (\eta - y)^2 + h^2} \qquad \text{(D.58)}$$

The E functions required for Procedure 4 can be evaluated recursively using equation (D.59) which we also repeat here for convenience:

$$P(I) = (x_2 + x_1)\, P(I-1) - x_1 x_2\, P(I-2) \qquad \text{(D.59)}$$

where

$$P(I) \equiv A_2 x_2^{I-1} - A_1 x_1^{I-1}$$

Examination of Procedure 4 indicates that we need to calculate the following E functions:

a.	$E(2, 1, K-2)$	$K = 3, MXFK, 2$	
b.	$E(1, 2, K-2)$	$K = 3, MXFK, 2$	
c.	$E(1, N-1, -1)$	$N = 2, MXQ$	
d.	$E(M-1, 1, -1)$	$M = 2, MXQ$	
e.	$E(1, 1, K-2)$	$K = 3, MXK - 2, 2$	(G.63)

These functions can be evaluated using equation (D.59). For this purpose we set $E = P$ where x_1, x_2, A_1, and A_2 are defined respectively as:

a. $x_2 = \rho_2^{-2}$, $x_1 = \rho_1^{-2}$, $A_2 = (\xi_2 - x)/\rho_2$, $A_1 = (\xi_1 - x)/\rho_1$; $I = 1, \frac{MXFK - 3}{2}$

b. $x_2 = \rho_2^{-2}$, $x_1 = \rho_1^{-2}$, $A_2 = (\eta_2 - y)/\rho_2$, $A_1 = (\eta_1 - y)/\rho_1$; $I = 1, \frac{MXFK - 3}{2}$

c. $x_2 = (\eta_2 - y)$, $x_1 = (\eta_1 - y)$, $A_2 = \rho_2$, $A_1 = \rho_1$; $I = 1, MXQ - 1$

d. $x_2 = (\xi_2 - x)$, $x_1 = (\xi_1 - x)$, $A_2 = \rho_2$, $A_1 = \rho_1$; $I = 1, MXQ - 1$

e. $x_2 = \rho_2^{-2}$, $x_1 = \rho_1^{-2}$, $A_2 = 1/\rho_2$, $A_1 = 1/\rho_1$; $I = 1, \frac{MXK - 5}{2}$ (G.64)

G.5 PROCEDURE 6 RECURSIONS: EQUATIONS (D.99) → (D.102)

The equations in Procedure 6 are obtained from recombinations of equations (D.96), (D.97) and (D.98), which we repeat here for convenience:

$$\nu_\xi G(M+1, N) + \nu_\eta G(M, N+1) = \bar{a}\, G(M, N) \tag{D.96}$$

$$-(M-1)\nu_\eta G(M-1, N) + (N-1)\nu_\xi G(M, N-1) = D(M, N) \tag{D.97}$$

where

$$D(M, N) = \xi^{M-1}\eta^{N-1}\Big|_1^2 \tag{D.98}$$

Equation (D.100) is obtained from equation (D.96) by replacing M by M − 1 and rearranging. Equation (D.102) is obtained from equation (D.96) by replacing N by N − 1 and rearranging. Equation (D.99) is obtained from equation (D.97) by setting M = 1 and replacing N by N + 1. Equation (D.101) is obtained from equation (D.97) by setting N = 1 and replacing M by M + 1.

We note from equations (D.99) and (D.101) that the D functions must be evaluated for the two cases:

a. $D(1, N+1)$ $N = 1, MXQ$

b. $D(M+1, 1)$ $M = 1, MXQ$ (G.65)

This can be done recursively using equation (D.59). We have

a. $x_2 = \eta_2,\ x_1 = \eta_1,\ A_2 = \eta_2,\ A_1 = \eta_1;\ I = 1, MXQ$

b. $x_2 = \xi_2,\ x_1 = \xi_1,\ A_2 = \xi_2,\ A_1 = \xi_1;\ I = 1, MXQ$ (G.66)

G.6 CONTINUITY PROPERTIES OF THE H AND F INTEGRALS

In this section we prove that h^J H(M, N, K) is bounded as a function of P(x, y, z) if $J = K - M - N$ and is continuous everywhere and equal to zero when $h = 0$ if $J > K - M - N$. In addition, we show that g^J F(M, N, K) is continuous everywhere and equal to zero when $g = 0$ if $J > K - M - N + 1$.

We first note that

$$\rho > |\xi - x|$$

$$\rho > |\eta - y|$$

$$\rho > |h| \tag{G.67}$$

where

$$\rho = \sqrt{(\xi - x)^2 + (\eta - y)^2 + h^2}$$

It follows that

$$\rho^K \geqslant |h|^{J-1}\ |\xi - x|^{M-1}\ |\eta - y|^{N-1}\ \rho^3 \quad \text{where } J = K - M - N. \tag{G.68}$$

Hence we have

$$h^J\ H(M, N, K) \leqslant \iint_\Sigma \frac{|h|^J\ |\xi - x|^{M-1}\ |\eta - y|^{N-1}}{\rho^K}\ d\xi d\eta \leqslant |h| \iint_\Sigma \frac{d\xi d\eta}{\rho^3}$$

$$= |hH(1, 1, 3)| \tag{G.69}$$

From equation (G.24) we see that $|h\ H(1, 1, 3)| \leqslant 4\pi$.

Hence

$$|h^J\ H(M, N, K)| \leqslant 4\pi \text{ if } J = M + N - K \tag{G.70}$$

This shows that h^J H(M, N, K) is bounded when J = M + N - K. Now from equation (D.25) it is clear that for arbitrary J, h^J H(M, N, K) is continuous everywhere except perhaps at h = 0. However, we have

$$h^J \, H(M, N, K) = h^{J - (K - M - N)} \left[h^{K - M - N} \, H(M, N, K) \right] \tag{G.71}$$

The term in square brackets on the right is bounded by 4π from the result above, hence, if $J > K - M - N$ the expression on the right tends to zero uniformly as $h \to 0$. Thus h^J H(M, N, K) is also continuous at h = 0 and equal to zero there.

Before considering the F integrals we prove one additional result concerning the H integrals, namely that when either M or N is even, then H(M, N, K) is continuous everywhere, except when h = 0 and (x, y, 0) belongs to the perimeter of Σ. Without loss of generality, we assume that M is even. When M = 2, the result follows from equation (D.38) by noting from equation (D.40) that all F integrals are continuous everywhere, except perhaps when h = 0 and (x, y, 0) belongs to L. For M > 2, the result follows inductively from (D.38).

Next we show that g^J F(M, N, K) is continuous everywhere and equal to zero when g = 0 if $J > K - M - N + 1$. From the fact that $\rho = \sqrt{g^2 + \ell^2}$, we have in addition to the inequalities (G.67), the inequality

$$\rho > g \tag{G.71a}$$

Hence

$$\rho^K \geqslant |g|^{J-1} \, |\xi - x|^{M-1} \, |\eta - y|^{N-1} \, \rho \qquad \text{if } J = K - M - N + 2 \tag{G.72}$$

It follows that

$$|g^J \, F(M, N, K)| \leqslant \int_L g^J \frac{|\xi - x|^{M-1} |\eta - y|^{N-1}}{\rho^K} \, d\ell \leqslant \int_L g \, \frac{d\ell}{\rho} = gF(1, 1, 1) \tag{G.73}$$

From equation (D.60) it is easily shown that

$$|F(1, 1, 1)| \leqslant C_1 + C_2 |\ln g| \tag{G.74}$$

for some constants C_1 and C_2 independent of g, hence

$$|g^J \, F(M, N, K)| \leqslant g \left(C_1 + C_2 |\ln g| \right) \text{ if } J = K - M - N + 2 \tag{G.75}$$

This shows that $|g^J$ F(M, N, K)| tends to zero uniformly as $g \to 0$. From equation (D.40), it is clear that for arbitrary J, g^J F(M, N, K) is continuous everywhere except perhaps at g = 0 where $\rho = \sqrt{g^2 + \ell^2}$ may be zero. However, we have

$$g^J \, F(M, N, K) = g^{J - (K - M - N + 2)} \left[g^{K - M - N + 2} \, F(M, N, K) \right] \tag{G.76}$$

The term in square brackets tends uniformly to zero as $g \to 0$ from the result above so that $g^J\, F(M, N, K)$ does likewise when $J \geqslant K - M - N + 2$. Hence, $g^J\, F(M, N, K)$ is continuous everywhere and equal to zero when $g = 0$ if $J > K - M - N + 1$.

G.7 PROPERTIES OF H*

In this section we discuss the properties of H* as defined by equations (D.51) and (D.52), which we repeat here for convenience

$$H^*(M, N, K) = H(M, N, K) - \epsilon(M, N, K) \tag{D.51}$$

$$\epsilon(M, N, K) = 2\pi\, \nu(M, N, K)\, |h|^{M + N - K}$$

$$\nu(M, N, K) = \begin{cases} 0 \quad \text{if M or N is even} \\ \dfrac{[1\cdot 1\cdot 3\cdot 5 \cdots |M - 2|]\,[1\cdot 1\cdot 3\cdot 5 \cdots |N - 2|]}{[(K - 2)(K - 4)(K - 6)\ \cdots\ (K - M - N)]} \end{cases} \tag{D.52}$$

First we show that H* satisfies the same recursions as H, in particular that H* satisfies the recursions of Procedure 1 for $h \neq 0$ with the exception of the initial condition (D.41). For this purpose, it is sufficient to show that $\epsilon(M, N, K)$ satisfies the homogeneous recursions (D.42) → (D.48), i.e., the recursions with all F functions set identically zero. For this purpose we note from equation (D.52) that $\epsilon(M, N, K)$ satisfies:

$$\epsilon(M, N, K - 2) = \frac{h^2\,(K - 2)\,\epsilon(M, N, K)}{(K - M - N - 2)} \tag{G.77}$$

$$\epsilon(M + 2, N, K) = \frac{h^2\, M\epsilon(M, N, K)}{(K - M - N - 2)} \tag{G.78}$$

$$\epsilon(M, N + 2, K) = \frac{h^2\, N\epsilon(M, N, K)}{(K - M - N - 2)} \tag{G.79}$$

We note that the initial condition

$$\epsilon(1, 1, 1) = 2\pi |h| \tag{G.80}$$

Then equation (D.42) (with $F \equiv 0$ and H replaced by ϵ) follows from equation (G.77) with $M = N = 1$. Equation (D.43) follows from the (D.52) and the fact that M is even. Equation (D.44) follows from equation (G.79) with $M = K = 1$ and N replaced by $N - 2$. Equation (D.45) follows from equation (G.78) with $K = 1$ and M replaced by $M - 2$. Equation (D.46) follows from equation (G.79) with $M = 1$ and N replaced by $N - 2$ combined with equation (G.77) with $M = 1$ and N replaced by $N - 2$. Equation (D.47) follows from equation (D.52) and the fact that M is even. Finally, equation (D.48) may be obtained by subtracting (G.77) from the sum of (G.78) and (G.79), and then replacing M by M - 2.

Next we prove that H*(M, N, K) is continuous when (x, y, 0) belongs to the interior of Σ. From section (G.6) we know that H(M, N, K) is continuous everywhere when $K < M + N$ and bounded when $K = M + N$. However, when $K = M + N$, either M or N must be even since K is odd, hence, we know in addition that for $K = M + N$, H(M, N, K) is continuous everywhere except perhaps when (x, y, 0) belongs to the perimeter of Σ and $h = 0$. It follows from equation (D.51) that H*(M, N, K) is continuous when (x, y, 0) is in the interior of Σ and $K \leqslant M + N$. Hence, we consider only the case $K > M + N$. For this case we shall show that

$$H^*(M, N, K) = - \iint_{\Sigma^*} \frac{(\xi - x)^{M-1} (\eta - y)^{N-1}}{\rho^K} \, d\xi d\eta, \tag{G.81}$$

where Σ^* is the exterior of Σ, i.e., the whole $\xi - \eta$ plane minus the quadrilateral Σ. From equations (D.51) and (D.35) it is sufficient to show that

$$\epsilon(M, N, K) = \iint_{\xi - \eta \text{ Plane}} \frac{(\xi - x)^{M-1} (\eta - y)^{N-1}}{\rho^K} \, d\xi d\eta \tag{G.82}$$

To do this we let $(\xi - x) = |h| r \cos\theta$ and $(\eta - y) = |h| r \sin\theta$. Then

$$\iint_{\xi - \eta \text{ Plane}} \frac{(\xi - x)^{M-1} (\eta - y)^{N-1}}{\rho^K} \, d\xi d\eta$$

$$= |h|^{M+N-K} \int_0^\infty \int_0^{2\pi} \frac{r^{M+N-1}}{(1 + r^2)^{K/2}} (\cos\theta)^{M-1} (\sin\theta)^{N-1} \, dr d\theta \tag{G.83}$$

Hence, it is sufficient to show that

$$\nu(M, N, K) = \frac{1}{2\pi} \int_0^\infty \int_0^{2\pi} \frac{r^{M+N-1}}{\left(1 + r^2\right)^{K/2}} (\cos\theta)^{M-1} (\sin\theta)^{N-1} \, dr d\theta$$

$$= \left[\int_0^\infty \frac{r^{M+N-1}}{\left(1 + r^2\right)^{K/2}} \, dr \right] \left[\frac{1}{2\pi} \int_0^{2\pi} (\cos\theta)^{M-1} (\sin\theta)^{N-1} \, d\theta \right] \tag{G.84}$$

By symmetry, the second integral in square brackets is zero unless M and N are both odd. Hence, we need only consider the case when M and N are both odd.

$$\frac{1}{2\pi}\int_0^{2\pi}(\cos\theta)^{M-1}(\sin\theta)^{N-1}\,d\theta = \frac{4}{2\pi}\int_0^{\pi/2}(\cos\theta)^{M-1}(\sin\theta)^{N-1}\,d\theta \tag{G.85}$$

The first integral in square brackets can be put in similar form by setting $r = \tan\phi$ to obtain

$$\int_0^{\infty}\frac{r^{M+N-1}}{\left(1+r^2\right)^{K/2}}\,dr = \int_0^{\pi/2}(\sin\phi)^{M+N-1}(\cos\phi)^{K-M-N-1}\,d\phi \tag{G.86}$$

From integral tables (ref. 29) we have that

$$\int_0^{\pi/2}(\cos x)^{M-1}(\sin x)^{N-1}\,dx = \frac{1}{2}\frac{\Gamma(M/2)\,\Gamma(N/2)}{\Gamma\left(\frac{M+N}{2}\right)} \tag{G.87}$$

where Γ is the Γ function and

$$\Gamma\left(\frac{M}{2}\right) = \frac{1\cdot 1\cdot 3\cdot 5\ \cdots\ |M-2|}{2^{(M-1)/2}}\sqrt{\pi} \qquad \text{if M is odd} \tag{G.88}$$

Applying (G.87) to (G.86) and (G.85), and substituting into (G.84), we need only to show that

$$\nu(M, N, K) = \frac{1}{2\pi}\,\frac{\Gamma\left(\frac{M}{2}\right)\Gamma\left(\frac{N}{2}\right)\Gamma\left(\frac{K-M-N}{2}\right)}{\Gamma\left(\frac{K}{2}\right)} \tag{G.89}$$

Upon applying (G.88) to (G.89) and comparing with equation (D.52) we obtain the desired result.

G.8 VALIDITY OF REVERSE RECURSIONS (PROCEDURES 2 AND 5)

In this section we justify use of the initial condition (D.49) in the reverse recursion (D.50). The argument is precisely the same for the use of equation (D.68) as an initial condition for equation (D.69) and we therefore consider only equations (D.49) and (D.50) which we repeat here for convenience

$$H(1, 1, NHK + MXK) = 0. \qquad (NHK = 16) \tag{D.49}$$

$$H(1, 1, K-2) = \frac{1}{(K-4)} \left[h^2 (K-2)\, H(1, 1, K) - \sum_{1}^{4} \bar{a}\, F(1, 1, K-2) \right] \tag{D.50}$$

for K = NHK + MXK, 3, − 2.

Without loss of generality, we assume $(x, y, 0) \notin \Sigma$. (If $(x, y, 0) \in \Sigma$, we replace H by H* in which case we are dealing with (D.49) and (D.50) as applied to Procedure 3.) In either case, we have $\rho > d_H$ where d_H is defined as the minimum distance from (x, y, 0) to the perimeter of Σ. Then

$$H(1, 1, K + J) = \iint_{\Sigma} \frac{d\xi d\eta}{\rho^{K+J}} \leq \frac{1}{d_H^{\,J}} \iint_{\Sigma} \frac{d\xi d\eta}{\rho^{K}} = \frac{1}{d_H^{\,J}}\, H(1, 1, K) \tag{G.90}$$

It follows from the assumption of Procedure 2 $\left(|h| < \delta_h\, d_H\right)$ that

$$|h^J\, H(1, 1, K + J)| \leq \left| \left(\frac{h}{d_H}\right)^J H(1, 1, K) \right| = \delta_h^{\,J}\, |H(1, 1, K)| \tag{G.91}$$

Setting K = MXK and J = NHK we have

$$|h^{NHK}\, H(1, 1, NXK + MXK)| \leq \delta_h^{\,NHK}\, |H(1, 1, MXK)| \tag{G.92}$$

By substituting equation (D.49) into equation (D.50) for K = NHK + MXK and then successively solving for H(1, 1, K) with lower values of K, we find

$$H(1, 1, MXK) = \frac{(NHK + MXK - 2)}{(MXK - 2)}\, h^{NHK}\, H(1, 1, NHK + MXK) + F \text{ terms} \tag{G.93}$$

Since $\delta_h = .01$ we see from (G.92) that the first term on the right of (G.93) is negligible compared with H(1, 1, MXK), hence, it can be ignored. This is easily accomplished by setting H(1, 1, NHK + MXK) = 0.

REFERENCES

1. Kellogg, O. D.: *Foundations of Potential Theory.* New York, Dover Publishing Company, 1953.
2. Hess, J. L. and Smith, A. M. O.: *Calculation of Nonlifting Potential Flow About Arbitrary Three-Dimensional Bodies.* ES40622, Douglas Aircraft Company, 1962.
3. Rubbert, P. E.: *Theoretical Characteristics of Arbitrary Wings by a Nonplanar Vortex Lattice Method.* D6-9244, The Boeing Company, 1964.
4. Rubbert, P. E., et al: *A General Method for Determining the Aerodynamic Characteristics of Fan-in-Wing Configurations.* vol. I Theory and Application, technical report 67-61A, USAAVLABS, 1967.
5. Rubbert, P. E. and Saaris, G. R.: *3-D Potential Flow Method Predicts V/STOL Aerodynamics.* SAE Journal, vol. 77, September 1969, pp. 44–51.
6. Rubbert, P. E. and Saaris, G. R.: *Review and Evaluation of a Three-Dimensional Lifting Potential Flow Analysis Method for Arbitrary Configurations.* AIAA Paper, no. 72-188, January 1972.
7. Woodward, F. A.: *Analysis and Design of Wing-Body Combinations at Subsonic and Supersonic Speeds.* Journal of Aircraft, vol. 5, No. 6, pp. 528-534, November-December 1968.
8. Hess, J. L.: *Calculation of Potential Flow About Arbitrary Three-Dimensional Lifting Bodies.* Final Technical Report, MDC J5679-01, McDonnell Douglas, Long Beach, California, October 1972.
9. Roberts, A. and Rundle, K.: *The Computation of First Order Compressible Flow About Wing-Body Configurations.* AERO MA No. 20, British Aircraft Corporation, February 1973.
10. Woodward, F. A.: *Improved Method for the Aerodynamic Analysis of Wing-Body-Tail Configurations in Subsonic and Supersonic Flow.* Part I–Theory and Application, NASA CR-2228 pt 1, May 1973.
11. Morino, L. and Kuo, Ching-Chiang: *Subsonic Potential Aerodynamics for Complex Configurations: A General Theory.* AIAA Journal, vol. 12, no. 2, pp. 191-197, February 1974.
12. Tulinuis, J., Clever, W., Nieman, A., Dunn, K., and Gaither, B.: *Theoretical Prediction of Airplane Stability Derivatives at Subcritical Speeds.* NASA CR-132681, 1973.

13. Hess, J. L.: *Higher Order Numerical Solution of the Integral Equation for the Two-Dimensional Neumann Problem.* Computer Methods in Applied Mechanics and Engineering, vol. 2, no. 1, February 1973, pp. 1–15.

14. Mercer, J. E., Weber, J. A., and Lesferd, E. P.: *Aerodynamic Influence Coefficient Method Using Singularity Splines.* NASA CR-2423, December 1973.

15. Lamb, H.: *Hydrodynamics.* New York, Dover Publishing Company, 6th edition, 1945.

16. Weber, J. A., et al: *A Three Dimensional Solution of Flows Over Wings with Leading-Edge Vortex Separation.* AIAA Paper, no. 75-866, June 16-18, 1975.

17. Brune, G. W., et al: *A Three Dimensional Solution of Flows Over Wings with Leading-Edge Vortex Separation.* Part I–Engineering Document, NASA CR-132709, September 1975.

18. Karamcheti, K.: *Principles of Ideal-Fluid Aerodynamics.* New York, John Wiley and Sons, Inc., 1966.

19. Van Spiegel, E: *Boundary Value Problems in Lifting Surface Theory.* Verslagen en Verhandelingen, 22, National Luchtvaart-laboratorium, Amsterdam, 1959.

20. Rowe, W. S.: *Collocation Method for Calculating the Aerodynamic Pressure Distributions on a Lifting Surface Oscillating in Subsonic Compressible Flow.* AIAA Symposium on Structural Dynamics and Aeroelasticity, Boston, Mass., August, 1965, pp. 31–45.

21. Abbott, I. H. and Von Doenhoff, A. E.: *Theory of Wing Sections.* New York, Dover Publishing Company, 1953.

22. Dahlquist, G. and Bjorck, A.: *Numerical Methods*, Englewood Cliffs, New Jersey. Prentice Hall, Inc., 1974.

23. Marsden, D. J., Simpson, R. W., and Rainbird, W. J.: *An Investigation Into the Flow Over Delta Wings at Low Speeds with Leading Edge Separation.* Rep. 114, ARC 20409, The College of Aeronautics, Cranfield, February 1958.

24. Peckham, D. H.: *Low-Speed Wind Tunnel Tests on a Series of Uncambered Slender Pointed Wings with Sharp Edges.* R & M No. 3186, British Aeronautical Research Council, 1961.

25. Polhamus, E. C.: *A Concept of the Vortex Lift of Sharp-Edge Delta Wings Based on a Leading-Edge-Suction Analogy.* NASA TN D-3767, December 1966.

26. Tinoco, E. N. and Mercer, J.E.: *FLEXSTAB. A Summary of the Functions and Capabilities of the NASA Flexible Airplane Analysis Computer System.* NASA CR-2564, December 1975.

27. Hess, J., Johnson, F. T., and Rubbert, P. E.: *Panel Methods Lecture Notebook.* pp.3-20 to 3-28, AIAA Short Course on Panel Methods, July 1978.

28. Bois, G. Petit: *Tables of Indefinite Integrals.* Dover Publications, Inc., New York, 1961.

29. Selby, S. M. (ed): *Standard Mathematical Tables.* 15th edition, Blackwell Scientific Publications, Oxford, England, 1967.

1 Report No
NASA CR-3079

2 Government Accession No

3 Recipient's Catalog No

4 Title and Subtitle
A General Panel Method for the Analysis and Design of Arbitrary Configurations in Incompressible Flows

5 Report Date
May 1980

6 Performing Organization Code

7 Author(s)
Forrester T. Johnson

8 Performing Organization Report No
D6-43808

9 Performing Organization Name and Address
Boeing Commercial Airplane Company
P.O. Box 3707
Seattle, Washington 98124

10 Work Unit No

11 Contract or Grant No
NAS2-7729

12 Sponsoring Agency Name and Address
National Aeronautics and Space Administration
Washington, DC 20546

13 Type of Report and Period Covered
Contractor Report
Task III, Cat. I

14 Sponsoring Agency Code

15 Supplementary Notes
Ames Technical Monitor: Larry L. Erickson
Final Report

16 Abstract

An advanced method for solving the linear integral equations of incompressible potential flow in three dimensions is presented. Both analysis (Neumann) and design (Dirichlet) boundary conditions are treated in a unified approach to the general flow problem. The method is an influence coefficient scheme which employs source and doublet panels as boundary surfaces. Curved panels possessing singularity strengths, which vary as polynomials are used, and all influence coefficients are derived in closed form. These and other features combine to produce an efficient scheme which is not only versatile but eminently suited to the practical realities of a user-oriented environment. A wide variety of numerical results demonstrating the method are presented.

17 Key Words (Suggested by Author(s))
Analysis
Design
Higher order
Influence coefficient
Linear
Panel method
Potential flow
Subsonic
Three dimensional

18 Distribution Statement
Unclassified—Unlimited

Subject Category 02

19 Security Classif. (of this report)
Unclassified

20 Security Classif. (of this page)
Unclassified

21 No. of Pages
193

22 Price*
$9.00

* For sale by the National Technical Information Service, Springfield, Virginia 22161

NASA-Langley, 1980

27. Hess, J., Johnson, F. T., and Rubbert, P. E.: *Panel Methods Lecture Notebook.* pp.3-20 to 3-28, AIAA Short Course on Panel Methods, July 1978.

28. Bois, G. Petit: *Tables of Indefinite Integrals.* Dover Publications, Inc., New York, 1961.

29. Selby, S. M. (ed): *Standard Mathematical Tables.* 15th edition, Blackwell Scientific Publications, Oxford, England, 1967.